The design and development of a time-resolved electron diffractometer for the investigation of molecular dynamics

Matthew Scott Robinson

PhD

University of York

Chemistry

January 2015

"A friend once told me that the first sign of madness was swearing at inanimate objects. I told them that they had obviously never done a PhD in science."

Dr. Paul D. Lane, 2014.

Abstract

A time-resolved gas electron diffractometer has been designed and constructed to study the photoinduced dynamics of molecular systems. An ultrafast pulsed electron beam is created by the ionisation of a thin-film gold photocathode, using the third harmonic of a femtosecond Ti:Sapphire laser, and accelerated across a potential of up to 100 kV. Time-averaged diffraction from a polycrystalline platinum sample has been carried out in order to calibrate the apparatus, and the results have been shown to match well with theory. In addition to the design of the apparatus, novel experimental methods and techniques have been implemented, and software for analysing and extracting data has been developed.

Other calibration experiments have been carried out, including measuring the diameter of the pulsed electron beam produced, and how this varies as a solenoid magnetic lens acts to focus the beam. An optimal FWHM beam width of 1.2 mm has been observed at the detector for pulses containing 10^4 electrons. The time-zero position between a pump laser and probe electron beam has been found by studying the laser-induced plasma emitted from a copper mesh, and methodologies have been established for grating-enhanced ponderomotive experiments to be carried out to determine the duration of the pulsed electron beam.

Extensive electron pulse dynamics simulations, using SIMION and General Particle Tracer, accompany the experimental work. These have allowed for a full and thorough understanding of how both the duration and transverse size of the pulse changes as it propagates through the apparatus with and without the influence of the magnetic lens. It has also allowed for the ultimate time resolution of the apparatus to be determined as 416 fs.

Quantum chemical calculations have been carried out for dimethyl disulfide and diethyl disulfide, molecules that readily dissociate along the S–S bond upon excitation using a low-energy ultraviolet light. This has included a full mapping of the reaction potential-energy surface, and study of the molecular dynamics of the molecules in the ground and excited states. These studies have shown that the molecules are suitable candidates for early time-resolved gas electron diffraction studies using the new apparatus.

Table of Contents

List of tables

List of figures

List of accompanying material

The appendices relating to the work presented in this thesis contain tables, drawings and code, which in total run to several hundred pages, and so have been presented as a DVD which can be found attached to the back cover of this book.

Appendix A – Technical drawings of the time-resolved electron diffractometer and accompanying equipment.

Appendix B – Extended results from simulations performed for the time-resolved gas electron diffractometer.

Appendix C – Related computational programs and code.

Appendix D – Models and parameters relating to the gas electron diffraction refinement of $(XMe_2Si)_2C(SiMe_3)_2$ (X = H, Cl, Br).

Acknowledgements

This PhD has been an experience that I have greatly enjoyed, yet, it never would have been possible, or as enjoyable, without the help of the following people, whom I would like to thank:

First and foremost, my supervisor, Dr Derek Wann, for providing the opportunity in the first place, as well as his patience and advice throughout the project.

The rest of the Wann group, past and present, including Dr Paul Lane, Stuart Young, Pedro Nunes, Lennart Remakers, Conor Rankine and Robin Virgo, for your good humour, advice and creating a welcoming work environment.

Dr Carole Morrison and Dr John Moore, for acting as my secondary supervisors at Edinburgh and York, respectively, willingly providing their knowledge and advice when asked and needed.

Professor Eleanor Campbell, Dr Olof Johansson and Elvira Bohl, of The University of Edinburgh, for providing the Wann group the opportunity to use their femtosecond laser, skills and knowledge at the start of this project.

Dr Michał Kochman, Professor Anita Jones at Edinburgh and Dr Alexandra Simperler of the NSCCS for their help in teaching me more about computational chemistry and molecular spectroscopy, and always being willing to provide further help when asked.

Dr Gilles Rousseau of Allectra, Dr Oleg Nerushev, David Paden and Dr Konstantin Kamenev of Edinburgh, and Dave Coulthard, Dr Chris Rhodes, Chris Mortimer, Wayne Robinson, Jon Hamstead, and Professor Jun Yuan of York, for their help and advice in the design and manufacture of multiple components relating to the apparatus presented here.

Professor Dwayne Miller and Dr Stuart Hayes of DESY, Hamburg, for their help, advice and experience of where to start designing a time-resolved electron diffractometer provided at the very beginning of this project. As well as Dr Will Bryan, of Swansea University, for the opportunity to work with him at the Central Laser Facility, and to learn so much more about lasers.

The University of Edinburgh, University of York, EPSRC, RSC, Central Laser Facility and the Moray Fund for providing places to work, lasers, and funding for conferences and projects, big and small.

Everyone in room 203 in Edinburgh and A057 in York for their advice, providing a great work environment, and plentiful supply of cake.

And finally, to my parents, my brothers and my friends, for always being awesome, supportive, putting up with me talking about work, my terrible jokes and generally being the best people that I know.

I thank you all.

Declaration

I declare that the work presented here, performed at both The University of Edinburgh and The University of York, is my own, unless stated otherwise by reference.

Matthew Robinson

Chapter 1. Introduction

1.1. Motivation for time-resolved electron diffraction

A fundamental concern of contemporary chemistry is to understand better the processes that take place within molecules as they undergo reactions with other molecules, as well as to study changes in structure initiated by external influences, such as light and heat. Although chemical reactions have been studied for hundreds of years, it is only within the last decade or so that we have truly been able "watch" a reaction take place on the atomic or molecular scale.

In many experiments the progress of a chemical reaction is measured by observing changes in the properties of the material of interest, such as temperature, mass, colour, resistivity, volume, or density. One might note whether the reagents are solids, liquids, gases, or in solution, the specific wavelengths of light that are absorbed or emitted, and how the atomic nuclear spins respond to changes in a magnetic field. From such spectroscopic measurements we are able to *infer* information about how molecular structures might change over time, and make educated guesses about possible reaction pathways from the starting materials to the end products. However, none of these techniques allow us to see *directly* the atoms involved and how they interact with one another in real time during a reaction.

Diffraction methods, such as those that utilise X-rays, neutrons, or electrons, can tell us accurately the structure of a molecule. However, until recently, only the time-averaged structures of molecules have been obtainable because of the use of continuous diffraction probes and detector limitations. Yet, with the advent of ultrafast pulsed lasers, it has become possible to create new diffraction sources that allow molecular structures to be observed on much shorter timescales than before, which in turn allows changes in molecular structures to be monitored throughout the course of a reaction. Significant successes in studying molecular dynamics using time-resolved X-ray diffraction have been well documented,[1,2] although these experiments generally require the use of large and expensive synchrotron sources for the desired time resolution and beam flux. Whilst such studies are important, it is also beneficial to be able to carry out similar experiments in a more cost-effective manner using table-top apparatuses in university laboratories.

Time-resolved electron diffraction (TRED) is one of the techniques that can provide such an opportunity. Although some TRED experiments have been performed at larger facilities using MeV electron sources,[3–5] there have also been many successes with smaller, laboratory-based TRED experiments.[6–9] TRED can allow us to observe directly how atoms interact with their neighbours, and to understand better the dynamic processes in molecules. Early experiments have imaged the melting of solids[10] and the dissociation of gas-phase molecules,[11] and have studied the subtle changes in structure within an organic molecular crystal during a reversible ring opening / closing event.[6]

Here in the Wann group there is a unique opportunity to combine the old with the new. With an already strong background in time-averaged gas electron diffraction, our aim was to take that knowledge and experience and apply it to develop a new TRED apparatus and associated experimental methods. It is for these reasons that the group sought to develop a novel time-resolved gas electron diffractometer (TRGED), which became the goal of this thesis.

1.2. Overview of a time-resolved gas electron diffraction experiment

Electron diffraction, demonstrated pictorially in Figure 1.1, is a well-established technique, dating back over 80 years.[12] In a typical experiment electrons are extracted from a suitable cathode source, such as a tungsten wire filament, and are accelerated across a potential between the source and a grounded anode; the electrons pass through an aperture in the anode, and travel through a vacuum towards a molecular sample. As the electrons interact with the sample they are scattered according to diffraction laws (see Section 2.1.1), and go on to create a molecule-specific diffraction pattern at a suitable electron detector. If the sample happens to be a single crystal these patterns will appear as distinct spots of varying intensities; if the sample is powdered, liquid, or gaseous, the patterns will consist of a series of concentric rings. By analysing these patterns, accurate geometries of the molecular structures can be determined for the samples.
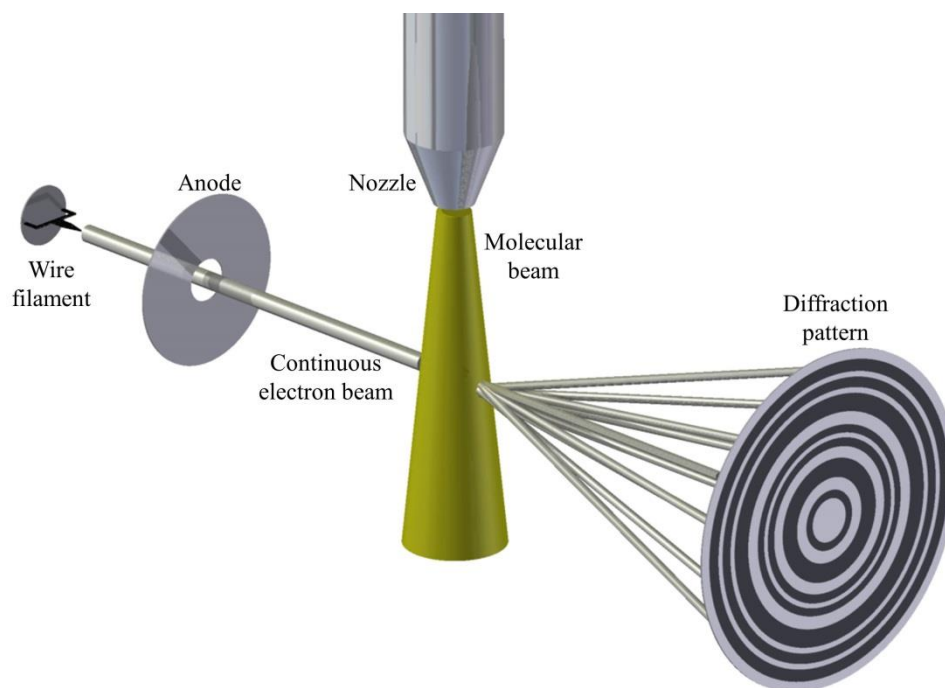
Figure 1.1: Diagram depicting the basics of a gas electron diffraction experiment. A continuous electron beam (silver) is created by passing a current through a tungsten filament, before being accelerated towards a grounded anode. The electron beam propagates towards a molecular beam (yellow) emitted from a nozzle, where the electrons interact with the sample and diffract from it. The diffracted electrons then travel towards a detector where the diffraction pattern is recorded.

Until recently, most electron diffraction experiments used continuous beams of electrons, with data collected over a period of a time, typically ranging from a few seconds to several minutes. During the period of the data collection, the continuous electron beam will observe a series of slightly different structures for the sample, due to many low-lying vibrational states being populated. As the time taken to collect the data is much longer than the duration of these vibrations, the information about the structure is essentially blurred, and hence the data obtained are time averaged. The idea of TRED is to not only remove some of this "blur" by capturing near instantaneous images of vibrationally cooled ground-state molecules, but also to monitor how a molecular structure may change upon excitation. This can be achieved by using ultrashort pulses of electrons, rather than the continuous beam, and using a laser pulse to induce excitation to higher electronic states.

In gas-phase experiments, vibrationally cooled samples are obtained by introducing the sample *via* a pulsed, supersonic expansion nozzle. This will ideally produce a gaseous sample with all of the molecules in the same vibrationally cooled

state. Figure 1.2 shows the basics of a TRED experiment where, prior to the electron probe arriving at the sample, the molecules can be excited with a laser pulse, inducing a change in their structure. By varying the delay between the arrival of the laser and the electrons at the sample it is possible to capture images at different points during any structural changes. These individual images can then be pieced together, like the frames on a film reel, to produce a "molecular movie". This method has the potential to allow for the observation of individual atoms within a molecule interacting with one another over time, including whilst undergoing a reaction. Although Figure 1.2 shows a set-up for a gas-phase experiment, the sample could easily be replaced by a polycrystalline solid or a thin single-crystal solid.
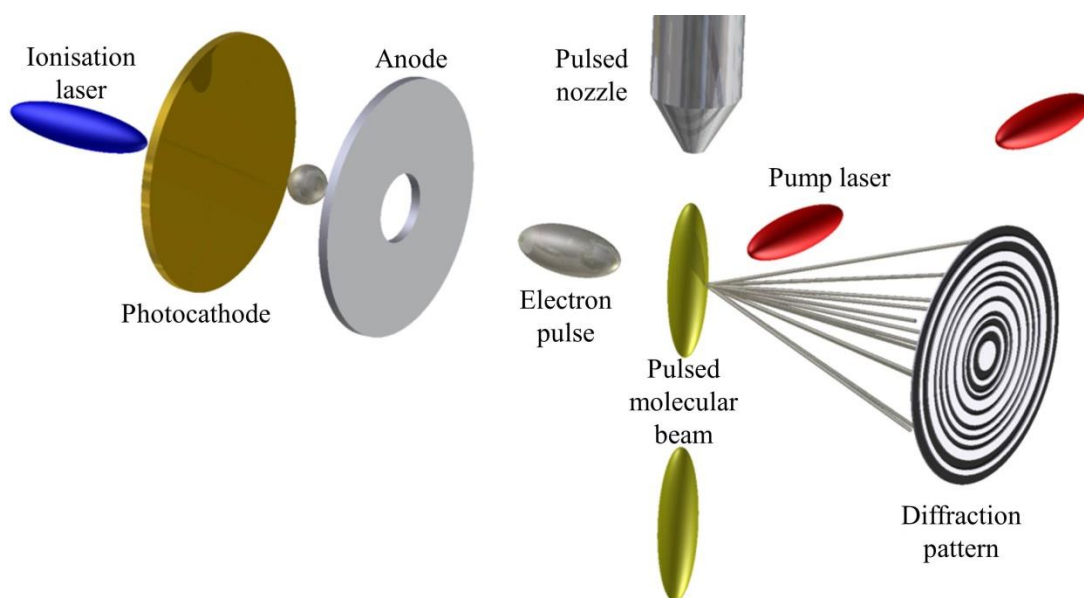
Figure 1.2: Diagram showing the basic TRGED experiment. A pulsed electron beam (silver) is created by the ionisation of a gold photocathode using a pulsed laser (blue), and accelerated towards a grounded anode. The electron beam then interacts with a pulsed molecular beam (yellow), from a pulsed nozzle, which has been excited by a pump laser pulse (red). The electrons diffract from the sample and scatter towards a detector where the diffraction pattern is recorded.

1.3. History and development of time-resolved gas electron diffraction

In 1924 Louis de Broglie presented his wave-particle duality theorem,[13] stating that all particles have wave-like properties; this means that, given the right conditions, electrons can diffract from molecular samples and create interference patterns. This was later confirmed by Davisson and Germer,[14] and by Thomson[15] who obtained diffraction patterns from crystalline samples that agreed with Bragg's

laws.[16] Several years earlier, Peter Debye had demonstrated that it was possible to obtain diffraction patterns from gaseous samples using X-rays.[17] In 1928, Mark and Wierl combined these ideas to perform the first gas electron diffraction (GED) experiments.[12]

Since these fundamental experiments were undertaken, electron diffraction has become a staple technique in determining the structures of countless molecules in the gas phase. However, as already mentioned, most of the molecular structures studied have been in the ground electronic state and averaged over many vibrational states. By the 1980s the goals of structural chemistry investigations were progressing from solely studying static molecular structures towards understanding better how those structures change over time. And so the electron diffraction technique started to evolve too.

In 1983, Ischenko *et al.* devised a method of creating an electron beam that would allow molecules to be studied on the microsecond timescale.[11] Their "stroboscopic beam" was created using electromagnetic deflection plates to chop a continuous electron beam into a series of pulses, which were then used to study the photodissociation of trifluoroiodomethane (CF_3I). By implementing the pump-probe technique,[18] an electron probe pulse arrived at different time intervals shortly after a laser pump pulse had excited the CF_3I molecules. This allowed for the photodissociation of the iodine atom from the rest of the molecule to be studied as a series of diffraction images, representing the first step towards time-resolved electron diffraction.

Until this point, data from most diffraction experiments were recorded using photographic plates or films. This was slow and cumbersome, and meant that the photographic medium had to be replaced after each exposure. Ewbank *et al.* implemented a new method of collecting data that used a phosphor screen and a photodiode array to detect electrons.[19] Data could be recorded and viewed almost instantaneously on a computer. There was also the added bonus that no films had to be replaced, increasing the number of measurements that could be made and reducing the time required between experiments. Additionally, the phosphor screen would only respond to the arrival of electrons, and not any stray light that could affect the quality of the image, as was the case when using a photographic medium.

Ewbank furthered the field of electron diffraction again a few years later. The shortest electron pulse that Ischenko's apparatus could produce was limited by how fast the electromagnetic deflection plates could be switched on and off. Ewbank showed that, by using nanosecond pulsed excimer lasers and a photocathode, he could achieve much shorter electron pulses.[20] This is because an electron pulse produced by the ionisation of a photocathode will have similar spatial and temporal properties to the laser pulse used to create it.[21] With this Ewbank was able to observe the photofragmentation of carbon disulfide, albeit only with nanosecond resolution.[20] Yet, with the advent of femtosecond lasers,[18] the observation of changes in molecular structures on ultrafast timescales soon became a reality.

During the 1990s development of time-resolved electron diffraction using ultrashort electron pulses was undertaken by Zewail *et al.*[22–25] Not only were they able to achieve electron diffraction on the picosecond timescale using a 50 kV accelerating potential, they also developed a significant body of theory to improve the technique.[23]

Most of the early TRED experiments focussed on observing large structural changes in single-atom systems, such as the melting process of polycrystalline aluminium,[10] or involved studying small molecules with heavy atoms and well-defined parameters, such as the elimination reactions of halogenated ethane analogues.[25] Only recently has the Miller group successfully carried out TRED experiments for larger organic and biological samples.[6,26] Such systems exhibit subtle structural changes, though the results are no less important and may have a significant impact on the wider chemical and biological worlds.

1.4. Current work in the field of time-resolved electron diffraction

The Miller group is considered to be one of the leaders in the field of TRED, having influenced almost every aspect of the technique, including gas[27] and crystal[26] diffraction, using both kilovolt (keV)[21] and megavolt (MeV)[28] electrons. Early work by Miller and his then student Bradley Siwick focussed on the development and theory of kilovolt TRED experiments. This included showing that the velocity distribution of electrons in a pulse has a linear chirp due to the space-charge effect that arises from Coulombic repulsions between electrons, and that consequently pulse durations could be controlled using electric fields.[29] In terms of practical

studies they observed the melting process of polycrystalline aluminium[10] and later that of bismuth.[30] The group also developed methods to characterise the duration of an electron pulse with the use of lasers and the ponderomotive scattering technique.[31–33] More recently they succeeded in observing the photoinduced dynamics of organic molecules, such as the motions that cause the insulator-to-metallic phase transition in an ethylenedioxytetrathiafulvalene complex [(EDO-TTF)$_2$PF$_6$],[26] as well as the ring opening / closing reaction of 1,2-bis(2,4-dimethyl-5-phenyl-3-thienyl)perfluorocyclopentene, shown pictorially in Figure 1.3.[6]
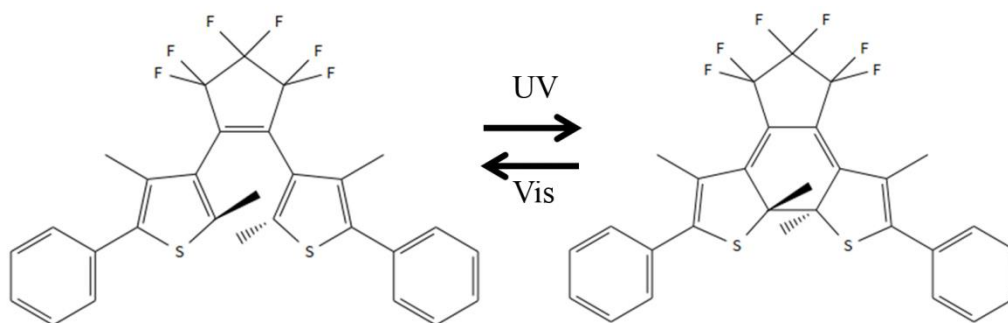
Figure 1.3: Reversible ring opening / closing reaction of 1,2-bis(2,4-dimethyl-5-phenyl-3-thienyl)perfluorocyclopentene. The image is redrawn from an image in Ref. 6.

After leaving the Miller group Siwick continued his work on TRED, first collaborating with Luiten *et al.* to develop radio-frequency (RF) compressed electron guns to yield shorter electron pulses.[34] Later, at a similar time to Miller, Siwick *et al.* successfully demonstrated the ability to measure the duration of an RF-compressed electron pulse using the ponderomotive scattering technique.[35] More recently Siwick has shown how the duration of an electron pulse varies with the charge density within the packet, by analysing pulses with different numbers of electrons and varying accelerating potentials.[7] His group has also investigated the photoinduced structural changes that cause the semiconducting-to-metal transition in polycrystalline VO$_2$.[36]

Other groups have also attempted to create shorter electron pulses by minimising the expansion of a pulse due to Coulombic repulsion, though they have done this without the use of RF cavities. One method, set out by Geiser and Weber, makes use of mode-locked lasers to produce a train of low-intensity light pulses to produce an equivalent train of low-density electron pulses, thus reducing Coulombic repulsion

effects.[37,38] Weber also worked on theory underpinning a reflectron electron gun,[39] which utilises equipment, commonly used to improve the resolution of mass spectrometry experiments, to produce ultrashort electron pulses. A design for a full reflectron gun apparatus was later published by Schwoerer *et al.*,[40] but appears not to have been built. Instead, Schwoerer *et al.* have focussed on embracing the space-charge broadening to create electron pulses with durations of several picoseconds.[9,41] After interacting with a sample for which a structural change has been induced, these picosecond pulses pass through the deflection plates of a streak camera, causing the pulse to be deflected in the transverse direction. As a result, a single point on a diffraction pattern is stretched in a fashion that allows one to observe the entire temporal profile of the pulse all at once and, therefore, see how the diffraction pattern changes as a result of the structural change. This has the potential to allow the observation of the entire molecular dynamics of a sample from a single shot of electrons, rather than by combining data from multiple pump-probe experiments.

The previously mentioned MeV apparatus of Miller *et al.*[28] is not the only one of its kind; nor was it the first to be built. In 2006 Hastings *et al.* observed the laser-induced melting of aluminium using relativistic electron diffraction at the SLAC National Acceleration Laboratory at Stanford.[3] MeV accelerating voltages were used to create electrons travelling at relativistic speeds, thus reducing the effects of Coulombic repulsion that would stretch an electron pulse; this has the potential to allow molecular dynamics to be studied with better time resolution compared to experiments using a keV apparatus. More recently, similar experiments involving the melting of gold have been carried out by Musumeci *et al.* at UCLA using a 3.5 MeV device.[4] Li *et al.* have also investigated the melting of gold samples using MeV TRED at the Tsinghua Thomson Scattering X-ray source in China,[5] although they combined this with an RF deflection cavity, which performed a similar function to the steak camera technology used by Schwoerer *et al*. to capture the full dynamics using a single pulse. Furthermore, the Wann group have been involved in the design of a new relativistic electron diffractometer at Daresbury Laboratory, which utilises a retired synchrotron electron injector as its electron gun.[42,43] To date static diffraction patterns have been recorded for platinum thin-film samples produced in York.[44] Figure 1.4 shows a diffraction pattern collected using several hundred electron pulses, with each pulse containing approximately 10^7 electrons, as well as a pattern

produced using a single pulse. As one can see from this single-shot image, the diffraction rings are clearly present, although not nearly as well defined as those in the pattern that uses several hundred shots. This, however, is an important first step towards carrying out practical single-shot TRED experiments.
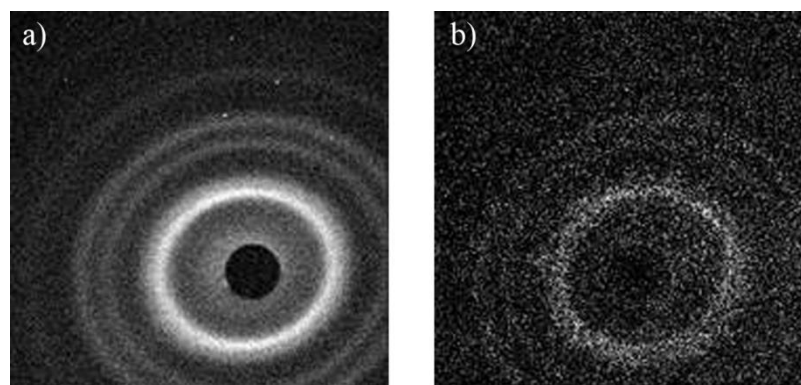
Figure 1.4: Diffraction patterns for polycrystalline platinum, collected using the Daresbury pulsed MeV electron gun, using a) several hundred electron pulses, and b) a single electron pulse.

Other groups have taken the basic ideas of TRED and moved in slightly different directions. For example, Zewail has now developed techniques for ultrafast electron microscopy (UEM), performing experiments that include mounting DNA nanostructures across thin porous carbon films, before exciting the vibrational modes of the carbon film. This excitation in turn excites the DNA, causing changes in its nanostructure that can be observed using UEM. From this they are able to measure the force constants relating to the oscillations within the DNA molecules.[45] Another experiment investigated the negative thermal expansion (*i.e.* contraction) of metal–cyanide nanoparticles as they were heated.[46] Here, nanoparticles of $Fe(pyrazine)Pt(CN)_4$ on a graphite substrate were cooled to 90 K, and then rapidly heated with a train of laser pulses, causing the nanoparticles to decrease in size. Initial electron diffraction experiments on the nanoparticle had suggested that the particles would shrink as the reciprocal space of the nanoparticle increased after laser exposure. This was later confirmed with UEM, where they were able to measure the change in size of the nanoparticle on the nanosecond timescale.

Another alternative TRED experiment has been implemented by Fill and Centurion *et al.* Initially they used ultrashort electron pulses to monitor the laser-induced plasmas that are required for high-harmonic systems.[47] Changes in the

plasma field were studied in the hope that this would lead to an improved understanding of ionisation processes. More recently Centurion *et al.* have begun using ultrafast laser pulses to induce rotational wavepackets in gaseous samples, producing a distribution of non-adiabatically aligned molecules in a field-free region; the structures of these molecules can then be studied using ultrafast electron diffraction.[8,48,49] This new method should help to reduce the loss of molecular structural information caused by the random alignment of molecules in a gaseous sample.

Meanwhile, efforts are ongoing to find new and better electron sources. The main focus of this work concerns sources that produce bunches of electrons with longer transverse coherence lengths within an electron pulse, allowing for improved spatial resolution of the diffraction pattern, yielding an increase in useful structural information. This may involve replacing the common gold thin-film photocathode with a metallic nanotip,[50–52] or using laser-cooled gas sources, which have been shown to give highly coherent electron beams that could be used in diffraction experiments.[53]

1.5. Why electron diffraction?

Electrons are not the only probe that can be used for diffraction experiments; as mentioned earlier, both neutrons and X-rays can also be used. However, each probe diffracts from a sample *via* different physical means. X-rays interact with the cloud of electrons that surrounds an atom, electrons interact with the charge gradient surrounding the atomic nucleus, whilst neutrons scatter from the nuclei themselves. One might therefore expect neutrons to be best suited to observing how the atoms in a molecule interact with one another during a reaction. However, while suitable for time-averaged single crystal diffraction experiments, most neutron sources are generated by spallation processes, which makes it difficult to produce the pulsed beam of particles needed for time-resolved diffraction experiments. One could conceive of implementing a shutter system to make a neutron version of the "stroboscopic beam" discussed in Section 1.3, but it would be extremely difficult to create a pulse of neutrons that was hundreds of femtoseconds long using this method, and with a sufficiently large flux to allow data to be collected in a timely manner. It is for these reasons that neutron diffraction is generally only used for analysing stable solid-state samples, where high-quality data can be recorded over an

extended period of time; short-lived and less stable systems are more commonly investigated using X-rays and electrons.

Time-resolved X-ray diffraction has already been routinely used to study the dynamics of small molecules and biological systems.[1,2] However, X-rays deposit far more energy into a sample than electrons do for the same number of scattering events.[29] This may damage the sample and is an important consideration when performing reversible experiments on crystalline samples. It is also important to note that most ultrafast X-ray experiments make use of synchrotron sources and so are necessarily performed in relatively few facilities. Whilst work on new table-top X-ray sources based on ultrafast lasers is lowering these barriers,[54] for now the technology is not yet sufficiently developed to perform gas-phase studies in a cost-efficient manner.

It is for these reasons that we have chosen the electron, with TRGED being the most effective and efficient method for analysing the dynamics of photoexcited structural changes in gas-phase molecules. The rest of this thesis details the theory underpinning electron diffraction (including TRGED), as well as the development of a novel apparatus that will allow both time-averaged and time-resolved experiments to be undertaken.

Chapter 2. Background theory

2.1. Introduction to gas electron diffraction

This section will discuss the theory and practice necessary to interpret the information contained within a diffraction pattern allowing a molecular structure to be determined. To provide context for this, examples will be taken from the studies of $(SiXMe_2)_2C(SiMe_3)_2$ (X = H, Cl, Br), the refinements for which were performed by myself during the first six months of my PhD using data that were collected several years previously, but not analysed. This work is complete, and has been published in *J. Phys. Chem. A*. A copy of the article can be found in the "Associated publications" section of this thesis, with molecular models and input parameters relating to these refinements being presented in Appendix D.

The equations and derivations presented in the next section relating to gas electron diffraction scattering theory, whilst accurate, have been simplified for ease of reading. Full equations and derivations on gas electron diffraction theory can be found in "*Stereochemical Applications of Gas-Phase electron Diffraction – Part A*" by Hargittai and Hargittai.[55]

2.1.1. Gas electron diffraction theory

Generally, a gas electron diffraction pattern will appear as a series of concentric rings, similar to those shown for $(SiClMe_2)_2C(SiMe_3)_2$ in Figure 2.1, caused by the scattering of electrons from the randomly orientated molecules in the gaseous sample. Where these electrons hit the detector depends on a number of factors including the energy of the electrons and the types of atoms from which they are scattered.
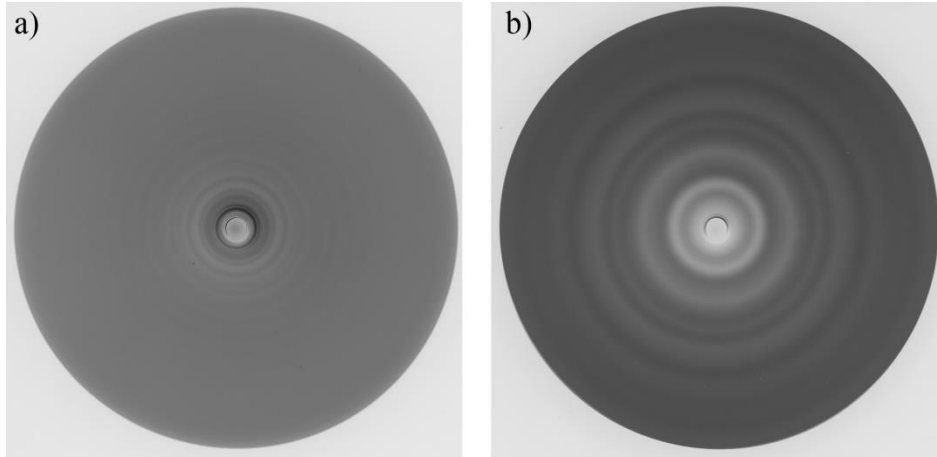
Figure 2.1: Examples of gas electron diffraction patterns for $(SiClMe_2)_2C(SiMe_3)_2$ collected at a) a short sample-to-detector distance, and b) a long sample-to-detector distance.

Electrons are scattered according to the charge gradient between the nucleus of an atom and its electrons; large and heavy atoms, with more electrons and protons, have a larger scattering cross section than their smaller counterparts. As with other diffraction techniques, the degree of scattering observed is also dependent on the wavelength, λ, of the probing medium. The wavelength of an electron can be determined using the de Broglie equation (Equation 2.1):

$$\lambda = \frac{h}{m_e v_e},$$ Eq. 2.1

where h is Planck's constant, m_e is the mass of an electron and v_e is the relativistic electron velocity, which is dependent on the accelerating potential, V, applied to the electrons. Knowing this, the de Broglie equation can be written as Equation 2.2:

$$\lambda = \frac{h}{\sqrt{2m_e eV}} \frac{1}{\sqrt{\left(1 + \frac{eV}{2m_e c^2}\right)}},$$ Eq. 2.2

where e is the electronic charge, and c is the speed of light.

The angle, θ, through which an electron is scattered is dependent on the change in momentum between its initial vector, $\mathbf{k_0}$, and its new trajectory, $\mathbf{k}$, after scattering, as demonstrated in Figure 2.2.
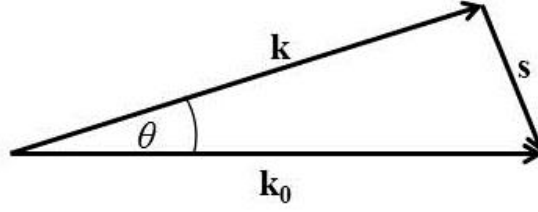
Figure 2.2: Diagrammatic representation of the change in momentum, **s**, of an electron from its initial momentum vector, **k₀**, to its new momentum vector, **k**, through a scattering angle, θ.

This change in momentum is known as the scattering vector, **s**. The magnitude of the scattering vector, s (where $s = |\mathbf{s}|$), can be determined by assuming that the scattering event is elastic (*i.e.* $|\mathbf{k_0}| = |\mathbf{k}|$), and knowing that $|\mathbf{k}|$ is inversely proportional to the electronic wavelength (*i.e.* $|\mathbf{k}| = 2\pi/\lambda$), to give Equation 2.3:

$$s = \frac{4\pi}{\lambda}\sin\left(\frac{\theta}{2}\right),$$

Eq. 2.3

where θ is the scattering angle. Comparing the two images in Figure 2.1, one can see that the observed diffraction rings are angle dependent; by collecting data at different sample-to-detector distances a wider range of data can be collected. The intensity of the scattering, $I(s)$, can be described by the Wierl equation (Equation 2.4):

$$I(s) = \sum_{i}^{N}\sum_{j}^{N}F_i(s)F_j(s)\frac{\sin(sr_{ij})}{sr_{ij}},$$

Eq. 2.4

where $F_i(s)$ is the scattering factor for atom i, and r_{ij} is the distance between atoms i and j. Values for $I(s)$ are obtained from the diffraction pattern by measuring the intensity at discrete values of s, which are radially averaged to produce the entire scattering intensity curve. The situation in Equation 2.4 where $i = j$ describes the scattering from a single atom, implying that the scattering equation can be written as a sum of atomic and molecular scattering events, as seen in Equation 2.5:

$$I(s) = I_{\text{atomic}}(s) + I_{\text{mol}}(s).$$

Eq. 2.5

The atomic scattering is independent of the species of interest and can be easily subtracted from the recorded data to leave only the information relating to the molecular scattering. Figure 2.3 shows the molecular scattering curves for $(SiClMe_2)_2C(SiMe_3)_2$ multiplied by s^4 [*i.e.* $s^4I_{\text{mol}}(s)$]. This step has been taken due to the scattering intensity rapidly dropping off as a function of the scattering angle.
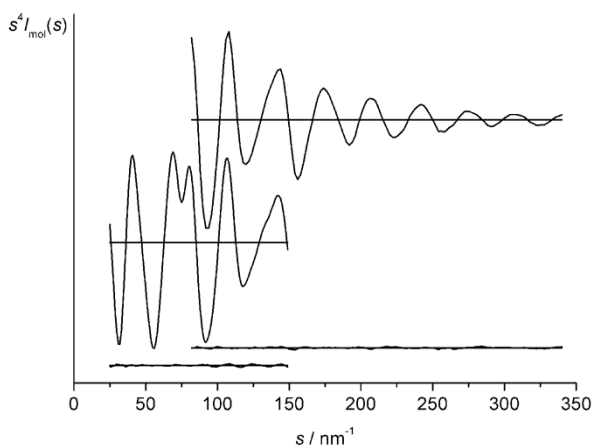
Figure 2.3: Molecular scattering curves for $(SiClMe_2)_2C(SiMe_3)_2$ collected at (top) a short sample-to-camera distance and (bottom) a long sample-to-camera distance.

As seen in Equation 2.4, the molecular scattering curve can be described as a series of sine functions and, therefore, a Fourier transform can be used to convert this curve into terms for each interatomic distance within a molecule. Equation 2.6 gives an example of the type of equation that may be used to convert the data:

$$\frac{P(r)}{r} = A\int_0^\infty \frac{sI_{mol}(s)}{|F(s)|^2} \sin(sr)ds,$$
<div align="right">Eq. 2.6</div>

where A is a scaling constant, and $F(s)$ is a weighted scattering factor that takes into account the amount of scattering contributed by different types of atoms. The information obtained from the Fourier transform can be plotted as a radial distribution curve (RDC), which shows the relative probabilities that certain interatomic distances within the molecule will provide a scattering event. The intensity of each peak is proportional to the number of times a certain interatomic distance appears within the molecule and the scattering factors [$F(s)$] of the atoms involved; it is inversely proportional to the interatomic distance itself. The RDC for $(SiClMe_2)_2C(SiMe_3)_2$ is shown in Figure 2.4, where one can see the distances relating to the C–H bonds at $r_a \approx 109$ pm, and C–Si and Si–Cl bonds under the peak at $r_a \approx 200$ pm. Other longer interatomic distances spanning the rest of the molecule can be seen at larger values of r_a.
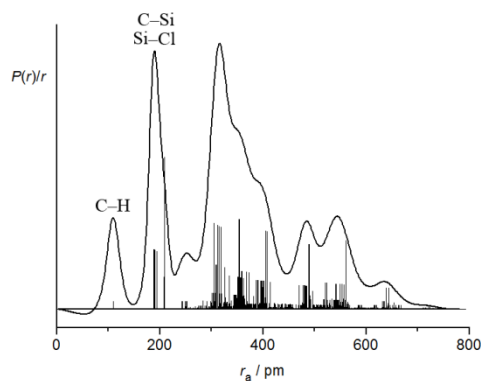
Figure 2.4: The radial distribution curve for $(SiClMe_2)_2C(SiMe_3)_2$.

2.1.2. Overcoming challenges associated with GED

Once the data from a diffraction pattern have been extracted using in-house software,[56] they are then refined in order to determine a molecular structure. However, before this step can be carried out, one must understand and counter the challenges that arise when interpreting electron diffraction data.

2.1.2.1. Molecular vibrations

Whilst the Wierl equation (Equation 2.4) describes how electrons are scattered by pairs of atoms separated by specific interatomic distances, it does not take into account any vibrations that will occur between the atoms involved. Vibrations cause a number of difficulties when trying to determine accurately molecular structures, especially at the relatively high temperatures often used to volatalise samples in GED experiments. How an electron diffracts depends on the positions of two atoms at the exact moment they are probed. However, regardless of whether a molecule is analysed using an ultrafast pulse or a continuous beam of electrons, each electron will probe a given atom pair at a different position in its vibrational cycle. This means that an averaged distance (r_a as quoted earlier in Figure 2.4) is observed rather than an equilibrium distance (r_e), leading to something called the shrinkage effect.[57] As illustrated in Figure 2.5, it is possible for the distance between two atoms to appear shorter than the equilibrium distance due to vibrations. One can clearly see from this image that there is only one moment where the molecule is linear and at all other times it is bent. This means that the average distance A$\cdots$C is shorter than twice the bonded distance A–B. By understanding how a molecule vibrates it is possible to predict average distances from calculated vibrational force constants; the

32

difference between the theoretical average and the calculated equilibrium distance can then be used to determine a correction value that can be applied to every distance in a molecule. This analysis is routinely carried out using a program called SHRINK,[58] and allows for an approximation of the equilibrium structure to be determined from a GED experiment.
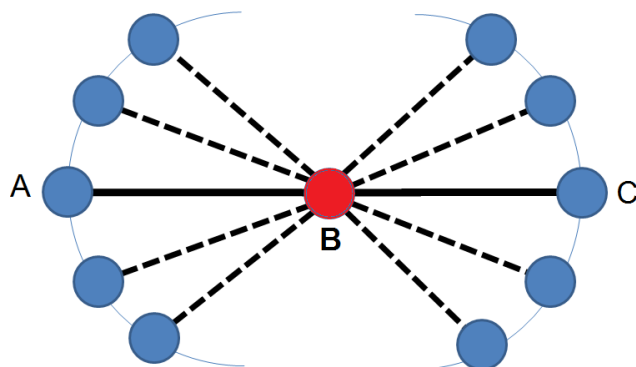
Figure 2.5: During vibration of the linear triatomic ABC, the distance between atoms A and C is less than twice the bonded distance between A–B.

SHRINK makes use of quantum chemical calculated force constants and Newtonian mechanics to describe the atomic motions away from the equilibrium structure.[58] However, this model breaks down when dealing with large and anharmonic amplitudes of vibrations. More recent work within the Wann group strives to use information from molecular dynamics simulations to better account for the effects that the vibrations have on the data collected and help determine approximate experimental equilibrium distances.[59]

2.1.2.2. Weak scattering, similar distances and multiple conformers

As suggested by Equation 2.4, a diffraction pattern is a superposition of interference patterns caused by scattering of electrons from every pair of atoms in a molecule. Information relating to the positions of lighter atoms, such as hydrogen, can therefore be less dominant than information from their stronger scattering, heavier atom, counterparts. This results in larger uncertainties in the distances involving lighter atoms, while problems also arise in resolving very similar interatomic distances. With reference to Figure 2.4, the C–Si and Si–Cl bond lengths in $(SiClMe_2)_2C(SiMe_3)_2$ fall under the same peak as they have similar interatomic distances ($r_a \approx 200$ pm). It is impossible to accurately determine similar distances that appear under these merged peaks using GED data alone.

Another challenge is that multiple conformers of a molecule may be present in a sample during a diffraction experiment. Although a molecule will have a global minimum, there will be other local minima on the potential energy surface of the molecule, some of which will be sufficiently close in energy to the global minimum that they may be populated at the temperature of the experiment. In the case of $(SiClMe_2)_2C(SiMe_3)_2$, calculations indicated that there were four conformers that could exist during the gas-phase experiment.

As problematic as these challenges may appear, methods have been developed to help overcome them. For example, Bartell demonstrated that information about interatomic distances in a molecule obtained from sources other than GED could be used as extra experimental data in the refinement process.[60] This idea was the basis of the STRADIVARIUS method[61] which, in certain cases, allows for information from liquid-crystal NMR and microwave spectroscopy[62,63] to be used in the refinement process. This helps to account for some of the missing information caused by very similar interatomic distances and allows for more complicated diffraction patterns to be resolved. However, the information obtained from these additional experiments are themselves limited, and can only help so far.

Schäfer suggested that information from theoretical methods could provide additional data, helping to further overcome the challenge of similar interatomic distances.[64] Quantum chemistry can supply estimates of the interatomic distances in a molecule and was the basis of the MOCED method,[64] which created constraints for the refinement process using theoretical information. However, a problem lies in the fact that this method assumes that the information from a single calculation is exactly correct; it is not able to take into account inaccuracies in any given calculation method.

The SARACEN method improved upon MOCED by using theoretical information as flexible restraints, rather than as absolute constraints.[65–67] SARACEN takes information from several calculations and generates restraints for parameters that may be poorly defined by GED alone. It defines uncertainties in these estimates by analysing the range of values from the series of calculations performed.

The solution to the multiple conformer problem is closely related to this. By obtaining theoretical information about all of the potential minima and their relative

energies, one can calculate the amount of each conformer present in the sample for a given experiment. The initial refinement process can then be weighted using this information before the relative amounts of each conformer are varied to find the best fit to the data.

These examples of the combination of theoretical information with experimental data have allowed for larger and more complex molecular structures to be refined.

2.1.3. GED refinements

With all of the challenges and solutions to resolving diffraction data discussed above being taken into consideration it is possible to carry out a refinement. As mentioned, the refinement can be performed more completely by taking into account information from external sources, such as quantum chemical calculations. These calculations (discussed in full in Section 2.3) are usually the first step in the process of determining a molecular structure, and give an idea of the what the structure of the molecule is, as seen for example in the case of $(SiClMe_2)_2C(SiMe_3)_2$ in Figure 2.6, as well as the presence, or otherwise, of multiple conformers.
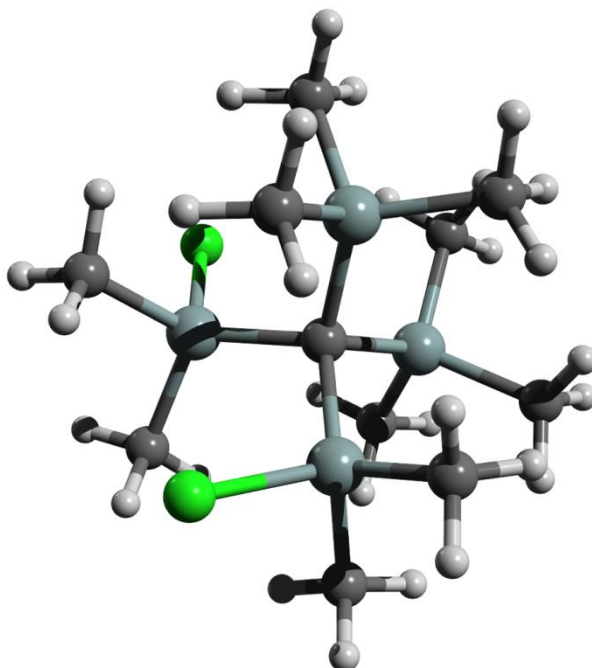
Figure 2.6: Predicted structure of $(SiClMe_2)_2C(SiMe_3)_2$, as given by an MP2/aug-cc-pVDZ calculation run using Gaussian 09.

Once an expected structure has been determined, a model of the molecule is written to describe its geometry in terms of bond lengths, bond angles, and dihedral

angles. This model is then used to create a theoretical diffraction curve that can be compared to the experimental data. The parameters of this model are then refined, using a least-squares method, to obtain a goodness-of-fit "R factor", the value of which gets smaller as the fit between the experimental and theoretical data improves. As mentioned in the previous section, multiple calculations are run, using different methods, in order to obtain the theoretical values for geometric parameters used to describe the molecular structure, as well as to yield an estimate in the uncertainty in the average value. In Figure 2.7, one can see how the experimental RDC compares to the theoretical data, in terms of the difference curve on the lower part of the graph. The closer the difference curve of the RDC tends to a flat line, the closer the theoretical data tend to the experimental data, and the GED refinement is considered complete.
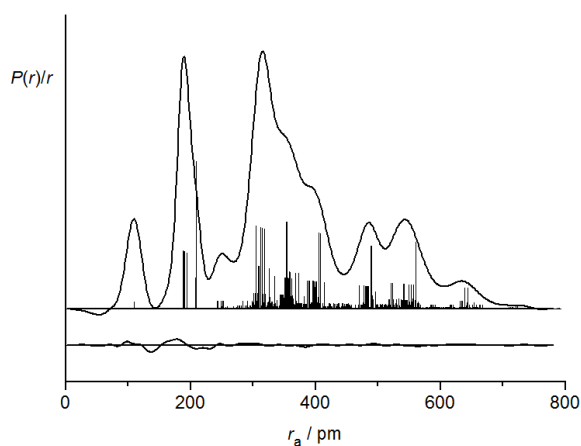
Figure 2.7: The refined RDC shows (top) the experimental curve and (bottom) the experimental-minus-theoretical difference curve.

2.2. Theory of time-resolved gas electron diffraction

Having discussed the theory and practice of refinements for a standard GED experiment, we should consider the features and challenges that are specific to time-resolved experiments. This section will also look at the methods for pulsed electron beam simulations, as well as the types of electron guns available for TRED experiments.

2.2.1. Pump-probe experiments

Pump-probe experiments form the basis of many modern spectroscopic techniques,[18,68,69] which allow for the study of the dynamics of numerous ultrafast chemical reactions that are elusive to many static techniques.

A typical pump-probe experiment starts by using an ultrafast laser to initiate a change in a molecule, such as an excitation into a higher rotational, vibrational, or electronic state, some of which may result in a change in structure. This initiating laser pulse is the "pump", and the time at which this pulse interacts with the sample is known as time zero.

Shortly after the pump pulse a second pulse will arrive at the sample to interrogate the molecular structure. In most experiments this second pulse will be a laser pulse that comes from a delayed beam path that was split from the original beam. This delayed beam may, or may not, have been modified in either wavelength or duration compared to the pump pulse, so as to be able to "probe" the sample spectroscopically. By varying the arrival time of the probe after the pump, one is able to monitor how the properties of a molecule evolve over time. TRED uses these same ideas, but utilises a bunch of electrons as its probe, instead of a second laser pulse.

2.2.2. Velocity mismatch

One of the main challenges with TRED is that the electron and laser pulses used in the pump-probe experiment do not have the same velocities.[23] The velocity of an electron, v_e, accelerated across a potential, V, can be determined by Equation 2.7:

$$v_e = c\sqrt{1 - \left(1 + \frac{eV}{m_e c^2}\right)^{-2}}\,, \qquad\qquad \text{Eq. 2.7}$$

where c is the speed of light, e is the electronic charge, and m_e is the mass of an electron. However, no matter how great the accelerating potential, an electron will never travel at the same speed as the laser pulse and this limitation poses a serious challenge.

Figure 2.8a is a representation of an electron beam and a laser beam crossing a molecular beam. The gaseous sample has a distinct width, w_M, and the time it takes for a laser pulse, t_l, and an electron pulse, t_e, to cross the width of the molecular beam can be determined by:

$$t_l = \frac{w_M}{c}\,, \qquad\qquad \text{Eq. 2.8}$$

and:

$$t_e = \frac{w_M}{v_e}.$$

As $c > v_e$, obviously $t_e > t_l$, suggesting that, if both the electron and laser pulses started at the edge of the gas pulse at the same time, the electron pulse will soon lag behind the laser pulse. Near the front edge of the sample the electron beam will essentially observe a molecule in the state initially induced by the laser pulse. However, as the laser moves ahead there will be a delay between the pump and probe interacting with the molecular beam. This means that, within the width of the sample, the electrons will probe a multitude of states and/or structures. One solution would be to reduce the width of the molecular beam to reduce the effect of the mismatch between the pulses. However, Zewail *et al.* showed that the experimental time resolution also depends on some additional factors.[23]
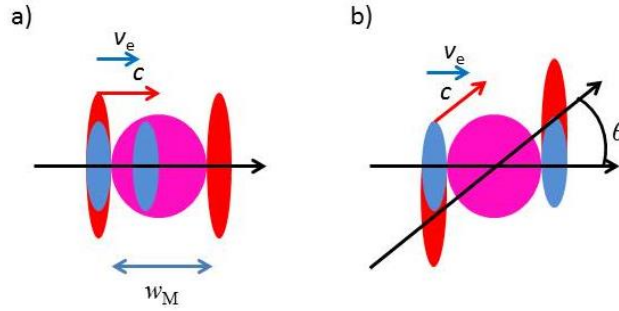
Figure 2.8: Diagram demonstrating a) the velocity mismatch between a laser (red) and electron pulse (blue) that travel along the same trajectory through a sample (pink), and b) showing how a laser with a tilted wavefront can reduce the velocity mismatch problem. Recreated from a figure in Ref. 72.

As one might expect, the resolution of the experiment also depends on the pulse duration of the electron and laser beams (τ_e and τ_l, respectively), as well as the respective widths of these pulses, w_e and w_l, their velocities, v_e and c, and the intersecting angle between the two, θ. Knowing these values the overall experimental time resolution, τ_t, can be determined by Equation 2.10:

$$\tau_t = \sqrt{\tau_e^2 + \tau_l^2 + \frac{1}{\alpha}}\,,$$

where α is given by:

$$\alpha = v_e^2 \left(\frac{w_M^2 \sin^2\theta + w_e^2 + w_l^2 + w_e^2 w_l^2 / w_M^2}{\beta} \right),$$

while β in Equation 2.11 is given by:

$$\beta = w_l^2 w_M^2 \left(k \cos \theta - 1\right)^2 + w_e^2 w_M^2 \left(k - \cos \theta\right)^2$$
$$+ w_e^2 w_l^2 \left(k^2 - 2k \cos \theta + 1\right),$$

<div align="right">Eq. 2.12</div>

where:

$$k = \frac{v_e}{c}.$$

<div align="right">Eq. 2.13</div>

These equations allow the overall resolution of a TRED experiment performed using simple laser wavefronts to be estimated. However, Baum and Zewail[70] later showed (with further work by Centurion *et al.*[71]) that by employing a tilted laser wavefront the time resolution can be further improved. Figure 2.8b shows how the velocity mismatch problem can be overcome. As a result of tilting the laser wavefront, both the electron and laser beams move across the sample at the same effective speed. The required angle for the laser wavefront can be found using Equation 2.14:

$$\theta \approx \arccos\left(\frac{v_e}{c}\right).$$

<div align="right">Eq. 2.14</div>

In the case of a 100 kV electron beam, the desired wavefront angle would be $\theta = 57°$.[72] If achieved, the resolution of the experiment would then be dependent only on the durations of the electron and laser pulses:

$$\tau_t = \sqrt{\tau_e^2 + \tau_l^2}.$$

<div align="right">Eq. 2.15</div>

However, all of this assumes that there is no jitter within the optical setup,[72] which would otherwise cause the laser pulse used to arrive at either the photocathode or sample at a slightly different time every time the laser was fired. Such a jitter could be caused by timing aberrations within the laser source(s), or small movements of the optics caused by vibrations or other artefacts of the experiment. This is the main limitation to sub-100 fs experiments that collect data using multiple pulses of electrons; hence, there is a drive to create an apparatus that can collect diffraction data in a single shot.[73]

2.2.3. Determining the electron pulse duration and time-zero position

In order to carry out a TRED experiment effectively, one must be able to determine accurately both the duration of the electron pulse and the time-zero position, where the pump and probe pulses cross the sample simultaneously. The

time-zero point is relatively easy to find using the method set out by Zewail *et al.*,[24] whereby an electron beam and a pump laser cross within the bounds of a molecular beam causing the undiffracted spot produced by the electrons on the detector to become smaller and more intense. This "lensing effect" is caused by the creation of a plasma within the molecular beam that focusses the electron beam, thus providing an accurate reference point for identifying the overlap of the pump and probe pulses. A similar method was used by Miller *et al.* for solid-state experiments, relying on the copper mesh supporting their sample to create the necessary plasma.[74]

In early TRED experiments the electron pulse duration was characterised using streak camera technology,[24,75] similar to that previously mentioned in relation to the TRED apparatus designed by Schwoerer *et al.*[41] By deflecting an electron pulse using a rapidly alternating electric field, a normally circular beam profile is streaked across the detector. Knowing the force that the electric field applies to the electrons, the pulse duration can be determined by measuring how far the electrons have been deflected. However, as the deflection plates need to be at least a few centimetres long to work effectively, it is not possible to measure the pulse duration at an instantaneous point using this method. In the time it takes for a pulse to cross these plates, its duration would increase due to space-charge repulsion (see Section 2.2.4). These problems increase further when shorter pulses are used as it becomes increasingly difficult to switch the electric field of the electrodes fast enough to observes sufficient streaking.

To overcome these problems Miller *et al.* developed a new technique that allows both the time-zero position and the instantaneous electron pulse duration to be determined simultaneously using the ponderomotive effect,[31,76] the force that an electron feels due to the spatial change in intensity of a laser beam. The ponderomotive force can be described by:

$$F(r,t) = -\frac{e^2 \lambda^2}{8\pi^2 m_e \varepsilon_0 c^3} \nabla I(r,t),$$
Eq. 2.16

where $F(r,t)$ is the force that the electrons feel due to a change in laser intensity, $\nabla I(r,t)$, at position r and time t. e and m_e are the charge and mass of an electron, respectively, whilst λ is the wavelength of the laser used, ε_0 is the permittivity of free space, and c is the speed of light. From Equation 2.16, one can see that the larger the

intensity gradient used the larger the force the electrons will feel. A large intensity gradient can be achieved using optics to focus a laser at the laser-electron interaction region, causing electrons to move to a region of lower laser intensity. A pair of apertures placed in the path of the electron beam, on either side of the interaction region, is used to remove some of the electrons from the outside edge of the pulse. As the focussed laser acts on the electron beam one can observe the electrons being scattered, causing some of them to be blocked as the pulse passes through the second aperture. This affects the intensity of the electron beam reaching the detector and, by varying the arrival time of the laser at the crossing point, the temporal shape of the electron pulse can be determined by careful measurement of the changes in intensity and beam current.

Whilst useful, the amount of scattering observed using this method is minimal, and so this technique has been further improved by Miller *et al.* to give the grating-enhanced method.[32] Here the electron beam is crossed by two counter-propagating laser beams from the same source, as seen in Figure 2.9. When aligned spatially and temporally the two laser beams interfere constructively and destructively, creating nodes of laser intensity in a very narrow region along the axis of laser propagation. These nodes create much larger intensity gradients than would be achieved by simply focussing a single laser beam. Scattering also now occurs at multiple locations (at each node) rather than at a single focal point, making this technique up to 100 times more effective than the previous method.[72] This allows less powerful lasers to be used, making the method more suitable for table-top experiments.
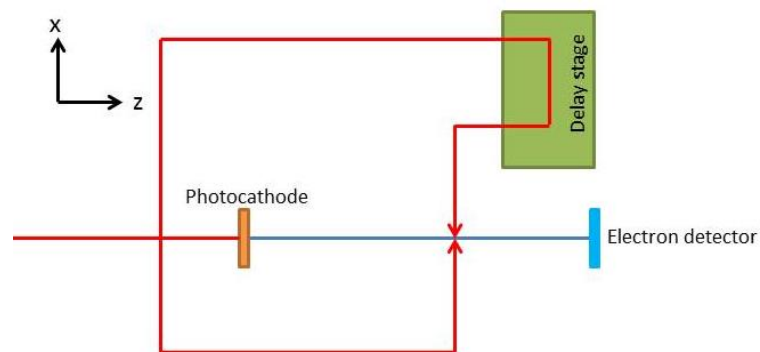
Figure 2.9: A simplified diagram representing the set-up used in a grating-enhanced ponderomotive scattering experiment. An electron beam (blue) is crossed by two counter-propagating laser beams (red), derived from the same source.

Where before scattering radiated out in all directions from the focal point, most of the scattering now occurs in the axis of the lasers (termed the x axis), due to the increased intensity gradient created between the nodes. The force that the electrons feel in this axis from the laser standing wave, assuming a Gaussian beam shape for the individual laser pulses, can be described by Equation 2.17 (full derivation can be found in Ref. 32) as:

$$F_x\left(x, y = 0, z = 0, t\right) \approx$$

$$\frac{I_0 e^2 \lambda}{2\pi m_e \varepsilon_0 c^3} \exp\left(-\frac{t^2}{2w_t^2}\right) \exp\left(-\frac{x^2}{2w_t^2 c^2}\right) \sin(2kx), \qquad \text{Eq. 2.17}$$

where t is time, x, y, and z are spatial coordinates, I_0 is the peak intensity of the lasers used, and $(8 \ln 2)^{\frac{1}{2}} w_t$ is equal to the pulse duration of the laser (equivalent to τ_l in Section 2.2.2). The above equation can then be rewritten as a product of a constant force, F_0, and four other terms, which are dependent only on one of the other variables (x, y, z, and t) as seen below:

$$F_x = f_t\left(t\right) f_x\left(x\right) f_y\left(y\right) f_z\left(z\right), \qquad \text{Eq. 2.18}$$

where:

$$f_t\left(t\right) = \exp\left(-\frac{t^2}{2w_t^2}\right), \quad f_x\left(x\right) = \exp\left(-\frac{x^2}{2w_t^2 c^2}\right) \sin(2kx),$$

$$f_y\left(y\right) = \exp\left(-\frac{y^2}{2w_f^2}\right), \quad f_z\left(z\right) = \exp\left(-\frac{z^2}{2w_f^2}\right), \qquad \text{Eq. 2.19}$$

and where $(8 \ln 2)^{\frac{1}{2}} w_f$ is equal to the width of the laser beam (equivalent to w_l in Section 2.2.2).

The image intensity of a laser pulse hitting a detector can be described by the term $S(\tau)$, where t_d is the delay time between the laser and the electron pulse, whilst the three-dimensional density of an electron pulse interacting with the lasers can be described by:

$$\rho\left(x, y, z, t\right) = \rho_{xy}\left(x, y\right) \rho_t\left(t + t_d - \frac{z}{v_e}\right), \qquad \text{Eq. 2.20}$$

where v_e is the velocity of the electrons, allowing $S(\tau)$ to be written as a convolution of both beams, as seen in Equation 2.21:

$$S(\tau) = \int F_0 f_t(t) |f_x(x)| f_y(y) f_z(z) \rho_{xy}(x, y)$$

$$\times \rho\left(t + t_d - \frac{z}{v_e}\right) dt\, dx\, dy\, dz$$

Eq. 2.21

$$\propto \int f_z(z) f_t(t) \rho_t\left(t + t_d - \frac{z}{v_e}\right) dz\, dt .$$

The variance in the pulse duration, σ_p, of the electron beam can then be determined from the variances of $S(\tau)$, $f_t(t)$, and $f_z(z)$ (σ_τ, σ_t, and σ_z, respectively) as:

$$\sigma_p^2 = \sigma_\tau^2 - \sigma_t^2 - \sigma_z^2 / v_e^2 ,$$

Eq. 2.22

giving the duration of the electron pulse as:

$$\tau_e = 2\sqrt{2\ln 2}\, \sigma_p .$$

Eq. 2.23

2.2.4. Electron pulse dynamics

As electrons are negatively charged they repel one another in accordance with Coulomb's law. This makes it difficult to confine a large number of them into a small volume, as is required in a TRED experiment. Although studies have shown that a bunch of electrons produced from a photocathode *via* laser ionisation will have a similar beam width and pulse duration to the laser pulse from which it was created,[21,38] the pulse will start to expand immediately. To obtain the optimal time resolution for a TRED experiment this problem must be overcome.

Whilst the main cause of pulse expansion is space-charge repulsion,[77] many other factors also determine how a pulse will behave. These factors include the energetic distribution of electrons at the creation of the pulse,[72,77] the initial width of the pulse,[29,78] and the relative orientations of the electrodes used to accelerate the electrons.[79] The group velocity of the pulse is also important, as the pulse expansion rate from space-charge repulsion slows as a factor of γ^3, where γ is the Lorentz factor:

$$\gamma = \frac{1}{\sqrt{1 - \frac{v_e^2}{c^2}}} ,$$

Eq. 2.24

where v_e is the velocity of the electrons and c is the speed of light.[72] This means that, at higher velocities, the electron pulse will expand at a slower rate.

Theoretical studies into ultrafast electron pulse dynamics have been carried out for decades, with early work focussing on characterising electron pulses inside streak cameras.[77] Observations were made about how a pulse created by ionising a photocathode evolves over its time of flight, which naturally set out the basis for TRED pulse dynamics. Early simulations made use of custom models that were based on electrodynamic theories. One such method, described by Qian *et al.* and called the "fluid model",[78] attempted to look at a pulse created from a photocathode and accelerated across a potential, $-V_0$, though an aperture towards a detector, with the electron beam width controlled using a magnetic lens. Whilst the basics were there, a number of problems existed with how these simulations were performed.[29,80,81] The problems started with the assumption that the pulse had a square profile with uniform density, and that the duration of the pulse could be determined by measuring the distance between the front and back of the pulse. As mentioned, an electron pulse has properties similar to that of the laser pulse that created it, suggesting that its shape should be Gaussian in three dimensions, with the highest electron density coinciding with the peak power of the laser pulse. This also means that the pulse duration should be measured by determining the full-width half-maximum (FWHM) distance, rather than the distance between the furthest out electrons.

Qian *et al.* also assumed that the transverse width of the electron pulse would remain constant because of the presence of a magnetic lens spanning the distance between the anode and the detector. Whilst technically one could do this if so inclined, it would not be beneficial to a TRED experiment. Constricting the width of the pulse would not only distort the diffraction images, but would also cause the pulse duration to stretch artificially. By not being able to expand in the transverse direction, space-charge effects will force electrons to spread along the axis of propagation, causing the pulse duration to increase.

Shortly after these studies, Siwick *et al.* published their own "mean-field model"[29] that dealt with a number of these inadequacies, and with it were able to better predict the electron pulse duration. They showed that electron pulses were expanding less rapidly in a temporal sense than Qian *et al.* had predicted. Not only this, they made a number of other key predictions with their simulations, including that the initial pulse duration has a large effect on how the pulse expands. Shorter initial pulse

durations do not necessarily mean that a better pulse duration will be achieved at the sample. Assuming that all other conditions are the same, a pulse with a short initial duration will have a higher electron density than that of a longer pulse, meaning that it will have a faster rate of expansion due to space-charge effects. Depending on the conditions, it is possible for the duration of a "shorter pulse" to overtake that of a "longer pulse" during propagation and yield a worse time resolution. For example, a 50 fs pulse containing 10^4 electrons, accelerated across a potential of just under 30 kV will expanded more rapidly than a 500 fs pulse containing the same number of electrons; once the pulse has propagated for about 2.5 ps (approximately 25 cm) the use of an initially shorter pulse will result in a worse time resolution. One must, therefore, perform a careful balancing act when trying to optimise the time resolution of a TRED experiment. Siwick also showed that although a pulse would have an initial Gaussian time profile, this would change over its flight into a more top-hat shape, causing FWHM analysis to no longer be as accurate.[29]

Possibly the most important outcome of Siwick's work was the discovery that the evolution of the velocity distribution of an electron pulse throughout its flight can be described as a linear chirp.[29] This arises because the electrons at the front of the pulse are accelerated by the electrons behind them, whilst the electrons at the back of the pulse are decelerated by the electrons ahead of them. This means that, with a rapidly switching electric field, it should be possible to induce an inverse chirp, slowing down the electrons at the front of the pulse, and accelerating those at the back, whilst keeping the group velocity the same. The effect of this is to temporarily compress the duration of an electron pulse, as will be described further in terms of an RF cavity electron gun in Section 2.2.6.3.

2.2.5. Particle tracer packages

As discussed in Section 2.2.4, when developing new pulsed electron sources it is important to have an understanding of how a pulse of electrons will propagate from its source to a detector. This is especially useful in the planning stages of a new apparatus, before committing to a design. Thankfully, several commercial particle tracer packages are available to help simulate and investigate these properties.

SIMION[82], a particle tracer code that makes use of 4th-order Runge-Kutta sequences (a series of iterative calculations that allow for the approximation of ordinary differential equations), has the ability to produce and render 2D/3D images

of an apparatus. These can be produced within SIMION itself, or using CAD drawings as a basis. From these models, and with user defined initial conditions, SIMION can predict the electric and magnetic field lines within the apparatus. The resolution of each simulation is determined by the user, set out by unit cells of a defined size, with smaller unit cells leading to more accurately described simulations. Time steps are then based on the time it takes for the fastest particle in a given simulation to cross a unit cell. In terms of an electron beam propagating through an apparatus, this allows one to see how the beam will behave within an apparatus and how the electrons will move through the various fields. This can quickly tell a user if certain designs of an apparatus are feasible, or not at all possible, as well as give approximate properties and dimensions to the electron beam being produced.

Whilst other particle tracers, such as ASTRA[83] are available, I opted to use General Particle Tracer (GPT)[84,85] for further beam dynamic simulations. GPT uses a 5th-order Runge-Kutta stepping sequence to measure accurately time steps within the simulation, and to predict the behaviour of the ions/electrons within the simulations. Whilst it lacks the CAD-like interface to produce representations of the magnetic/electric field lines within an apparatus, GPT can perform more precise and statistically accurate simulations. This is due to GPT carrying out simulations in a space that can be intimately described by the user, rather than defined unit cells as in SIMION. GPT is also designed to produce a statistically averaged result within a single simulation, unlike SIMION, which uses slightly different initial conditions yielding slightly different results each time it is run. If sufficient SIMION calculations are run they would eventually combine to produce similar a result to that produced in a single GPT calculation, though obviously GPT saves the user time in the long run.

2.2.6. Review of time-resolved electron diffraction equipment

Now that we have explored the general properties of an electron pulse and how it behaves we can look at the types of electron guns that have been designed to best control the pulse to obtain the optimal time resolution for a TRED experiment.

2.2.6.1. Compact electron gun

This is the simplest electron gun available, and was used in the earliest experiments by Zewail *et al.*[86] As was discussed in Section 2.2.4, the longer an

electron pulse propagates, the longer the pulse will stretch due to space-charge effects. With this gun, the distance between the electron source and the sample is kept as short as possible (usually a few centimetres) in order to reduce the time that the pulse has to expand.

Generally, this type of electron gun allows experiments to be performed that can observe molecular dynamics on the picosecond timescale although, with careful design, sub-picosecond resolution can be achieved. The overall time resolution is still limited by other factors such as the original pulse duration of the ionising laser, the acceleration potential of the gun, and the number of electrons within each pulse, with a general upper limit of 10^4 electrons for sub-picosecond experiments. Experiments are normally carried out over extended periods of time, with hundreds, if not thousands, of electron pulses used to obtain a significant signal-to-noise ratio. For experiments using solid-state samples, this can limit the types of systems that can be studied to those that display reversible dynamics, or can require a very large number of samples to be prepared.[6,26]

2.2.6.2. Relativistic electron gun

The relativistic electron gun is based on the ideas discussed in Section 2.2.4 where, as the group velocity of the electron pulse tends towards the speed of light, the space-charge repulsion lessens due to relativistic effects. This means that there is little expansion of the pulse between the electron source and the sample, allowing electron pulses to be generated that contain many more electrons (approximately 10^7 electrons)[43,44] without excessive space-charge broadening being observed. This raises the possibility of collecting an entire diffraction pattern using a single electron pulse, allowing experiments to be run over shorter periods of time, and for samples with non-reversible dynamics.

The biggest obstacle to using a relativistic gun, typically operating at 3-5 MeV, is that it needs a high-energy source for the electron pulse. This can generally only be provided by national laboratories, using either a specially designed particle injector or using "run-off" electron beams from linear accelerators.

2.2.6.3. RF cavity electron gun

In Section 2.2.4 the linear chirp associated with an electron pulse as it expands in the temporal frame was discussed. At the time, it was suggested that, with a

sufficiently fast alternating electric field, one could induce a negative chirp to recompress the electron pulse. With a radio-frequency (RF) cavity this idea can become a reality.[34] The RF cavity creates a large electric field that then rapidly decreases on the GHz cycle timescale, which is linked to the arrival of the electron pulse in the cavity. The rapidly decreasing field strength causes the electrons at the front of the pulse to be slowed down, whilst those at the back are accelerated, causing the pulse to narrow along the propagation axis, yielding the desired shorter pulse duration.

This method has been used to shorten the electron pulse duration for both relativistic[28] and non-relativistic[87] TRED experiments. Whilst successful, the technique does have difficulties in that the timing of the cycle of the electric field in the cavity has to match extremely accurately the arrival of the electron pulse. If the timing is not correct there is the possibility that the pulse will be stretched instead of being compressed.

2.2.6.4. Reflectron electron gun

As mentioned earlier, the reflectron electron gun takes ideas that are commonly utilised to improve the resolution of data obtained from mass spectrometers.[88] When used for diffraction, the electron gun fires a bunch of electrons, not directly at a sample, but towards a second negatively charged potential source, which is at a similar potential to the accelerating potential of the electron gun, as shown in Figure 2.10. As the electrons travel towards this second potential source they slow down, and are eventually reflected back out and directed towards the sample of interest. The faster electrons at the front of the pulse penetrate further into the electric field of the second potential source than those slower electrons at the back of the pulse. The deeper penetrating electrons therefore gain more kinetic energy when their velocities are reversed than their slower counterparts. As the pulse leaves the second electric field, the slower electrons are now at the front of the pulse and the faster electrons at the back. This arrangement causes the pulse to compress in the temporal frame, potentially allowing for better time resolution. Although this type of electron gun has been simulated to demonstrate its feasability,[40] no apparatus using this design has yet been built.
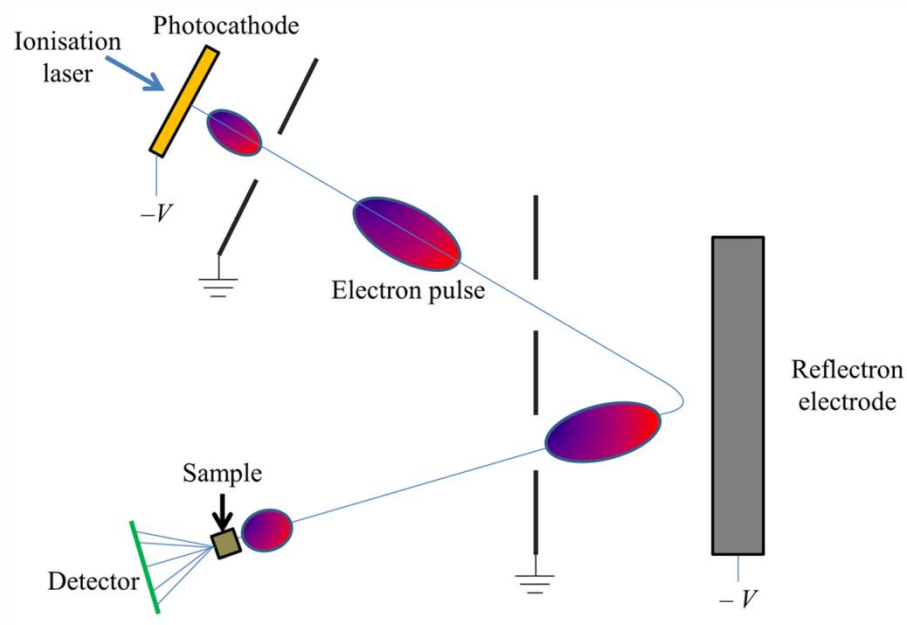
Figure 2.10: Simplified diagram of a reflectron gun showing the temporal compression of an electron pulse containing relatively fast (red region of pulse) and slow (blue region) electrons.

2.2.6.5. Single-electron electron gun

Whilst the relativistic electron gun described in Section 2.2.6.2 overcomes space-charge repulsion by accelerating the electrons to near the speed of light, an easier method to overcome this repulsion is to drastically reduce the number of electrons to almost a single electron per pulse. This is achieved by reducing the laser power used to ionise the electron source, so that statistically only a single electron is produced per laser pulse. This electron "pulse" will then have the same duration as the laser used to create it, and will retain that duration throughout its flight. The "pulse" will also effectively remain well collimated, improving the spatial resolution and coherence of the experiment.[38]

The major problem with this method is the extended length of time it would take to collect data using a "pulse" that contained only a single electron. One technique used to overcome this involves the use of mode-locked lasers to produce a train of low-energy laser pulses that can create multiple electron "pulses" in quick succession,[37] as discussed in Section 1.4. However, this means that the pump laser would also have to be a train of pulses, essentially limiting this method to gas-phase experiments, as it would be difficult to examine most crystalline samples that require

time to relax between shots. With gas-phase experiments, a steady stream of new molecules can be sampled with each shot as a near-continuous molecular beam enters the diffraction region.

2.2.6.6. Streak camera electron gun

A streak camera electron gun is based on the acceptance that an electron pulse will stretch in the temporal domain and uses this fact to its advantage.[5,9] Here, the electron pulse typically has a duration of several picoseconds by the time it reaches the sample. As discussed earlier (see Section 2.1.2.1), every pulse passing through a sample will see that sample in a slightly different state. In a standard TRED apparatus this would result in a "blur" being added to the diffraction data obtained, hence the need for short pulses. However, in this gun, shortly after the sample the electron pulse passes through a streak camera which causes the pulse to be "streaked" across the detector. Different regions, relating to different time domains within the pulse, land at different points on the camera, which allows the entire dynamics of sample to be observed over the timescale of the pulse. This removes the need to perform multiple pump-probe experiments with different delays between the pulses in order to see the overall dynamics of the sample. However, the potential use of this technique is limited. The time resolution of the experiment is not only dependent on how fast the streak camera can streak the pulse (the faster the streak, the better the time resolution obtained), but also by the transverse size of the pulse in the streaking direction. Also, because the diffracted electrons have been acted upon by an external force, the observed pattern may be distorted affecting the spatial resolution of the experiment.

2.2.6.7. Electron sources

As mentioned in Section 1.2, the way that the electrons are produced for TRED experiments is very different than for a continuous electron beam, which is created by passing a current through a wire filament. Most pulsed electron sources are created by the ionisation of a suitable photocathode using an ultrafast laser. The photocathode can be made from various materials such as copper,[43] or tungsten,[51] but the most commonly used is gold.[89] Gold photocathodes are particularly popular because the third harmonic of a Ti:Sapphire laser acts to produce electrons with just-above-threshold energies, and thus with very little kinetic energy. This helps to

improve both the spatial and time resolution of a TRED experiment, as well as the transverse coherence of the electron pulses.[72]

The shape of the photocathode is also important as it affects the nature of the electron pulse produced. The most common photocathode is the thin-film cathode. In this the laser usually acts on the photocathode by rear illumination to eject electrons from the opposite side. This produces an electron pulse that has a similar size and duration to the laser that acted upon the photocathode,[21] and the electrons can then be accelerated and used for diffraction. Whilst simple and commonly used for diffraction experiments this photocathode does not necessarily produce the most coherent beam, a factor important in analysing larger molecular samples and protein structures.[38,72]

Another option is to use a metallic rod with a shaped nanotip end to produce electrons.[50–52] The width of the laser used to ionise the nanotip is usually much larger than the tip itself, though the narrowness of the tip creates a very localised beam source. With the correct magnetic lens and aperture set-up this can produce a very narrow electron beam, with high transverse coherence. However, because the source is so localised there is also a high electron density, which can cause significant divergence and rapid pulse expansion.[38]

Recently there have been suggestions that ultracold gases could provide a suitable electron source.[38,53] These laser-cooled atoms and molecules have very little energy when the ionisation laser arrives at the ultracold gas, and hence with just-above-threshold ionisation the electrons produced have very little kinetic energy. This produces a highly collimated and coherent electron beam for diffraction purposes. The major problem, however, is obtaining the ultracold gases in the first place, as they are difficult and expensive to maintain, and one must wait for the gas to cool after each ionisation event.

2.3. Computational methods

Quantum chemical studies are becoming ever more important in chemistry, and these techniques are vital to understanding results from both standard GED and TRGED. Quantum chemistry has the ability to predict the ground-state and excited-state structures, energies, and spectroscopic features of almost any molecule. With these calculations it is possible to simulate experimental diffraction patterns for a

molecule of interest, as well as to use the theory to help interpret experimental data that have already been collected.

2.3.1. Schrödinger equation and approximations

A wavefunction is a concept in quantum physics that contains all the information about an atomic or molecular system in a particular eigenstate. It is possible to retrieve information about the eigenstate, in the form of eigenvalues, from the wavefunction with the use of specific operators in an eigenequation, as shown:

$$\hat{H}\Psi = E\Psi .$$

Eq. 2.25

Equation 2.25 is the Schrödinger equation,[90] and it uses the Hamiltonian operator, $\hat{H}$, to retrieve the energy, E, of a system from its wavefunction, Ψ. For atomic and molecular systems the Hamiltonian consists of two main parts: one that describes the kinetic energy terms for the nuclei and electrons in a system, and another that describes the potential-energy terms that arise from the electron-electron, nuclear-nuclear, and nuclear-electron Coulombic interactions within the system, as shown in Equation 2.26:

$$\hat{H} = -\frac{\hbar}{2m_e}\nabla^2 - \frac{\hbar}{2m_n}\nabla^2 + \sum_{i,j(i\neq j)}\frac{Z^2e^2}{4\pi\varepsilon_0\left|R_i - R_j\right|} +$$
$$\sum_{i,j}\frac{Ze^2}{4\pi\varepsilon_0\left|r_i - R_j\right|} + \sum_{i,j(i\neq j)}\frac{e^2}{4\pi\varepsilon_0\left|r_i - r_j\right|},$$

Eq. 2.26

where $\hbar$ is the reduced Planck constant, m_e is the mass of an electron, m_n is the mass of a nucleus, R_i and r_i are the positions of the nucleus i and electron i, respectively, Z is the charge on the nucleus, e is the electronic charge, and ε_0 is the permittivity of free space. Theoretically, the exact energy of a system can be determined by solving the Schrödinger equation. However, due to the many-body problem, it is impossible to do this for anything other than single-electron systems, such as H, He^+, and H_2^+. Yet, with the use of several approximations, it is possible to get useful information from the Schrödinger equation for multi-electron systems.

The Born-Oppenheimer approximation states that, because the mass of the atomic nucleus is much greater than that of an electron, and that the velocity of an electron is greater than that of the nucleus, we can assume that the nucleus will remain stationary on the timescale of the electronic motion. This approximation means that the kinetic energy between two nuclei will be zero, and allows the potential energy

between them to be considered constant. Therefore, the Hamiltonian can be rewritten in the form shown in Equation 2.27:

$$\hat{H} = -\frac{\hbar}{2m_e}\nabla^2 + \sum_{i,j}\frac{Ze^2}{4\pi\varepsilon_0\left|r_i - R_j\right|} + \sum_{i,j(i\neq j)}\frac{e^2}{4\pi\varepsilon_0\left|r_i - r_j\right|}.$$

Eq. 2.27

Furthermore, one can assume that the electrons in the system move independently of each other. As electrons are indistinguishable this approximation allows for the whole wavefunction to be described by a combination of many single-electron wavefunctions, as detailed in Equation 2.28:

$$\Psi(r_1, r_2, r_3, ..., r_N) = \psi_1(r_1)\psi_2(r_2)\psi_3(r_3)...\psi_N(r_N)$$
$$= \prod_{i=1}^{N}\psi_N(r_i).$$

Eq. 2.28

This means that the system need only be solved for one electron, since all of the others will be the same. However, it would be a mistake to assume that the electrons do not interact with each other at all and a number of methods have been developed to account for this.

2.3.2. Hartree-Fock theory

The Hartree-Fock method[91] assumes that each electron within a molecular system feels the average effect of all of the other electrons. Hartree assumed that the electrons effectively move in a sea of electrons with a density, $n(r)$, described by the electronic wavefunction as shown in Equation 2.29:

$$n(r) = \sum_i\left|\psi_i(r_i)\right|^2,$$

Eq. 2.29

which can then be incorporated into the Hamiltonian to better approximate the energy of the system, as shown in Equation 2.30:

$$\hat{H} = -\frac{\hbar}{2m_e}\nabla^2 + \sum_{i,j}\frac{Ze^2}{4\pi\varepsilon_0\left|r_i - R_j\right|} + \sum_i\int_0^\infty\frac{e^2n(r')}{4\pi\varepsilon_0\left|r_i - r'\right|}dr.$$

Eq. 2.30

However, Equation 2.30 overestimates the energy of the system, because it allows the electrons to come closer together than Coulombic forces would normally permit. This is the "Coulomb correlation problem", which we will return to.

Another inaccuracy that is apparent in Equation 2.30 is the "exchange problem". As previously mentioned electrons are fermions and hence indistinguishable, each with a spin, $s_i = \frac{1}{2}$. Since they must obey the Pauli exclusion principle, if the position

of two electrons were to be swapped, the wavefunction would have to change sign, as demonstrated in Equation 2.31:

$$\Psi(...,r_i s_i,...,r_j s_j,...) = -\Psi(...,r_j s_j,...,r_i s_i,...).$$

Eq. 2.31

This can be accounted for using Fock operators, whereby the electron wavefunction is rewritten as a series of Slater determinants, taking into account both the asymmetry of the system and the exchange principle.

By combining the Hartree Hamiltonian with the Fock-operated electron wavefunction, this yields the Hartree-Fock (HF) method. One can then invoke the variational principle by first estimating the wavefunction of the system, before determining its energy using the HF method. The initial conditions are then changed slightly and the system is recalculated to see if it has a lower energy than before. This method is repeated iteratively until no further change in energy is observed, indicating that the system has converged. This method is known as self-consistent-field (SCF) theory, and is the basis for most quantum chemical calculations.

The HF method is one of the most commonly used computational methods available, though it is still less than perfect because it does not account for the Coulombic correlation problem. Several other methods, however, are available to account for this effect, with many of them using the HF method at their core.

2.3.3. Møller-Plesset theory

Møller-Plesset (MP)[91,92] theory starts with HF and attempts to account for the Coulombic correlation by assuming that the electronic state can be described by a perturbation of the HF energy, as the electron correlation will effectively cause a slight energy change in the system. The Hamiltonian for MP theory can therefore be written as in Equation 2.32:

$$\hat{H}(\lambda) = \hat{H}_0 + \lambda \hat{H}',$$

Eq. 2.32

where $\hat{H}(\lambda)$ is the perturbed Hamiltonian, $\hat{H}_0$ is the unperturbed Hamiltonian (generally HF), and $\hat{H}'$ is the perturbing potential that is taken to an order of λ. The higher the order taken for the calculation, the more accurate the result will be; however, this comes at the cost of longer calculation times.

The most commonly used version of MP theory is MP2,[93] which uses the second-order perturbation to carry out calculations, and has a balance between accuracy and

rapid computation time. It should be noted that higher levels of theory are available (*e.g.* MP3, MP4).[94,95]

2.3.4. Density functional theory

Density functional theory (DFT) is another method that attempts to tackle the correlation problem. The theory is based on the Hohenberg-Kohn theorem,[96] which states that the ground-state energy of a system can be directly linked to its electron density *via* a unique functional. This functional describes all of the properties of the electrons and how they interact with one another, without explicitly knowing their positions. The system can be described by a series of single-electron wavefunctions acting within an effective potential mapped by the functional, $U_{DFT}(r_i)$, as seen in Equation 2.33:

$$\hat{H} = -\frac{\hbar}{2m_e}\nabla^2 + \sum_{i,j}\frac{Ze^2}{4\pi\varepsilon_0|r_i - R_j|} + \sum_i\int_0^\infty\frac{e^2 n(r')}{4\pi\varepsilon_0|r_i - r'|}dr$$
$$+ \sum_i U_{DFT}(r_i). \qquad \text{Eq. 2.33}$$

The main problem with this method is that the functional that relates the electron density to the wavefunction is unknown, although several approximations are commonly used to simulate the functional. One such approximation is the local density approximation (LDA), which assumes that the functional can be simulated by an electron moving inside a homogeneous electron gas that has the same density as the real system. This can be improved upon using the generalised gradient approximation (GGA), which takes into account the electron density variations throughout a system.

One of the most commonly used DFT methods is B3LYP.[97–99] This hybrid functional makes use of Becke's third functional (an adapted HF method that uses Slater determinants with corrections for the electron density gradient) and the LYP functional, which accounts for electron correlation.[91]

Time-dependent DFT (TD-DFT) methods, such as TD-B3LYP,[100] are available to study the excited states of molecules, and assume that a system is initially in a ground state before being adiabatically excited. The response of the electron density of the system is then analysed before its energy is determined.

2.3.5. Complete active space self-consistent-field theory

The main feature of complete active space self-consistent-field (CASSCF)[101] theory is its ability to focus on specific electronic configurations within a molecular system, by selecting whether orbitals are in an active or inactive space, as shown pictorially in Figure 2.11. The user-defined active space contains orbitals, both occupied and unoccupied, that allow the calculations to be focussed on the electronic states of interest, such as those orbitals involved in the electronic transitions. The remaining orbitals are in the inactive space, and are left untouched, populated by either two or zero electrons. Within the active space, orbitals are not required to have integer numbers of electrons (but do tend towards this) as electrons are partially free to move about, helping to account for electron correlation effects.
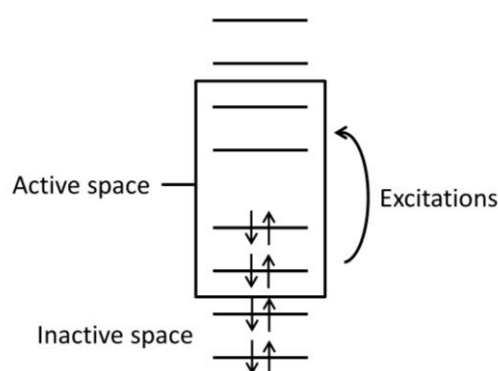
Figure 2.11: Pictorial representation of the active and inactive space within a molecule in a CASSCF calculation. Figure based on an image from Ref. 91.

As the active space is defined by the user (unlike in TD-DFT), a good spectroscopic knowledge of the molecule of interest is necessary in order to choose the correct orbitals for the active space. Within the chosen active space, the user is able to define the electronic transitions required to investigate the state in which they are interested. If needed, one can restrict the active space further with the use of restricted active space self-consistent-field (RASSCF) theory, which allows a specified number of electrons to be associated with an orbital, in order to observe particular transitions.

As with most computational methods, CASSCF calculates its wavefunction as a series of Slater determinants and coefficients. In most SCF techniques, for example HF, these determinants are based on the molecular orbitals of the system of interest,

whilst the coefficients are constants that can be optimised to determine the energy minimum of the system. However, in multi-configuration self-consistent-field (MCSCF) theories, such as CASSCF, the determinants that describe the orbitals are optimised as well as the coefficients to obtain an energy minimum. To reduce the computational time, it is common for the starting determinants to be taken from HF or other SCF methods.[91]

2.3.6. Basis sets

Although the methods used to solve a molecular wavefunction have been discussed here, the wavefunctions themselves have not yet been examined. If the type of wavefunction used in a calculation cannot describe the system effectively then the calculation is meaningless.

Generally, the region in which an electron is likely to be found around a nucleus can most easily be calculated using a series of Gaussian functions, and so naturally these tend to be used to define a wavefunction. The collection of Gaussian functions used to describe each atom in a system is called its basis set. The more Gaussian functions used to describe the orbitals, the more accurate the calculations become, as features of the orbitals are described more precisely. Basis sets that only use one function to describe an orbital are generally termed as single-ζ basis sets, while those that use two functions to describe an orbital are known as double-ζ basis sets, and so on in a similar fashion for higher level basis sets.[91] In this work, two main types of basis sets were used: Pople-style basis sets, and correlation-consistent basis sets.

2.3.6.1. Pople-style basis sets

Pople-style basis sets[102] are some of the most commonly used basis sets in computational chemistry.[91] They utilise a series of Gaussian functions to describe the different orbitals for each atom, and are generally denoted in the following fashion: k-nlmG, where the G tells us that Gaussian functions have been used. For example, the basis set 6-31G,[103,104] used for low-level calculations, uses 6 Gaussian functions to describe the core electrons, and a set of split-valence functions, with 3 to describe the inner valence electrons and 1 to describe the outer valence orbitals. 6-311G[105] is a similar type of basis set, generally used for heavier atoms, but the valence shell is split into three parts, with 3, 1, and 1 functions used.

Certain additional modifications can be made to Pople-style basis sets. If a "+" is indicated after the *nlm* terms (*e.g.* 6-31+G), this shows the addition of diffuse s- or p-type orbitals for all of the heavy atoms. A second "+" (*e.g.* 6-31++G) also adds diffuse s orbitals for hydrogen atoms. Terms after the G relate to additional polarisations that one may wish to consider. For example 6-311++G(2df) will add an extra two d orbitals and one extra f orbital to all of the heavy atoms, whilst 6-311++G(2df,2pd) will also add an extra two p orbitals and a d orbital to the hydrogen atoms. If one only wants to add one extra polarisation to the basis set, it can be achieved by placing a "*" after the G. For example 6-31G* is the same as 6-31G(d), whilst 6-31G** is equivalent to 6-31G(d,p).

2.3.6.2. Correlation-consistent basis sets

As the name suggests, correlation-consistent basis sets aim to account for the correlation term between electrons.[91] This is achieved by grouping together all of the types of orbitals with similar correlation terms. For example, the energy of a system can be lowered by initially looking at the first d orbital. To increase the accuracy of the calculation again, the second d orbital can be included. However, this orbital has similar correlation characteristics to the first f orbital, and so it must also be included. Likewise, the third d orbital has similar correlation characteristics to the second f orbital and the first g orbital. Overall, to increase the accuracy of a calculation, the sets of orbitals are added in the following order: 1d, 2d1f, 3d2f1g.

Different levels of correlation-consistent basis sets, including cc-pVDZ, cc-pVTZ, cc-pVQZ, cc-pV5Z (standing for "correlation consistent polarisation valence double / triple / quadruple / quintuple zeta"),[106,107] are available. Each step up increases the ζ-factor by one and adds another group of polarisations to the calculation. These basis sets can be augmented using an "aug-" prefix, which adds an additional series of small diffuse functions (*e.g.* 1s1p1d) to the basis set. One significant advantage of correlation-consistent basis sets over Pople-style ones is that calculated parameters can be extrapolated to the basis-set limit.

2.3.6.3. Pseudopotentials

Pseudopotentials, also known as effective core potentials (ECPs), are a special type of basis function that can be added to calculations to reduce the amount of computational power needed. They are generally used for heavy atoms and work by describing the core electrons of an atom using a single function. However, it must be

ascertained that the single function used gives a similar energy to the full basis set, otherwise the approximation will be useless. Certain basis sets are designed to do this automatically; for example, placing the suffix "-PP" after a correlation-consistent basis set will create a pseudopotential for heavier atoms.

2.3.7. Computational packages

To investigate the theoretical properties of a molecule there are several readily available computational packages that can carry out the large number of calculations that are necessary. One commonly used package is Gaussian,[108] which allows for most theoretical calculations (HF, DFT, CASSCF, *etc*.) to be carried out relatively easily. It allows initial estimated structures of molecules to be inputted and for these to be analysed using the theoretical method and basis sets of choice. Gaussian is a general-purpose package that can be used to study molecules of almost any size given enough time.

Another package used in this study was MOLPRO,[109,110] which specialises in implementing the MCSCF methods, such as CASSCF, and molecules with high degrees of symmetry. It uses the high symmetrical features of a molecule to its advantage in order to reduce the amount of time a calculation takes to run.

2.3.8. Molecular dynamics and Newton-X

The computational techniques discussed so far can yield the structures of stable and intermediate species, but struggle (at least without some help) to determine how exactly the molecules move between these states, and over what timeframe. As the focus of TRED is to understand better the dynamics of the structural changes that a molecule undergoes following some stimulus it would be beneficial also to study such dynamics computationally. Thankfully, computational packages that help to simulate these types of experiments exist, with Newton-X used for this work.

Newton-X[111–113] allows for the nuclear motions of a molecule to be studied in response to changes in its electronic structure. Starting with an initial set of atomic coordinates, force constants are calculated using a software package of choice (such as Gaussian) at a level of theory chosen by the user. From these calculations, Newton-X determines the kinetic energy of each atom within a molecule using simple Newtonian mechanics, determining how the individual atoms are likely to move over a set time step. Once the atoms have propagated to their new positions,

the new atomic coordinates are fed back to computational package and the process of calculating the force constants is repeated.

When carrying out the force-constant calculations Newton-X looks at multiple electronic states and, with the use of non-adiabatical statistics and a stochastic algorithm, makes a decision about which electronic state the molecule is likely to be in, making any necessary changes between the time steps. Energy is conserved in the system during these changes of state by scaling the kinetic energy of the atoms between time steps. For example, if the calculation determines that there is a statistical probability that the molecule will hop from a lower potential-energy surface to a higher one (*i.e.* it enters an excited state), the kinetic energy of the system is reduced, and *vice versa*. If there is not enough kinetic energy in the system, no surface hopping is observed.

Temperature is also taken into account using the Andersen thermostat,[114] which generates a canonical ensemble of random energies for each atom with a mean kinetic energy determined by the force-constant calculations, though now with a standard deviation equal to $k_B T(3N/2)^{1/2}$ (where k_B is the Boltzmann constant, and N is the number of atoms). It keeps the kinetic energy in check with a series of random collisions, which follow the Poisson distribution using a chosen collision frequency, v, which redistributes the kinetic energy across the system after each collision.

In order to have good statistics, Newton-X has the ability to run multiple calculations all at once, with each calculation starting from a slightly different geometric structure, and hence evolving in a slightly different way. This allows the user to get a better idea of the overall average mechanics of the molecular system.

Chapter 3. Apparatus design, development and experimental set-up

3.1. Compact electron gun

As discussed in Section 2.2.6, there are numerous types of TRED electron gun designs that could have been adopted for this project. In order to keep things simple, however, a TRED apparatus based upon the ideas of the compact electron gun design was chosen as it met our requirements, and was the most likely to yield results in the timeframe set for this project. Other apparatus designs, such as ones that included RF cavities, would not have been a wise choice for a group starting out in TRED studies, such as ours, as other groups, with a decade or more of experience in the field, were still struggling to build a reliable apparatus. Nor was a relativistic TRED apparatus ever an option, as this would have required a source of MeV electrons, well beyond the capabilities of most universities. The simplicity of the compact electron gun allowed for on-the-fly adjustments to be made when necessary and for new components to be incorporated with relative ease. Any other type of gun would have left less room for customisation further down the line if it was ever needed.

The apparatus that has been built for this project is shown in Figure 3.1, as it looked when it was first assembled. It can be described as two separate chambers: the electron gun chamber, and the diffraction chamber. The electron gun chamber consists of the electron gun, high-voltage feedthrough, and an anode plate that acts the division between the electron gun chamber and the diffraction chamber. The diffraction chamber has numerous ports to allow for various instruments to be inserted, a magnetic solenoid lens for electron beam control, translators for sample manipulation, and a detector to collect diffraction data.
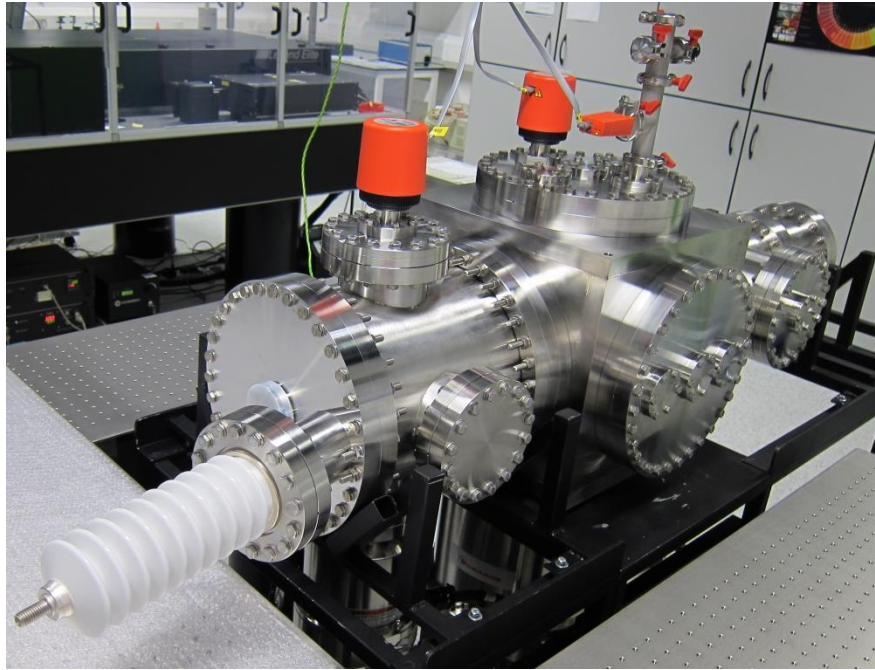
Figure 3.1: Photograph of the assembled apparatus.

3.2. Apparatus design

The following sections detail the design of each chamber and its associated components in full. Most of the vacuum components for the TRED were manufactured by Allectra GmbH, unless stated otherwise. Where applicable, technical drawings for the original components are given in Appendix A.

3.2.1. General set-up

Figure 3.2 shows a simplified version of the experimental set-up to help understand the design and structure of various aspects of the apparatus as they are discussed throughout this chapter.
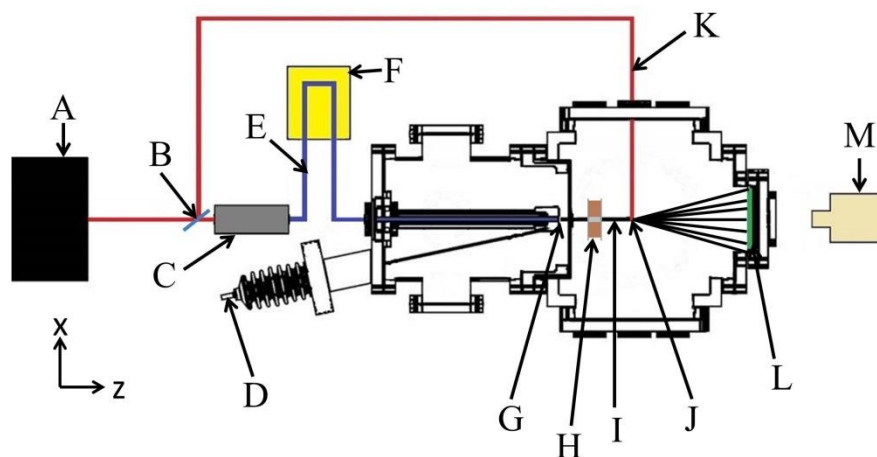
Figure 3.2: A schematic representation of the general experimental set-up showing A) Ti:Sapphire laser, B) beam splitter, C) third harmonic generation set-up, D) high-voltage feedthrough, E) photocathode ionisation laser path, F) delay stage, G) photocathode, H) magnetic lens, I) electron beam, J) sample position, K) pump laser path, L) electron detector, and M) CCD camera.

In this set-up a laser from a Ti:Sapphire source (A) is split in two using a beam splitter (B), with one branch passing through a THG set-up (C) converting 800 nm light to 267 nm. This 267 nm ionisation laser beam (E) is directed using mirrors onto the translation stage (F), which allows the time delay to be controlled for pump-probe experiments. From this delay stage the laser is directed into the electron gun chamber *via* a viewport, passing through the electrode mount to the photocathode (G). The ionisation of the photocathode by the laser creates the pulsed electron beam (I) that is accelerated by the negative potential applied to the photocathode from the high-voltage feedthrough (D), towards the grounded anode, which effectively isolates the electron gun chamber from the diffraction chamber. A small aperture in the anode allows the electron beam to pass into the diffraction chamber, where it is focussed using a magnetic lens (H), before travelling towards the sample (J). With successful diffraction the electron beam is scattered towards the microchannel plate (MCP) and phosphor screen detector (L), where images are recorded using a charge-coupled device (CCD) camera (M). Meanwhile, the other 800 nm laser beam (K) from the beam splitter (B) enters the diffraction chamber perpendicularly to the electron beam and is used for pump-probe and electron beam diagnostic experiments.

3.2.2. Electron gun chamber

The electron gun depicted in Figure 3.3 is where the pulsed electron beam is created, from the ionisation of a gold photocathode using a 267 nm femtosecond pulsed laser beam. As mentioned already, the main components of the electron gun include the photocathode (which is discussed in more detail in Section 3.2.4), an electrode and its mount, a high-voltage feedthrough, and the vacuum chamber that encloses all of this. Most of the components described here are made from non-magnetic 316LN stainless steel unless stated otherwise.
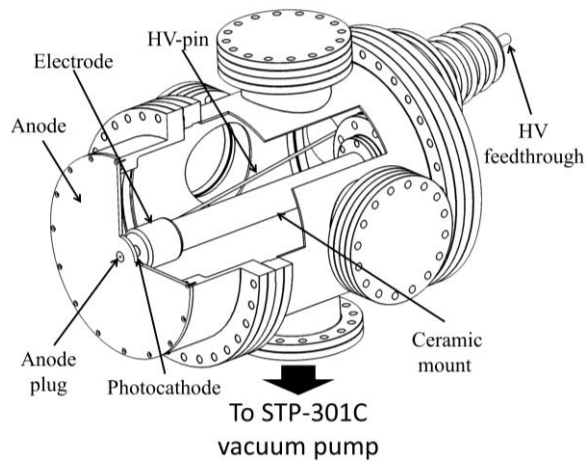
Figure 3.3: Cut-through diagram of the electron gun chamber, detailing its assembled form.

The cylindrical electrode, shown in more detail in Figure 3.4, is 50 mm in both diameter and length, and has its outside edges rounded to a 2 mm diameter to prevent unwanted discharge from discontinuities in the electric field that may be caused by sharp corners.[115] A 10 mm diameter bore runs from one face of the electrode to the other to allow the laser beam to reach the photocathode, which sits in a 13 mm wide, 0.5 mm deep recess in the front face of the electrode. Due to the precise shape of this groove, the photocathode is able to sit in the electrode freely whilst the electrode cover (discussed shortly) is in place.
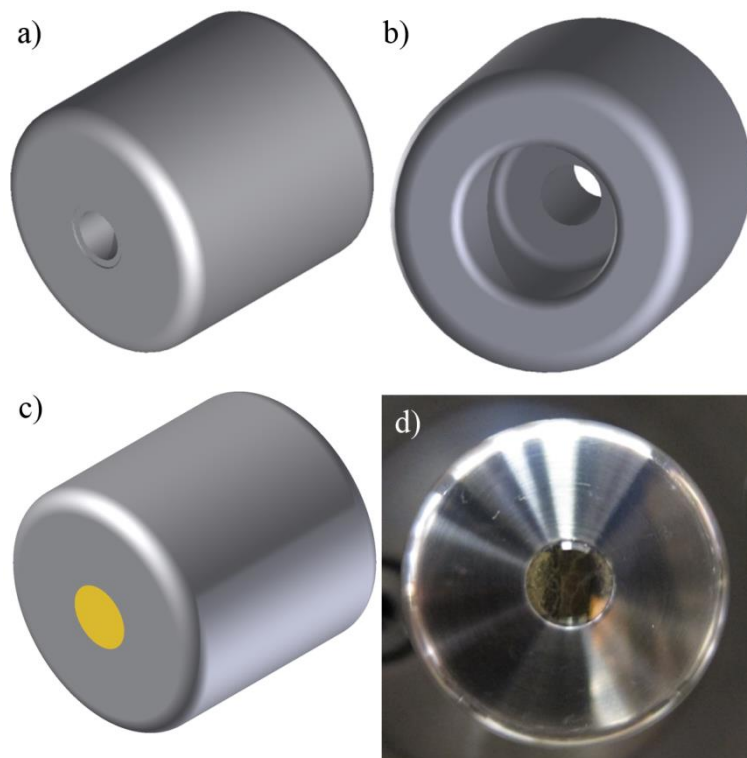
Figure 3.4: CAD drawings of a) the front view of the electrode, b) the rear view of the electrode, c) the photocathode in the electrode, and d) a photograph of photocathode sitting in the electrode.

A 25 mm diameter, 25 mm deep rounded bore in the back of the electrode (visible in Figure 3.4b) allows for the ceramic electrode mount to be inserted. This cylindrical mount, manufactured from MACOR by Multilab, is 315 mm long, 37 mm wide, and has a 19 mm diameter bore down the centre. The front end of the ceramic narrows to a 25 mm diameter, so that it can be inserted into the back of the electrode, and is fixed to the electrode with ceramic cement. The opposite end of the ceramic is similarly fixed into a bored 2.75" CF flange. The inner and outer surfaces of the mount are ribbed to increase the surface area of the ceramic to help prevent any charge creep that may occur from the use of high voltages.[115]

The 2.75" CF flange of the ceramic mount is attached to a 4.5" CF "degassing" flange, which has a series of holes in it that allow for the bore in the mount to be evacuated and vented effectively. The complete electrode and mount is shown in Figure 3.5.
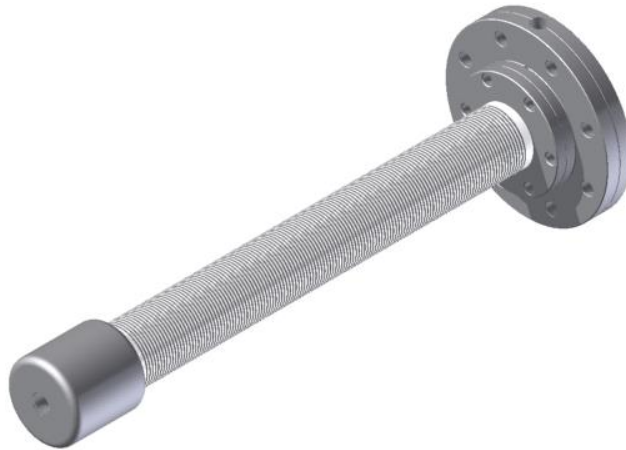
Figure 3.5: CAD drawing showing the electrode mounted on the ribbed ceramic mount and 2.75" CF flange, and attached to the 4.5" degassing flange.

The electrode and mount are then attached to the rear 12" CF flange of the electron gun chamber, as shown in Figure 3.6. On the opposite face of this flange there is a 2.75" CF flange with a DUV quartz window to allow entry for the photocathode ionisation laser.
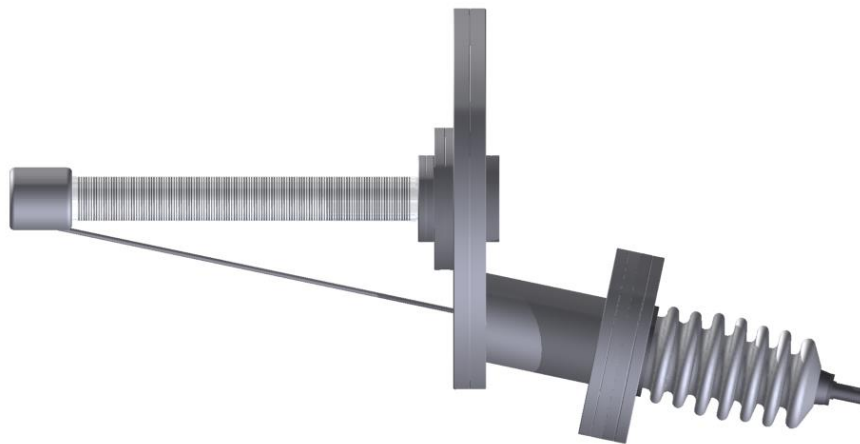
Figure 3.6: CAD drawing showing the electron gun mounted on the rear flange of the electron gun chamber, with a 2.75" DUV quartz viewport on the air side, and high-voltage feedthrough entering the chamber.

The high-voltage feedthrough is mounted on a 6" CF flange and enters the gun *via* a flanged pipe on the rear 12" flange of the chamber. A connection between the high-voltage feedthrough and the electrode is made using a shaped ¼" steel rod, which is held in place against the electrode by a ceramic cover that sits over the electrode. This ceramic cover, also made of MACOR by Multilab, helps to prevent unwanted discharge between the electrode and the walls of the chamber.

Outside the chamber, a Faraday cage was built to prevent any in-air arcing at the point where the high-voltage source enters the apparatus *via* the feedthrough, and to prevent any person coming into contact with the high-voltage when it is on. The cage, seen in Figure 3.7, consists of a 1 m long, 22 cm diameter Perspex tube, with aluminium ends, and has a grounded wire mesh wrapped around the outside of this tube to help to disperse any discharges that may occur.
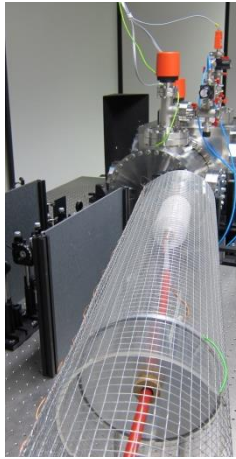
Figure 3.7: Photograph of the Faraday cage surrounding the high-voltage feedthrough.

The cylindrical electron gun chamber, shown in Figure 3.8, is 11" long, and capped at both ends by two 12" CF flanges. Four 6" CF ports at right angles to each other around the circumference of the chamber allow for vacuum pumps (see Section 3.2.6 for more detail) and other instruments to be attached.
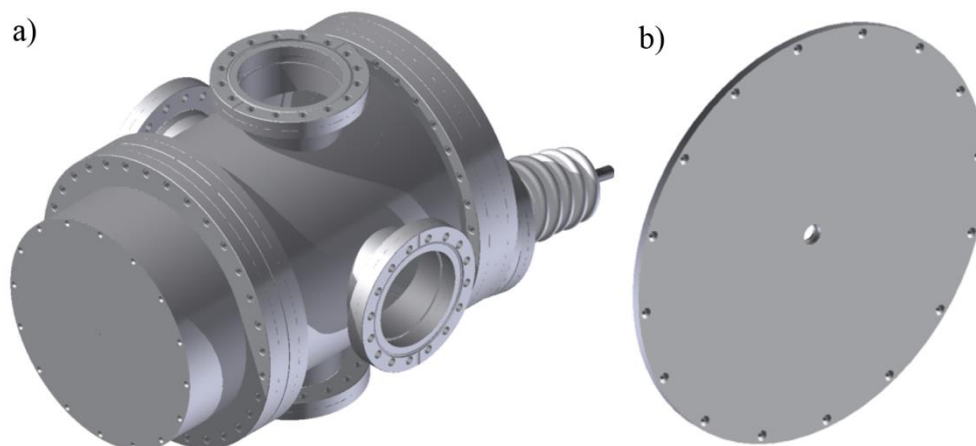
Figure 3.8: CAD drawing of a) the sealed electron gun with the protruding barrel and attached anode plate, and b) the anode plate itself, with a hole in centre for the anode plug to be inserted.

On the front end of the chamber is the barrel of the electron gun, a 70 mm long extrusion built upon a double-knife-edge 12" CF flange. When the electron gun chamber is attached to the diffraction chamber, this allows the electron gun to protrude into the diffraction chamber. A titanium anode plate, shown in Figure 3.8b, is attached to the front of the barrel, and acts a barrier between the two chambers, helping to prevent any gas that may be introduced into the diffraction chamber during experiments from entering and contaminating the electron gun. As the name suggests, the anode plate also acts as the grounded electrode used to accelerate the electrons produced at the photocathode. In the centre of the anode plate there is a 10 mm wide hole for a titanium anode plug, shown in Figure 3.9, to be inserted.
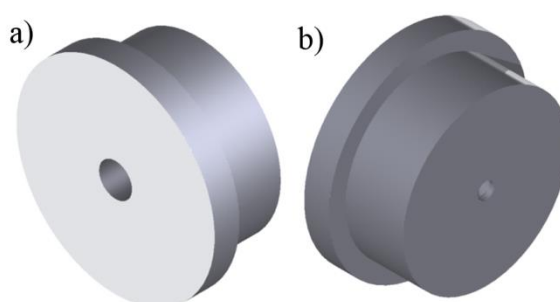
Figure 3.9: CAD drawings of a) the front face and b) the rear face of the anode plug.

The anode plug is the final component of the electron gun, allowing for an even electric field between it and the photocathode. The front face of the anode plug (Figure 3.9a) is 12 mm wide and has a 2 mm hole in its centre that goes most of the

way through the plug for an aperture to be inserted, allowing more control over the properties of the electron beam that enters the diffraction chamber. The rear face of the plug (Figure 3.9b) has a reduced diameter of 10 mm, allowing it to be inserted into the anode plate. The bore through the centre narrows to 1 mm on this face to prevent the inserted aperture from falling into the electron gun.

With the electron gun set-up as detailed as above, the distance between the photocathode and the anode is approximately 17 mm, and this is the distance used for most of the experiments detailed in this thesis. The photocathode-to-anode distance can be reduced by introducing spacer plates between the electron gun mount and the electron gun rear flange.

3.2.3. Diffraction chamber

The diffraction chamber mainly consists of the 14" cube that is shown in Figure 3.10. The cube has 1" thick walls, and has a 12" CF flange port on each face of the cube. Four tapped M12 holes can be found on the top and bottom external faces of the cube that help with the initial positioning of the apparatus, and allow for "feet" to be inserted, to control the level of the chamber. Four tapped M6 holes can also be found in the internal top and bottom faces of the cube, to allow for extra components to be fixed securely within the chamber.
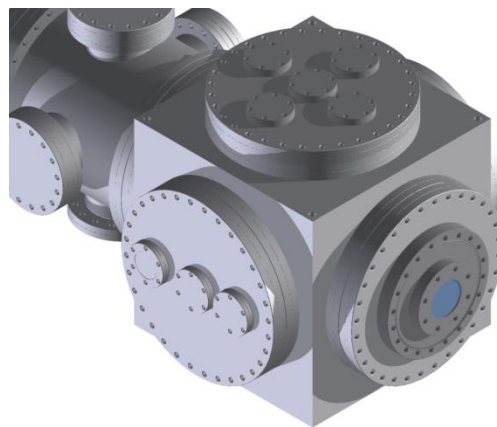
Figure 3.10: CAD drawing of the 14" cubic diffraction chamber with flanges and the electron gun (seen to the top left) attached.

Of the six flanged faces on the cube, one is used to attach the electron gun to the diffraction chamber, whilst the flange opposite has a 12"-8" CF reducer flange

attached, which can either allow for electron detection equipment to be installed directly, or for the addition of other vacuum chambers to increase the flight region for the electrons. Attached to the bottom flange is the main vacuum pump (detailed further in Section 3.2.6). The remaining side and top flanges are sealed with customised 12" CF flanges, pictured in Figure 3.11, which also allow instruments to be inserted into, and viewports to be attached to, the chamber. The side flange (Figure 3.11a) has three 2.75" CF flange ports that run through the horizontal axis, and are unevenly spaced to allow for a range of port positions. The top flange (Figure 3.11b) has three 2.75" CF ports in the same positions as the side flange, but also two extra ports to allow for extra instruments to be attached.
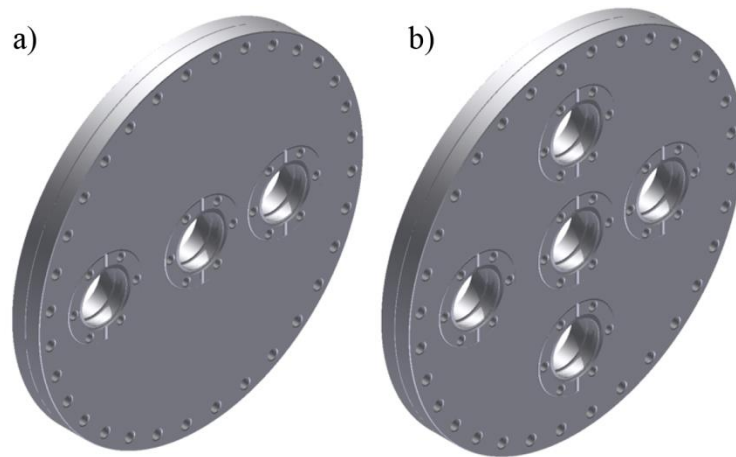
Figure 3.11: CAD drawings of a) the 12" CF side flange and b) the top flange used to seal the main diffraction cube.

3.2.4. Photocathodes

The photocathodes created for the apparatus, represented pictorially in Figure 3.12, are based on photocathodes used by Miller *et al*.[21,72] A 13 mm wide sapphire disc is coated with a thin film of gold on one side, and a thicker film of a conductive metal (*e.g.* chromium/aluminium) on the other side and around the edges. The gold thin film creates the electron pulses after ionisation by a laser; the conductive metal layer on the opposite side and around the edges ensures a strong conduction between the gold side of the photocathode and the electrode. So as not to impede the arrival of the laser at the gold film, a "window" on the back side of the sapphire is left metal-free to allow for the laser to pass through the disc.
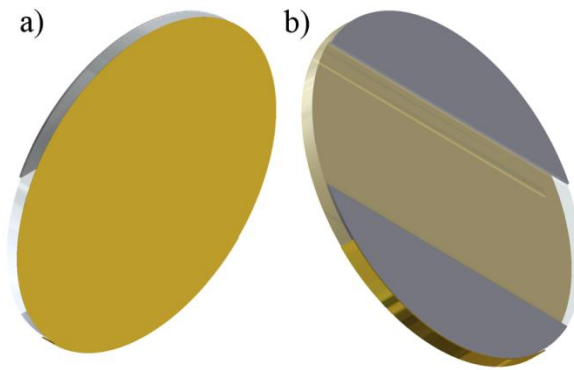
Figure 3.12: CAD drawings of a) the front and b) the rear sides of the photocathode.

The metallic films were applied to the sapphire disc using evaporation-deposition techniques (as provided by Dr Oleg Nerushev at Edinburgh and Dave Coulthard in York). To ensure that the there is a good overlap between the two films the sapphire disc is held at angle during deposition to coat the disc edge where the films meet. A custom holder, made of aluminium and shown in Figure 3.13, was designed to allow multiple photocathodes to be coated at once.
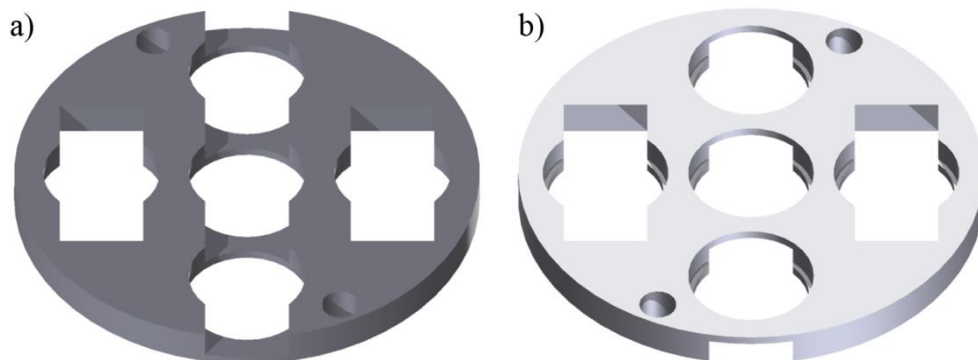
Figure 3.13: CAD drawing of a) the front and b) the back of the photocathode holder.

The holder allows for up to five photocathodes to be created at once, with each sapphire disc placed in a hole, and supported on small ledges. Square notches above and below the position of each disc allow for gold/conductive metals to be deposited onto the edge of the disc when the holder is held at an angle. As shown in Figure 3.14, the conductive layer is applied first to the back and sides of the sapphire disc, with a small piece of aluminium foil in place to prevent deposition in a region to obtain the desired "window". The thickness of this layer, although never measured, is at least 100 nm to ensure it has bulk-like properties.
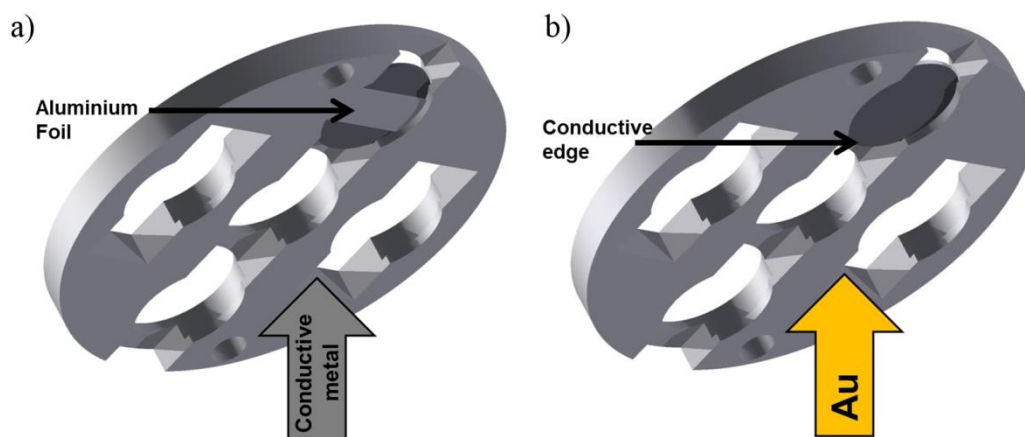
Figure 3.14: A diagrammatic representation of a) a conductive metal layer and b) a gold film being deposited onto the sapphire disc.

The gold film is then added to the opposite side of the photocathode, with the disc sitting so that the conductive edge faces the rectangular slot in the holder. As the thickness of the gold layer is important, the deposition rate is carefully monitored, so that a suitable thickness of approximately 20 nm is obtained. The finished product is shown in Figure 3.15; the layer of gold is thin enough that the conductive metal on the opposite side of the sapphire disc can be seen.
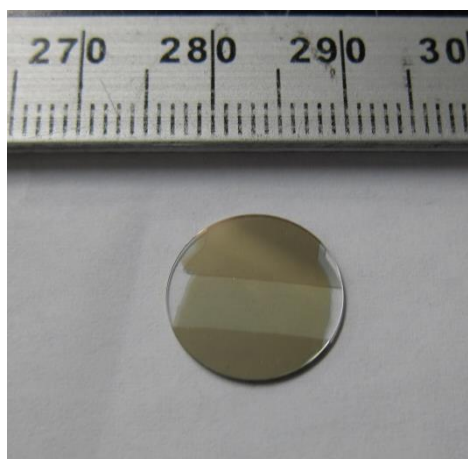
Figure 3.15: Photograph showing the complete photocathode with the gold side facing up.

Once complete, the photocathodes are tested to ensure that there is a good electrical contact between its two sides; this is achieved by placing the photocathode gold-side down on a sheet of aluminium foil, and testing the resistance between the foil and the conductive metal using a multi-meter. Those cathodes that show an

infinite resistance on the multi-meter do not have a suitable overlap between the two layers, and are discarded. The photocathodes that do pass the resistance test can be used in the apparatus, being mounted in the electrode of the electron gun, with the conductive edge pointing downwards to ensure that there is sufficient electrical contact between the photocathode and electrode.

3.2.5. Electron detection equipment

The electron beam can be observed either visually using the diffraction detector equipment shown in Figure 3.16 and a CCD camera, or by measuring its charge using a Faraday cup and electrometer.
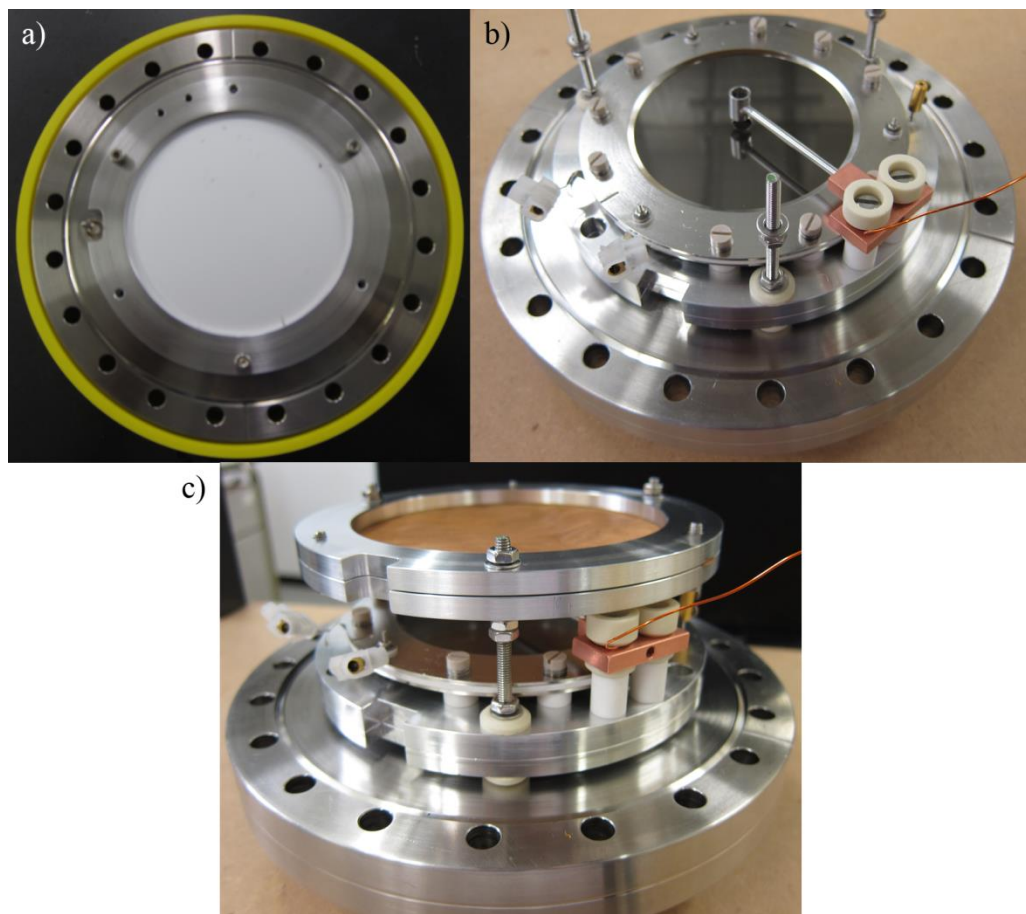
Figure 3.16: Photographs of the detector set-up consisting of a) a phosphor screen and b) a microchannel plate, mounted upon an 8"-4.5" CF reducer flange. An aluminium beam block, used to measure the current of the beam, sits in front of the MCP. Photograph c) shows the fully assembled detector, complete with a grounding mesh in front of the MCP.

The detector is constructed from a phosphor screen and a microchannel plate (MCP) image intensifier. The phosphor screen, made by TMS Vacuum, consists of a

115 mm diameter, 3 mm thick glass plate coated with approximately 50 μm of P22 phosphor, with a secondary 50 nm aluminium coating on top of that. When electrons strike the phosphor they cause it to phosphoresce, allowing the position of the electron beam on the detector to be observed using a CCD camera. The aluminium coating on top of the phosphor is thin enough for electrons to pass through unimpeded; the conductive coating also helps to dissipate the build-up of charge caused by electrons hitting the detector. The screen is mounted in an aluminium case (manufactured by York's Department of Chemistry mechanical workshop) which itself can either be mounted directly onto an 8"-4.5" reducer flange (Figure 3.16a) or upon a series of rods before being fixed to the flange (Figure 3.16b). As briefly mentioned, the phosphor screen can be viewed using a CCD camera (Stingray F-146B) and lens (Schneider 17 mm focal length) through a 4.5" CF viewport attached to the opposite side of the 8"-4.5" CF reducer flange. Images are recorded on a computer and analysed as described in Section 5.4. When working with the MCP, the phosphor screen must have a positive potential across it, which is provided using a Stanford PS350 power supply.

The MCP image intensifier placed in front of the phosphor screen is used to enhance any image produced by the diffracted electrons. The MCP used here was previously used in Edinburgh as part of a time-averaged electron diffraction apparatus and is described in detail in the thesis of Dr. Robert S. Fender.[116] The MCP has a 75 mm diameter active area (with a 6 mm diameter hole in the centre) consisting of semiconducting micropores made from metallised glass. These pores create a cascade of electrons when an energetic particle hits one of the channel walls (generally 10^6 electrons are created for every impinging electrons).[116] Eventually the cascade will leave the opposite side of the MCP, and the electrons are drawn towards the phosphor screen by the positive potential applied to the screen. The image is therefore enhanced compared to one collected without an MCP. The MCP helps to reduce the time needed to collect diffraction data, as well as allowing the observation of less intense scattering rings in the diffraction pattern. For the MCP to work a potential must be applied across it, so as to draw the cascading electrons through. This is achieved by grounding the front face of the MCP (*i.e.* the face nearest to electron gun), whilst applying a potential from a Vortec 3 kV power source across its back face.

In front of this detector, a 7.5 mm diameter aluminium beam block sits over the hole in the MCP. This prevents the main part of the undiffracted beam from hitting the phosphor screen, effectively increasing the dynamic range of the camera. The block also acts as a Faraday cup for measuring the electron beam current. The block is attached to a wire that passes through a BNC connector which then leads to a picoammeter. The Keithley 6485 digital picoammeter allows the current of the electron beam to be measured accurately, and is linked to the laser signal-delay generator in order to be triggered to read around the arrival time of the electron beam on the detector.

As seen in Figure 3.16, a grounded copper mesh is mounted before the assembly described above. This helps to ensure that much of the flight region of the electrons between the anode and the detector is free of electric fields. The mesh is sufficiently transparent to the electrons that they pass through unimpeded.

3.2.6. Vacuum system

All of the pumps and associated vacuum equipment used in this project were purchased from Edwards, except where otherwise stated. A diagram showing the set-up can be seen in Figure 3.17. To prevent gas flow from one chamber to another, the electron gun and diffraction chambers are differentially pumped. The diffraction chamber is pumped by an STP-A2203C magnetically levitated turbomolecular vacuum pump which is backed by an XDS35i scroll pump; the electron gun is evacuated by a smaller STP-301C turbomolecular pump, backed by an nXDS10i scroll pump.
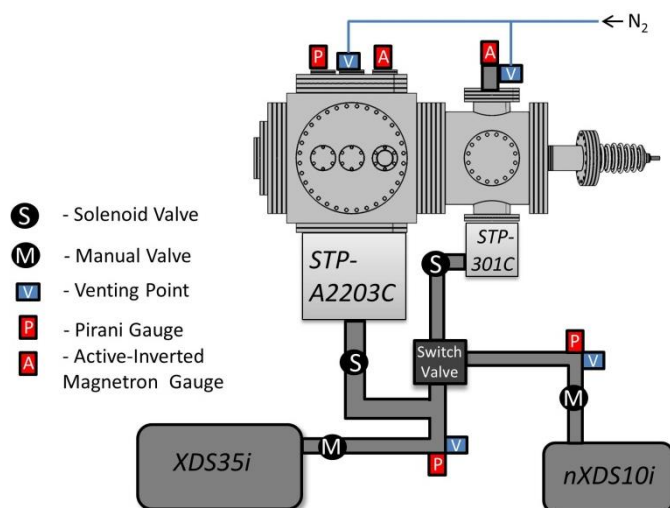
Figure 3.17: Diagram showing the vacuum set-up for the apparatus, which includes a pair of turbomolecular pumps (STP-A2203C and STP-301C), backed by scroll pumps (XDS35i and nXDS10i).

Both chambers are initially evacuated using the XDS35i scroll pump, to ensure an even pressure drop on either side of the anode plate. Once the pressure has dropped to a sufficient level (around 4×10^{-2} mbar) a switch valve is used in the backing line to effectively isolate the two chambers, allowing each chamber to be pumped by its respective scroll pump. The pressure in the apparatus can be returned to atmospheric pressure by the controlled introduction of nitrogen *via* a gas line attached to both chambers. To ensure that the apparatus remains vacuum tight when the pumps are off, and to prevent a backflow of air through the turbo-pumps as the scroll pumps shutdown, a pair of solenoid valves are used in the backing line to isolate the chambers.

For relatively low vacuums (*i.e.* above 1×10^{-4} mbar) the pressures in both backing lines and the diffraction chamber are monitored by Active Linear Pirani gauges. Pressures below this (down to 1×10^{-9} mbar) are monitored using a set of Active-Inverted Magnetron gauges. All pressures are indicated using an Edwards Instrument Controller.

3.2.7. High-voltage power supply

The PNChp-100000-1-neg high-voltage power supply was purchased from Heinzinger, and has the ability to provide a potential of up to −100 kV, with a precision of ± 0.01 kV, and a stability of up to 0.001%. A current of up to 20 mA can

also be applied using the power supply if required (to a precision of 1×10^{-4} mA). However, for the purpose of the experiments described here the current was only set to a level to allow for a stable potential to be put across the electrode, and generally did not exceed 1×10^{-4} mA under normal operating conditions.

3.2.8. Magnetic lens

The magnetic lens used to focus the electron beam is based on the principles of a simple solenoid and is shown in Figure 3.18.[117] The base of the lens was manufactured by Edinburgh's School of Chemistry mechanical workshop, and is a 70 mm diameter, 20 mm deep, spool-like iron core, with a 9 mm diameter hole through the centre. A 0.4 mm wide, 110 m long Kapton-coated copper wire is wound around this core, to give approximately a thousand turns. A series of other holes can also be seen on the face of the lens (Figure 3.18a) to help feed wires through and mount the lens.
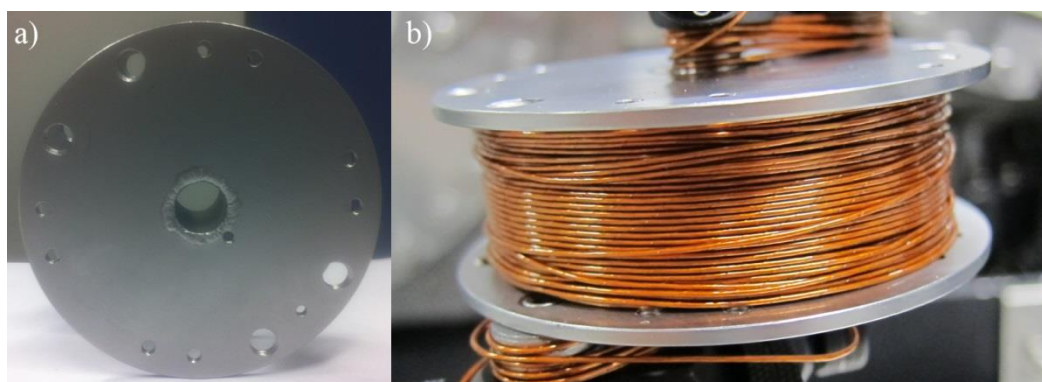
Figure 3.18: Photographs of the magnetic lens, with its Kapton-coated copper wire windings, as seen from a) the front and b) the side.

When in the apparatus (as shown in Figure 3.19) the flat side of the lens is parallel to the anode of the electron gun so that the electron beam can pass through the central hole of lens.
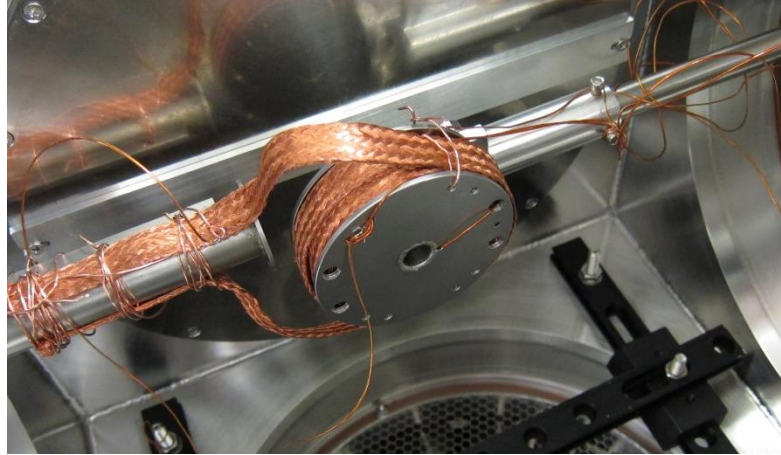
Figure 3.19: Photograph showing the lens mounted in the apparatus, with the cold trap set-up, and thermocouples attached.

The lens uses an Iso-Tech power supply that has the ability to maintain a steady current, whilst allowing the applied voltage to vary automatically. This is necessary because, whilst in operation, the lens heats up and this in turn causes an increase in the resistivity of the lens. The maximum current that can be used is 3 A, though the standard operating current does not normally exceed 1.5 A.

To help dissipate the heat produced, the lens is cooled by a series of copper braids that are attached to a liquid nitrogen cold trap. The temperature of the magnetic lens can be monitored using thermocouples attached at various points between the cold finger and the lens. However, as the thermocouples are only in contact with the outermost windings of the lens, and little is known of the core temperature, it can be useful to estimate the temperature (T) of the lens by determining the change in the resistance (ΔR) of the wire in the lens from the current (I) and voltage (V) being supplied, and extrapolating the temperature using the following equations:

$$\Delta R \cong \rho \Delta T \, , \qquad\qquad \text{Eq. 3.1}$$

$$\Delta T \cong \frac{\Delta V}{I\rho} \, , \qquad\qquad \text{Eq. 3.2}$$

where ρ is the change in the resistance of the wire, per Kelvin.

In order to fine adjust the position of the lens, it is mounted upon an *xyz* translator. This mainly allows for control of the trajectory of the electron beam as it flies towards the sample and detector, but will also allow for small changes in how the electron beam is focussed.

3.2.9. Beam-width measurer

To determine accurately the width of the electron beam, and to measure how that varies during its propagation through the apparatus, the aluminium piece shown in Figure 3.20 was manufactured by York's Department of Chemistry mechanical workshop. The beam width measurer has a pair of holes (200 and 500 μm in diameter) that can be scanned across the electron beam, blocking most of it, and allowing the current that passes through the hole to be measured using the picoammeter. The triangular cut out that can be seen in line with the two apertures, along with a slit above each hole, is used to help position the holes over the electron beam.

Figure 3.20: Photograph of the electron beam-width measurer.

The size of the electron beam can be determined by first finding where the current is highest (*i.e.* where the centre of the beam is passing through the aperture) and scanning until no more current is measured (*i.e.* the edges of the beam). The differently sized apertures are used to measure the size of the electron beam with different degrees of precision.

3.2.10. Solid-sample mounting

A mount for holding solid-state samples is shown in Figure 3.21. The circular brass mount is designed to hold an 8 mm diameter mesh, which supports the sample of choice.

Figure 3.21: Photograph of the solid-state sample mount used on the TRED apparatus.

The mount has an L-shaped bracket that allows the sample holder to be mounted upon a series of optics post. These optics posts are then attached to a 2.75" CF flange that connects to an *xyz* manipulator, allowing for full control of the position of the sample. With this the sample can easily be moved into the best position within the electron beam for optimal diffraction or, if required, retracted entirely from the path of the electrons.

3.2.11. Beam aligner

To carry out pump-probe experiments it is imperative that the electron and pump laser beams cross one another both in time and space. To help with this alignment an aluminium piece, shown in Figure 3.22, was made.
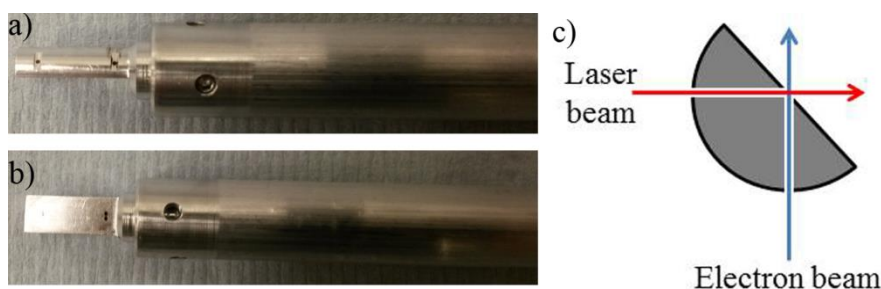
Figure 3.22: Photographs of the aluminium beam alignment piece from a) the side and b) the front. Diagram c) shows how the beams enter and then cross after passing through the alignment piece.

The hemicylindrical piece has two pairs of perpendicular apertures that run at a 45° angle to the flat face. The apertures are paired with another of the same size, with one set being 500 μm in diameter, and the other 200 μm in diameter. As these apertures tend towards the flat side of the piece they converge so that if two beams were to travel independently down them they are sure to cross one another as they pass through. When each beam travels down its respective bore through the piece

unperturbed, like that depicted in Figure 3.22c, the beams are considered correctly aligned.

3.2.12. Simple gas-handling system

Figure 3.23 shows the simple gas-handling system used for early gas-phase test experiments.
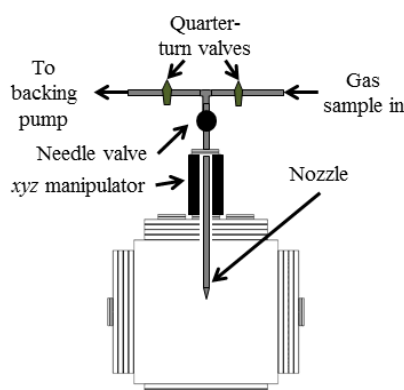
Figure 3.23: Diagram showing the main features of the system used to inject gas into the diffraction chamber.

A simple nozzle is mounted upon a 2.75" CF flange and introduced into the apparatus *via* an *xyz* manipulator, which allows the nozzle position to be controlled. The nozzle has a 0.5 mm wide orifice, and the volume of gas that may pass through it is controlled externally using a Swagelok needle valve. This valve comes immediately after a Swagelok T-piece, where one branch is connected to the sample supply, which may be a gas cylinder or ampoule containing a sample *via* a quarter-turn valve. The other branch is connected to a quarter-turn valve and an Edwards RV5 rotary backing pump that is used to evacuate the gas line before the sample is injected into the main apparatus.

3.3. Lasers and optics

The majority of the experimental findings presented in this thesis were obtained in the Photochemistry Laboratory in the Department of Chemistry at the University of York, using the laser system described below. However, early testing and calibration work on the apparatus was performed in the lab of Professor Eleanor Campbell within the School of Chemistry at the University of Edinburgh. Whilst both laser systems will be described, only the optics layout used in York will be

detailed in full. This is because both set-ups used similar optical methods, with slightly different positioning of the individual mirrors and lenses. The majority of the optics described here were purchased from Thorlabs, unless stated otherwise.

3.3.1. Laser systems

3.3.1.1. Edinburgh

The femtosecond laser used in the Edinburgh lab is a Coherent Legend Elite, pumped by a Coherent Mantis laser. This produces a horizontally polarised laser pulse with a central wavelength of 800 nm (9 nm bandwidth), a duration of 120 fs, and an optimal output power of 3.8 W (3.8 mJ per pulse), when operating at 1 kHz. Further detailed information on the laser can be found in the theses of Dr Olof Johansson[118] and Dr Gordon Henderson.[119]

The output laser from the Legend Elite was split in two, with one branch used by the Campbell group, whilst the second was used for TRGED experiments. The power of the beam that came on to the optics table for the TRGED experiments was approximately 1.25 W. This beam was then split in two by a 90:10 beamsplitter, where the 10% was used to create the electron beam, whilst the remaining 90% was used for ponderomotive scattering and TRED pumping experiments.

3.3.1.2. York

The laser system used in York was a Coherent Libra Ti:Sapphire amplifier and oscillator laser system, acquired through the EPSRC Laser Loan Pool. As with the Edinburgh laser this too produced horizontally polarised light, with a central wavelength of 800 nm (15 nm bandwidth). However, unlike the Coherent Legend Elite, the Libra's pulse duration was slightly longer, on the order of 150 fs (as measured with an APE-pulse check autocorrelator), with an average maximum power of 1 W (1 mJ per pulse) when operating at a 1 kHz repetition rate.

3.3.2. Optics set-up

The overall optics set-up used in the TRGED experiments is shown in Figure 3.24.
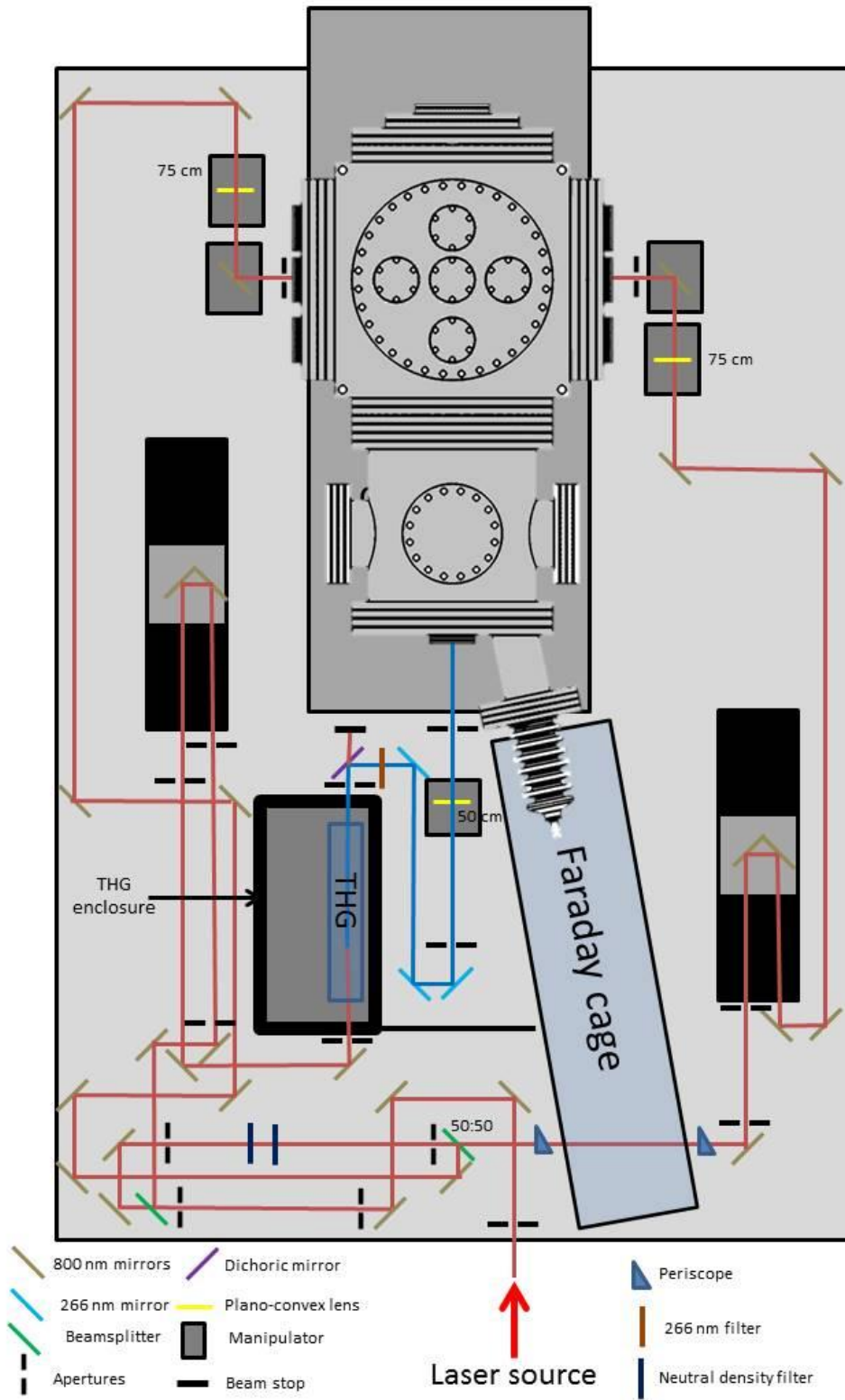
Figure 3.24: Diagram showing the general optics layout used for TRGED experiments.

3.3.2.1. Electron beam production

Figure 3.25 shows the general optics that are necessary to produce a laser suitable to ionise a photocathode for pulsed electron beam production within the main apparatus.
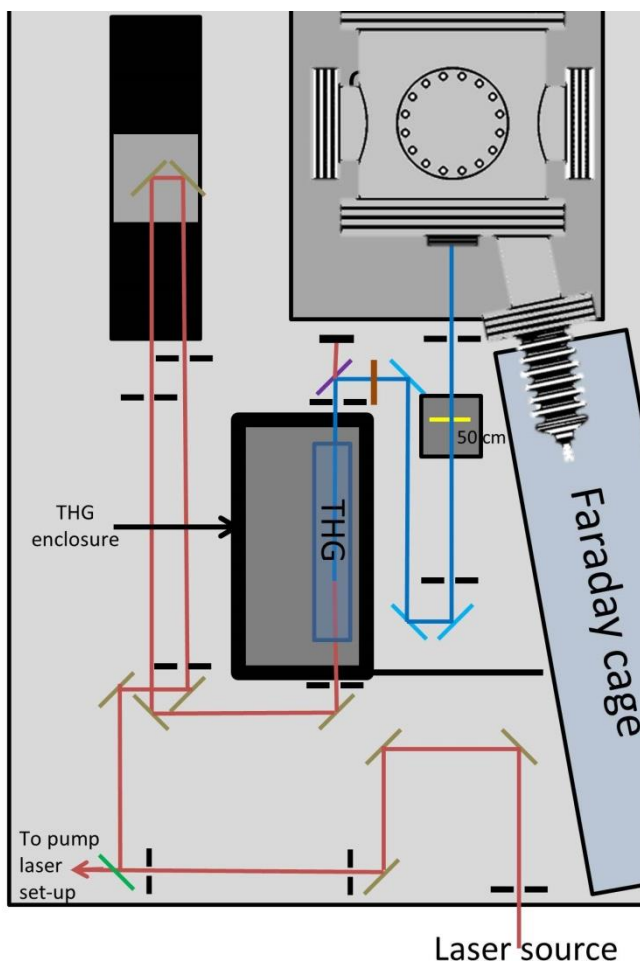
Figure 3.25: Diagram showing the path of the 800 nm laser from source to triple harmonic generation (THG) set-up, where it is converted into 267 nm light, and then into the apparatus where it ionises the photocathode under vacuum. The pump laser path has been removed for clarity. The key to this diagram can be found in Figure 3.24.

First, the full laser beam passes through a beamsplitter to create separate electron gun and pump laser paths. The electron gun beam is then directed towards a 30 cm long Newport translation stage, used to control the arrival time of the electron pulse when carrying out pump-probe experiments. Apertures are used before and after the laser interacts with mirrors on the stage to ensure that the laser is well aligned, so that when the stage moves, the laser continues along the same path. After leaving the

stage the laser is directed through a series of optics in an enclosed triple harmonic generation (THG) set-up, purchased from Eksma Optics.

The third harmonic is obtained from this THG set-up by first passing the laser through a BBO second harmonic generation (SHG) crystal, which combines photons of 800 nm light to produce photons of 400 nm light. The conversion efficiency of this crystal is dependent on the optical axis angle of the crystal with respect to the polarisation of the laser used, and so must be carefully positioned to obtain the optimal conversion. The beam that exits this crystal is a mixture of 400 and 800 nm light, with the 400 nm light travelling behind, and with its electromagnetic component oscillating in an axis perpendicular to that of the non-converted 800 nm light. To help account for the delay between the colours, a group velocity delay (GVD) calcite crystal is used to increase the optical path length for the 800 nm light, allowing the 400 nm light to "catch up". To ensure that both wavelengths of light have the same polarisation, the beam is passed through a zero-order $\lambda/2@800$ nm / $\lambda@400$ nm waveplate to rotate the 800 nm light into the same plane as the 400 nm light. These two colours are then combined in a second BBO crystal to produce the third harmonic (267 nm) light. As the alignment of the laser through these optics is important, a pair of apertures placed at either end of the THG set-up is used to ensure that the laser beam is travelling along the desired path. With the crystals well aligned to produce the maximum amount of 267 nm light, one can easily control the amount of 267 nm light produced by "detuning" one the crystals by rotating its optical axis.

A dichroic mirror is used to separate the 267 nm light from the 400 and 800 nm light and direct it towards the apparatus, while the remaining 400 and 800 nm light is killed at a beam stop. A 267 nm filter placed shortly after the dichroic mirror ensures that only 267 nm light is allowed to continue on to the main apparatus.

A set of mirrors is used to direct the beam towards a 50 cm lens, which focusses the beam onto the photocathode in the apparatus. These mirrors also allow for the fine positioning of the laser on the photocathode, so that any light that passes through the photocathode eventually passes through the aperture in the anode plug as well. If the laser is not aligned correctly in this way, the electrons produced from the photocathode may not be accelerated directly through the aperture in the anode, and hence some or all of the electron beam will be lost. The 50 cm lens itself sits upon a flip mount, so that it can easily be removed / inserted during alignment procedures

without losing its position. It is also on a translation stage so that the optimal focal position on the photocathode can be found more easily. To help with realigning the laser, two adjustable apertures are placed after the final mirror, on either side of the 50 cm lens, before the apparatus.

3.3.2.2. Pump-probe experiments

The optics for this experiment have been established in such a way that, along with the electron gun laser path, one can have the optics for both standard pump-probe experiments (*i.e.* single laser entering the apparatus), and grating-enhanced ponderomotive scattering experiments [which require two counter-propagating laser beams, from the same source, entering the chamber at once (Section 2.2.3)] assembled at the same time, with the ability to switch between the two. Because of this, after the pump-probe laser path leaves the electron gun laser at the first beamsplitter on the optics table, it is directed towards a 50:50 beamsplitter, creating two branches that are further directed to opposite sides of the apparatus as seen on Figure 3.24. These beams will, therefore, be referred to as the left and right branches as seen when looking down on the set-up from the electron gun end of the apparatus. Just before the beamsplitter that creates the two branches there are two apertures that are used to ensure that, if there is a misalignment, the path of the laser can be recovered, reducing down time in recovering the beam alignment of both branches.

The left branch is the main experimental branch that is used for both standard pump-probe experiments and ponderomotive experiments. The right branch is only used for grating-enhanced ponderomotive experiments, and at all other times will be killed shortly after the 50:50 beamsplitter using a beam stop.

As mentioned in the previous section, a 30 cm translation stage is used in the electron beam production laser path to control the arrival time of the electron pulse, and hence control the delay between the pump and probe beams in the TRED experiments. Therefore, for the simplest of pump-probe experiments the left branch need only be directed into the apparatus, through a suitable port, as seen in Figure 3.26.
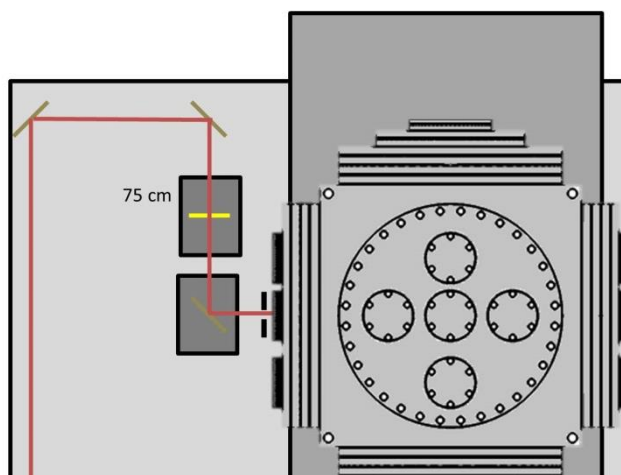
Figure 3.26: Diagram showing the left branch of the pump laser beam path, directed into the main diffraction chamber of the apparatus, *via* mirrors, through a 75 cm lens on a translation stage, with the final mirror also on a translation stage.

Here the laser is directed towards the diffraction chamber, *via* a set of mirrors, with the final mirror before the chamber mounted on a small translation stage. If one uses the two mirrors before this final mirror to ensure that the laser is traveling in a straight path, the final mirror / translation stage combination allows for easier fine adjustments to be made when directing the beam to a point of interest in the chamber. With this translation stage, one can scan the beam across the point of interest without the need to modify the angle at which the laser hits said point. As one will also note from Figure 3.26, there is a 75 cm plano-convex lens before the final mirror, on its own translation stage and flip mount, used to focus the beam onto the point of interest in the apparatus as and when needed.

This set-up is suitable for most simple pump-probe experiments, where mirrors and lenses can be swapped out where necessary depending on the wavelength of light being used. If one wanted, a second THG setup could be inserted into the space just before the third mirror from the chamber, to be able to use the second and third harmonics of the 800 nm beam in pump-probe experiments. This would be more favourable than taking a beam from where the current THG setup is, as this would involve a large propagation distance for the 267 nm light, which attenuates in air,[120] and a need to change the position of the main delay stage, and the general set-up of the electron beam production laser.

Figure 3.27 shows the additions made to the left branch to allow single-laser ponderomotive experiments to be performed (Section 2.2.3). One can see that a $\lambda/2$ waveplate and polariser have been inserted into the beam path in front of the third last mirror before the chamber in order to rotate (and ensure the correct rotation of) the polarisation of the laser from horizontal to vertical. This is necessary for single-laser ponderomotive experiments as they require the polarisation of the laser to be parallel to the plane of the electron detector to observe any perturbation of the electron beam that may occur.
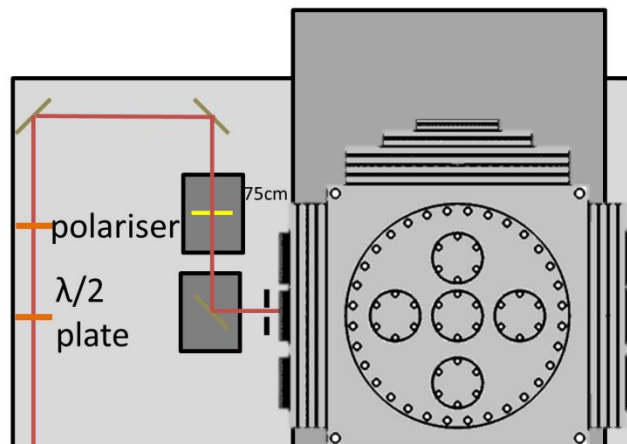
Figure 3.27: Addition of a 800 nm $\lambda/2$ plate and polariser into the left branch to allow for single-laser ponderomotive experiments.

For grating-enhanced ponderomotive experiments, polarisers are not necessary as the perturbation of the electron beam occurs along the axis of the two counter-propagating electron beams. As seen in Figure 3.28, the beams from the 50:50 beamsplitter form the left and right branches. Whilst the left branch effectively remains as shown in Figure 3.26, getting the right branch to the correct port introduces a few extra challenges. Due to the position of the Faraday cage on the optics table, the right branch is first guided underneath the cage, and then back up to the height of the viewports on the apparatus using a pair of periscope mirror mounts. The beam is then directed towards a second 30 cm long translation stage, to allow for control of the arrival time of the right branch, with respect to both the electron pulse and the left branch, at the point of interest in the diffraction chamber. Again, apertures are used to ensure that beam is travelling along the same path as the stage moves. Once the laser leaves the stage, the right branch is directed towards, and

enters, the apparatus in a similar fashion to the left branch, albeit from the opposite side.
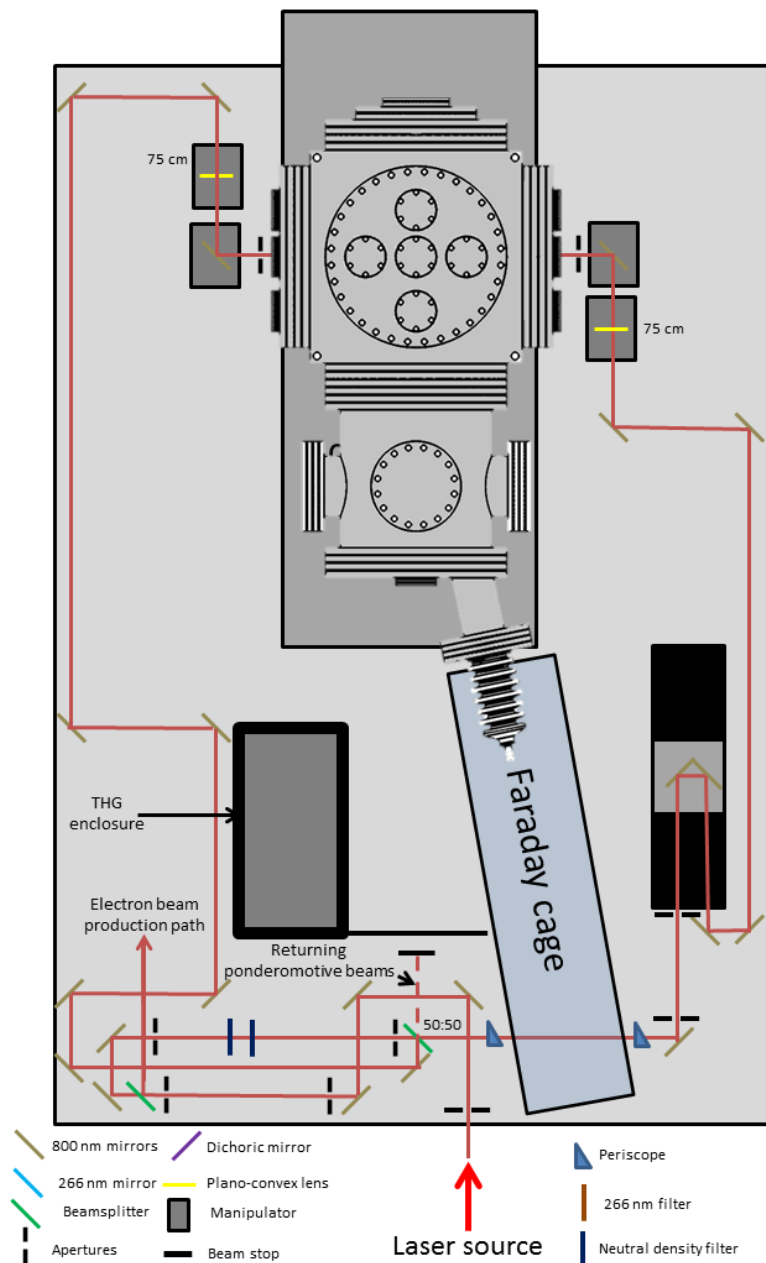
Figure 3.28: Diagram showing the laser set-up for grating-enhanced ponderomotive experiments, with the electron beam production path removed for clarity.

By careful adjustment of the final mirrors, and the translation stages on which the mirrors are mounted, one can ensure that the two counter-propagating beams for the grating-enhanced ponderomotive experiment are travelling along the same beam path, in opposite directions. If set up correctly, both beams will now travel in the

reverse direction, back towards the 50:50 beamsplitter. Here one must be cautious that the returning laser beams do not travel all the way back to the laser source, nor do they propagate for a long distance in a fourth direction from the beamsplitter, as shown in Figure 3.28. Once an acceptable beam path has been established, a set of apertures are placed on either side of the apparatus to mark the path.

As depicted in Figure 3.24, the power of the laser used in all of the experiments described above can be controlled using neutral density (ND) filters that are positioned between the two beamsplitters. These filters sit upon flip mounts that allow for the power of the laser to be adjusted on-the-fly if need be. They can easily be swapped out for different grades of power attenuation between experiments.

Chapter 4. Electron beam simulations

4.1. Introduction to electron beam simulations

As with most modern-day research, it is highly desirable to have a strong theoretical understanding of what may occur during an experiment before one begins. This idea is even more important when designing a new piece of apparatus. In the case of designing a TRED apparatus, it is imperative to have an understanding of how an electron beam will behave inside it. This could include performing a simple check to see if the electrons are able to make it to the sample to diffract, obtaining a better understanding of how the beam profile evolves throughout its propagation through the apparatus, or predicting the overall spatial and temporal resolution of the experiment as a whole.

In this project, simulations of the Wann group apparatus were carried out using the commercially available particle tracer packages, SIMION[82] and general particle tracer (GPT),[84,85] detailed further in Section 2.2.5. With its ability to relatively quickly produce 3D images and estimations of electric field gradients, SIMION was used in the early design stages of the project to get a rough idea of how the electrons would behave for different electron gun designs. However, whilst useful in these early design stages, SIMION was slow to produce more statistically relevant data when investigating the properties of the electron beam. Simulations therefore switched to GPT for these more detailed investigations.

The first part of this chapter is dedicated to the simulations carried out using SIMION, leading to some of the design choices made for the apparatus described in Chapter 3. The second part, and main body of work discussed here, will look at the simulations carried out using GPT, investigating the properties of the pulsed electron beam produced in the apparatus under different initial conditions, as it propagates from the electron gun to the detector. Discussion will focus on how the simulations predict that the beam will react to variations in the acceleration potential of the electron gun, the distance between the photocathode and the anode, and the size of the aperture in the anode itself. Furthermore, the simulations will look at how the magnetic lens affects the beam as it focusses the electrons onto the detector. By the end, these simulations will provide a better understanding of how the electrons

behave in the apparatus, and the trends they follow under different experimental conditions.

4.2. Initial simulations and apparatus design

After obtaining a rough design for the apparatus, one of the early investigations involved looking at the shape of the electric field between the photocathode and anode of the electron gun, in order to simulate how the electrons would travel between the two, whilst also highlighting any major problems with the set-up before committing to any designs. Figure 4.1 shows an early model of the apparatus, created in SIMION, focussing on the electrode, photocathode, and anode plate of the electron gun, as well as a short field-free flight region in the diffraction chamber. The distance between the photocathode and the anode is 10 mm and, as the reader will note, this model includes a slightly different design for the anode plate, compared to that seen in Section 3.2.2, where an exchangeable anode, for various aperture sizes, has been included. This exchangeable anode was later replaced in favour of the anode plug but, as one will see shortly, this change does not affect the results presented.
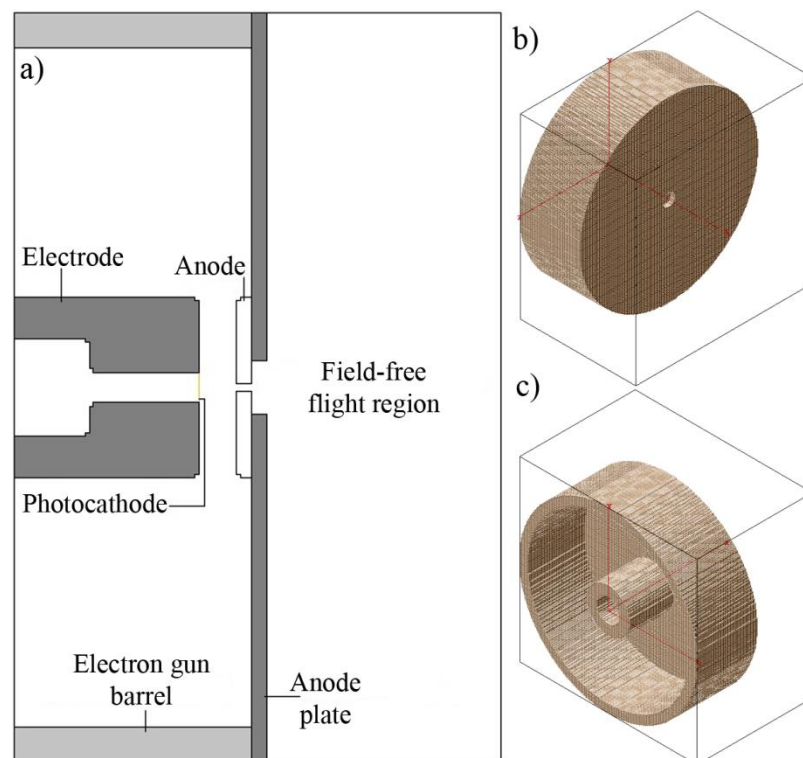
Figure 4.1: Diagram showing an early design of the TRED electron gun, recreated in SIMION, to investigate its properties, as seen from a) the side, b) the front, and c) the back.

Due to the circularly symmetric design of the electron gun, a cylindrical model was used to describe the apparatus, with the axis of rotation passing through the centre of the photocathode and the aperture in the anode. This initial model was described by unit cells of $1 \times 1 \times 1$ mm. This resolution is sufficient to give a basic, yet accurate, idea of how the electric field would behave in the gun, and whilst higher resolutions could be achieved by decreasing the size of these cells, it would be at the cost of increased computational time.

With a complete model, a potential of -100 kV was applied across the photocathode and electrode, whilst the anode and barrel of the electron gun remained at ground. From this, a contour map of the electric field was obtained, as depicted in Figure 4.2a, showing a region of high electrostatic potential at the electrode, with parallel field lines rapidly falling to ground as one moves towards the aperture in the anode and the barrel of the electron gun. In addition, warping of the field lines can be seen at the corners of the electrode and the protruding anode. One can also see that there is little-to-no potential in the field-free flight region.
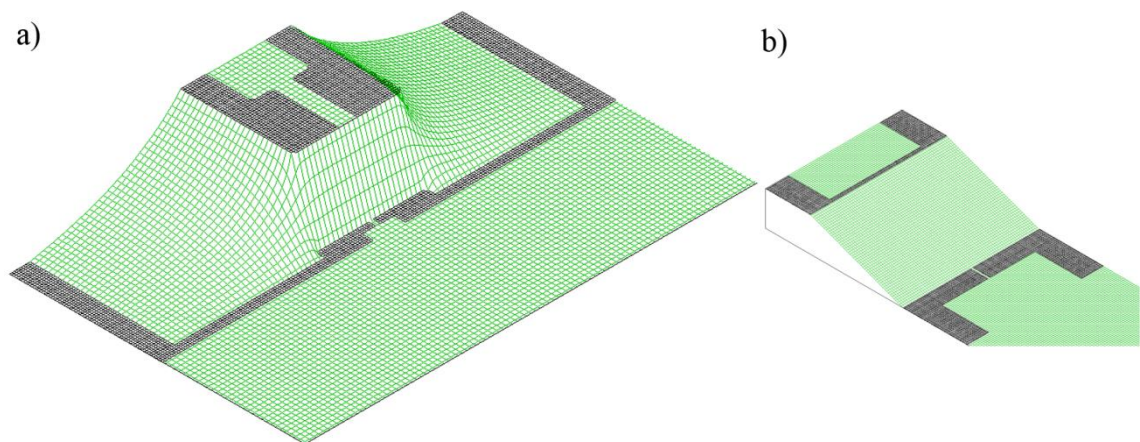
Figure 4.2: Diagram showing SIMION simulated contour maps of the electric field in the TRED apparatus, depicting the electric field over a) the whole gun, and b) the area between the anode and photocathode.

Two important inferences can be made from this map. The first is that any electron in the field-free flight region will indeed feel no electrostatic forces from the electron gun, and hence be able to fly unperturbed (bar any external forces) towards the sample and detector. The second important feature is that whilst a warping of the electric field is observed at the corners of the electrode and the protruding anode,

there is an even drop in the potential between the centre of the electrode / photocathode and the aperture in the anode, as shown by parallel, evenly spaced and steep contour lines. This suggests that the electrons have little chance of being accelerated from the photocathode in any direction other than towards the aperture in the anode. This, therefore, allows a large amount of the apparatus to be ignored in the simulation, without affecting the ability to map the overall flight of the electrons, freeing up space to increase the resolution of the simulation.

Figure 4.2b shows a higher resolution simulation, using unit cells of 0.025 × 0.025 × 0.025 mm, with the steep electric field between the photocathode and anode present once again. The higher resolution also allows the aperture in the anode to be reduced to 150 μm in diameter, the same size as the smallest aperture that was expected to be used in the apparatus. While the electric field contour lines are parallel most of the way from the photocathode, a small amount of warping in the field lines can be seen at the anode aperture, with a small "leak" of the electric field protruding into the field-free flight region. However, this tends to zero after a few hundred micrometres, meaning that we can still assume the diffraction chamber to be a field-free region.

From this basic set-up, it is possible to see how an electron beam would behave within the apparatus. Initial simulations made use of an electron pulse containing 10^3 electrons, created over a Gaussian time-frame of 120 fs, and an initial FWHM transverse beam size of 0.2 mm, mimicking the typical temporal and spatial properties of a laser pulse used to create the electron pulse.[21] To simulate electrons that have been emitted from a gold photocathode by an ultra-violet laser pulse, the electrons were set to have an initial energy spread described by a Gaussian centred at 0.7 eV with a width of 0.6 eV.[89] It should be noted that this ionisation is equivalent to a 250 nm laser pulse hitting the photocathode, which is a shorter wavelength than the 267 nm light used in the practical experiments discussed in Chapters 3 and 5. While this means that the electrons in these simulations have slightly more kinetic energy than those in the real experiment, this energy spread was used because the data existed at 250 nm (whereas no data exist for longer wavelengths), and would allow us to compare our results to literature theoretical investigations.[29] Space-charge effects between electrons were also taken into account by including

Coulombic forces. These general electron pulse conditions would be used again for GPT calculations, although with a different numbers of electrons in each pulse.

The final part of the electron gun design simulations focussed on the effect of the photocathode-to-anode distance on the overall shape of the electron beam. In practice there is a limit to how close the electrode can be placed to the anode as an electric field will start to break down in a direct current set-up once it exceeds 200 kV cm^{-1}.[115] This break down will cause arcing between the electrode and anode that, if a discharge is large enough, could damage the apparatus, including the delicate photocathode, affecting the quality of the electron beam produced. This should obviously be avoided, and therefore the photocathode-to-anode distance is limited to a minimum of 5 mm, when operating at 100 kV.

The following simulations investigated the general behaviour of the electron beam assuming photocathode-to-anode distances of 5 and 10 mm. The same general electron gun set-up and resolution shown in Figure 4.2b was used, but with the simulation extending 40 mm into the field-free flight region, where we might expect to place a sample. Figure 4.3 shows the path taken and general spread of the electrons as they propagate through these set-ups.
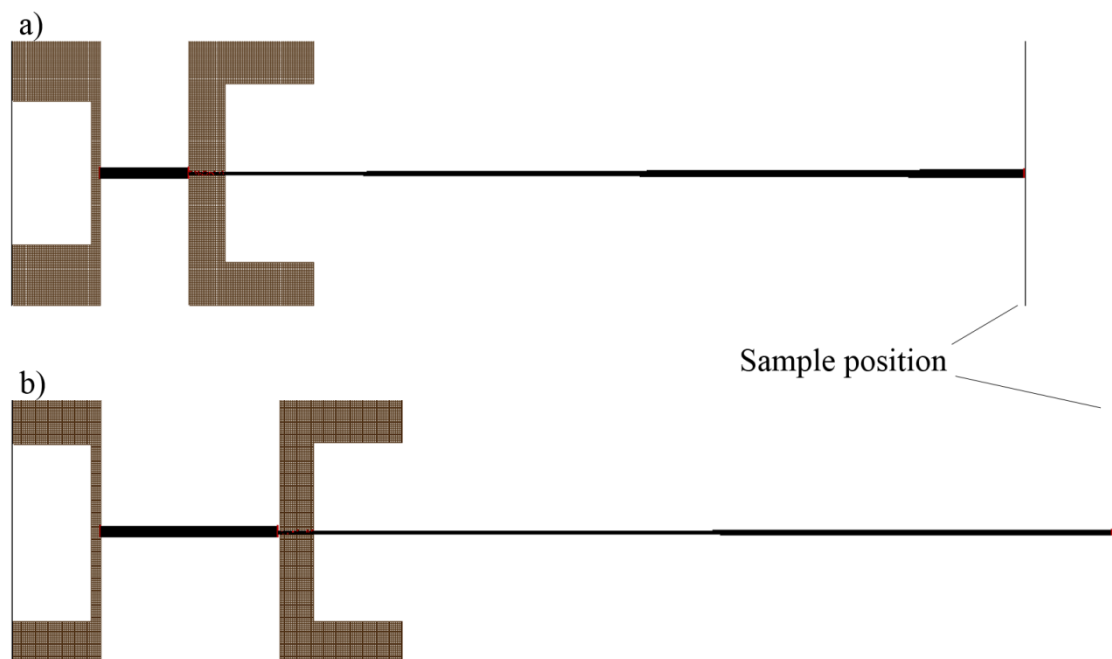
Figure 4.3: Diagram showing SIMION simulations of a 10^3-electron, 120 fs pulse propagating in the region between the photocathode and a sample (approximately 40 mm away from the anode), for an electron gun in which the electrode sits (a) 5 mm, and (b) 10 mm from the anode.

The results of these simulations showed that the number of electrons passing through the 150 μm aperture, at 100 kV, was not greatly affected by the photocathode-to-anode distance with a 21.5 and 22.8% transmittance, for the 5 mm and the 10 mm set-ups, respectively. Both results compare favourably to yields that have been obtained by other groups with similar set-ups.[27] The small difference possibly arises from a focussing effect in the electric field, caused by warping at the anode aperture, resulting in the electrons being more efficiently collimated in the 10 mm set-up than in the 5 mm set-up.

With any rapidly diverging electrons being killed at the anode, the transverse electron beam profile, after passing through the anode aperture, could be described as a "top hat",[29] and hence an estimate of the beam size could be made by measuring the distance between the furthest out electron and the centre of the beam. As shown in Figure 4.3, the 5 mm electron gun set-up has a wider transverse size with a 0.22 mm radius, than in the 10 mm electron gun, which widens to only a 0.14 mm radius over the same field-free distance. As there is little difference in the number of electrons predicted to pass through the aperture for each set-up, the results suggest that a larger photocathode-to-anode distance could be used in an electron gun to obtain a narrow electron beam, and hence a higher spatial resolution. However, this gain in spatial resolution comes at a cost in time resolution, due to the extra distance that the electron pulse has to travel. The exact effects and trends will become more apparent as we carry out more thorough investigations of the pulse dynamics.

4.3. Pulsed electron beam dynamics

The remainder of the simulations that are discussed here made use of GPT, performed to better understand the dynamics of a pulsed electron beam, in terms of its duration and transverse beam size, as it propagates from the electron gun, past the sample, and on to the detector.

In these calculations we will initially investigate the effect that different electron gun settings have on the quality of the electron beam. This involves looking at simulations where the acceleration potential, photocathode-to-anode distance, and anode aperture size are all varied. Once an understanding had been reached on how the electron beam behaves for each variable, we will look at how a magnetic lens affects these properties, in terms of the position and current passing through the lens.

Data were recorded at set positions during the flight of the pulse through the apparatus, including the positions 10, 20, 30, 40, 50, 90, 130, 210, 220, 290, 400, and 500 mm from the anode, marking possible sample positions, the detector and other points of interest in the apparatus. In general, the 130 mm distance is considered to be the "sample position", as this is the distance from the anode to the central 2.75" flange on the top and side flanges of the diffraction chamber (Figure 3.11). Also, when referring to the "detector position", it will be assumed that the detector is 500 mm from the anode. This anode-to-detector distance is in fact 170 mm longer than the 330 mm distance seen in the final experimental set-up described in Chapters 3 and 5. This is because the apparatus was still undergoing its testing phase when these simulations were started, and an extra vacuum chamber was initially planned for after the main diffraction chamber, thus extending the anode-to-detector distance. As a large body of simulations had already been carried out by the time this chamber was removed, the decision was made to continue to use this longer distance as the standard, as the dynamics would still be the same up to the new detector position, and one could always truncate the data as needed.

The magnetic lens modelled here was based on the designs of the magnetic lens described in Section 3.2.8. The lens is modelled as a single solenoid, 20 mm long, and 10 mm in diameter. A current of $1000I$ passes through the solenoid, representing a thousand turns of wire with a current, I (in Amps), being used to focus the electron beam.

In all of the simulations that follow, we look at pulses that contain 10^4 electrons, a number deemed by other groups to give a balance between good temporal resolution, and a sufficient number of electrons to observe enough scattering events to collect data in a timely manner.[29,72] All other initial conditions, (*i.e.* energetic spread, beam size, and pulse duration) were kept as detailed in Section 4.2. To help with computational time, the 10^4 electron pulse was represented by 10^3 macro particles, where each particle represented 10 electrons. Columbic repulsions between the particles were also included to account for the space-charge effect in the pulses.

As an electron pulse has similar properties to the laser that produces it,[21] the envelope that describes the duration of the pulse will be of a Gaussian nature, and so values relating to this will be presented as its full-width half-maximum (FWHM). Whilst the transverse width of the pulse also has an initial Gaussian shape to it, this

can soon change as the beam passes through the aperture in the anode of the electron gun. As electrons on the outside edge of the pulse are lost, the pulse seen in the diffraction chamber can be described as flat disc. Therefore, the transverse size of the electron beam will generally be described by the root-mean-square (rms) radial position of all of its electrons with respect to the centre of the pulse.

A diffraction pattern is generally deemed to be of high spatial resolution, where data points from the scattering pattern can be read at intervals of less than $\Delta s = 2$ nm^{-1}. However, as can be seen in the equation for calculating s (Equation 2.3), this resolution is dependent on a number of factors, including the sample-to-detector distance, and electron wavelength. Figure 4.4 shows how the predicted spatial resolution of the simulated apparatus, with its 370 mm sample-to-detector distance, varies with both the radius of the electron beam, and the acceleration potential of the electron gun. As expected, a smaller electron beam will produce a better resolved diffraction pattern. However, whilst a higher acceleration potential may provide a better time resolution, it is at the cost of the experimental spatial resolution. For the range of acceleration voltages that are expected to be used with this apparatus (*i.e.* 40 – 100 kV), a beam radius of 0.25 mm, or less, is needed to achieve the desired spatial resolution. The radius of the beam must be half this size (*i.e.* $r = 0.125$ mm) to obtain well resolved data when the detector is at the closer 330 mm anode-to-detector (/ 200 mm sample-to-detector) distance. All of these factors will need to be taken into account when trying to determine the optimal set-up for the experiment.
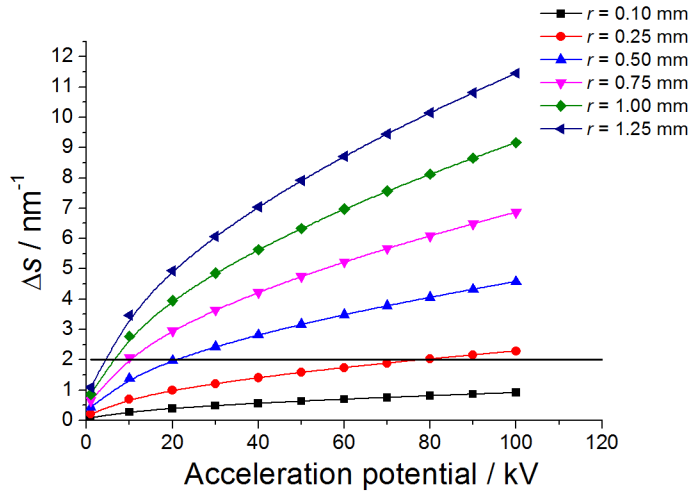
Figure 4.4: Graph showing how the spatial resolution of a diffraction experiment, with a 370 mm sample-to-detector distance, varies with the acceleration potential of the gun, and the radius of the electron beam at the detector. A line at $\Delta s = 2$ nm^{-1} marks the upper limit for "well-resolved" diffraction data.

The most important feature for TRED is the expected time resolution for the overall apparatus. This obviously depends on the durations of the electron pulse and excitation laser, but (as seen for the velocity mismatch equations, in Section 2.2.2) also on the transverse size of the electron beam at the sample. This will, therefore, also have to be investigated, in order to better predict the capabilities of the apparatus.

4.3.1. Pulse properties without a magnetic lens

The properties of the pulsed electron beam were studied under a series of different initial electron gun conditions, at first without the active presence of the magnetic lens. The results from these simulations would act as a control for the results presented later in Section 4.3.2 when the lens is active, and also to determine the "natural" characteristics of the pulsed beam. Here, various acceleration potentials (45, 65 and 100 kV), photocathode-to-anode distances (10 and 15 mm), and anode aperture diameters (150 and 400 μm) were investigated to see how they would affect the beam. The previously discussed 5 mm photocathode-to-anode distance (Section 4.2) was not studied, as the electric field here was more likely to break down at higher potentials than longer photocathode-to-anode set-ups. The effect of a 1 mm diameter aperture in the anode of the electron gun (like that used in the experiments presented in Chapter 5) was also not explicitly investigated because, as one will see

shortly, a significant number of electrons were predicted to already pass through the 400 μm aperture, and the two sets of results would be extremely similar.

4.3.1.1. Aperture transmission of the pulsed electron beam

The first investigation concerned how many electrons passed through a specific aperture under different electron gun conditions, the results of which are summarised in Table 4.1. As expected, more electrons pass through the larger aperture than the smaller one, with just over 86% and 23% of the electrons passing through each aperture, respectively. The simulations also predict that the number of electrons that pass through a given aperture is not greatly dependent on the acceleration potential of the electron gun, although slightly more electrons pass through an aperture at a higher potential, than at a lower potential.

Table 4.1: The percentage of electrons passing through a given aperture compared to the number produced from the photocathode for various electron gun conditions.

Photocathode-to-anode distance / mm	Aperture size / μm	Acceleration potential / kV	% of electron beam passing through aperture
10	150	45	23.8
		65	23.9
		100	24.1
	400	45	86.0
		65	86.2
		100	86.4
15	150	45	23.3
		65	23.8
		100	23.9
	400	45	86.0
		65	86.4
		100	86.8

It also appears that the photocathode-to-anode distance has little effect on the number of electrons that pass through to the diffraction chamber, with only slightly more electrons passing through at longer photocathode-to-anode distances. This trend was also observed in the SIMION calculations for the 5 and 10 mm photocathode-to-cathode distances presented in Section 4.2.

With more electrons passing through the larger aperture there is the potential for data to be collected in a shorter time frame, as more scattering events are likely to

occur from the sample. However, whether this larger aperture beam is useful for TRED experiments depends on a few other factors.

4.3.1.2. Temporal and spatial properties of the pulsed electron beam

Figure 4.5 contains a series of graphs that show how the pulse duration and transverse radius of the electron beam vary as a pulse propagates through the apparatus.
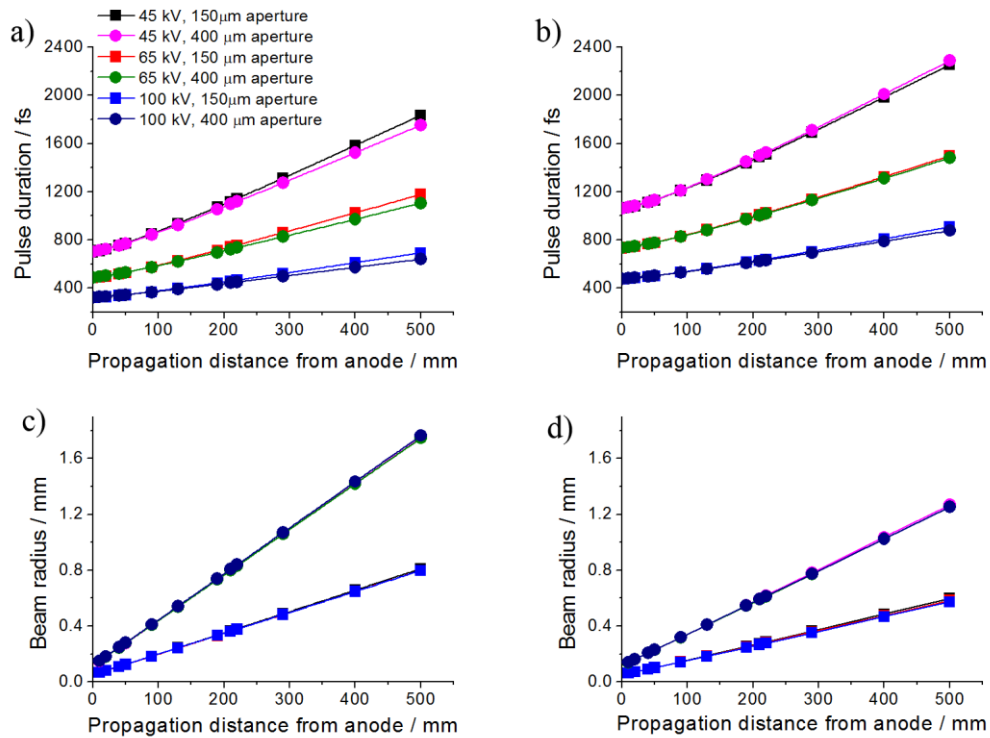
Figure 4.5: Graphs showing how the duration (top) and transverse radius (bottom) of the pulsed electron beam, from a 10 mm (a and c) and 15 mm (b and d) photocathode-to-anode distance electron gun, vary as a pulse propagates through the apparatus with various sizes of anode aperture and acceleration potentials.

As expected, the duration of the electron pulse for all conditions studied increases as the pulse propagates through the apparatus, in a similar fashion to that predicted by Siwick *et al.*[29] The amount that a pulse expands also depends on the accelerating potential used, with lower acceleration potentials producing relatively longer pulses after propagating for the same distance. This is purely because electrons accelerated across a lower potential take longer to reach the same point in the apparatus. Larger photocathode-to-anode distances also produce longer pulse durations, as expected

because the electrons have to travel an extra 5 mm before entering the diffraction chamber.

It is interesting to note, however, that the pulse duration is apparently not dependent on the size of the aperture used. This is most likely due to the fact that, whilst the outside of the pulse is removed by the aperture, the core of the pulse still remains. It does not, therefore, feel the loss of the other electrons due to a "shielding" effect provided by the new outermost electrons and, hence, continues to expand in a similar fashion as to before.

In terms of the transverse radius of the electron pulse, it is immediately notable that the beam size appears to be independent of the acceleration potential. This is most likely due to the electrons having a relatively insignificant amount of transverse kinetic energy after ionisation from the photocathode, compared to the kinetic energy imparted on the pulse by the acceleration potential of the electron gun. However, the transverse radius is highly dependent on the size of the aperture used in the anode of the electron gun. One can also see that the a narrower electron beam is observed for the longer photocathode-to-anode distance, a feature first noted in the results from the SIMION calculations in Section 4.2. Whilst a longer pulse duration will be observed for an apparatus with a longer photocathode-to-anode distance, one can imagine a situation where an apparatus could be designed for higher spatial resolution (at the cost of temporal resolution) that uses this feature.

By comparing the beam radii in Figure 4.5 with the estimated spatial resolution information in Figure 4.4, it is apparently not possible to achieve the desired high spatial resolution for the diffraction experiments with any of the initial conditions investigated, when the detector is 500 mm from the anode. Even with the detector moved forward to the 330 mm position that was used in the experiments described in Chapter 5, the set-up that produces the smallest natural beam radius at the detector (*i.e.* 150 μm, 15 mm photocathode-to-anode distance, $r \sim 0.40$ mm) is at least three times larger than that required to collect highly spatially resolved data. This suggests the need for a magnetic lens to focus the beam on the detector in order to overcome this challenge with the experiment. However, the effect of this lens on the experiment as a whole, including the expected time resolution, must be thoroughly investigated.

4.3.2. Pulse properties with a magnetic lens

The effect of the magnetic lens on the pulsed electron beam was investigated by varying both the current passing through the lens and its position relative to the anode and the sample. The current passing through the lens was varied between 0 and 2 A (the maximum current that could comfortably be passed through the lens described in Section 3.2.8 without damaging it), in steps of 0.2 A, whilst the centre of the magnetic lens was placed at various 10 mm intervals between the anode of electron gun and the sample position (*i.e.* from 10 mm through 120 mm from the anode).

As all combinations of the magnetic lens position and current were investigated for each of the different initial electron gun conditions (*i.e.* accelerating potential, anode aperture size, and photocathode-to-anode distance) observed in Section 4.3.1, this resulted in over 1,500 individual simulations being run; the results of which can be found in full in Appendix B. However, as most calculations showed similar general trends, we will focus here on some specific examples that best highlight the results and trends observed.

4.3.2.1. Beam radius

As the main goal of the magnetic lens is to improve the spatial resolution of an experiment by narrowing the transverse size of the electron beam at the detector, we will focus on the calculations that achieve this to a reasonable degree, and forego detailed discussions of the calculations that either A) had little effect on the radius at all, or B) caused the resolution to be worse than that observed for the natural beam in Section 4.3.1.2. As an example, Figure 4.6 contains an extract of data from the 45 kV, 400 μm anode aperture, 15 mm photocathode-to-anode electron gun, showing how the beam radius, at both the sample and the detector positions, varies with the current passing through the magnetic lens, when the lens itself is fixed at different positions between the anode and the sample.
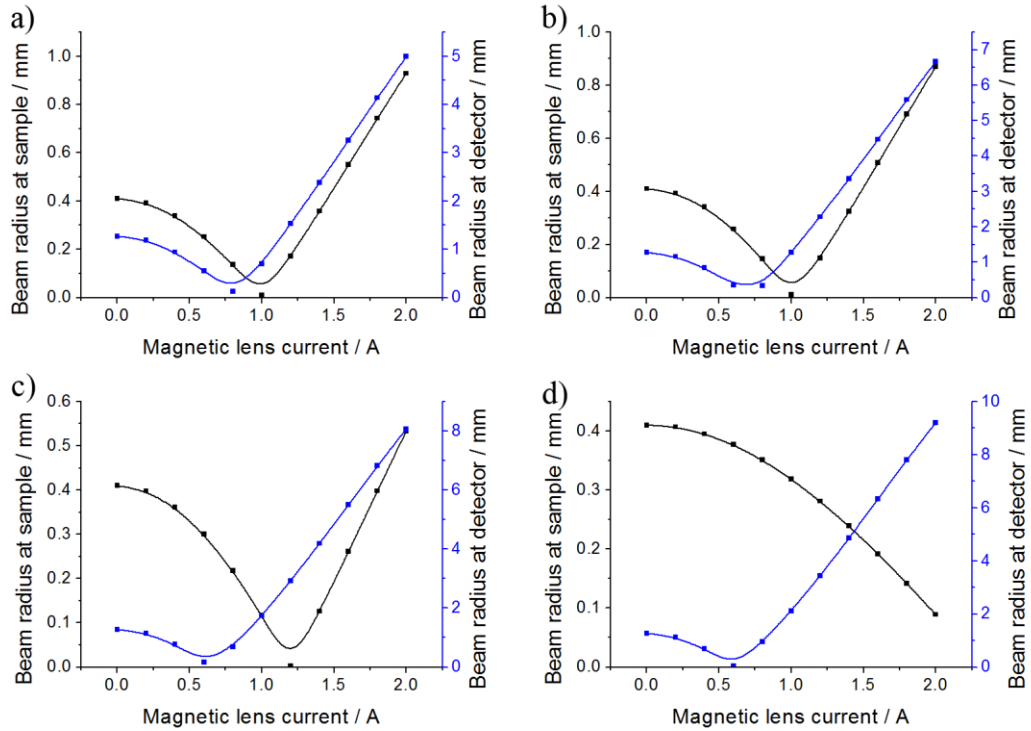
Figure 4.6: Graphs showing how the radius of the electron beam from a 45 kV, 15 mm photocathode-to-anode distance, 400 μm anode aperture electron gun varies with the current passing through the lens at the sample (black) and detector (blue) positions when the lens is a) 30, b) 60, c) 90 and d) 120 mm from the anode.

As one can see from Figure 4.6, situation A) was generally observed where the magnetic lens had little current passing through it (*i.e.* $I < 0.4$ A), and was not strong enough to perturb the electrons sufficiently. Situation B) was generally true where the magnetic lens current was large (*i.e.* $I > 1.4$ A), and caused an over-focussing of the electron beam, where it would reach its narrowest size long before arriving at the detector. In some of these cases the size of the electron beam at the sample was small enough that it could potentially increase the temporal resolution of the experiment once velocity mismatch (Section 2.2.2) is taken into account. However, with the rapid increase in size of the beam after this point, to diameters in some cases exceeding 10 mm, this gain in time resolution would be at the cost of the spatial resolution of the experiment. A solution to this could be to introduce a second magnetic lens, to reduce the effect of this over-focussing problem after the sample position. However, it is possible that this over-focussing or the second lens could have a negative effect on the scattered electrons, distorting the diffraction pattern, as they would not fly in a field-free region. To investigate this thoroughly, one would

need to carry out full simulations using a pair of lenses, greatly complicating matters; time did not permit this to be investigated here.

It is also interesting to note from Figure 4.6 that when the magnetic lens is closer to the anode the optimal beam radius at both the sample and the detector is observed at roughly the same current. However, when one moves the lens closer to the sample the optimal beam radius for the two positions occurs at quite different currents. One might assume from this finding that it is best to place the magnetic lens closer to the anode, and fine tune the lens current to obtain the smallest spot at both positions at the same time. However, one must remember that each minimum seen in each graph is a relative minimum, and that the true optimal set-up may be at another magnetic lens position and current. To understand this better it is important to see how the transverse radius of the pulse evolves as a whole as it passes though the apparatus under various magnetic lens conditions. Figure 4.7 presents a graph that shows how the beam radius of a 45 kV, 15 mm photocathode-to-anode distance electron gun varies as it propagates through the apparatus for various conditions (A – F) involving different anode aperture sizes, and magnetic lens positions and currents.
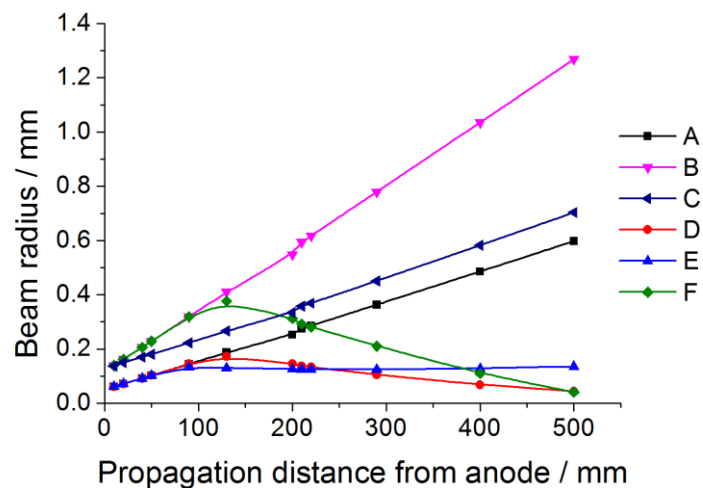
Figure 4.7: The predicted beam radius at different propagation distances for a 45 kV, 15 mm photocathode-to-anode distance electron gun, with various magnetic lens and aperture conditions, including A) 150 μm aperture, no magnetic lens, B) 400 μm aperture, no magnetic lens, C) 400 μm aperture, with the magnetic lens at 120 mm (from the anode) and 0.6 A (passing through it), D) 150 μm aperture, with the magnetic lens at 120 mm, 0.6 A, E) 400 μm aperture, with lens at 10 mm, 0.6 A, and F) 150 μm aperture, with lens at 80 mm, 0.6 A.

In situations A and B, shown in Figure 4.7, we once again see that, without the magnetic lens present, the aperture size has a significant effect on the size of the electron beam. The radius of the beam at the detector for the 400 μm aperture set-up is twice as large (at 1.27 mm in radius) than the 150 μm aperture set-up (at 0.60 mm in radius). Looking back at Figure 4.4, we can see that both beams are too large for the diffraction pattern to be considered to have good spatial resolution, and hence a magnetic lens is needed.

By introducing a magnetic lens 120 mm from the anode, and with a current of 0.6 A passing through it, the beam from the 400 μm aperture (situation C) can be focussed to obtain an optimal beam size of 0.041 mm at the detector. This magnetic lens position and current also produced the optimal beam size at the detector for the 150 μm aperture set-up (as exemplified in situation D), producing a similar beam radius of 0.044 mm. It should be noted that this feature of both aperture sizes having similar optimal beam sizes for the same focussing conditions was not noted to be a general trend, as the predicted beam radius would vary slightly, case-by-case.

Whilst having similar beam sizes at the detector, one can see from Figure 4.7, that the two beams represented by cases C and D have different radii at the sample, with the 150 μm aperture, in D, achieving the smaller radius of 0.17 mm, compared to the 0.38 mm beam radius observed with the 400 μm aperture gun, in C. Whilst both beams will achieve similar spatial resolutions, the smaller radius at the sample for D would produce an overall better time resolution compared to C once velocity mismatch was taken into account. However, one must remember that, with the 150 μm aperture, there are almost four times fewer electrons per pulse than with the 400 μm aperture. This means that it will take longer to observe the same number of diffraction events in order to collect the same quality of diffraction patterns. As well, if there was a serious jitter problem within the experimental set-up, the data collected over the extended period of time with the smaller aperture, could in fact, end up having an overall worse time resolution than for the larger aperture. However, this problem will be heavily dependent on the experimental set-up, and so each experiment will need to be analysed on a case-by-case basis.

As shown by situations C and D, the optimal beam radius at the detector is observed when the magnetic lens is further away from the anode, and closer to the sample position. This was generally the case for most experimental set-ups where the

electron beam was not over-focussed, and can be explained by two related points. With the lens closer to sample, and hence the detector, the electron beam has less time to "react" to the compression exerted by the lens, which would potentially allow it to expand again. It also has to do with the fact that, when the lens is further from the source of electrons, the pulse has had more time to expand both temporally and spatially, causing the electron density to be much lower at the time of compression; with a lower density the pulse is easier to focus. To highlight this further, situation E positions the magnetic lens at a distance of 10 mm from the anode, but retains a lens current of 0.6 A and the 400 μm aperture in the anode. Whilst the radius of the electron beam at the detector is smaller here than that observed with the similar electron gun set-up of situation B (which used no magnetic lens), it is still larger than the beam produced using the 150 μm aperture seen in situation A (which also used no lens). For one to obtain a reasonable beam radius with the lens this close to the anode, a larger current would have to be passed through the lens. However, this can lead to an increased stretching of the pulse in the temporal dimension (as will be discussed in Section 4.3.2.2), and it still may not achieve as small a radius. As an added problem, more current passing through the lens increases the likelihood of the lens overheating and becoming damaged.

Situation F, presents an interesting result that was achievable for all of the possible electron gun set-ups, in which a relatively well-collimated electron beam was observed between the sample and the detector. Here, the magnetic lens focusses a beam (produced from the 150 μm anode) when placed 80 mm from the anode, and has 0.6 A passing through it (*i.e.* same conditions as D, but with the lens closer to the anode by 40 mm). Here we observe a beam radius of 0.130 mm at the sample, which expands only slightly to 0.136 mm by the time it reaches the detector. Whilst the beam may be three times larger at the detector than that observed with the lens closer to the sample (as in D), it is almost a third smaller at the sample position. Whilst a smaller beam size is always desirable at the detector, it is still small enough to be considered well resolved when considering the data in Figure 4.4. This set-up could represent a configuration which yields both well resolved temporal and spatial information. As mentioned, this was achievable for all the electron gun initial conditions tested, but the exact position of the lens, and current needed, varied from case to case. It was this result that suggested the necessity to be able to adjust the

position of the magnetic lens on-the-fly using an *xyz* translator, rather than fix it in place, as is the case in the experimental set-ups of other groups.[121]

4.3.2.2. Pulse duration

As the pulse duration at the sample position is one of the principal factors in determining the resolution of a TRED experiment, it is important to understand how this varies under different magnetic lens conditions. As the pulse is compressed the Coulombic repulsion between electrons causes it to stretch in the temporal dimension. How much this compression affects the pulse duration is dependent on the current passing through, and the position of, the magnetic lens. Figure 4.8 shows how the electron pulse duration varies at the sample position when 150 and 400 μm anode apertures are used at accelerating potentials of 45 and 100 kV with different magnetic lens conditions.
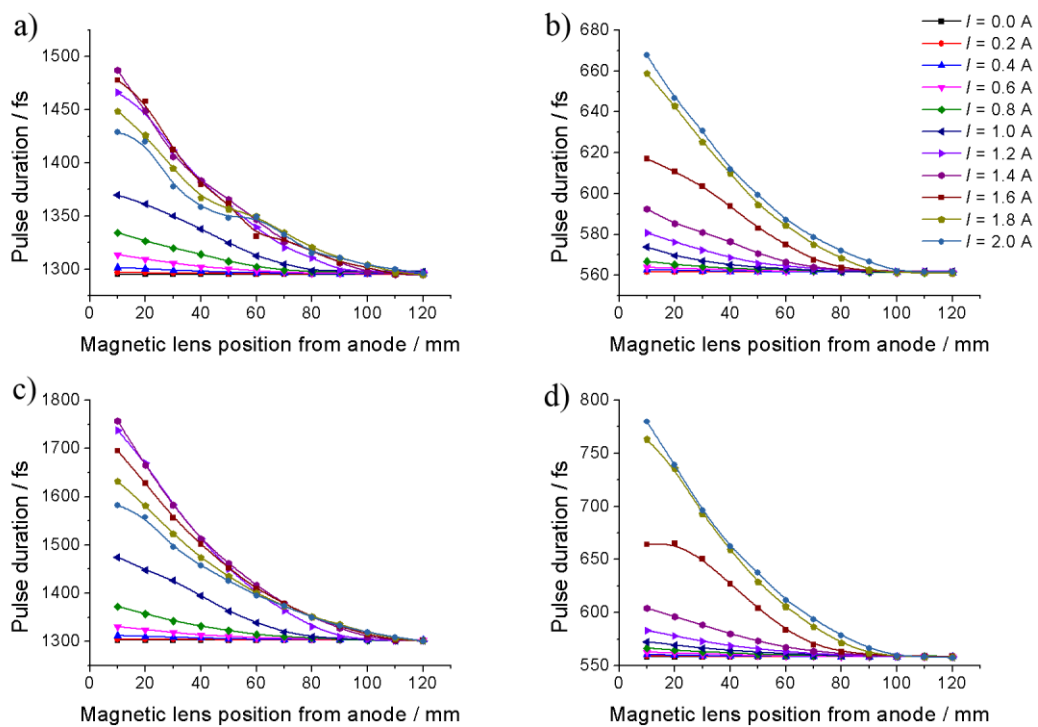
Figure 4.8: Predicted electron pulse duration at the sample position for a 15 mm photocathode-to-anode distance electron gun, with a 150 μm (a and b) or 400 μm (c and d) anode aperture, and 45 kV (a and c) or 100 kV (b and d) accelerating potential for various magnetic lens positions and currents (*I*).

From Figure 4.8, one can see immediately that the pulse duration is generally longer when the magnetic lens sits closer to the anode (and further away from the

position of the sample). Also, the pulse duration is generally longer as the current in the lens is higher. Both of these results are expected. With the lens closer to the anode, it acts on the pulse while it has a high electron density. The compression in the transverse direction increases this pulse density further and so, to alleviate this effect, the pulse must stretch in the temporal dimension. This is similar to the discussion between Siwick and Qian that was reported in Section 2.2.4. As the lens moves closer to the sample, the pulse duration tends to that observed with no magnetic lens present. This is because the pulse has already had the opportunity to expand naturally and, when acted on by the lens, there is little time for it to stretch in the temporal dimension before it reaches the sample.

As briefly mentioned, in most cases, as the current in the magnetic lens increases the duration of the pulse also increases. Again this is expected as, at higher operating currents, the lens will compress the electron pulse more in the transverse dimension, and cause it to stretch temporally. However, it is interesting to note that at the lower acceleration potential of 45 kV, an upper limit is observed in the temporal stretch with increasing current (of $I > 1.4$ A), before the observed duration starts to shorten again. This is most likely due to the large over-focussing effect discussed in relation to Figure 4.6, which occurs around the same lens current. At these currents the transverse radius of the pulse rapidly narrows to a minimum, before just as quickly expanding again, minimising the time the pulse is compressed. This period of time only shortens as the lens current increases, providing less and less time for the pulse to stretch in the temporal dimension.

Finally, by comparing the data from the simulations run with different aperture sizes in the electron gun, one can see that compression of a pulse that comes from the larger aperture expands faster in the temporal dimension than for the smaller aperture. This is interesting because in Section 4.3.1.2 we saw that without the magnetic lens present the observed pulse duration from the electron gun was relatively independent of the aperture size. However, here with the larger aperture, more electrons are contained within a pulse than with the smaller aperture. When compressed, the electron density of the pulse from the larger aperture increases more rapidly than for the smaller aperture, and hence the larger pulse will stretch more rapidly in the temporal dimension.

Whilst Figure 4.8 shows that in the worst case scenario the magnetic lens can cause the pulse duration to stretch by up to 50%, we can see that for the more likely operating conditions of the magnetic lens (*i.e.* with it positioned around 6 cm, and with 1.0 A passing through it), the overall change is almost negligible, especially for higher acceleration potentials. However, the overall time resolution of the experiment is dependent on many factors (not just the overall pulse duration) as set out in the equations for velocity mismatch (Section 2.2.2), and these must all be taken into account in order to determine the optimal set-up.

4.4. Predicted experimental resolution

Tables 4.2 − 4.4 contain a summary of the predicted electron beam radii at the sample and detector positions, as well as the electron pulse duration at the sample and the overall predicted experimental time resolution for experiments carried out at 45 kV (Table 4.2), 65 kV (Table 4.3), and 100 kV (Table 4.4). Each table goes further, detailing how each result changes depending on the photocathode-to-anode distance and anode aperture size used. The results presented also show how the different magnetic lens focussing conditions, including none (*i.e.* natural beam), smallest beam at detector, and collimated beam, affect the overall resolution of the experiment.

For all the results presented in the tables, the overall experimental time resolution has been calculated using the velocity mismatch equations detailed in Section 2.2.2, assuming the simplest experimental set-up, where the pump (whose duration is set to 120 fs) and probe beams meet perpendicularly. This set-up represents the one that will most likely be used in the earliest TRED experiments with the York apparatus. Slightly better time resolution can be achieved by changing the intersection angle of the pump and probe beams, and using tilted wavefronts, but this will be different for each set-up seen, and some will be discussed as necessary. The results in the tables, however, allow for the electron beams to be compared on their own merits.

The widths of the pump laser and the molecular beam have also been adjusted in each experiment to be of similar size to the electron beam at the sample position. This set-up will allow for the maximum amount of scattering to be observed from a pump-probe experiment. With careful planning, and sufficient control of the laser

optics and gas inlet nozzle, one should be able to establish any of these set-ups experimentally.

As noted in the tables, an "equivalent FWHM beam size" (diameter) at the sample position is presented; this has been introduced because it is required for the velocity mismatch calculations. So far this has not been discussed, in favour of the rms beam radius, because whilst the FWHM will be relatively accurate for the 400 μm aperture experiments (where over 86% of the electrons are able to pass through the anode) it will be less accurate for the smaller 150 μm aperture where a large amount of the beam has been removed towards the edges (and only 24% of the electrons pass through).

Table 4.2: Predicted time resolution and electron beam radius at the detector for experiments carried out at 45 kV, for various initial electron gun set-ups, and magnetic lens focussing conditions.

Energy / keV	Photocathode -to-anode distance / mm	Aperture size / μm	Lens position / mm	Lens current / A	Electron beam focus type [a]	Electron beam rms radius at sample / mm	Equivalent FWHM beam size / mm	Electron pulse duration / fs	Laser and sample width / mm	Time resolution / fs	Electron beam rms radius at detector / mm
			-	0	N	0.244	0.341	938	0.350	2440	0.811
45	10	150	120	0.6	O	0.224	0.308	937	0.325	2289	0.077
			90	0.6	C	0.180	0.249	937	0.250	1866	0.176
			-	0	N	0.536	0.706	923	0.700	4605	1.749
45	10	400	120	0.6	O	0.493	0.645	925	0.650	4286	0.113
			80	0.6	C	0.375	0.490	927	0.500	3348	0.407
			-	0	N	0.187	0.263	1295	0.275	2192	0.600
45	15	150	120	0.6	O	0.172	0.241	1297	0.250	2067	0.040
			80	0.6	C	0.130	0.181	1296	0.200	1825	0.136
			-	0	N	0.410	0.543	1303	0.550	3772	1.269
45	15	400	120	0.6	O	0.377	0.496	1303	0.500	3474	0.041
			70	0.6	C	0.268	0.354	1307	0.350	2610	0.283

[a] N – Natural, O – Optimal detector focus, C – Collimated.

Table 4.3: Predicted time resolution and electron beam radius at the detector for experiments carried out at 65 kV, for various initial electron gun set-ups, and magnetic lens focussing conditions.

Energy / keV	Photocathode-to-anode distance / mm	Aperture size / μm	Lens position / mm	Lens current / A	Electron beam focus type [a]	Electron beam rms radius at sample / mm	Equivalent FWHM beam size / mm	Electron pulse duration / fs	Laser and sample width / mm	Time resolution / fs	Electron beam rms radius at detector / mm
			-	0	N	0.242	0.335	630	0.350	2067	0.798
65	10	150	100	0.8	O	0.180	0.248	629	0.250	1547	0.018
			70	0.8	C	0.146	0.202	632	0.200	1299	0.137
			-	0	N	0.537	0.702	621	0.700	3996	1.746
65	10	400	90	0.8	O	0.368	0.479	621	0.475	2753	0.051
			30	1	C	0.199	0.261	644	0.275	1676	0.216
			-	0	N	0.185	0.259	886	0.275	1782	0.584
65	15	150	90	0.8	O	0.126	0.173	886	0.175	1330	0.026
			60	0.8	C	0.104	0.143	891	0.150	1231	0.104
			-	0	N	0.408	0.535	881	0.550	3218	1.252
65	15	400	80	0.8	O	0.254	0.334	883	0.350	2157	0.041
			50	0.8	C	0.218	0.287	888	0.300	1908	0.226

[a] N – Natural, O – Optimal detector focus, C – Collimated.

Table 4.4: Predicted time resolution and electron beam radius at the detector for experiments carried out at 100 kV, for various initial electron gun set-ups, and magnetic lens focussing conditions.

Energy / keV	Photocathode-to-anode distance / mm	Aperture size / μm	Lens position / mm	Lens current / A	Electron beam focus type [a]	Electron beam rms radius at sample / mm	Equivalent FWHM beam size / mm	Electron pulse duration / fs	Laser and sample width / mm	Time resolution / fs	Electron beam rms radius at detector / mm
			-	0	N	0.243	0.335	398	0.350	1761	0.797
100	10	150	100	1	O	0.182	0.248	398	0.250	1296	0.015
			40	1.2	C	0.100	0.137	399	0.150	840	0.101
			-	0	N	0.543	0.707	392	0.725	3576	1.764
100	10	400	100	1	O	0.406	0.528	392	0.525	2614	0.026
			60	1	C	0.319	0.415	393	0.425	2123	0.366
			-	0	N	0.184	0.255	562	0.250	1359	0.572
100	15	150	90	1	O	0.125	0.173	562	0.175	1033	0.019
			110	0.8	C	0.162	0.223	561	0.220	1226	0.158
			-	0	N	0.410	0.535	558	0.550	2754	1.252
100	15	400	80	1	O	0.258	0.337	559	0.350	1805	0.032
			50	1	C	0.222	0.291	563	0.300	1577	0.224

[a] N – Natural, O – Optimal detector focus, C – Collimated.

The set-up that matches most closely to the experiments described in Chapter 5, involves the 45 kV, 15 mm photocathode-to-anode distance, 400 μm anode aperture electron gun. Without the magnetic lens, a pulse duration of 1,303 fs at the sample is predicted, and a beam radius of 1.269 mm at the detector, giving a spatial resolution of $\Delta s \approx 7.5$ nm^{-1}. The overall experimental time resolution for this set-up would be 3,772 fs. This is a relatively poor time resolution, but represents the worst-case scenario if the magnetic lens was not working. If we were to obtain the optimal radial beam focus on the detector of 0.04 mm ($\Delta s \approx 0.2$ nm^{-1}), the overall experimental time resolution would only drop by 8% to 3,474 fs. However, while the collimated electron beam has a wider radius of 0.28 mm at the detector ($\Delta s \approx 1.7$ nm^{-1}), the time resolution improves by 31% to 2,610 fs, and is still able to produce the high spatial resolution desired.

If we were to use tilted wavefronts with this set-up, Equation 2.14 suggests that best angle of intersection between the pump and probe beam would be approximately 67°. With the two beams simply intersecting at this angle, the time

resolution at the sample position would increase to 2,300 fs when using the collimated electron beam. If tilted wavefronts were used to remove the velocity mismatch problem, the ultimate time resolution possible with this set-up would be 1,308 fs; a 65% improvement on the set-up without the magnetic lens, assuming no jitter.

However, this is just the best time resolution possible with the set-up used to collect the data presented in Chapter 5. With time and conditioning, the apparatus will be able to achieve a much higher time resolution, when operating at 100 kV. In fact simulations at 100 kV show that, with careful manipulation of the magnetic lens, a more rapid gain in improving the time resolution of the experiment can be achieved compared to that of the lower acceleration potential experiments.

The optimal 100 kV set-up would make use of the 10 mm photocathode-to-anode distance, and the 150 μm anode aperture electron gun, and would have a pulse duration of 398 fs. The natural beam has a radius of 0.80 mm at the detector ($\Delta s \approx$ 7.3 nm^{-1}), and provide a time resolution of 1,761 fs when crossing the pump and probe beams perpendicularly. An optimal radial focus at the detector can be achieved of 0.015 mm ($\Delta s \approx 0.1$ nm^{-1}), with a time resolution of 1,296 fs (26% improvement). However, by compromising the spatial resolution slightly to produce a collimated beam with a radius of 0.10 mm at the detector ($\Delta s \approx 0.9$ nm^{-1}), a time resolution of 840 fs can be attained (53% improvement).

If we set the angle of the intersecting beams to 57° (as calculated with Equation 2.14, in Section 2.2.2), the resolution can be improved once again to 667 fs (62% improvement) whilst using the collimated beam, with an ultimate time resolution of 416 fs (76% improvement) when using tilted wavefronts, again assuming no jitter.

These results also suggest that, whilst generally producing the best overall time resolution, the collimated electron beams from a 150 μm electron gun will also provide relatively well-resolved spatial data when the detector is 500 mm from the anode, and when the detector is moved forward to a distance of 330 mm from the anode. In most cases with this closer anode-to-detector distance, the radius of the beam predicted for these 150 μm anode aperture experiments are either smaller than, or just above the barrier of $r \approx 0.125$ mm at the detector, and hence the collected structural data will be considered highly resolved. However, experiments using the

larger aperture, which in turn produce a larger collimated beam that may be too big to acquire this level of resolution, and a different balance between spatial and time resolution will need to be found.

In any case, the time resolution of 416 fs is likely to represent the fastest event that one will be able to observe with the apparatus, in its present format, for a pulse that initially contains 10^4 electrons.

4.5. Summary

With these calculations it has been possible to model how a pulse containing 10^4 electrons behaves as it propagates through the apparatus under many different electron gun conditions, as well as to study how it responds to the presence of a magnetic lens. The simulations have also predicted the ultimate time resolution of the apparatus to be 416 fs. The exact value may vary slightly depending on the exact magnetic lens and experimental conditions, but not by an appreciable amount.

The calculations have also allowed us to make the decision of where to place the magnetic lens in the apparatus so as to be as flexible as possible. With its centre approximately 60 mm from the face of the anode, it is in the optimal position to allow for more efficient beam focussing at the detector and at the sample. However, as the calculations showed that even small changes in the position of the magnetic lens could have a large effect on the overall resolution of the apparatus, the decision was also made to place the lens on a manipulator to allow for its position to be fine-tuned.

As well, the results presented here show how the electron beam behaves without the magnetic lens, and that the trends observed here, in terms of how the duration of the pulse evolves as it propagates through the apparatus, match those reported by other groups.[29] It also appears that the percentage of electrons passing through the 150 μm aperture, agrees with the results seen in the calibration of the experimental apparatus that will be discussed in Section 5.2.1.

Chapter 5. Apparatus calibration and diffraction experiments

As might be expected for new piece of equipment, early work on the TRED apparatus following its construction consisted of determining the most suitable methods for producing and detecting a stable electron beam. This first involved conditioning the electron gun and optimising the electron beam ionisation laser path. Later the electron detection equipment was upgraded from a simple phosphor screen and web camera set-up to the more sophisticated MCP / phosphor screen / CCD camera set-up described in Chapter 3.

The first part of this chapter is dedicated to detailing briefly the early experiments carried out in Edinburgh, which involved producing the first electrons, before moving on to more quantitative experiments performed in York, which focussed on the calibration of the pulsed electron beam. The latter section of this chapter details the progress made towards full TRGED experiments, with the pump-probe time-zero position determined and basic diffraction experiments carried out.

5.1. Initial set-up and observations

5.1.1. Conditioning of the electron gun

Before any electron beam could be observed or measured, the electron gun itself had to be conditioned. As high voltages are being used in the apparatus, the electric field between the electrode and anode can break down if there are any imperfections on the surface of either component, which may be caused by scratches or foreign bodies. When new, the individual components of the apparatus will generally be well polished, with no major scratches, and so the main priority is to keep all of the internal components of the apparatus clean. However, when dealing with such high voltages there will initially always be some small imperfection that can cause the electric field in the gun to break down; with careful conditioning this can be overcome.

The gun was conditioned by slowly increasing the voltage applied to the electrode. Eventually imperfections on either the cathode or anode will cause the electric field to break down, and an electrical discharge will be observed. Although one generally tries to avoid such electrical discharges during normal operation, at this early stage it can help the apparatus. The energy imparted in the discharge will

be directed towards the imperfection and may cause it to be removed, allowing for higher voltages to be reached. In some cases it may take several discharges to get above a certain voltage, and there comes a point where the main limiting factor is the slow degassing of components and the pressure in the electron gun chamber.

The general operating pressure of the electron gun that was used for most of the experiments described here was around 1×10^{-7} mbar. This was the pressure that the electron gun would generally reach after being pumped from atmospheric pressure for 12-16 hours. The rate at which the pressure drops greatly slows after this point, and generally takes several days to get appreciably lower. At this operating pressure, the highest stable voltage across the electrode that generally could be obtained was around −55 kV. However, the maximum voltage observed across the electrode was −70 kV, and was obtained at an operating pressure of 5×10^{-8} mbar, early on in testing. To reach this pressure the apparatus was continuously pumped for a couple of weeks. Operating at reduced pressures and the higher potentials that they permit was difficult during the testing period because the apparatus was opened so often. As testing of the apparatus got underway, changes to the apparatus would be made on an almost daily basis, including installing new pieces of equipment (*e.g.* magnetic lens / apertures / detectors), adjusting the positions of components, and inserting samples for diffraction. All of these would involve breaking the vacuum, and require the pressure in the apparatus to be returned to atmospheric levels. As detailed in Section 3.2.6 the pressure in the apparatus would generally be brought back to atmospheric levels by introducing dry nitrogen into it and, unless replacing the photocathode, there would generally be no need to open the electron gun. This prevented contamination of the gun, and with only dry nitrogen being used, the amount of time needed to evacuate the chamber to operating pressures was reduced, as well as removing the need to recondition the gun.

5.1.2. Initial electron beam observations

With this apparatus, an electron beam can be detected in one of two ways; using a phosphor screen and camera, or using a Faraday cup and picoammeter. The earliest electron beam was observed using the first method, by placing a phosphor screen approximately at the sample position within the diffraction apparatus (*i.e.* approximately 130 mm from the anode). The screen was placed relatively close to the source of the electrons as it was not known how the electron beam would behave;

117

for instance the beam might have been deflected past the phosphor had the detector set-up been placed further from the anode. Figure 5.1 shows one of the earliest beam images recorded.

Figure 5.1: Early image of the electron beam (lower larger spot), recorded on a phosphor screen using a web camera. A smaller spot can also be seen, and is the residual intensity of the laser used to ionise the photocathode.

One can see from Figure 5.1 that there are two spots: one larger spot relating to the electron beam, and another resulting from the remaining intensity of the laser beam used to produce the electrons passing through the photocathode. To confirm that an electron beam was being produced, a strong magnet was brought near to the diffraction chamber; this deflected the electron beam from its natural propagation path while leaving the laser spot unmoved. With visual confirmation that the apparatus was producing a stable beam of electrons, more accurate measurements of the beam properties were performed.

5.2. Electron beam calibration

5.2.1. Electron beam current

As detailed in Section 3.2.5, the electron beam current can be measured using the beam stop that is positioned in front of the detector, and a picoammeter. As an ultrafast pulsed electron beam is being created, the picoammeter was linked to the signal generator of the Ti:Sapphire laser, allowing a reading to be taken at the approximate time that the electron beam arrived at the beam cup. It was important to understand how the current of the electron beam varied with different properties of the electron gun; such variables included the accelerating potential of the electron gun, the power of the laser used to ionise the photocathode, the focus of the laser, and the size of aperture in the anode.

The ionisation laser impinging on the photocathode must be focussed in order to produce any notable electron beam. Without this focussing most of the laser will impinge on the conductive metal on the back of the photocathode, preventing it from passing through sapphire disc to the gold on the other side. The remainder of the beam that does pass through the window in the conductive metal will be unfocussed and produce electrons over a large area. After accelerating form the photocathode, most of these electrons will come into contact with the grounded anode and be lost. The number of electrons that do pass through the aperture in the anode are too few to be accurately measured. Therefore, the focussed laser beam is necessary to produce a localised source of electrons that are in a position to pass through the aperture in anode.

As described in Section 3.3.2.1, a 50 cm plano-convex lens is used to focus the laser beam on to the photocathode. As shown in Figure 3.25, the 50 cm lens sits on a 1" translation stage with the intention to allow for the focus of the laser to be fine adjusted. However, it was noted that over the range that the stage could move no significant change in the quality of the electron beam was observed. It is assumed that this is because the width of the focussed laser does not vary appreciably when the lens is moved over the range of this translation stage, and the emitted electron beam remains sufficiently small for most of it to still pass through the aperture in the anode of the electron gun.

The other variables mentioned above do have a significant effect on the number of electrons observed. The size of the aperture in the anode can be varied easily due to its set-up (as detailed in Section 3.2.2), and the potential applied across the electron gun can be changed using the Heinzinger power supply. The power of the 267 nm laser beam can also be adjusted by rotating the polarisation angle of the SHG crystal, to vary the amount of 267 nm light produced in the THG set-up. Figure 5.2 contains a series of plots that show how the energy of the laser pulse varies with the polarisation angle of the SHG crystal, and how the number of electrons per pulse varies with different electron gun set-ups.
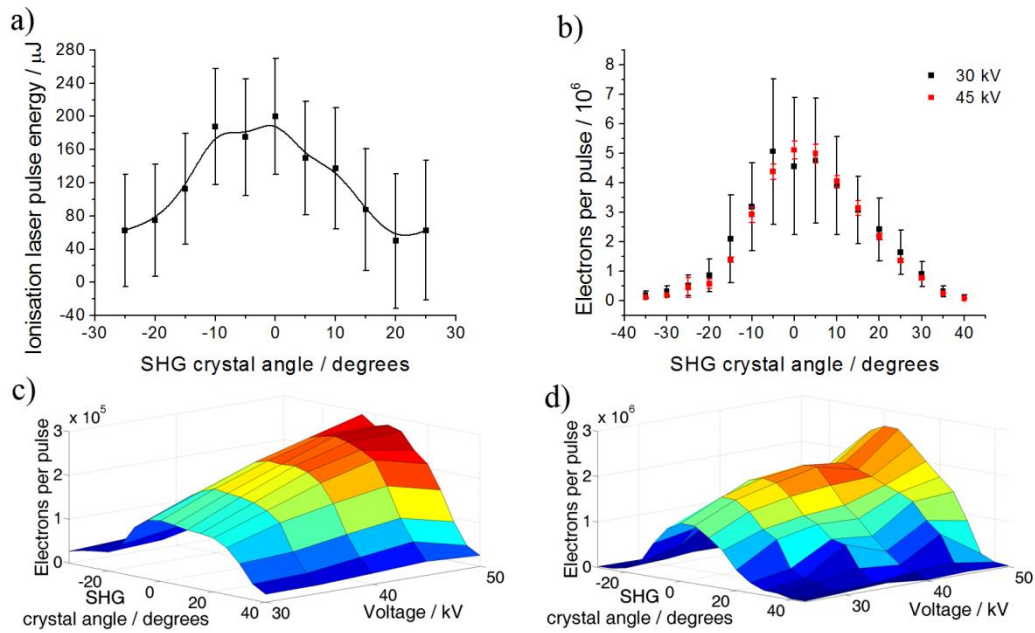
Figure 5.2: Graphs showing a) the energy of a 267 nm laser pulse as function of SHG crystal polarisation angle, and observed number of electrons per pulse when using b) a 1000 μm aperture c) a 150 μm aperture, and d) a 300 μm aperture for various different electron gun conditions.

One will note from the results shown in Figure 5.2, that no beam current data are reported for the 150 μm aperture, 25 kV set-up, as no stable current above the noise level of the detector was observed. Also, due to time constraints with the Laser Loan Pool laser, the beam current for the 1,000 μm aperture set-up, was only investigated for the two most commonly used acceleration potentials, 30 and 45 kV. Laser powers are also only shown for the range of SHG polarisation angles from –25° to 25°, as the power meter used was not sufficiently sensitive to measure the laser power when rotated further. All values shown in Figure 5.2 are averages of numerous individual readings, with standard deviations of these values being presented for results relating to the laser power and 1,000 μm aperture experiments, but have been omitted from the results of the 150 and 300 μm aperture experiments for clarity.

From Figure 5.2 one can see that number of electrons observed per pulse at the detector is highly dependent on the angle of the SHG crystal and, hence, the power of the laser. Comparing the plots shown in Figure 5.2, one can see a similar trend with respect to the SHG angle amongst all of the plots, suggesting that the number of electrons produced from the photocathode scales almost linearly with the power of

the laser, as would be expected for a single-photon ionisation process. From this one can see that it is possible to fine tune the number of electrons produced from a maximum of $5.1{\times}10^6$ electrons per pulse (45 kV, 1,000 μm aperture), to below the noise level of the picoammeter (500 electrons per pulse). Obviously, the number of electrons that make it into the diffraction chamber is dependent on the size of the aperture through which they must pass, with the maximum number of electrons per pulse observed with each aperture being $2.9{\times}10^5$, $2.6{\times}10^6$, and $5.1{\times}10^6$ for the 150 μm, 300 μm, and 1,000 μm apertures, respectively.

It is also interesting to note that the maximum number of electrons that can pass through a given aperture depends on the potential of the electron gun. With smaller apertures, fewer electrons are observed at lower acceleration potentials. This is likely due to the pulse having more time to expand in the transverse direction at lower voltages (and consequently lower velocities), before reaching the anode, thus preventing more electrons from passing through. In the case of the 1,000 μm aperture, there is no appreciable difference in the number of electrons that pass through at the two voltages investigated, suggesting that the aperture is large enough to allow almost all of the electrons to pass through. However, one can also see from Figure 5.2b that the measured standard deviation of the number of electrons passing through at 30 kV is much larger than those at 45 kV. This is most likely related to the fact that with higher acceleration voltages, the electrons are less likely to diverge and deviate off course on their path to the detector.

Accepting that the 1,000 μm aperture is large enough to allow all of the electrons produced at the photocathode to enter the diffraction chamber, we can estimate the percentage of the electron beam that can pass through one of the smaller apertures. Figure 5.3 shows how the percentage for the 150 and 300 μm apertures is dependent on the SHG angle / laser power, and accelerating voltage used in the experiments.
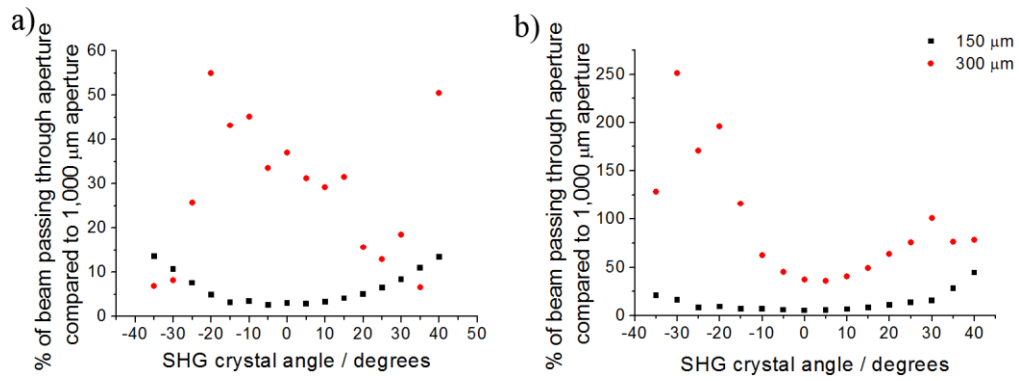
Figure 5.3: Graphs show the percentage of the electron beam current passing through the (blue) 150 μm aperture and the (red) 300 μm aperture compared to the 1,000 μm aperture at a) 30 kV and b) 45 kV, as a function the polarisation angle of the SHG crystal.

Figure 5.3 shows that the largest percentage of electrons to pass through the 150 μm aperture occurs when the laser power is at its lowest, with the percentage minima being observed at the maximum laser power. This is likely to be related to the "Coulomb explosion" problem; with a higher laser power, more electrons and, hence, a denser electron pulse is produced, increasing the number of Coulombic repulsion events within the pulse. The pulse then expands in all directions faster than would be expected for a low-density pulse, causing a larger divergence of the beam in the transverse direction. With the beam diverging more rapidly fewer of the electrons produced pass through the smaller 150 μm aperture compared to the 1,000 μm aperture. This highlights the need to select carefully the appropriate laser power to produce the optimal electron beam for diffraction experiments.

At lower laser powers (where the SHG angle is between 35 and 40° to the axis of the laser beam) 1.8–2.4×10^4 electrons per pulse pass through the 1,000 μm aperture at 45 kV. The number of electrons that pass through the 150 μm aperture at these same angles is 7.5–3.1×10^4 electrons per pulse, which is 44–28%, respectively, of what is seen with the 1,000 μm aperture. This is not far off the percentage yield (23.3%) of electrons seen passing through the 150 μm aperture in the simulations of Section 4.3.1.1, for a pulse containing a similar number of electrons (*i.e.* ~10^4 electrons).

A similar, though less clear, trend is observed for the 300 μm aperture where, in the 45 kV set-up, one can see the same minima occurring around where the

maximum laser power is observed, and generally larger transmission percentages at lower powers. These are not as conclusive as for the 30 kV set-up, but the cause of the poor data is most likely related to the previously discussed point of the beam having a larger divergence in the transverse direction before passing through the aperture in the anode. This would also explain why the trend is clearer with the 150 μm aperture, as it is small enough to remove all of the rapidly diverging electrons, yielding a relatively well-collimated electron beam.

It should be noted that whilst the laser was not adjusted between these experiments, the laser could impinge on different parts of the photocathode after opening the apparatus to change the aperture in the anode of the electron gun. This new area of the photocathode could have slightly different electron ionisation properties from the previous area and, hence, produce a slightly different beam. This could be the reason why an unusually large percentage of electrons are observed for the 300 μm aperture at 45 kV compared to the 1,000 μm aperture. The results here further show the care that must be taken when choosing the laser power, acceleration potential and aperture size to use in experiments, as each has an effect on the properties of the electron beam produced.

5.2.2. Electron beam width

The width of the electron beam was measured using the equipment and methods described in Section 3.2.9. As detailed in Chapters 2 and 4, it is important to know the transverse size of the electron beam at the sample position in order to accurately determine the time resolution of the experiment. Here we look at how the number of electrons affects the width of the beam, as well as measure variations in the beam width as the magnetic lens focusses it. In the experiments described, the beam width measurer was brought in through the middle port of the side flange of the diffraction chamber, mounted on an *xyz* manipulator. In this position, one could determine the width of the electron beam after it had travelled approximately 130 mm through the diffraction chamber. The 1,000 μm aperture in the anode of the electron gun was used throughout these experiments. Other aperture sizes were not investigated because of time restrictions with the Laser Loan Pool laser. All of the measurements were made using the 500 μm aperture on the beam-width measurer.

5.2.2.1. Unfocussed electron beam

The transverse profile of electron beam was measured in both the *x* and *y* directions (with reference to axes defined in Figure 2.9). Experiments were performed using both 1×10^4 and 5×10^4 electrons per pulse, representing the likely range that will be employed for future TRED experiments. Figure 5.4 shows how the current of the two beams varied as the beam-width measurer was scanned across them. Each data point shown is an average of numerous recordings, with the accompanying error bars representing the standard deviation of these readings.
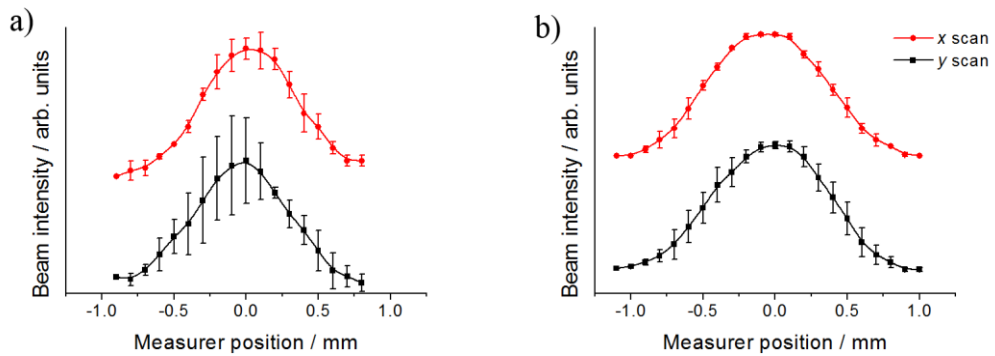
Figure 5.4: Point-to-point fits showing the intensity of a pulse containing a) 1×10^4 and b) 5×10^4 electrons passing through a 500 μm aperture in the beam width measurer, as scanned in the *x* (top) and *y* (bottom) directions.

When the 1,000 μm aperture is used the transverse profile of the electron beam is Gaussian in nature, as expected when being created by a laser pulse that is itself Gaussian. By fitting the data observed to a Gaussian, the full-width half-maximum (FWHM) value for each beam can be obtained as 0.41 mm for the 1×10^4 electron pulse and 1.5 mm for the 5×10^4 electron pulse. This demonstrates that the width of the pulse is heavily dependent on the number of electrons it contains, with the pulse more than tripling in FWHM diameter when the current is increased fivefold.

Looking at the error bars in each figure, one can see that data are more precise for the 5×10^4 electron pulse. This is due to the observed number of electrons passing through the aperture in the measurer being well above the noise limit for each measurement, which is not the case for the 1×10^4 pulse. One can also see that measurements made in the *x* direction are more accurate for both pulses, and this is simply due to a more accurate Vernier scale being available on this axis during measurements.

Assuming that the pulse duration measured for the 1×10^4 electron pulse has a similar duration to the closest simulation presented in Chapter 4 (400 μm aperture, 45 kV, 15 mm photocathode-to-anode distance electron gun), an overall experimental time resolution of approximately 3,000 fs is predicted when the pump and probe beams cross orthogonally, and 2,640 fs when they intersect at an angle of 67°.

5.2.2.2. Magnetic lens

As the purpose of the magnetic lens is to reduce the transverse size of the electron beam, it was important to measure how this behaved. In the following experiments the centre of the magnetic lens was placed 60 mm from the face of the anode plate, meaning that the distance from the centre of the magnetic lens to the beam width measurer was approximately 70 mm. The beam width was investigated for magnetic lens currents of 0.0, 0.3, 0.6, 0.9 and 1.18 A, where 1.18 A produced the optimal beam focus at the detector, 200 mm downstream from the sampler. For comparison, Figure 5.5a, shows the measured transverse profile of the electron beam (in the *x* axis) at the sample position for both the natural beam and the one optimally focussed by the magnetic lens. As one can see the narrowed electron beam retains its Gaussian profile, and the observed peak intensity is larger than when the lens is off, as more electrons are able to pass through the measurer when it is positioned over the centre of the beam.
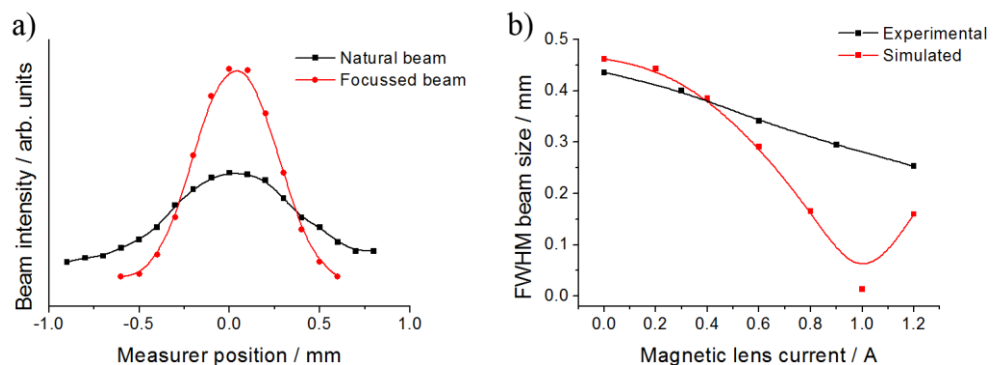
Figure 5.5: Graphs showing a) Gaussian-fit comparison of the transverse beam profile of an electron pulse containing 1×10^4 electrons, at its natural (black) and focussed (red) widths, and b) a *β*-spline-fit comparison of the FWHM of the transverse beam width at various magnetic lens currents, as determined by experiment (black) and simulation (red).

Figure 5.5b shows the FWHM of the electron beam at the sample position for various currents passing through the magnetic lens, as measured experimentally and as predicted in the simulations discussed in Chapter 4. The simulated curve shown uses the initial conditions most similar to that used in the experiment (*i.e.* 10^4 electrons per pulse, 45 kV, 400 μm aperture, 15 mm photocathode-to-anode distance, magnetic lens positioned 60 mm from the anode). One can see that with the magnetic lens off the predicted and experimentally measured FWHM widths are relatively similar, giving confidence that the initial conditions used in the simulations are believable. As the magnetic lens is applied to the electron beam, experimentally we see the FWHM of the transverse width of the beam decrease in an almost linear fashion with respect to the current used. However, the simulations predict that the beam width narrows much faster than is observed. The simulations also predict that, at higher operating currents, the magnetic lens causes an over-focussing of the beam before the sample position, which is not observed experimentally. This suggests that in the simulations the force that the magnetic lens exerts on the electron beam is greater than in reality. This most likely comes from the fact that the magnetic lens in the simulations is modelled as a single solenoid with 1,000 turns of wire, of radius *r*. With the practical set-up one can see from Figure 3.18, that whilst the lens contains around 1,000 turns of wire, they form layers, with each new layer being more distant from the electron beam than the last. However, whilst this may be true, it does not take away from the trends discovered and discussed in Chapter 4, and instead suggests that they all occur at slightly higher currents than predicted.

5.3. Time-zero determination

Knowing accurately that the electron and laser beams used in the pump-probe experiments are crossing each other in both time and space is imperative for carrying out TRED experiments. To help find this position the piece of equipment described in Section 3.2.11 was used to align both beams, so that they intersected with each other perpendicularly, as shown in Figure 5.6a. To help find the point where both beams reach the intersection point at the same time (*i.e.* the time-zero position), a fine copper mesh was fixed to the flat side of the beam aligner. With the pump laser off, after passing through the copper mesh, a grid-like structure can be seen in the image produced by the electron beam as it arrives at the detector, shown in Figure 5.6b.
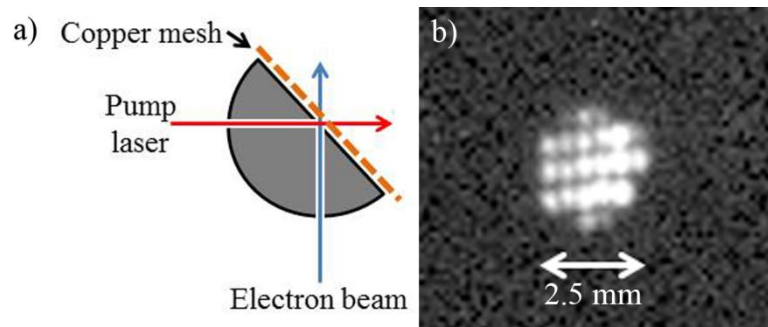
Figure 5.6: a) Pictorial representation of the set-up used to determine the time-zero position between the pump laser and the electron beam, utilising the beam aligner and a fine copper mesh, and b) the appearance of electron beam after passing through the copper mesh.

The experiment to determine time zero uses the idea that an electron pulse can be perturbed by a plasma. Such a plasma can be produced by the ionisation of the copper mesh using the pump laser beam. Using the experimental set-up shown in Figure 5.6, a plasma was created by focussing the laser through the beam aligner and onto the copper mesh. A maximum power of 67 μJ per pulse was used, as a larger energy than this would destroy the copper mesh. The time delay between the pump and probe beams was then varied using the delay stage in the photocathode ionisation laser path, whilst observing the image produced by the electron beam on the detector, taking note of any changes in its appearance. When the beams are aligned spatially and temporally, the image produced by the electron beam becomes distorted as seen in Figure 5.7.

| -6.7 ps | -670 fs | 0 fs | 670 fs | 1.34 ps |

| 2.10 ps | 4.02 ps | 6.70 ps | 10.05 ps | 13.40 ps |

| 16.75 ps | 20.10 ps | 22.11 ps | 23.45 ps | 26.80 ps |
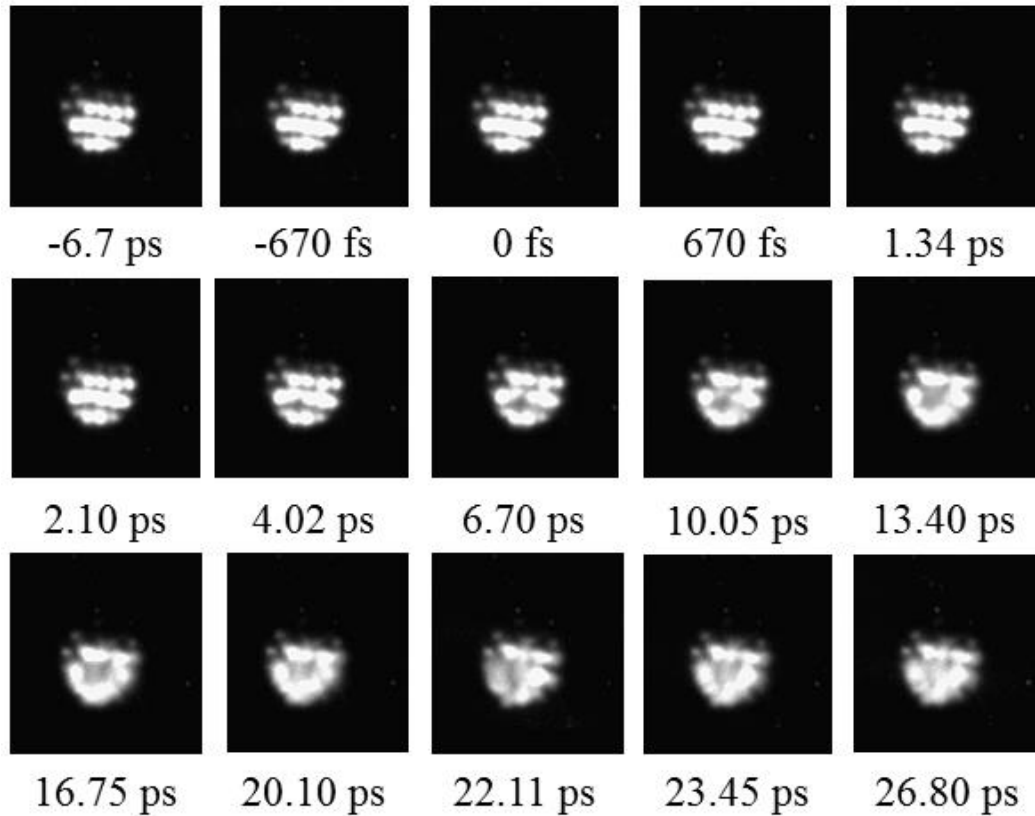
Figure 5.7: Images showing the interaction of an electron beam with a plasma produced by the ionisation of a copper mesh, taken at various time delays between the pump and probe beams.

In this experiment it was possible to observe how the electron beam varied in time steps as small as 670 fs; time zero has been defined as the position where one first observes a change in the pattern produced by the electron beam at the detector. As there is a small delay for the plasma beam to be created after the pump laser interacts with the copper mesh, the true time-zero position (where the pump laser and electron beam cross, rather than where the electron beam and plasma interact) is within approximately 10 ps of this observed time zero,[74] and must be taken into account when carrying out further pump-probe experiments.

5.4. Diffraction experiments

Before full TRED experiments could be carried out, a series of simple diffraction experiments were performed to determine the capabilities of the apparatus. This first involved looking at a polycrystalline sample of platinum, as it would be easier to diffract from than a gas sample, which would need careful handling and control to observe sufficient scattering. However, later experiments did move onto carrying out

basic attempts to observe scattering from gaseous samples of argon and carbon tetrachloride (CCl_4).

5.4.1. Polycrystalline platinum diffraction

A series of polycrystalline samples of platinum were prepared on 3 mm diameter carbon-coated TEM grids, by electro-deposition techniques to a thickness of 20 nm, with the assistance of Professor Jun Yuan, from the Department of Physics, at the University of York's JEOL Nanocentre. For use in the TRED these TEM grids were fixed to an 8 mm diameter copper mesh using silver solder, and placed in the sample mount described in Section 3.2.10.

For these experiments the electron gun was set to an acceleration potential of 45 kV, with the THG set-up adjusted so that there were approximately 10^4 electrons per pulse. The total distance between the electron gun anode and the detector was 330 mm. The distance from the anode to the sample was approximately 115 mm, leaving 215 mm between the sample and the detector. At this position, with the 80 mm active area of the MCP, diffraction data were collected out to $s = 195$ nm^{-1}, at 45 kV (as determined from Equation 2.3). For all of the experiments described below, the potentials applied to the MCP and the phosphor screen were +1.9 kV and +4.1 kV, respectively. The Stingray CCD camera was used to record a series of images, each with a 28 second exposure. The aperture of the Schneider lens was fully opened allowing the maximum amount of light from the phosphor screen to reach the CCD camera.

Diffraction experiments were performed for various magnetic lens currents, including with the lens off, to observe how this affected the diffraction patterns. In each experiment, 13 images were recorded, with the Pt sample directly in the path of the electron beam. The sample mount was then moved slightly so that the electron beam was passing through a region of the copper mesh that did not contain the Pt sample, and the same number of background images was recorded. Once collected, a custom piece of MATLAB code (See Appendix C, *Stack_ImageV2.m*) was used to stack and normalise the collected images, before removing a normalised-stacked-background image. The diffraction patterns obtained with the magnetic lens off (*i.e.* when the electron beam is at its natural width) and with the lens set to a new optimal focussing current of 1.19A (after replacing the photocathode used in the previous experiments), are shown in Figure 5.8.
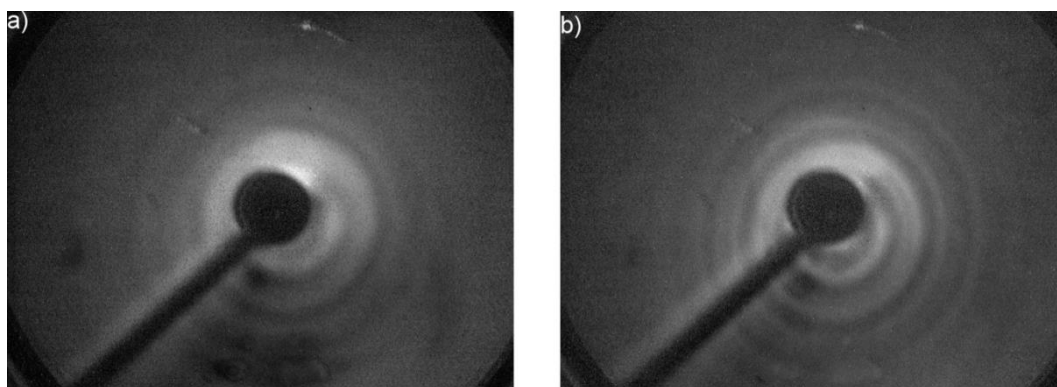
Figure 5.8: Diffraction patterns obtained from a polycrystalline sample of platinum when the magnetic lens is a) off and b) on and running at its optimal current of 1.19 A.

One can see from Figure 5.8 that with the magnetic lens on the resolution of the diffraction pattern is better; the rings observed are narrower and better defined. The images were then extracted and analysed using a custom piece of MATLAB code (See Appendix C, *TRED_Extraction_V2.m*). The extracted intensities from both experiments, where the magnetic lens is off and on, can be seen in Figure 5.9. These plots again show that the diffraction data improve when the magnetic lens is focussing the electron beam onto the detector; the intensity peaks become narrower and more distinct, compared to the broader and overlapping peaks observed with the lens off.
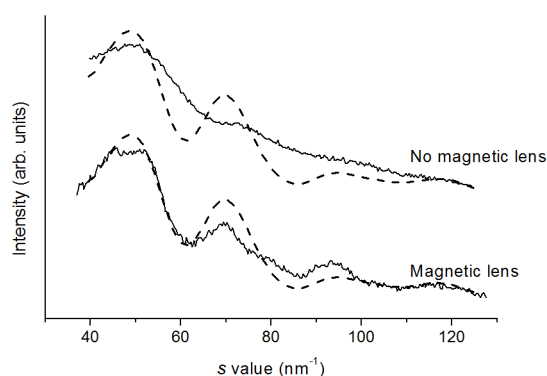
Figure 5.9: The observed scattering intensities extracted from the diffraction patterns of polycrystalline platinum, with the magnetic lens off (top) and on (bottom). The theoretically calculated scattering curves expected for a well-focussed electron beam (dashed) have been superimposed on both sets of data for comparison.

To further confirm that the diffraction patterns were concurrent with polycrystalline platinum, a theoretical model of scattering intensities was generated. This was achieved by taking the Bragg equation:[16]

$$\frac{\lambda}{2a_0} = \sin\left(\frac{\theta}{2}\right) \Big/ \left(h_i^2 + k_i^2 + l_i^2\right)^{\frac{1}{2}} , \qquad \text{Eq. 5.1}$$

where h_i, k_i, and l_i are the Miller indices of the crystal plane, i, involved in diffraction, with a unit cell of size a_0 (392.42 pm for polycrystalline Pt),[122] using electrons with a wavelength, λ, and inserting it in to Equation 2.3, to obtain a scattering equation for a polycrystalline sample:

$$s = 4\pi\left(h_i^2 + k_i^2 + l_i^2\right)^{\frac{1}{2}} / 2a_0 , \qquad \text{Eq. 5.2}$$

where s is still a function of the scattering angle. Knowing the expected s values, one can predict the positions of the diffraction rings that should appear in the pattern by rearranging Equation 2.3 to give:

$$r_i = L \tan\left[2\sin^{-1}\left(\frac{\lambda s}{4\pi}\right)\right], \qquad \text{Eq. 5.3}$$

where r_i is the radial distance from the centre of the diffraction pattern, and L is the sample-to-detector distance. This model used the parameters for a face-centred cubic (FCC) Pt crystal, and takes into account only scattering from planes that are classically allowed for a FCC crystal (*i.e.* where Miller indices are either all odd or all even), and weighted for the multiplicity of each plane. The width of each peak in the model was dependent on an estimation of the size of the undiffracted electron beam spot at the detector. The intensities are divided by s^4 to take into account the fact that observed scattering decreases at wider diffraction angles. In Figure 5.9 the scattering from the theoretical model, in which the magnetic lens has narrowed the electron beam width at the detector, has been superimposed onto the extracted experimental intensities, as a dashed line. One can see that the theoretical and experimental scattering curves for where the magnetic lens is on match well, confirming that the electrons are being scattered as expected from the polycrystalline platinum sample. With the same theoretical data compared to data extracted when the magnetic lens is not on, it again shows the how the resolution has been improved. While the fit is good, one can see that it is not perfect, and this is simply because it was not possible to determine exactly the beam size at the detector, nor determine to

a high enough accuracy the sample-to-detector distance. However, with further calibration experiments, with more standard samples, it should be possible to obtain a more accurate fit.

From the fittings carried out it was possible to estimate the spatial resolution of the experiment without the magnetic lens as $\Delta s = 11$ nm^{-1}, which improves to $\Delta s = 6.7$ nm^{-1} with the lens on. From the calculations presented in Chapter 4, this suggests that the electron beam has been focussed down to a comparable width of around 1.2 mm ($r \approx 0.6$ mm). This is relatively large, compared to the results seen for optimal magnetic lens focussing conditions discussed in Chapter 4, but could be further improved by placing a clean-up aperture before the sample to remove the most divergent electrons from the electron beam.

With the information obtained from the theoretical scattering curves, it was possible to create a theoretical diffraction pattern, using MATLAB code (See Appendix C, *Mock_Diff_pattern.m*), that could be compared to the experimental diffraction pattern, as shown for the well-focussed electron beam in Figure 5.10.
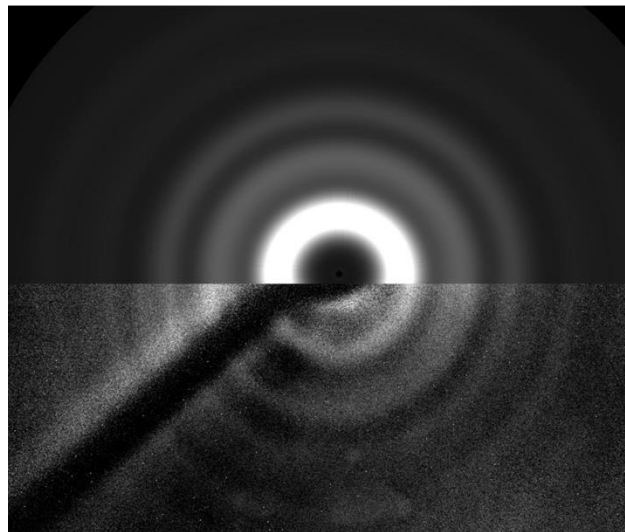
Figure 5.10: The theoretical diffraction pattern (top) of polycrystalline platinum superimposed onto the experimental diffraction pattern (bottom).

The results from these experiments show that the apparatus is capable of collecting diffraction data that can be refined to obtain structural information from a sample, in a reasonable time frame. It also shows the effectiveness of the magnetic lens to allow diffraction patterns to be collected with higher spatial resolution.

5.4.2. Electron diffraction of gases

Once data had been collected using the sample of polycrystalline platinum, the next stage was to try to obtain a gas-phase diffraction pattern using the apparatus. This involved using the gas handling set-up described in Section 3.2.12 to inject gas samples into the path of the electron beam in the diffraction chamber. The nozzle enters the diffraction apparatus through the central 2.75" port in the top 12" flange, giving an approximate sample-to-camera distance of 200 mm. The nozzle was positioned so that its tip was approximately 1-2 mm away from the path of the electron beam, which would maximise the amount scattering that could be observed. In these experiments the same parameters were used for collecting data with the CCD camera and lens as detailed in Section 5.4.1.

The first gaseous sample that was studied was argon, from which, as a single atom scattering centre, only atomic scattering will be observed, with no distinct rings of diffraction. The argon gas was introduced through the nozzle as a continuous stream, supplied from a gas reservoir held at atmospheric pressure and room temperature. Whilst expansion from the nozzle will cause the gas to cool (with the Knudsen number being much less than 1, at approximately 1.61×10^{-4} for the set-up described above),[123] it is assumed that the nozzle is close enough to the electron beam that scattering will not be observed from a fully formed molecular beam.[123] It is also unlikely that one will observe the formation of a plasma as a result of electron-impact ionisation of the gas sample, as the cross section for this occurring decreases at a near exponential rate, with respect to acceleration energy, for keV electrons.[124]

As no distinct diffraction rings would be observed from the scattering of the atomic sample, there was no need to focus the electron beam with the magnetic lens, nor direct the beam onto the beam stop to improve the dynamic range of the images. Instead, one was only likely to observe a slight increase in intensity around the electron beam, caused by the scattering of electrons, which would then quickly drop off at wider scattering angles. Figure 5.11 (part a and b) shows images collected at the detector with and without gas flowing into the chamber, whilst Figure 5.11c shows the radially averaged intensity curve as a function of the distance from the centre of the electron beam, once Figure 5.11a (the background) has been removed from Figure 5.11b (the signal).
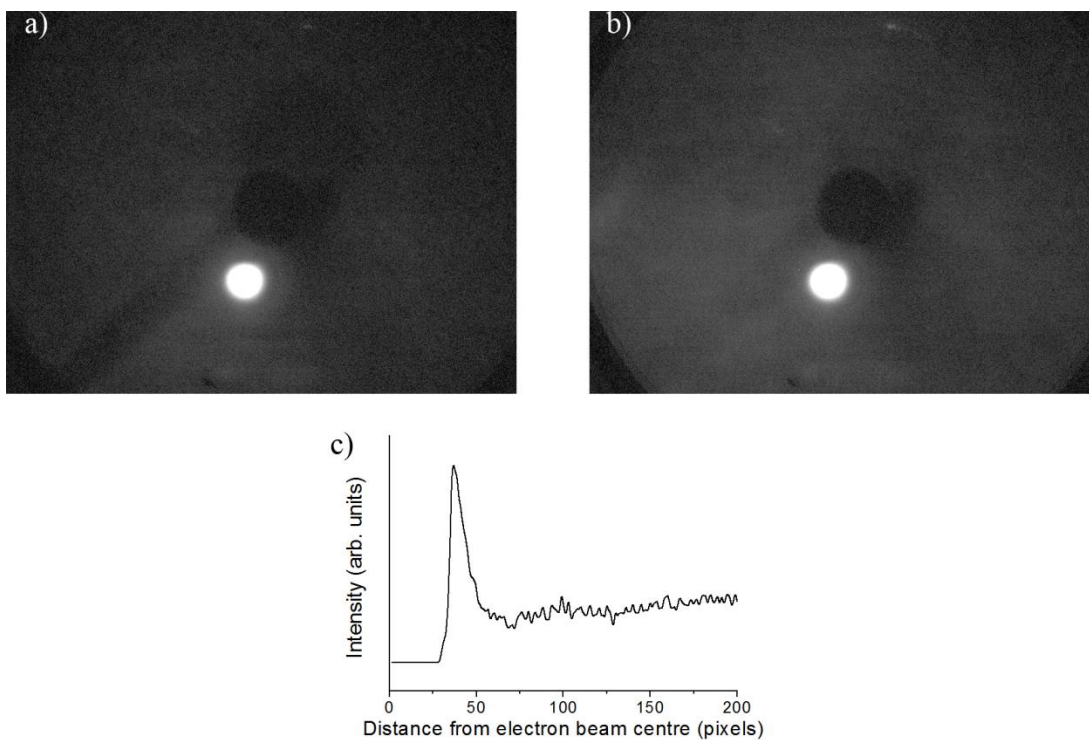
Figure 5.11: Images showing an unfocussed electron beam hitting the detector, with data collected a) with no argon gas flowing into the diffraction chamber, b) with gas flowing, and c) a graph showing the radially average intensity curve, as function of the distance from the centre of the electron beam, observed at the detector once a background has been removed.

From these images it was determined that it was possible to obtain scattering information from a gas-phase sample with the new apparatus, although the amount of scattering was small and only just above the noise level. However, with this knowledge that gas scattering was possible, the argon sample was replaced with an ampoule of CCl_4, in an attempt to observe molecular scattering.

Before injecting the sample into the apparatus (but with the ampoule attached to the gas injection line) the liquid sample of CCl_4 was frozen using liquid nitrogen and degassed. This was repeated several times to ensure that the sample had been fully degassed. Once degassing was complete, and the sample had returned to room temperature, the sample was injected by opening the valves linking it to the chamber. However, very little scattering was observed, as shown in Figure 5.12.

Figure 5.12: Scattering observed from a sample of CCl_4 using the TRED apparatus (background removed).

It is possible that a single diffraction ring is present just outside the beam stop in Figure 5.12, although it is not sufficiently clear to claim that molecular scattering has been observed. It is suspected that so little scattering was observed because there was an insufficient gas density at the moment the electron beam interacted with the molecular beam.

Whilst a high enough gas density could theoretically be achieved with the set-up used here, it would not be done so in a safe manner. As only a simple nozzle was in place, it meant that a continuous stream of gas would be let into the chamber. However, the vacuum system is not powerful enough to allow a continuous flow of the high density gas needed to observe sufficient diffraction for anything more than a few seconds. To overcome this problem, a pulsed nozzle system with a relatively high pressure of sample gas behind it would need to be used, with the nozzle pulsing in time with the electron beam crossing the sample position. This set-up should be sufficient to allow gas electron diffraction to be observed for both standard time-averaged and simple time-resolved diffraction experiments. However, due to time constraints with the Laser Loan Pool laser, it was not possible to implement these ideas and to observe improved gas-phase molecular diffraction.

5.5. Conclusion and summary

Whilst the ultimate goal of time-resolved gas electron has not yet been achieved with this apparatus, all of the steps leading to it have been achieved to one degree or another. The apparatus has been shown to produce a stable pulsed electron beam, whose width can be controlled using a calibrated magnetic lens. A suitable detector has been established that can measure accurately the number of electrons in each

pulse, and record diffraction patterns from a polycrystalline sample in a timely manner. The diffraction pattern from polycrystalline platinum collected with this apparatus shows that sensible diffraction patterns can be obtained, and that the data provided from these images match theoretical expectations. The images produced have also allowed for the quality of the electron beam, and the spatial resolution of the experiment, to be further calibrated. Whilst minimal amounts of gas diffraction were observed with the current gas inlet system, plans for a new, more efficient, delivery system have been completed, and are in production. This apparatus is limited only by the lack of a permanent laser source.

When a suitable laser becomes available for this apparatus, the author is confident that it will not take long, compared to what has already been achieved, for this piece of scientific equipment to be able to produce reliable high-quality time-resolved diffraction data.

Chapter 6. Quantum chemical studies on the dissociation of dimethyl disulfide and diethyl disulfide

6.1. Introduction

One significant focus of structural chemistry is to better understand the structures and folding processes of protein molecules; how and why these processes occur has a major impact on our everyday lives. The disulfide bond (S–S) present between cysteine residues of peptides is one of the key factors that control the overall structure of protein molecules.[125–127] Understanding how such bonds form and break within molecules helps to understand better the structures observed within proteins. However, as proteins are large molecules with many different types of chemical bonds, it is easier to study this specific bond by looking at smaller molecular analogues.

Simple aliphatic molecules with sulfur-sulfur bonds (*e.g.* $H_{2x+1}C_xSSC_xH_{2x+1}$) are useful for studying the dissociation of disulfide bridges as they can be small (when x is small), allowing for the feature of interest to be studied in detail. Several spectroscopic studies have focused on the dissociation of both S–S and S–C bonds within these molecules,[128,129] with several interesting observations being made.

When the aliphatic molecules with a disulfide bridge were acted upon by a light source with a wavelength of $\lambda < 200$ nm, it was generally reported that both the S–S and S–C bonds would break. However, when the energy of the photons used was lowered to a wavelength of $\lambda \approx 230$ nm, only the S–S bond would dissociate. This is interesting because, in general, the S–S bond is stronger than the S–C bond at 280 kJ mol^{-1} compared to 235 kJ mol^{-1},[129] and so one would expect that it would require more energy to dissociate.

As a result of these observations it was suggested that the dissociation of the S–S bond occurs *via* an electronic excited-state pathway. Whilst a dissociation on the electronic ground state is theoretically possible *via* a large enough vibrational excitation, this is unlikely to occur due to a small transition probability between the initial lower vibrational states and these higher vibrational states on the electronic ground state. To investigate the idea of an electronically excited-state dissociation further, a series of quantum calculations were carried out by Luo *et al*. on dimethyl disulfide (DMDS / CH$_3$SSCH$_3$), the structure of which is shown in Figure 6.1a.[127]

These calculations, which used CASSCF theory and the cc-pVTZ basis set, showed that the initial hypothesis was correct. When looking at the potential-energy surface (PES) of DMDS in ground state, the energy of the system increased as the S–S distance increased, keeping the molecule together. Yet, when an electron was excited from the ground-state highest occupied molecular orbital (HOMO) to the ground-state lowest unoccupied molecular orbital (LUMO) the potential energy of the system rapidly decreased as the bond lengthened, favouring the dissociation. Something similar was observed as the S–C bond length was increased, though there is an energy barrier in the excited state that must first be overcome for the S–C bond to dissociate. This explains why one only observes the dissociation of the S–C bond above a certain photon energy threshold.
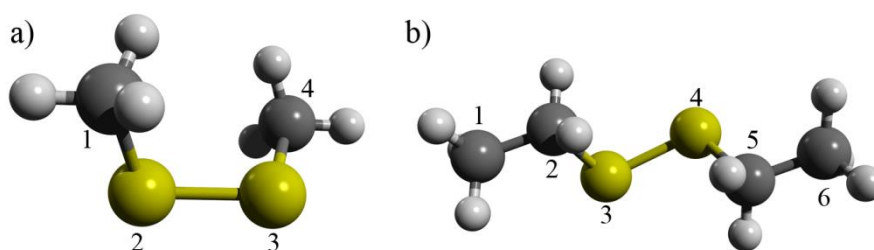
Figure 6.1: Molecular structure of a) dimethyl disulfide, and b) diethyl disulfide, with important atoms numbered.

Whilst these calculations were carried out for DMDS, Bookwalter *et al*. showed that several other aliphatic molecules containing S–S bonds had similar dissociations properties. Of particular interest was diethyl disulfide (DEDS, shown in Figure 6.1b), which had a larger relative yield of S–S dissociations, compared to S–C dissociations, when using the lower energy photons (nearly twenty times more than was observed for DMDS).[129] However, Barone *et al*. showed that, in any case, DMDS still has a high quantum yield, detecting 1.65 ± 0.38 $^\bullet$SCH$_3$ radicals for every photon absorbed after irradiating DMDS with a 248 nm pulsed excimer source.[130]

Whilst DMDS has already been shown to be a suitable candidate for GED, with its structure determined by Bauer *et al*.,[131] along with that of methyl ethyl disulfide (MEDS, a molecule similar in structure to that of DEDS), this section of the thesis will focus on calculations to investigate the possibility of using these molecules for TRED studies. First, calculations similar to those performed by Luo *et al*. will be carried out to look at and better understand the potential-energy surfaces for DMDS

and DEDS, as they go through the dissociation of S–S and S–C bonds, before simulations will be performed to show what is likely to be observed in TRED studies. These simulations will include molecular dynamic calculations to predict the expected dissociation time, and a prediction of the radial distribution curves that would be obtained from a diffraction experiment.

6.2. Static quantum calculations

A series of "static" calculations were carried out for DMDS and DEDS to obtain the ground-state geometries and vibrational frequencies for each molecule, before performing PES scans for the S–S and S–C dissociations. The calculations described here were carried out using the B3LYP[97–99] method and 6-31G* basis set[132] with the Gaussian 09 program.[108] As mentioned, the work by Luo *et al*. used a larger basis set (cc-pVTZ), though here we are only interested in quickly recreating the calculations for our own understanding of the system, and this level of theory will be more than sufficient for the molecular dynamic simulations that will be discussed in Section 6.4.

Previous electron diffraction studies by Bauer *et al*. indicated that there was only one conformer of DMDS present in the gas phase and so, in this case, only one conformer was investigated. However, for MEDS, Bauer *et al*. identified the potential for multiple conformers depending on the SS–CC dihedral angle present in the molecule. These conformers generally appeared every 60° (*i.e.* 0°, 60°, 120°, 180°, 240°, and 300°) when rotating about the SS–CC dihedral angle. As there are two SS–CC dihedral angles within DEDS (*i.e.* between atoms 1–2–3–4 and 3–4–5–6 in Figure 6.1b), this leads to 36 (= 6^2) possible ground-state structures. This therefore had to be taken into account in determining the ground-state structure. By carrying out calculations for each of the possible conformers at the B3LYP/6-31G* level of theory, it was found that each initial geometry would converge to one of six unique conformers; three with C_2 symmetry and three with C_1 symmetry. All of these conformers were confirmed to be real ground-state structures, with all of their vibrational frequencies being real. These conformers have been summarised in Table 6.1.

Table 6.1: Summary of the potential conformers of DEDS that are likely to be present at room temperature.

Conformer	Symmetry	Dihedral angle 1 / degrees	Dihedral angle 2 / degrees	Energy / Hartrees	ΔG / kJ mol^{-1}	Multiplicity	% abundance
1	C_2	67.4	67.4	-954.702822	0.000	2	24.5
2	C_2	176.9	176.9	-954.701720	2.894	2	7.4
3	C_2	287.2	287.2	-954.700324	6.559	2	1.6
4	C_1	292.3	173.6	-954.701710	2.920	1	14.7
5	C_1	67.3	177.1	-954.702281	1.421	1	27.2
6	C_1	66.2	291.8	-954.702189	1.662	1	24.6

As DMDS and DEDS are volatile at room temperature,[131] the number of molecules of conformer i, N_i, compared to the total number of molecules, N, at room temperature was calculated using the Boltzmann distribution equation seen in Equation 6.1.

$$\frac{N_i}{N} = \frac{\exp\left(-\dfrac{\Delta G_i}{RT}\right)/h_i}{\sum_i \exp\left(-\dfrac{\Delta G_i}{RT}\right)/h_i} \ , \qquad \text{Eq. 6.1}$$

where ΔG_i is the Gibbs free energy difference of conformer i with respect to the lowest energy conformer, R is the gas constant, T is the temperature of the experiment, and h_i is the multiplicity of conformer i. By knowing N_i, it was possible to obtain the relative percentage abundance of each conformer that would be expected in the diffraction experiment. This information will also be used to predict the ground-state radial distribution curves of DEDS later in this chapter.

With the ground-state properties of both molecules having been investigated, a quick look at the excited-state energies was attempted. For these investigations the TD-DFT method, discussed in Section 2.3.4, was used to obtain an approximation of the excitation energy for each molecule. In these calculations the first five singlet excited energy levels were taken into account, but with optimisations focussing on the first excited state (*i.e.* the resultant product from the HOMO to LUMO transition). Again these calculations were carried out using the B3LYP/6-31G* method and basis set. Here, the calculations suggested that the excitation energies for both DMDS and DEDS were around 452 kJ mol^{-1}, which is equivalent to an excitation from a laser with a 266 nm wavelength. This suggests that both molecules

would be perfect to investigate with the current TRED set-up as the predicted wavelength falls within the bandwidth of the 267 nm light produced by the third harmonic of the ultrafast Ti:Sapphire laser, and is of a similar energy to the experimentally observed absorption at 250 nm for DMDS.[133] The molecules would be excited into the S_1 state, with very little extra energy being put into the system (assuming single-photon excitations).

As well as being able to predict the structure and energy levels of the molecules with these calculations, the appearance of the molecular orbitals can also be investigated. Figure 6.2 shows both the HOMO and LUMO molecular orbitals for both DMDS and DEDS. In it one can see the bonding σ orbital between the two sulfur atoms in the HOMO, which becomes an anti-bonding orbital in the LUMO. This again confirms the idea that the bond will stretch and likely break in the excited state.
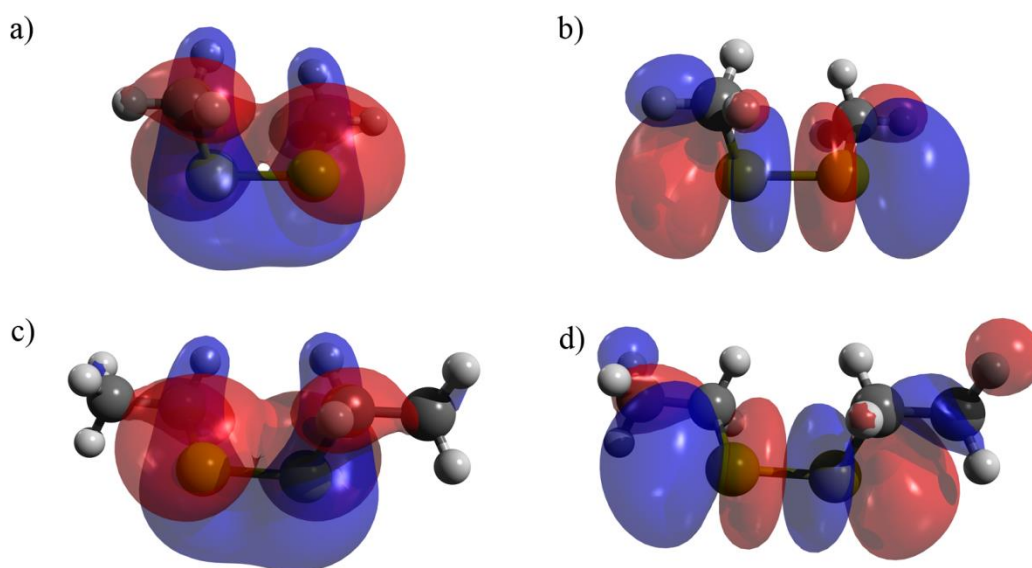
Figure 6.2: The HOMO (a and c) and LUMO (b and d) orbitals of DMDS (top) and DEDS (bottom) showing strong bonding nature in the HOMO and anti-bonding in the LUMO across both the S–S and S–C bonds.

6.3. Potential energy surface scans

To see how the energies of both DMDS and DEDS change in the ground and excited states a series of PES scans were carried out. CASSCF was initially used for this work,[101] as it allows the user to optimise the molecular orbitals that are involved in the electronic transitions, and hence allow us to compare results to those found by

Luo *et al.*[127] However, due to restrictions in CASSCF being implemented in Newton-X (the program later used for molecular dynamic simulations), PES scans were also carried out using DFT (B3LYP) methods, to see how the results compare. If similar trends were observed in the PES for both methods, then the B3LYP method would be suitable for the molecular dynamic calculations. Once again, these calculations were carried out with a smaller basis set (compared to the work Luo *et al.*) of 6-31G* to save computational time. CASSCF calculations were performed using the MOLPRO[110] quantum chemistry package, whilst the DFT calculations made use of Gaussian 09.[108]

In the CASSCF calculations, the ten-electron nine-orbital (10,9) active space chosen by Luo *et al.* was also implemented for both DMDS and DEDS, starting from their respective ground-state structures. The PES scans show how the energies of the systems in both the ground and first excited states vary as the S−S and S−C bonds are stretched, the results of which are shown in Figure 6.3.
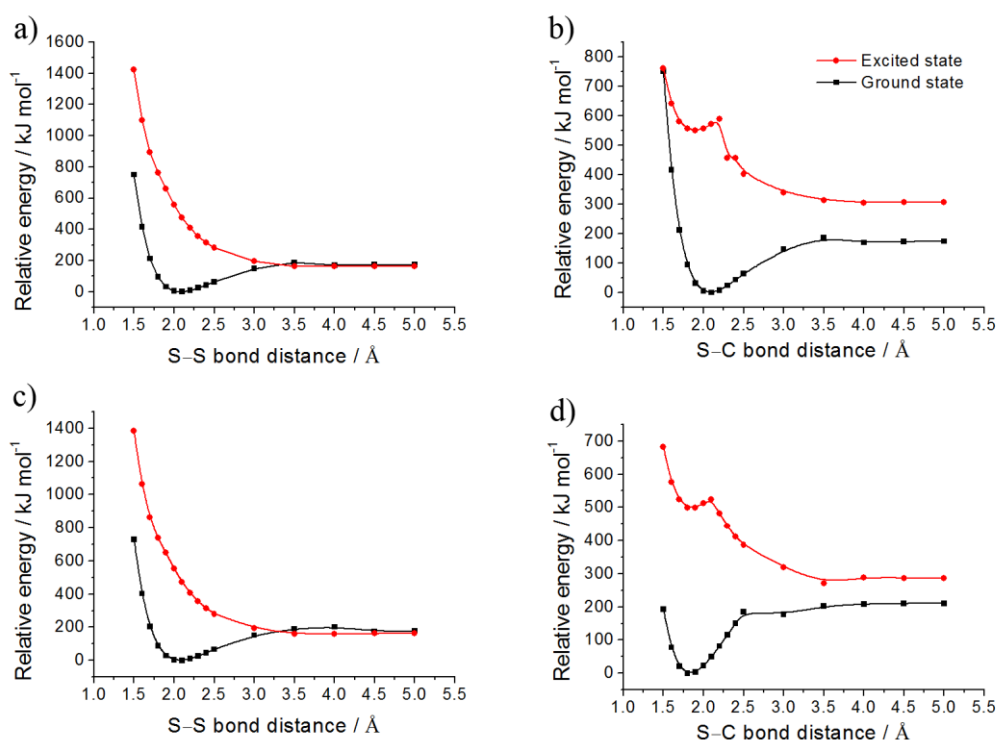
Figure 6.3: Potential energy surface scans for the ground (black) and excited state (red), for DMDS (top two graphs) and DEDS (bottom), during the dissociation of the S−S (a and c) and S−C (b and d) bonds.

For both molecules it can be seen that in the ground state both the S–S and S–C bonds have a minimum energy corresponding to their respective equilibrium bond lengths. However, the potential energy surface for the first excited state for both molecules, with respect to the S–S bond, rapidly drops off in energy, favouring the dissociation of the bond. Also for both molecules we see a small energy barrier with respect to the dissociation of the S–C bond in the excited state, caused by the conical intersection between a bound and dissociative state, which must be overcome for the bond to dissociate. The results seen here for DMDS match the trends seen by Luo *et al.* in their calculations[127] and help to explain the experimental observations for the dissociation of both DMDS and DEDS in the work of Bookwalter *et al.*[129] However, it should be noted that whilst the PESs presented here give an idea of what the likely dissociation pathway may be, they are in fact only a 2-D slice of what is really a multidimensional surface. A more energetically favourable dissociation path may become apparent as the molecule "explores" the excited-state PES.

Meanwhile, the ground-state PES for both molecules were re-investigated with the standard B3LYP (DFT) method, whilst the excited state was re-investigated with the TD-DFT / B3LYP method, taking into account the first five singlet excitations, and optimising for the first excited state. Whilst slightly different energies are produced from these calculations compared to the CASSF calculations (as would be expected from using different methods), overall the same trends as described above were observed. This gave confidence that the B3LYP method would be suitable for carrying out the molecular dynamic simulations.

6.4. Molecular dynamic calculations

Having an idea of the time it takes for a chemical reaction to occur is obviously an important factor in TRED, and so a series of Newton-X calculations were carried out to obtain an estimate of the time it takes for each molecule to dissociate. These calculations first required a basic geometry, and force constants, both taken from the ground-state calculations discussed in the Section 6.2. From the information inputted, Newton-X creates a series of unique expected geometries, which act as starting points for the molecular dynamics simulations. This allows the simulation to take into account the possibility that the "experiment" may start (*i.e.* the point at which a molecule becomes excited) from different points throughout the vibration cycle of the molecule. For DMDS and DEDS, ten different starting geometries were

used to obtain an average dissociation time for the molecules. Calculations were set to run for up to 100 fs, in steps of 0.5 fs (*i.e.* 200 steps in total), and would end when either all steps had been run, or when the distance between two sulfur atoms had increased beyond 3 Å, enough for it to be considered broken and unlikely to recombine with the added kinetic energy of the stretching.

Whilst in reality the experiment would take place at room temperature (as both molecules have a high enough vapour pressure to enter the gas phase at room temperature), the Andersen isotherm was switched off and the simulations run at $T = 0$ K. This was due to the fact that the isotherm keeps the simulated temperature in check *via* a series of collisions that redistribute the kinetic energy of the system. As the dissociation of a bond produces a large amount of kinetic energy in the system (which is outside the isotherm's expected energetic distribution) after a collision, the kinetic energy between the two sulfur atoms would be redistributed amongst all the other atoms in the system, and would cause the dissociation to artificially stop. One could tend the collision frequency to zero, but this would mean that the temperature of the system would not be checked, and hence might as well be switched off. This means that all of the structural changes observed here are purely a result of the molecules moving to their respective most energetically favourable position on the PES.

For both DMDS and DEDS it was found that, whilst in the ground state, all of the calculations would run the whole course of the simulation (*i.e.* 100 fs / 200 steps) without any major changes in the structure of the molecules, beyond small changes in the bond angles and dihedral angles. However, it was a different story in the case where the molecules were already in the first excited state. Here, both DMDS and DEDS started to dissociate immediately at the S–S bond, due to the steep potential-energy surface seen in the excited state. In the case of DMDS, the bond is considered broken 28 ± 2 fs (on average) after excitation, and in the case of DEDS, the dissociation time was almost the same, taking on average 30 ± 2 fs to dissociate. In all of the calculations run, there was no observation of the dissociation of the S–C bond. This was mostly due to not enough energy being available in the system to overcome the small energy barrier seen in the PES of the S–C dissociation. Sufficient energy may have been available in the system if the simulations were run

at a non-zero temperature but, due to the nature of the Andersen isotherm, this was not possible.

The timescales predicted here indicate that the dissociation of the S–S bond occurs on a timescale that will be far too fast to be observed with the TRED apparatus in the traditional sense of a "molecular movie". At best, one will be able to observe the initial reactants and end products of the dissociation. However, as a first reaction to "watch" with the apparatus, this situation would be ideal, as one would simply see a "complete" molecule in the diffraction patterns recorded before time zero, and a dissociated molecule (*i.e.* methyl/ethyl sulfide radicals) in the post-time-zero diffraction patterns.

6.5. Theoretical radial distribution curves and conclusions

To ascertain how easily the structural information from the parent molecules, DMDS and DEDS, and their radicals, might be deconvoluted, information from the geometry and frequency calculations discussed in Section 6.2 was used to produce mock radial distribution curves (RDCs) for both molecules, as seen in Figure 6.4. These were produced by inputting the ground-state geometries into the ed@ed[56] electron diffraction analysis package. SHRINK[58] (Section 2.1.2.1) was also used to take into account the expected molecular vibrations that would be associated with each molecule.
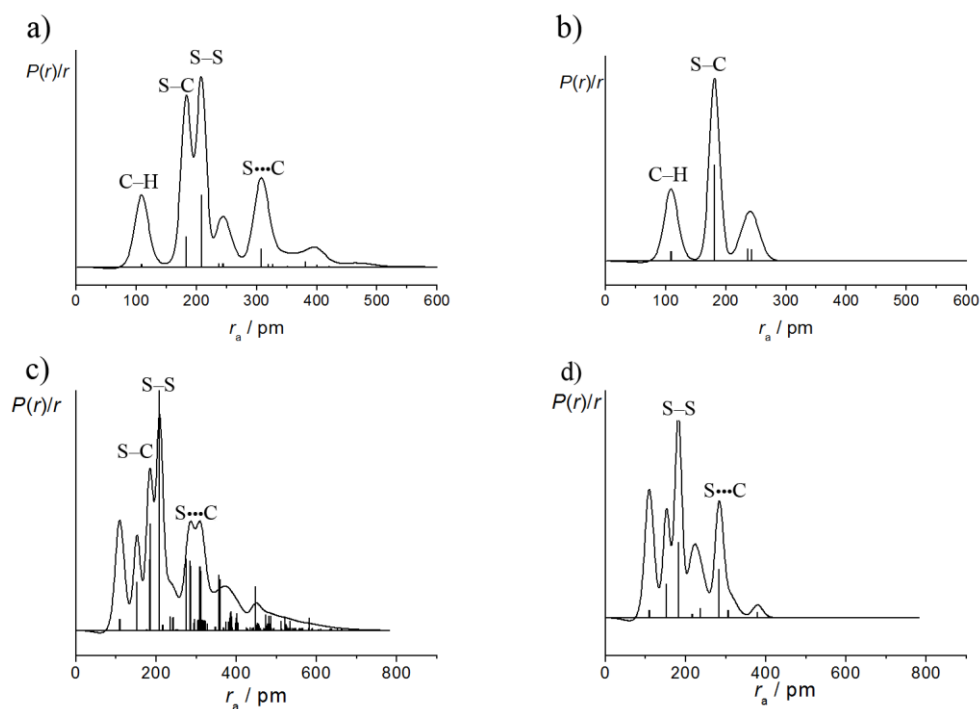
Figure 6.4: Expected radial distribution curves for a) DMDS, b) $^\bullet$SCH$_3$ radical, c) DEDS and d) $^\bullet$SCH$_2$CH$_3$ radical.

As discussed in Section 6.2, only one conformer was likely to be present in DMDS, and this formed the basis for the RDC shown in Figure 6.4a. However, it was predicted that there were up to six unique conformers for DEDS that could be present in the gas-phase experiments. The RDC of DEDS presented in Figure 6.4c, is based on the geometries of conformers 1, 4, 5 and 6 (as labelled in Table 6.1). The other two conformers (2 and 3) were, together, predicted to make up less than 10% of the whole gas sample at the temperature at which the experiment is expected to be carried out and so were omitted. The RDC has been weighted to take into account the likely presence of each of the remaining conformers within the gas sample.

In Figure 6.4b and d, we see the RDC for the radicals $^\bullet$SCH$_3$ and $^\bullet$SC$_2$CH$_3$, the likely products of the dissociations of DMDS and DEDS, respectively. Each radical was created by removing one half of the parent molecule, before full geometry optimisation and frequency calculations were carried out using the same level of theory and method as was used for the respective parent molecule. The output geometry of each radical is suspected to be real as no imaginary frequencies were

observed. The RDCs of each radical were then produced using the method described at the beginning of this section.

Looking at Figure 6.4a and c, one can clearly see peaks in each curve relating to the bonded C–H ($r_a \approx 110$ pm), S–C ($r_a \approx 190$ pm), and S–S ($r_a \approx 210$ pm) interatomic distances of each molecule (with an added C–C bond in Figure 6.4c at $r_a \approx 150$ pm for DEDS). One can also see the long range S$\cdots$C interaction occurring across the disulfide bridge (*i.e.* S–S–C [or atoms 1–2–3 / 2–3–4 in Figure 6.1a for DMDS and 2–3–4 / 3–4–5 in Figure 6.1b for DEDS]) at $r_a \approx 310$ pm in each molecule, with a second peak occurring close by at $r_a \approx 280$ pm in DEDS caused by the S–C–C interatomic distance (*i.e.* atoms 1–2–3 / 4–5–6 in Figure 6.1b). There are also a number of other peaks beyond $r_a \approx 350$ pm, relating to long interatomic distances that occur from scattering between atoms that sit on opposite sides of the disulfide bridge in both molecules. As an added observation, Figure 6.4a shows a strong resemblance to the RDC produced by Bauer *et al.* from their refinement of gas-phase DMDS by electron diffraction,[131] adding weight that these predictions are correct.

When the molecules dissociate, we lose much of the long-range scattering information, as seen for the RDCs of the radical species in Figure 6.4b and d. There is no longer a peak relating to the S–S bond in either molecule, nor the longer S$\cdots$C interaction distance for either of the molecules. The long-range interactions seen past $r_a \approx 350$ pm are also completely lost in both molecules (albeit with a small peak at $r_a \approx 380$ pm in $^{\bullet}$SCH$_2$CH$_3$ attributed to the long-range S$\cdots$H interactions).

This stark loss of information in the RDC for the dissociated molecules would make it very easy to be able to determine whether or not either molecule had dissociated. The fact that the reactions occur on fast timescales almost makes things easier as well, as recorded information would appear in an on/off nature, as the electron probe in the experiment crosses the time-zero position.

However, it should be noted that in these RDCs it has been assumed that each molecule of DMDS and DEDS will dissociate directly into the $^{\bullet}$SCH$_3$ and $^{\bullet}$SCH$_2$CH$_3$ radicals; in reality challenges will arise. As Barone *et al.* showed, whilst DMDS has a high quantum yield, not every molecule will dissociate, leaving behind some DMDS/DEDS molecules intact. There is also the chance that some molecules will

cleave at the S–C bond instead (this is more likely for DMDS than DEDS). All of these events will lead to "noise" occurring in the diffraction patterns of the dissociated molecules post the time-zero position of the experiment, which will have to be taken into account.

All in all the expected results point towards DMDS and DEDS being suitable candidates for initial TRGED studies with the new apparatus. With the added fact that, to observe dissociations, one does not necessarily need to cool the molecule by supersonic expansion to get a clear idea of what is going on, it simplifies the experimental procedures down to being able to use a simple pulsed nozzle delivery system.

Chapter 7. Conclusions and future work

This thesis has shown the successful construction of a novel pulsed-beam electron diffractometer, which will be used for the investigation of ultrafast molecular dynamics. Whilst time-resolved electron diffraction experiments have not yet been performed, significant progress, outlined in Chapter 5, has been made towards this goal. One can consider the apparatus to be commissioned, and ready for future experimental research projects.

In the rest of this concluding chapter, I will give a personal perspective on the future experiments that could be carried out, and further examples of molecules that could be investigated using the TRED apparatus. I will discuss how to take the machine forward from here in terms of new or upgraded equipment that could be implemented into the current design. I will also discuss methods that could improve the beam simulations discussed in Chapter 4, as well as progress with other projects relating to my PhD work that are currently being undertaken within the Wann group by MChem students and others.

7.1. Towards time-resolved electron diffraction

In the short term, the Wann group has secured a second loan of a femtosecond laser from the Laser Loan Pool until June 2015. With the experimental set-up described in Chapter 3 still assembled, immediate focus will be to re-optimise the electron beam, and complete the final calibration experiments. This will involve carrying out further solid-state diffraction experiments to more accurately determine certain parameters of the apparatus, such as the *s* range of the detector, as was discussed in Section 5.4. These experiments will not only examine polycrystalline platinum again, but new thin-film polycrystalline samples of gold and aluminium will also be investigated (prepared with the help of Dave Coulthard, from the Department of Physics at the University of York), so as to observe diffraction from multiple scattering sources.

Work will also be carried out towards obtaining more efficient scattering from gas samples, by implementing a simple pulsed nozzle into the apparatus, as briefly discussed in Section 5.4.2. With the pulsed nozzle, gas diffraction experiments can be run in such a way so as to optimise the amount of scattering observed from the sample, whilst allowing for sufficient extraction of any gas that enters the apparatus

by the vacuum system. Again, early proof of concept experiments will involve scattering electrons from argon, before attempting to observe molecular scattering from standard GED samples like CCl_4 and benzene. Once this has been completed work will tend towards carrying out full TRGED experiments. As was shown in Chapter 6, both DMDS and DEDS are perfect candidates for this, where one looks for the loss of longer interatomic distances in the radial distribution curve as the disulfide bridge dissociates in the excited state.

To observe more subtle gas-phase structural changes, such as those resulting from molecular isomerisations, the simple pulsed nozzle will not suffice, as samples will most likely need to be vibrationally cooled. Plans have already been put in place to incorporate a more sophisticated supersonic expansion system towards the end of the Laser Loan Pool period to achieve this. Literature and computational investigations of suitable candidates for these experiments have already begun within the Wann group, with select potential candidates being discussed further in Section 7.3.

In any downtime between diffraction experiments, further electron beam calibration experiments can be carried out to expand on what has been presented in Chapter 5. For example, the width of the electron beam could be measured at several other points between the anode and the detector, rather than just at the sample position. Alternatively, the properties of the electron beam could be measured for a combination of different apertures sizes, photocathode-to-anode distances and acceleration potentials. All of the results from this work can be compared to the theoretical simulations presented in Chapter 4, furthering our understanding of how a pulsed electron beam behaves under different initial conditions.

As was shown in Section 3.3.2.2, an experimental set-up was established to allow for the duration of an electron pulse to be measured with the use of the grating-enhanced ponderomotive technique. However, as one will note, no experimental results were reported in this thesis. Whilst Section 5.3 showed the successful crossing of the electron and laser beams in both time and space (which was achieved with both branches of the ponderomotive set-up) the main problem lay with the sensitivity of the detector system being used at the time (a simple phosphor screen, similar to that shown in Figure 3.16a). As implied, the MCP / phosphor screen set-up, seen in Section 3.2.5, had not yet been installed when these experiments were being carried out. This would have provided the necessary sensitivity to observe the

small perturbations in the transverse profile of the electron beam caused by the ponderomotive force. However, once the new detector had been installed focus shifted to collecting diffraction data, as time was limited at the end of the Laser Loan Pool period. The author is confident that with the new detector set-up, over the next Laser Loan Pool period the duration of the electron pulse will be measured.

7.2. Magnetic lens and related beam simulations

One of the major limiting factors with the magnetic lens described in Section 3.2.8 is that it can only be run for around 30 minutes before its core temperature reaches a level that may cause the Kapton coating around the wires to melt. This is likely due to the main body of the lens being manufactured out of iron, which has poor thermal conductivity. Therefore, a new magnetic lens, shown pictorially in Figure 7.1, has been designed in conjunction with summer / MChem student Conor Rankine, and is currently being built by the mechanical workshop in the Department of Chemistry at the University of York.
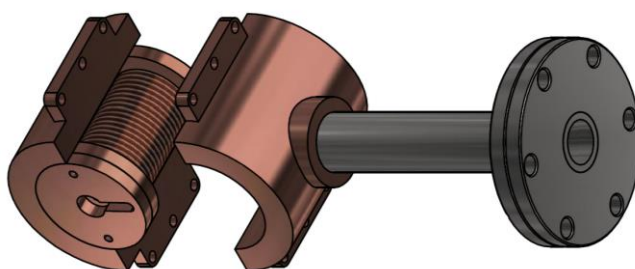
Figure 7.1: CAD drawing of the new magnetic lens for the TRED apparatus, designed by Conor Rankine.

This new magnetic lens still has an iron core as part of its central spool, but the sides are now made of copper to help to draw heat away from the lens. The magnetic lens is also enclosed in a copper casing, attached to a hollowed mount (also seen in Figure 7.1), allowing for coolant (water / liquid nitrogen) to reach the casing and cool the lens further if proven necessary. Whilst the same number of turns of wire are to be used on this lens as for the previous iteration (*i.e.* 1,000), the wire will be thicker, and hence have a lower resistance, preventing the lens from heating up as quickly. To reduce potential heating even further, the lens has been made longer, so that it acts on the electron pulse over a longer period of time, reducing the number of layers of wire and allowing heat to escape from the core of the lens more easily.

Due to the many differences between this lens and the original version, further GPT simulations have been started, taking into account experiences that have been obtained from the work presented in Chapter 4. Where the previous model made the approximation that the lens could be represented by a single solenoid, which in turn caused the electron beam to be focussed more extremely than what was observed in reality, the new model accounts for the layered feature of the wires in the lens. As a test, this new model was used to simulate the lens already present in the apparatus, described in Section 3.2.8. Figure 7.2 shows the predicted transverse FWHM beam size of a pulse containing 10^4 electrons at the sample position, as predicted by both the old and new models, when produced from a 45 kV, 400 μm aperture, 15 mm photocathode-to-anode distance electron gun, with the centre of the magnetic lens placed 60 mm from the anode, and with various currents passing through it. As a comparison to what was observed with the real TRED apparatus in Section 5.2.2.2, the measured beam widths from the experimental set-up that most closely resembles the simulations (*i.e.* 45 kV 1,000 μm aperture, 17 mm photocathode-to-anode distance electron gun) have also been included.
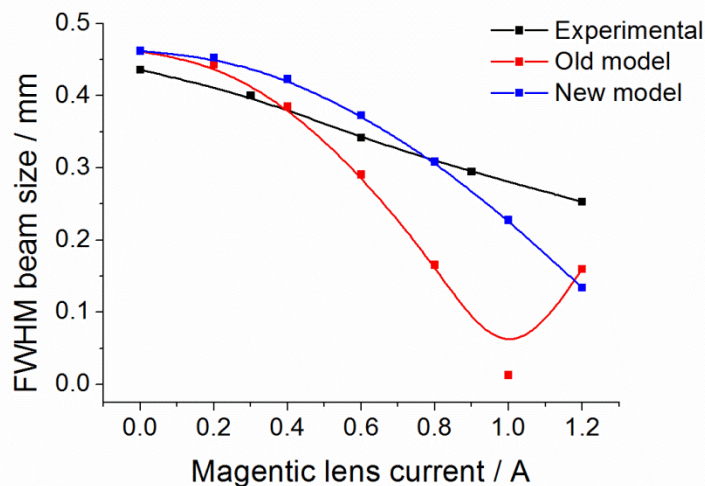
Figure 7.2: Electron beam width under the influence of different magnetic lens currents, observed experimentally (black) and simulated using the old (red) and new (blue) magnetic lens models.

As one can see from Figure 7.2, on increasing the current in the lens, the new model does not predict the focussing of the electron beam to occur as steeply as for the original model. The results from the new model are also closer to the

experimentally observed results, with no over-focussing being observed, yielding beam widths that are closer to those observed experimentally. Deviations from the experimentally observed results are clear though, with the experimental beam width still appearing to reduce linearly with lens current. This may be due to the lens in the simulations having perfect windings, whilst the real lens will have imperfect windings, causing the position of each layer to be different than that seen in the model. However, the results show that the new model is a step in the right direction to more accurate simulations.

Further simulations using this new model are now being carried out within the Wann group for the new magnetic lens, in a similar style to those seen in Chapter 4, so far predicting that it will have similar focussing capabilities to the old lens. Other simulations that are ongoing are concerned with predicting how the electron beam would respond to being focussed by two separate magnetic lenses. This will investigate the ideas discussed in Section 4.3.2.1, where the first lens can be used to tightly focus the electron beam at the sample to obtain an optimal time resolution, and the second lens can be used to counter the effects of over-focussing, to obtain higher spatial resolution at the detector.

7.3. Future molecules of interest

7.3.1. Azobenzene

Azobenzene,[134,135] as shown in Figure 7.3, consists of two phenyl rings, joined by a nitrogen double-bonded bridge, and undergoes a *trans–cis* isomerisation *via* a photo-reversible π-π* transition, a reaction commonly seen as a model "molecular switch".[136]
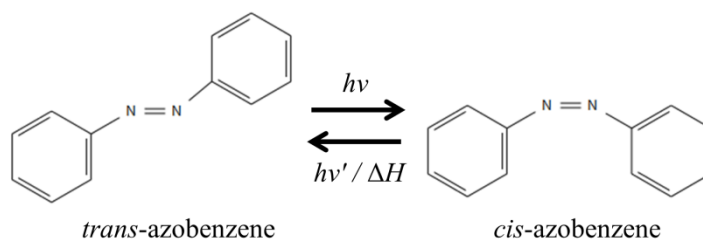
Figure 7.3: *Trans-cis* isomerisation of azobenzene.

However, the time it takes to isomerise between the two forms is dependent on any substituent groups attached to the phenyl groups, with isomerisation times ranging

from hundreds of femtoseconds to a few picoseconds.[137,138] The isomerisation pathways, depicted in Figure 7.4a, are also dependent on the substituent group, with structural changes either occurring *via* a single inversion (angle θ) or a two-stage rotation (angles τ_1 and τ_2).[136] In some substituted azobenzenes, dative bonds that occur between the nitrogen atoms and the substituted group give rise to the potential of the molecule first undergoing a "pedal motion" to an alternate *trans* structure (shown in Figure 7.4b) to alleviate energy before isomerising to the *cis* state.[139,140]
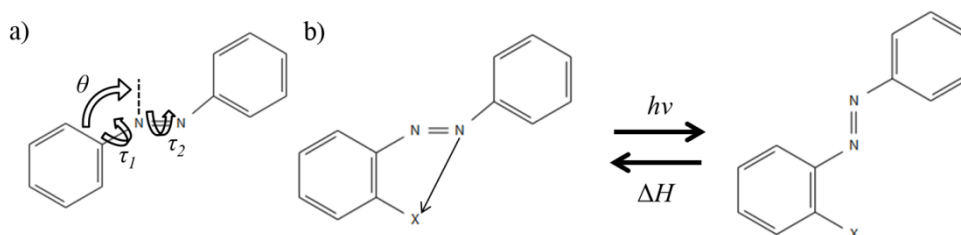
Figure 7.4: Diagrams showing a) the *trans–cis* isomerisation pathways of azobenzene, and b) the pedal motion of substituted *trans*-azobenzene.

As azobenzene has already been shown to be a suitable candidate for GED experiments,[141] the presence of different pathways for different substituted molecules, allows for plenty of interesting studies to be carried out. As well, once in the *cis* state, azobenzene is relatively stable; it can only revert back to the *trans* form *via* a photo-reversible reaction, or through heat loss upon a collision event with another molecule. As either of these events are unlikely to occur on the timescale over which a TRED experiment observes the molecules, azobenzene is unlikely to revert back, allowing for the excited-state transition process and changes in structure to be studied in detail.

7.3.2. Dimethylaminobenzonitrile

Dimethylaminobenzonitrile (DMABN), shown in Figure 7.5, follows on from azobenzene with the idea of studying model molecular switches. However, while for azobenzene only a structural change is observed, DMABN undergoes a structural change and a twisted intramolecular charge transfer (TICT).[142]
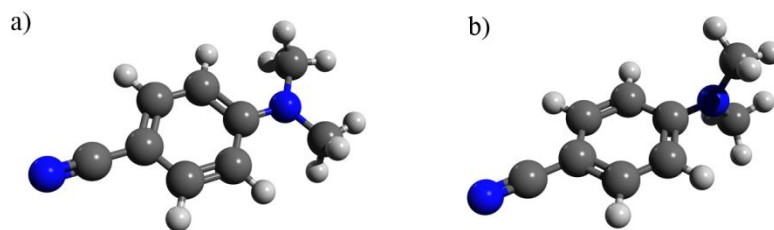
Figure 7.5: Diagram showing a) the off-planar and b) twisted forms of DMABN.

Upon excitation using a UV light source, the initially off-planar DMABN molecule (exhibiting a small angle between the planes of the dimethylamino group and phenyl ring) seen in Figure 7.5a, undergoes an intramolecular charge transfer that occurs on the picosecond timescale,[143] causing it to obtain a slight dipole character. Once in this excited state, the PES of the molecule no longer favours the off-planar structure,[144] and, if free to do so (as is the case in the gas phase), it starts to twist so that the plane of the dimethylamino group becomes perpendicular with respect to the rest of the molecule, as depicted in Figure 7.5b. This isomerisation is accompanied by a larger charge transfer, with the molecule obtaining a larger dipole character than that observed in the ground state, providing the possibility for further novel molecular switch properties. The rate at which charge is transferred, and the amount of twisting observed, can be modified with the addition of other substituent groups to the molecule.[143–145]

Already the Wann group have carried out a number of quantum chemical calculations to better understand the nature of the twisting motion in DMABN, predicting that, in the gas phase, it takes several picoseconds after the molecule enters the excited state before the molecule settles in the twisted state. However, further work is needed to decide whether it is best to have substituent groups attached to the molecule, which have higher scattering factors than the carbon and nitrogen atoms found in the parent DMABN molecule, to help highlight the twisting motion. In the meantime, progress is being made with the Wann group time-averaged diffraction apparatus to carry out the first time-averaged diffraction analysis of DMABN, which is an important prerequisite for full TRED studies.

7.3.3. Dithiane

In Chapter 6, it was discussed how disulfide bridges play an important role in the structures of protein molecules,[125–127] and how DMDS and DEDS are simple molecules that allow for this S–S bond to be studied with relative ease. However, we saw that these molecules readily dissociated upon excitation using ultraviolet light; an occurrence that is not often observed in proteins. Dithiane, a ringed disulfide-bridge-containing structure, shown in Figure 7.6, is a molecule that is likely to model the disulfide bridges seen in proteins more accurately than DMDS / DEDS.[146]
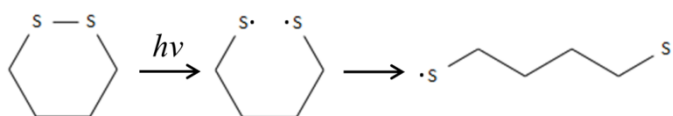
Figure 7.6: Dithiane molecule undergoing structural changes after photoexcitation. The image is redrawn from an image in Ref. 146.

Like its linear counterparts, the disulfide bridge in dithiane will start to dissociate after irradiation by a UV light source, although the rate at which this occurs, and the likelihood that it completes, is much less. As shown in Figure 7.7, once on the excited-state surface, above the ground-state minimum, the disulfide bridge will start to dissociate as it tends to the lowest energy point on that surface. Yet unlike DMDS/DEDS, at larger S–S distances, the energy of the excited state starts to increase again and tends towards that of the ground state at a conical intersection. This is caused by the ring structure of the dithiane molecules becoming strained at larger S–S distances, resisting the dissociation of the bond and forcing the atoms back together. If enough energy is supplied to the system it can overcome this barrier and the bond will break, converting the ring to a straight-chain structure.
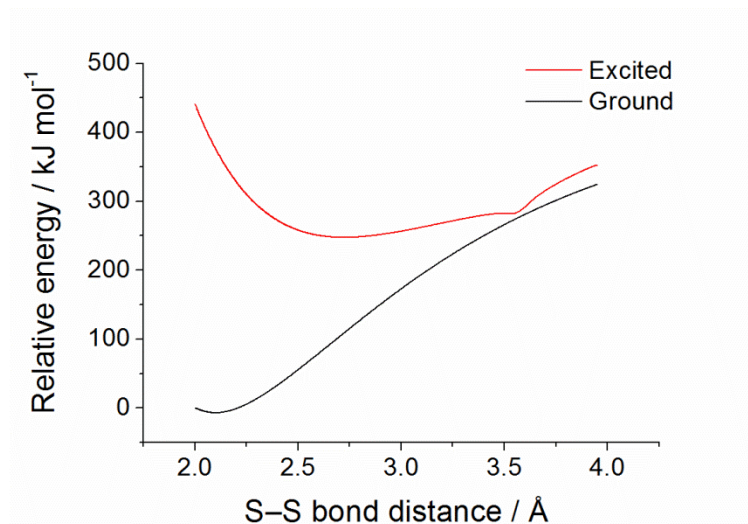
Figure 7.7:Figure showing the potential energy surfaces of the ground and excited states of dithiane. [Calculations were performed by Robin Virgo, using Gaussian 09 B3LYP /6-31G(d,p).]

On the other hand, if the molecule does not unravel and instead decays to back the ground-state PES, the structure will relax and return to the unstrained ring structure. All of these processes are predicted to occur on the picosecond timescale,[146] and with the added fact that there are multiple reaction end products, and a relatively stable intermediate between the two, it makes dithiane an interesting subject for TRED. Currently, computational work on the molecule is being carried out in the Wann group by MChem student Robin Virgo, including performing novel Newton-X calculations, which will hopefully shed more light on the dynamics of the system, helping to predict what might be observed in the TRED experiments performed using the supersonic expansion set-up.

7.4. Other projects

7.4.1. Electron beam coherence studies

As discussed in Section 2.2.6.7, the electron beam produced from a thin-film photocathode is not as spatially coherent as those produced from other sources, such as ultracold gases or metallic nanotips. However, whilst current plans for experiments for the new TRED involve looking at small isolated molecules, short coherence lengths are not a major issue. It only becomes an issue when looking at larger molecules, such as proteins or nanoparticles, where one looks at the overall general structure rather than studying specific interatomic distances. If the

information provided by an electron diffracting from one region of the sample is not coherent with the information from an electron from another region of the sample, then the collected data are worthless. This coherence problem applies to electron microscopy as well as that of diffraction, and so therefore further research into the coherence of pulsed electron beams is needed.

With Will Bryan from the Department of Physics at Swansea University, the Wann group has carried out novel experiments to study the coherence of pulsed electron beams at the Central Laser Facility, within the Rutherford Appleton Laboratories.[50] The author spent two weeks there working on this project in the summer of 2013. These experiments implemented the grating enhanced ponderomotive technique to determine the temporal and spatial properties of the electron beam *via* electron holography experiments, as shown pictorially in Figure 7.8.
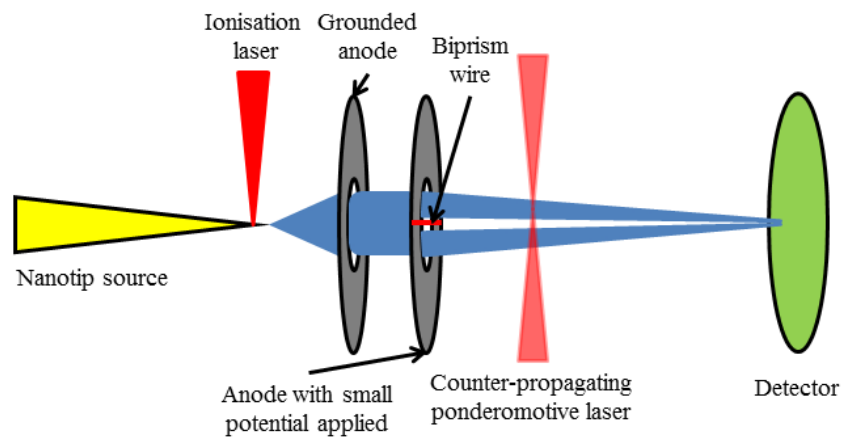
Figure 7.8: Pictorial representation of the experimental set-up used in electron holography experiments at the Central Laser Facility.

In this experiment, an electron beam produced by the ionisation of a nanotip source, is split in two using a biprism nanowire (held at a small negative potential) before being recombined at a detector by the electrostatic lensing effect of a series of anodes. This electron interferometer allows the electron beam coherence to be measured by analysing the fringes produced by recombining the electron beams at the detector. However, by perturbing one of the electron beam branches after the nanowire using the grating-enhanced ponderomotive technique, one can determine not only the pulse duration of the electron beam but also study how the temporal-

spatial profile of the electron beam varies as a whole. By comparing the fringes produced at the detector when the laser is on and off, one can see how the spatial properties of the electron beam have been perturbed by the counter-propagating laser beams, and how this is linked to the time at which the laser beams interact with the electrons.

So far only preliminary experiments have been carried out in this research project, and it is hoped that, when the equipment necessary for these experiments returns to the Central Laser Facility, full holography experiments will be carried out.

7.4.2. Electron microscopy

There are many parallels between TRED and ultrafast electron microscopy in terms of how the electrons are generated with the use of ultrafast lasers and the pump-probe methodology used to observe structural changes. Therefore, it is of no surprise that some electron diffraction groups carry out work in both fields.[45,46] A new joint project with Professor Jun Yuan of the Department of Physics at the University of York, will allow the Wann group to also expand into this field, generating a new UEM apparatus, using the knowledge of novel apparatus design and pulsed electron beams obtained from this project.

However, as microscopy generally involves the examination of larger samples compared to the mostly single molecules investigated with TRGED, transverse beam coherence plays a much more important role. As discussed in the previous section, whilst providing a certain ease of use, the thin-film photocathode used in the apparatus described here is not the most coherent electron beam source available. Therefore this new apparatus will most likely make use of a nanotip electron source, as well as techniques developed for the electron holography experiments described in Section 7.4.1. With both the TRED and UEM machines running alongside each other, there is the opportunity for each technique to benefit from the other, as well as investigate interesting samples by the thorough analysis of two interlinked techniques.

7.4.3. MeV diffraction

As was discussed in the Introduction (Section 1.4), the Wann group has been involved in the commissioning of a relativistic electron diffractometer using the Versatile Electron Linear Accelerator (VELA) at Daresbury Laboratories.[147] This

machine has already yielded time-averaged electron diffraction patterns from a polycrystalline sample of platinum using multiple electron pulses, as well as a pattern recorded using a single electron pulse,[43] as shown in Figure 1.4. As mentioned then, this time-averaged single electron pulse diffraction pattern represents an important first step towards carrying out single-shot TRED experiments, allowing one to analyse short-lived / unstable / small quantity samples, which would be difficult to analyse with a table-top set-up. With relativistic electrons and single-shot capabilities, this apparatus has the potential to allow for both the jitter and velocity mismatch problems in the pump-probe set-up to be removed, providing more temporally resolved results. However, this machine is still in its early stages of commissioning, and it will take time before full TRED experiments can be carried out. Coupled with the high cost of each relativistic experiment, there is still a need to further develop the capabilities of table-top TREDs.

Common abbreviations

BBO	barium borate (crystal)
CASSCF	complete active space self-consistent field
DFT	density functional theorem
DEDS	diethyl disulfide
DMABN	dimethylaminobenzonitrile
DMDS	dimethyl disulfide
DUV	deep ultraviolet (viewport)
ECP	effective core potential
FCC	face-centred cubic
FWHM	full-width half maximum
GED	gas electron diffraction
GGA	generalised gradient approximation
GPT	General Particle Tracer
GVD	group velocity delay (crystal)
HF	Hartree-Fock
HOMO	highest occupied molecular orbital
keV	kilo-electron volt
LDA	local density approximation
LUMO	lowest unoccupied molecular orbital
MCP	microchannel plate
MCSCF	multi-configuration self-consistent field
MeV	mega-electron volt
MP	Møller-Plesset
ND	neutral density (filter)
PES	potential energy surface
RASSCF	restricted active space self-consistent field
RDC	radial distribution curve
rms	root mean square
SCF	self-consistent field
SHG	second harmonic generation
SNR	signal-to-noise ratio
THG	third harmonic generation
TICT	twisted intramolecular charge transfer
TOF	time of flight
TRED	time-resolved electron diffraction/diffractometer
TRGED	time-resolved gas electron diffraction/diffractometer
UED	ultrafast electron diffraction
UEM	ultrafast electron mircroscopy

References

1.   T. Reusch, D. Mai, M. Osterhoff, D. Khakhulin, M. Wulff, and T. Salditt, *Phys. Rev. Lett.*, 2013, **111**, 268101.

2.   F. Schotte, M. Lim, T. A. Jackson, A. V. Smirnov, J. Soman, J. S. Olson, G. N. Phillips Jr, M. Wulff, and P. A. Anfinrud, *Science*, 2003, **300**, 1944–1947.

3.   J. B. Hastings, F. M. Rudakov, D. H. Dowell, J. F. Schmerge, J. D. Cardoza, J. M. Castro, S. M. Gierman, H. Loos, and P. M. Weber, *Appl. Phys. Lett.*, 2006, **89**, 184109.

4.   P. Musumeci, J. T. Moody, C. M. Scoby, M. S. Gutierrez, and M. Westfall, *Appl. Phys. Lett.*, 2010, **97**, 063502.

5.   R. Li, W. Huang, Y. Du, L. Yan, Q. Du, J. Shi, J. Hua, H. Chen, T. Du, H. Xu, and C. Tang, *Rev. Sci. Instrum.*, 2010, **81**, 036110.

6.   H. Jean-Ruel, M. Gao, M. A. Kochman, C. Lu, L. C. Liu, R. R. Cooney, C. A. Morrison, and R. J. D. Miller, *J. Phys. Chem. B*, 2013, **117**, 15894–15902.

7.   V. R. Morrison, R. P. Chatelain, C. Godbout, and B. J. Siwick, *Opt. Express*, 2013, **21**, 21–29.

8.   C. Hensley, J. Yang, and M. Centurion, *Phys. Rev. Lett.*, 2012, **109**, 133202.

9.   M. Eichberger, N. Erasmus, K. Haupt, G. Kassier, A. von Flotow, J. Demsar, and H. Schwoerer, *Appl. Phys. Lett.*, 2013, **102**, 121106.

10. B. J. Siwick, J. R. Dwyer, R. E. Jordan, and R. J. D. Miller, *Science*, 2003, **302**, 1382–1385.

11. A. A. Ischenko, V. V. Golubkov, V. P. Spiridonov, A. V. Zgurskii, A. S. Akhmanov, M. G. Vabischevich, and V. N. Bagratashvili, *Appl. Phys. B*, 1983, **32**, 161–163.

12. H. Mark and R. Wierl, *Naturwissenschaften*, 1928, **18**, 778–786.

13. L. de Broglie, *Philos. Mag. Lett.*, 1924, **86**, 411–423.

14. C. Davisson and L. Germer, *Nature*, 1927, **119**, 558–560.

15. G. P. Thomson, *Nature*, 1927, **120**, 802.

16. W. H. Bragg, *Philos. Mag.*, 1920, **40**, 169–189.

17. P. Debye, *Ann. Phys.*, 1915, **46**, 809–823.

18. T. S. Rose, M. J. Rosker, and A. H. Zewail, *J. Chem. Phys.*, 1988, **88**, 6672–6673.

19. J. D. Ewbank, L. Schäfer, D. W. Paul, O. J. Benston, and J. C. Lennox, *Rev. Sci. Instrum.*, 1984, **55**, 1598–1603.

20. J. D. Ewbank, W. L. Faust, J. Y. Luo, J. T. English, D. L. Monts, D. W. Paul, Q. Dou, and L. Schäfer, *Rev. Sci. Instrum.*, 1992, **63**, 3352–3358.

21. B. J. Siwick, *PhD Thesis,* The University of Toronto, 2004.

22. J. C. Williamson and A. H. Zewail, *P. Natl. Acad. Sci. USA*, 1991, **88**, 5021–5025.

23. J. C. Williamson and A. H. Zewail, *Chem. Phys. Lett.*, 1993, **209**, 10–16.

24. J. C. Williamson, J. Cao, H. Ihee, H. Frey, and A. H. Zewail, *Nature*, 1997, **386**, 159–162.

25. H. Ihee, V. A. Lobastov, U. M. Gomez, B. M. Goodson, R. Srinivasan, C. Y. Ruan, and A. H. Zewail, *Science*, 2001, **291**, 458–462.

26. M. Gao, C. Lu, H. Jean-Ruel, L. C. Liu, A. Marx, K. Onda, S.-Y. Koshihara, Y. Nakano, X. Shao, T. Hiramatsu, G. Saito, H. Yamochi, R. R. Cooney, G. Moriena, G. Sciaini, and R. J. D. Miller, *Nature*, 2013, **496**, 343–346.

27. S. A. Hayes, *Personal communication*, 2013.

28. *REGAE: Time-resolved diffraction with relativistic electrons*, http://regae.desy.de, accessed on 15th July 2014.

29. B. J. Siwick, J. R. Dwyer, R. E. Jordan, and R. J. D. Miller, *J. Appl. Phys.*, 2002, **92**, 1643–1648.

30. G. Sciaini, M. Harb, S. G. Kruglik, T. Payer, C. T. Hebeisen, F.-J. M. zu Heringdorf, M. Yamaguchi, M. Horn-von Hoegen, R. Ernstorfer, and R. J. D. Miller, *Nature*, 2009, **458**, 56–59.

31. C. T. Hebeisen, R. Ernstorfer, M. Harb, T. Dartigalongue, R. E. Jordan, and R. J. D. Miller, *Opt. Lett.*, 2006, **31**, 3517–3519.

32. C. T. Hebeisen, G. Sciaini, M. Harb, R. Ernstorfer, T. Dartigalongue, S. G. Kruglik, and R. J. D. Miller, *Opt. Express*, 2008, **16**, 3334–3341.

33. M. Gao, H. Jean-Ruel, R. R. Cooney, J. Stampe, M. de Jong, M. Harb, G. Sciaini, G. Moriena, and R. J. D. Miller, *Opt. Express*, 2012, **20**, 799–802.

34. T. van Oudheusden, E. F. de Jong, S. B. van der Geer, W. P. E. M. Op't Root, O. J. Luiten, and B. J. Siwick, *J. Appl. Phys.*, 2007, **102**, 093501.

35. R. P. Chatelain, V. R. Morrison, C. Godbout, and B. J. Siwick, *Appl. Phys. Lett.*, 2012, **101**, 081901.

36. V. R. Morrison, R. P. Chatelain, K. L. Tiwari, A. Hendaoui, A. Bruhacs, M. Chaker, and B. J. Siwick, *Science*, 2014, **346**, 445–448.

37. J. D. Geiser and P. M. Weber, *SPIE*, 1995, **2521**, 136–144.

38. P. Baum, *Chem. Phys.*, 2013, **423**, 55–61.

39. P. M. Weber, S. D. Carpenter, and T. Lucza, *SPIE*, 1995, **2521**, 23–30.

40. G. H. Kassier, K. Haupt, N. Erasmus, E. G. Rohwer, and H. Schwoerer, *J. Appl. Phys.*, 2009, **105**, 113111.

41. G. H. Kassier, K. Haupt, N. Erasmus, E. G. Rohwer, H. M. von Bergmann, H. Schwoerer, S. M. M. Coelho, and F. D. Auret, *Rev. Sci. Instrum.*, 2010, **81**, 105103.

42. P. A. McIntosh, D. Angal-Kalinin, N. Bliss, S. Buckley, J. Clarke, G. Diakun, A. Gallagher, A. Gleeson, A. Goulden, C. Hill, S. Jamison, J. Jones, T. Jones, A. Kalinin, B. Martlew, J. McKenzie, B. Militsyn, K. Middleman, A. Moss, L. Nicholson, T. Ng, M. Roper, B. Shepherd, R. Smith, S. Smith, N. Thompson, A. Wheelhouse, and C. White, *Proc. IPAC2012*, 2012, 4074–4076.

43. M. Surman, P. Aden, R. J. Cash, J. A. Clarke, D. M. P. Holland, J. W. McKenzie, M. D. Roper, W. A. Bryan, P. D. Lane, D. A. Wann, and J. G. Underwood, *Proc. IPAC2014*, 2014, 2218–2220.

44. *Electron Diffraction on VELA*, http://www.stfc.ac.uk/astec/44772.aspx, accessed on 11th December 2014.

45. U. J. Lorenz and A. H. Zewail, *P. Natl. Acad. Sci. USA*, 2013, **110**, 2822–2827.

46. R. M. van der Veen, A. Tissot, A. Hauser, and A. H. Zewail, *Phys. Chem. Chem. Phys.*, 2013, **15**, 7831–7838.

47. M. Centurion, P. Reckenthaeler, S. A. Trushin, F. Krausz, and E. E. Fill, *Nat. Photonics*, 2008, **2**, 315–318.

48. J. Yang, V. Makhija, V. Kumarappan, and M. Centurion, *Struct. Dyn.*, 2014, **1**, 044101.

49. J. Yang and M. Centurion, *arXiv preprint arXiv:1410.6429*, 2014, 1–22.

50. A. R. Bainbridge, D. Thorne, W. A. Bryan, R. Chapman, P. Rice, E. Springate, P. D. Lane, M. S. Robinson, S. Young, and D. A. Wann, *Coherence studies of pulsed electron beams from point sources*, https://www.stfc.ac.uk/clf/resources/PDF/ar12-13_full_lsf_physics.pdf, 2013.

51.   A. R. Bainbridge and W. A. Bryan, *New J. Phys.*, 2014, **16**, 103031.

52.   A. Mustonen, P. Beaud, E. Kirk, T. Feurer, and S. Tsujino, *Appl. Phys. Lett.*, 2011, **99**, 103504.

53.   A. J. McCulloch, D. V. Sheludko, S. D. Saliba, S. C. Bell, M. Junker, K. A. Nugent, and R. E. Scholten, *Nat. Phys.*, 2011, **7**, 785–788.

54.   T. Elsaesser and M. Woerner, *Acta Crystallogr. A*, 2010, **66**, 168–178.

55.   I. Hargittai and M. Hargittai, *Stereochemical Applications of Gas-Phase Electron Diffraction - Part A*, VCH Verlagsgesellschaft mbH, Weinheim, 1988.

56.   S. L. Hinchley, H. E. Robertson, K. B. Borisenko, A. R. Turner, B. F. Johnston, D. W. H. Rankin, M. Ahmadian, J. N. Jones, and A. H. Cowley, *Dalton Trans.*, 2004, 2469–2476.

57.   Y. Morino, S. J. Cyvin, K. Kuchitsu, and T. Iijima, *J. Chem. Phys.*, 1962, **36**, 1109–1110.

58.   V. A. Sipachev, *J. Mol. Struct.-Theochem*, 1985, **121**, 143–151.

59.   D. A. Wann, A. V Zakharov, A. M. Reilly, P. D. McCaffrey, and D. W. H. Rankin, *J. Phys. Chem. A*, 2009, **113**, 9511–9520.

60.   D. J. Romenesko, T. C. Wong, and L. Bartell, in *Molecular Structure by Diffraction Methods*, eds. G. A. Sim and L. E. Sutton, The Chemical Society, Volume 3, 1975, pp. 72–80.

61.   P. B. Liescheski and D. W. H. Rankin, *J. Mol. Struct.*, 1989, **196**, 1–19.

62.   R. Blom, S. Cradock, S. L. Davidson, and D. W. H. Rankin, *J. Mol. Struct.*, 1991, **245**, 369–377.

63.   M. J. Davis, D. W. H. Rankin, and S. Cradock, *J. Mol. Struct.*, 1990, **238**, 273–287.

64.   V. Klimkowski, J. D. Ewbank, C. Van Alsenoy, J. N. Scarsdale, and L. Schäfer, *J. Am. Chem. Soc.*, 1982, **104**, 1476–1480.

65.   A. J. Blake, P. T. Brain, H. McNab, J. Miller, C. A. Morrison, S. Parsons, D. W. H. Rankin, H. E. Robertson, and B. A. Smart, *J. Phys. Chem.*, 1996, **100**, 12280–12287.

66.   N. W. Mitzel and D. W. H. Rankin, *Dalton Trans.*, 2003, 3650–3662.

67.   P. T. Brain, C. A. Morrison, S. Parsons, and D. W. H. Rankin, *Dalton Trans.*, 1996, 4589–4596.

68.   B. Mallick, A. Lakhsmanna, and S. Umapathy, *J. Raman Spectrosc.*, 2011, **42**, 1883–1890.

69.   R. Guo, S. Mukamel, and D. R. Klug, *Phys. Chem. Chem. Phys.*, 2012, **14**, 14023–14033.

70.   P. Baum and A. H. Zewail, *P. Natl. Acad. Sci. USA*, 2006, **103**, 16105–16110.

71.   P. Zhang, J. Yang, and M. Centurion, *New J. Phys.*, 2014, **16**, 083008.

72.   G. Sciaini and R. J. D. Miller, *Rep. Prog. Phys.*, 2011, **74**, 096101.

73.   R. Li, W. Huang, Y. Du, J. Shi, and C. Tang, *Nucl. Instrum. Meth. A*, 2011, **637**, S15–S19.

74.   J. R. Dwyer, C. T. Hebeisen, R. Ernstorfer, M. Harb, V. B. Deyirmenjian, R. E. Jordan, and R. J. D. Miller, *Philos. Trans. A*, 2006, **364**, 741–778.

75.   J. C. Williamson, M. Dantus, S. B. Kim, and A. H. Zewail, *Chem. Phys. Lett.*, 1992, **196**, 529–534.

76.   B. J. Siwick, A. A. Green, C. T. Hebeisen, and R. J. D. Miller, *Opt. Lett.*, 2005, **30**, 1057–1059.

77.   W. Sibbett, H. Niu, and M. R. Baggs, *Rev. Sci. Instrum.*, 1982, **53**, 758–761.

78.   B.-L. Qian and H. E. Elsayed-Ali, *J. Appl. Phys.*, 2002, **91**, 462–468.

79.   A. T. J. B. Eppink and D. H. Parker, *Rev. Sci. Instrum.*, 1997, **68**, 3477–3484.

80.   B.-L. Qian and H. E. Elsayed-Ali, *J. Appl. Phys.*, 2003, **94**, 803–806.

81.   B. J. Siwick, J. R. Dwyer, R. E. Jordan, and R. J. D. Miller, *J. Appl. Phys.*, 2003, **94**, 807–808.

82.   D. A. Dahl, *Int. J. Mass Spectrom.*, 2000, **200**, 3–25.

83.   *ASTRA - A Space Charge Tracking Algorithm*, http://www.desy.de/~mpyflo/, Version 3.0, 2014.

84.   G. Pöplau, U. van Rienen, B. van der Geer, and M. de Loos, *IEEE T. Magn.*, 2004, **40**, 714–717.

85.   S. B. van der Geer, O. J. Luiten, M. J. de Loos, G. Pöplau, and U. van Rienen, in *Institute of Physics Conference Series No. 175*, 2005, p. 101.

86.   R. Srinivasan, V. A. Lobastov, C.-Y. Ruan, and A. H. Zewail, *Helv. Chim. Acta*, 2003, **86**, 1763–1838.

87.   T. van Oudheusden, P. L. E. M. Pasmans, S. B. van der Geer, M. J. de Loos, M. J. van der Wiel, and O. J. Luiten, *Phys. Rev. Lett.*, 2010, **105**, 264801.

88.   B. A. Mamyrin, *Int. J. Mass Spectrom.*, 2001, **206**, 251–266.

89.   L. M. Rangarajan and G. K. Bhide, *Vacuum*, 1980, **30**, 515–522.

90.   E. Schrödinger, *Phys. Rev.*, 1926, **28**, 1049–1070.

91.   F. Jensen, *Introduction to computational chemistry*, John Wiley & Sons, Limited, Chichester, Second Edition, 2007.

92.   C. Møller and M. Plesset, *Phys. Rev.*, 1934, **46**, 618–622.

93.   M. Head-Gordon, J. A. Pople, and M. J. Frisch, *Chem. Phys. Lett.*, 1988, **153**, 503–506.

94.   J. A. Pople, R. Seeger, and R. Krishnan, *Int. J. Quantum Chem.*, 1977, **12**, 149–163.

95.   R. Krishnan and J. Pople, *Int. J. Quantum Chem.*, 1978, **14**, 91–100.

96.   P. Hohenberg and W. Kohn, *Phys. Rev.*, 1964, **136**, 864–871.

97.   A. D. Becke, *J. Chem. Phys.*, 1993, **98**, 5648–5652.

98.   C. Lee, W. Yang, and R. Parr, *Phys. Rev. B*, 1988, **37**, 785–789.

99.   B. Miehlich, A. Savin, H. Stoll, and H. Preuss, *Chem. Phys. Lett.*, 1989, **157**, 200–206.

100.   R. Bauernschmitt and R. Ahlrichs, *Chem. Phys. Lett.*, 1996, **256**, 454–464.

101.   D. Hegarty and M. A. Robb, *Mol. Phys.*, 1979, **38**, 1795–1812.

102.   P. C. Hariharan and J. A. Pople, *Mol. Phys.*, 1974, **27**, 209–214.

103.   J. S. Binkley, J. A. Pople, and W. J. Hehre, *J. Am. Chem. Soc.*, 1980, **102**, 939–947.

104.   M. S. Gordon, J. S. Binkley, J. A. Pople, W. J. Pietro, and W. J. Hehre, *J. Am. Chem. Soc.*, 1982, **104**, 2797–2803.

105.   A. D. McLean and G. S. Chandler, *J. Chem. Phys.*, 1980, **72**, 5639–5648.

106.   R. A. Kendall, T. H. Dunning Jr, and R. J. Harrison, *J. Chem. Phys.*, 1992, **96**, 6796–6806.

107.   A. K. Wilson, T. van Mourik, and T. H. Dunning Jr, *J. Mol. Struct.*, 1996, **388**, 339–349.

108. M. J. Frisch, G. W. Trucks, H. B. Schlegel, G. E. Scuseria, M. A. Robb, J. R. Cheeseman, G. Scalmani, V. Barone, B. Mennucci, G. A. Petersson, H. Nakatsuji, M. Caricato, X. Li, H. P. Hratchian, A. F. Izmaylov, J. Bloino, G. Zheng, J. L. Sonnenberg, M. Hada, M. Ehara, K. Toyota, R. Fukuda, J. Hasegawa, M. Ishida, T. Nakajima, Y. Honda, O. Kitao, H. Nakai, T. Vreven, J. A. Montgomery Jr., J. E. Peralta, F. Ogliaro, M. Bearpark, J. J. Heyd, E. Brothers, K. N. Kudin, V. N. Staroverov, T. Keith, R. Kobayashi, J. Normand, K. Raghavachari, A. Rendell, J. C. Burant, S. S. Iyengar, J. Tomasi, M. Cossi, N. Rega, J. M. Millam, M. Klene, J. E. Knox, J. B. Cross, V. Bakken, C. Adamo, J. Jaramillo, R. Gomperts, R. E. Stratmann, O. Yazyev, A. J. Austin, R. Cammi, C. Pomelli, J. W. Ochterski, R. L. Martin, K. Morokuma, V. G. Zakrzewski, G. A. Voth, P. Salvador, J. J. Dannenberg, S. Dapprich, A. D. Daniels, Ö. Farkas, J. B. Foresman, J. V. Ortiz, J. Cioslowski, and D. J. Fox, *Gaussian 09, Revision D.01*, Gaussian Inc, Wallingford, CT, 2010.

109. Molpro, http://www.molpro.net/, accessed on 1st October 2014.

110. H.-J. Werner, P. J. Knowles, G. Knizia, F. R. Manby, M. Schütz, P. Celani, T. Korona, R. Lindh, A. Mitrushenkov, G. Rauhut, K. R. Shamasundar, T. B. Adler, R. D. Amos, A. Bernhardsson, A. Berning, D. L. Cooper, M. J. O. Deegan, A. J. Dobbyn, F. Eckert, E. Goll, C. Hampel, A. Hesselmann, G. Hetzer, T. Hrenar, G. Jansen, C. Köppl, Y. Liu, A. W. Lloyd, R. A. Mata, A. J. May, S. J. McNicholas, W. Meyer, M. E. Mura, A. Nicklass, D. P. O'Neill, P. Palmieri, D. Peng, K. Pflüger, R. Pitzer, M. Reiher, T. Shiozaki, H. Stoll, A. J. Stone, R. Tarroni, T. Thorsteinsson, and M. Wang, 2012.

111. Newton-X, http://www.univie.ac.at/newtonx, accessed on 1st October 2014.

112. M. Barbatti, G. Granucci, M. Ruckenbauer, F. Plasser, J. Pittner, M. Persico, and H. Lischka, *A package for Newtonian dynamics close to the crossing seam*, Version 1.4, www.newtonx.org, 2013.

113. M. Barbatti, G. Granucci, M. Persico, M. Ruckenbauer, M. Vazdar, M. Eckert-Maksić, and H. Lischka, *J. Photoch. Photobio. A*, 2007, **190**, 228–240.

114. H. C. Andersen, *J. Chem. Phys.*, 1980, **72**, 2384–2393.

115. G. Blaise, A. J. Duran, C. le Gressus, B. G. A. Jüttner, R. Latham, A. Maitland, B. Mazurek, H. C. Miller, H. Padamsee, M. F. Rose, A. M. Shroff, and N. Xu, *High Voltage Vacuum Insulation: Basic Concepts and Technological Practice*, Academic Press Limited, London, 1995.

116. R. S. Fender, *PhD Thesis*, The University of Edinburgh, 1996.

117. D. J. Griffiths, *Introduction to electrodynamics*, Pearson, Third Edition, 1998.

118. J. O. Johansson, *PhD Thesis*, The University of Edinburgh, 2011.

119. G. G. Henderson, *PhD Thesis*, The University of Edinburgh, 2013.

120. W. A. Baum, *Attenuation Of Ultraviolet Light By The Lower Atmosphere*, California Institute of Technology, 1950.

121. G. H. Kassier, *PhD Thesis*, Stellenbosch University, 2010.

122. *Platinum: crystal structures*, http://www.webelements.com/platinum/crystal_structure.html, accessed on 10th October 2014.

123. R. Campargue, *J. Phys. Chem.*, 1984, **88**, 4466–4474.

124. R. Rejoub, B. G. Lindsay, and R. F. Stebbings, *Phys. Rev. A*, 2002, **65**, 042713.

125. J. J. Butler, T. Baer, and S. A. Evan Jr, *J. Am. Chem. Soc.*, 1983, **105**, 3451–3455.

126. Y. Baba, K. Yoshii, and T. A. Sasaki, *J. Chem. Phys.*, 1996, **105**, 8858–8864.

127. C. Luo, W.-N. Du, X.-M. Duan, J.-Y. Liu, and Z.-S. Li, *Chem. Phys. Lett.*, 2009, **469**, 242–246.

128. R. K. Vatsa, C. Majumder, O. D. Jayakumar, P. Sharma, S. K. Kulshreshtha, and J. P. Mittal, *Rapid Commun. Mass Spectrom.*, 2001, **15**, 1941–1946.

129. C. W. Bookwalter, D. L. Zoller, P. L. Ross, and M. V. Johnston, *J. Am. Soc. Mass Spectrom.*, 1995, **6**, 872–876.

130. S. B. Barone and A. A. Turnipseed, *J. Phys. Chem.*, 1994, **98**, 11969–11977.

131. A. Yokozeki and S. H. Bauer, *J. Phys. Chem.*, 1976, **80**, 618–625.

132. P. C. Hariharan and J. A. Pople, *Theor. Chim. Acta.*, 1973, **28**, 213–222.

133. S. D. Thompson, D. G. Carroll, F. Watson, M. O'Donnell, and S. P. McGlynn, *J. Chem. Phys.*, 1966, **45**, 1367–1379.

134. E. Mitscherlich, *Ann. Pharm.*, 1834, **12**, 311–314.

135. G. S. Hartley, *Nature*, 1937, **140**, 281.

136. E. Merino and M. Ribagorda, *Beilstein J. Org. Chem.*, 2012, **8**, 1071–1090.

137. A.-H. Gao, B. Li, P.-Y. Zhang, and K.-L. Han, *J. Chem. Phys.*, 2012, **137**, 204305.

138. M. Böckmann, N. L. Doltsinis, and D. Marx, *Angew. Chem. Int. Edit.*, 2010, **49**, 3382–3384.

139. J. Harada and K. Ogawa, *J. Am. Chem. Soc.*, 2001, **123**, 10884–10888.

140. N. Kano, F. Komatsu, and T. Kawashima, *J. Am. Chem. Soc.*, 2001, **123**, 10778–10779.

141. M. Traetteberg, I. Hillmo, and K. Hagen, *J. Mol. Struct.*, 1977, **39**, 231–239.

142. A. Gourdon, J.-P. Launay, M. Bujoli-Doeuff, F. Heisel, J. A. Miehé, E. Amouyal, and M.-L. Boillot, *J. Photoch. Photobio. A*, 1993, **71**, 13–25.

143. V. A. Galievsky, S. I. Druzhinin, A. Demeter, Y.-B. Jiang, S. A. Kovalenko, L. P. Lustres, K. Venugopal, N. P. Ernsting, X. Allonas, M. Noltemeyer, R. Machinek, and K. A. Zachariasse, *Chem. Phys. Chem.*, 2005, **6**, 2307–2323.

144. X. Xu, Z. Cao, and Q. Zhang, *J. Chem. Phys.*, 2005, 194305.

145. R. Nakagaki, S. Kohtani, Y. Nakamura, M. Okamura, S. Kitoh, and K.-K. Kunimoto, *Anal. Sci.*, 2003, **19**, 5–6.

146. A. B. Stephansen, R. Y. Brogaard, T. S. Kuhlman, L. B. Klein, J. B. Christensen, and T. I. Sølling, *J. Am. Chem. Soc.*, 2012, **134**, 20279–20281.

147. VELA, *http://www.stfc.ac.uk/2617.aspx*, accessed on 29th December 2014.

Associated publications

The work performed during my PhD has led to two articles, both published in peer-reviewed journals. The articles have been appended here to aid the examiners. Publications include:

Structures of Tetrasilylmethane Derivatives (XMe$_2$Si)$_2$C(SiMe$_3$)$_2$ (X = H, Cl, Br) in the Gas Phase, and their Dynamic Structures in Solution – D. A. Wann, M. S. Robinson, K. Bätz, S. L. Masters, A. G. Avent, P. D. Lickiss, *J. Phys. Chem. A*, 2015, **119**, 786-795, DOI: 10.1021/jp511301s

A compact electron gun for time-resolved electron diffraction – M. S. Robinson, P. D. Lane, D. A. Wann, *Rev. Sci. Instrum.*, 2015, **86**, 013109, DOI: 10.1063/1.4905335

Structures of Tetrasilylmethane Derivatives (XMe$_2$Si)$_2$C(SiMe$_3$)$_2$ (X = H, Cl, Br) in the Gas Phase, and their Dynamic Structures in Solution

Derek A. Wann,*,[†] Matthew S. Robinson,[†] Karin Bätz,[‡] Sarah L. Masters,[§] Anthony G. Avent,[∥,⊥] and Paul D. Lickiss*,[‡]

[†]Department of Chemistry, University of York, Heslington, York, U.K. YO10 5DD
[‡]Department of Chemistry, Imperial College London, London, U.K. SW7 2AZ
[§]Department of Chemistry, University of Canterbury, Private Bag 4800, Christchurch 8140, New Zealand
[∥]Department of Chemistry, School of Life Sciences, University of Sussex, Falmer, Brighton, U.K. BN1 9QJ

S *Supporting Information*

ABSTRACT: The structures of the molecules (XMe$_2$Si)$_2$C(SiMe$_3$)$_2$, where X = H, Cl, Br, have been determined by gas electron diffraction (GED) using the SARACEN method of restraints, with all analogues existing in the gas phase as mixtures of C_1- and C_2-symmetric conformers. Variable temperature ^{1}H and ^{29}Si solution-phase NMR studies, as well as ^{13}C NMR and ^{1}H/^{29}Si NMR shift correlation and ^{1}H NMR saturation transfer experiments for the chlorine and bromine analogues, are reported. At low temperatures in solution there appear to be two C_1 conformers and two C_2 conformers, agreeing with the isolated-molecule calculations used to guide the electron diffraction refinements. For (HMe$_2$Si)$_2$C(SiMe$_3$)$_2$ the calculations indicated six conformers close in energy, and these were modeled in the GED refinement.
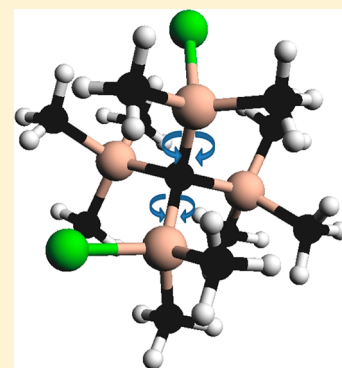
INTRODUCTION

The chemistry of tetrasilylmethane derivatives has been the subject of numerous studies, and many novel structures and unusual reactivities have been attributed to having four silicon centers in a sterically crowded environment.[1−4] The most widely studied tetrasilylmethane derivatives have the general structures (XMe$_2$Si)$_4$C, (Me$_3$Si)$_3$CSiRR′X, (PhMe$_2$Si)$_3$CSiRR′X, and (Me$_3$Si)$_2$C(SiMe$_2$X)(SiR$_2$Y) (where R and R′ = Me, Et, Ph, *etc.*, and X and Y = H, halide, OAc, *etc.*).[1−5]

A range of simple bis-functionalized tetrasilylmethanes (XMe$_2$Si)$_2$C(SiMe$_3$)$_2$ (for example, X = H,[6−9] F,[9−11] Cl,[7,9−14] Br,[6,7,9,15,16] I,[7,9,11,12,17] OH,[7,9,10,18,19] OMe,[10,20−22] OAc,[7,10,20] O$_2$CCF$_3$,[10−12,16,19] OClO$_3$,[9] OSO$_2$CF$_3$,[9] OSO$_2$-*p*-C$_6$H$_4$Me,[9] and vinyl[12,15]) are known, but apart from the diol (HOMe$_2$Si)$_2$C(SiMe$_3$)$_2$,[18] little structural information is available for them. The structure of the permethyl species, (Me$_3$Si)$_4$C, has, however, been studied by NMR spectroscopy,[23−27] X-ray diffraction,[28−30] gas electron diffraction (GED),[31,32] computational methods[33,34] and vibrational spectroscopy.[34]

Solution-phase NMR spectroscopy has been used to probe dynamic processes in bulky tetrasilylmethane derivatives previously, for example, in C(SiMe$_3$)$_2$(SiMePh$_2$)-(SiMe$_2$ONO$_2$),[35] C(SiMe$_3$)$_2$(SiClPh$_2$)(SiMe$_2$OMe),[36] (Me$_3$Si)$_3$CSiX$_3$ (X = Cl or Br),[37] and (PhMe$_2$Si)$_3$SiCl$_3$.[37] GED studies have also been carried out on the tetrasilyl-

methane (Me$_3$Si)$_3$CSiCl$_3$,[38] and on (HMe$_2$Si)$_3$CSiH$_3$,[39] the latter of which showed the presence of 11 distinct conformers.

The work presented here comprises two related studies. First, the structures of (XMe$_2$Si)$_2$C(SiMe$_3$)$_2$ [X = H (**1**), Cl (**2**), Br (**3**)] are described in the gas phase as determined by the combination of GED experiments and *ab initio* calculations, and second, NMR studies of the dynamic processes occurring for the same species in solution are presented.

EXPERIMENTAL SECTION

Syntheses. The syntheses of (HMe$_2$Si)$_2$C(SiMe$_3$)$_2$,[9] (ClMe$_2$Si)$_2$C(SiMe$_3$)$_2$,[13] and (BrMe$_2$Si)$_2$C(SiMe$_3$)$_2$[9] were carried out according to the literature methods shown in Scheme 1, and the compounds were purified for structural

Scheme 1. Synthetic Routes to (XMe$_2$Si)$_2$C(SiMe$_3$)$_2$ (X = H, Cl, Br)
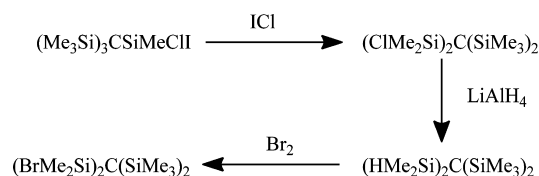
$$(\text{Me}_3\text{Si})_3\text{CSiMeClI} \xrightarrow{\text{ICl}} (\text{ClMe}_2\text{Si})_2\text{C}(\text{SiMe}_3)_2$$

$$\downarrow \text{LiAlH}_4$$

$$(\text{BrMe}_2\text{Si})_2\text{C}(\text{SiMe}_3)_2 \xleftarrow{\text{Br}_2} (\text{HMe}_2\text{Si})_2\text{C}(\text{SiMe}_3)_2$$

studies by sublimation. Thus, treatment of $(Me_3Si)_3CSiMeClI$ with ICl leads to a rearrangement of the type often seen in tetrasilylmethane derivatives[1] to give $(ClMe_2Si)C(SiMe_3)_2$ (**2**), which is readily reduced by $LiAlH_4$ to give $(HMe_2Si)C-(SiMe_3)_2$ (**1**), which then affords $(BrMe_2Si)_2C(SiMe_3)_2$ (**3**) in high yield upon treatment with bromine. The fluorine analogue $(FMe_2Si)_2C(SiMe_3)_2$ can be prepared by reaction between $(AcOMe_2Si)_2C(SiMe_3)_2$ and CsF,[10] while the iodine analogue $(IMe_2Si)_2C(SiMe_3)_2$ can be prepared by reaction of $(HMe_2Si)_2C(SiMe_3)_2$ and I_2,[9] though neither compound was readily available for use in the current study.

NMR Measurements. ^1H, ^{13}C and ^{29}Si NMR spectra were recorded in $CDCl_3/CD_2Cl_2$ or $CDCl_3/acetone-d_6$ solutions using a Bruker AMX 500 spectrometer at 500, 126, and 99 MHz, respectively, unless otherwise stated. The $^{29}Si\{^1H\}$ NMR INEPT spectra were recorded on a Bruker AMX 500 NMR spectrometer at 99 MHz, and $^{29}Si\{^1H\}$ inverse-gated NMR spectra were recorded on a Bruker Avance 600 spectrometer at 119.23 MHz. Chemical shifts of all NMR spectra are reported in ppm relative to TMS.

All solid-state $^{13}C\{^1H\}$ and $^{29}Si\{^1H\}$ MAS NMR spectra were recorded on a Bruker DSX 200 WB NMR spectrometer. Samples were spun at 3−5 kHz and simple Bloch decay techniques (standard single-pulse excitation method) were used. Approximately 1000 scans per sample were collected. The operating frequencies for ^{13}C and ^{29}Si NMR experiments were 50.28 and 39.7 MHz, respectively.

X-ray Crystallography. The attempted single-crystal X-ray study for $(BrMe_2Si)_2C(SiMe_3)_2$ was carried out using an OD Xcalibur 3 diffractometer, using X-rays of wavelength 0.71073 Å, at a temperature of 100 K.

Computational Methods. Previous studies for similar molecules[39] suggested that $(XMe_2Si)_2C(SiMe_3)_2$ compounds would have a series of potential-energy minima leading to a number of conformational isomers, dependent on the relative rotations of the two XMe_2Si groups. Figure 1 shows one possible conformation of $(XMe_2Si)_2C(SiMe_3)_2$ as an illustration.
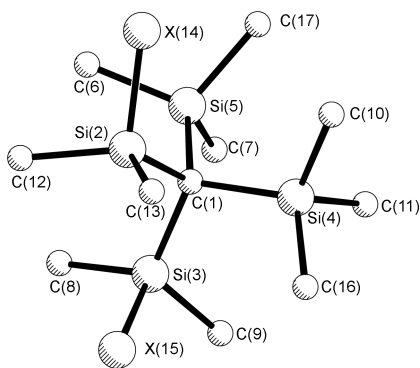

Figure 1. Structure, with atom numbering, of one conformer of $(XMe_2Si)_2C(SiMe_3)_2$. Hydrogen atoms have been removed for clarity. Atoms in subsequent conformers are numbered by adding multiples of 47 to these.

These minima occurred at three approximate X(14/15)−Si(2/3)−C(1)−Si(3/2) dihedral angles: 80, −40 and −160°. By independently setting the two XMe_2Si to all possible combinations of these angles, it can be seen that there are nine ($=3^2$) possible minimum-energy conformers for each of **1**−**3**. Experience of studying a similar set of species $(XMe_2Si)_4C$,

where X = H, F, Cl, Br, has shown that the opposite sense of each angle (i.e., −80, +40, and +160°) should also be considered when looking to identify all possible conformers.[40]

All calculations used Gaussian 09[41] on either the University of Edinburgh's ECDF cluster[42] or the UK's National Service for Computational Chemistry Software clusters.[43] Geometry optimizations and frequency calculations were carried out to determine which ground-state conformers had the lowest energies. For comparison, both the B3LYP[44−46] and M06-2X[47] methods with the 6-31G(d)[48,49] basis set were used for these calculations.

Further geometry optimizations and frequency calculations were carried out on conformers deemed to have low lying energies. The B3LYP hybrid method with the aug-cc-pVDZ basis set[50,51] was used for **1** and **2**, while the pseudopotential basis set aug-cc-pVDZ-PP[52,53] was used for **3**. These basis sets will be denoted as aug-cc-pVDZ(-PP) from hereon in. As a comparison, geometry optimizations were performed for every conformer using the M06-2X method and the aug-cc-pVDZ(-PP) basis set, as well as calculations using the MP2 method[54] with the 6-31G(d) and aug-cc-pVDZ(-PP) basis sets. The relative amounts of each conformer that would be present in the GED samples at the temperature of each experiment were calculated using the Gibbs free energy for each conformer (obtained from quantum calculations carried out at 0 K) and the Boltzmann distribution equation:

$$\frac{N_i}{N} = \frac{g_i \exp\left(-\frac{\Delta G_i}{RT}\right)}{\sum_i g_i \exp\left(-\frac{\Delta G_i}{RT}\right)}$$

where N is the total number of molecules, and N_i is the number of molecules in a given state i, at temperature T. R is the gas constant, while ΔG_i and g_i are the Gibbs free energy difference (with respect to the lowest energy conformer) and degeneracy, respectively, of state i, where g_i is equal to 1 for C_1 symmetric, and 2 for C_2 symmetric molecules.

Gas Electron Diffraction (GED). Data for **1**, **2**, and **3** were collected using the GED apparatus that was used in Edinburgh until 2010.[55] An accelerating potential of 40 keV was applied, producing electrons with an approximate wavelength of 6.0 pm. Each molecule was analyzed with two different nozzle-to-camera distances, increasing the range of data collected. Exact nozzle-to-camera distances were calibrated by analyzing the results of benzene diffraction experiments that were carried out immediately after collecting data for the molecules of interest. The scattering intensities were recorded on Kodak Electron Image films, and measured with the use of an Epson Expression 1680 Pro flat-bed scanner and converted to mean optical densities using a method described elsewhere.[56] A full list of experimental parameters, including the measured nozzle and sample temperatures for each experiment, can be found in Table S1, Supporting Information.

The data were analyzed using the ed@ed least-squares refinement program v3.0,[57] incorporating the scattering factors of Ross et al.[58] Weighting points for the off-diagonal weight matrices, and scale factors can be found in Table S1, while Tables S2−S4 show the correlation matrices.

RESULTS AND DISCUSSION

Gas-Phase Static Structures. By starting geometry optimization for structures with all possible combinations of minimum-energy dihedral angles, six unique conformers were

identified. Frequency calculations, carried out using M06-2X/6-31G(d) and B3LYP/6-31G(d), suggested that all of the unique conformers of **1** had similar ground-state energies, and hence all could be present in the gas phase at the temperature of the experiments. Three of these conformers have C_1 symmetry (**1a−c**), and three have C_2 symmetry (**1d−f**). The calculations also suggested that for **2** and **3** four of these six conformers were likely to be observable in the gas electron diffraction experiments. For each of these molecules, two conformers have C_1 symmetry (**2a/b** and **3a/b**) and two have C_2 symmetry (**2c/d** and **3c/d**). Tables 1−3 show the zero-point-corrected

Table 1. Indicative Dihedral Angle, Symmetry, Relative Energy, and Proportion for Each Conformer of 1[a]

conformer	indicative dihedral angle[b]	point-group symmetry	relative energy[c]	proportion[d]
1a	−160/−40	C_1	1.47	0.204
1b	−160/80	C_1	0.00	0.311
1c	80/−40	C_1	0.31	0.285
1d	−160/−160	C_2	4.13	0.048
1e	80/80	C_2	2.18	0.083
1f	−40/−40	C_2	2.87	0.069

[a]Calculations performed using B3LYP/aug-cc-pVDZ. [b]These are the starting values of the H(14)−Si(2)−C(1)−Si(3)/H(15)−Si(3)−C(1)−Si(2) dihedral angles in degrees; no interconversion was observed upon optimization. See Figure 1 for atom numbering. [c]Gibbs free energy in kJ mol^{-1} (ZPE corrected). [d]Calculated at 431 K.

Table 2. Indicative Dihedral Angle, Symmetry, Relative Energy, and Proportion for Each Conformer of 2[a]

conformer	indicative dihedral angle[b]	point-group symmetry	relative energy[c]	proportion[d]
2a	−160/−40	C_1	0.00	0.720
2b	−160/80	C_1	7.56	0.106
2c	−160/−160	C_2	6.19	0.075
2d	80/80	C_2	5.07	0.099

[a]Calculations performed using B3LYP/aug-cc-pVDZ. [b]These are the starting values of the Cl(14)−Si(2)−C(1)−Si(3)/Cl(15)−Si(3)−C(1)−Si(2) dihedral angles in degrees; no interconversion was observed upon optimization. See Figure 1 for atom numbering. [c]Gibbs free energy in kJ mol^{-1} (ZPE corrected). [d]Calculated at 485 K.

Table 3. Indicative Dihedral Angle, Symmetry, Relative Energy, and Proportion for Each Conformer of 3[a]

conformer	indicative dihedral angle[b]	point-group symmetry	relative energy[c]	proportion[d]
3a	−160/−40	C_1	0.00	0.785
3b	−160/80	C_1	8.76	0.086
3c	−160/−160	C_2	8.63	0.044
3d	80/80	C_2	6.07	0.085

[a]Calculations performed using B3LYP/aug-cc-pVDZ-PP. [b]These are the starting values of the Br(14)−Si(2)−C(1)−Si(3)/Br(15)−Si(3)−C(1)−Si(2) dihedral angles in degrees; no interconversion was observed upon optimization. See Figure 1 for atom numbering. [c]Gibbs free energy in kJ mol^{-1}(ZPE corrected). [d]Calculated at 486 K.

ground-state Gibbs free energies for all conformers of **1**, **2**, and **3**, as obtained from the B3LYP/aug-cc-pVDZ(-PP) calculations, and relate these to the relative abundance of each conformer at the temperature of the experiment, which for each species **1−3** is an average of the recorded temperatures for both nozzle and sample (seen in Table S1) at both camera distances.

The geometry optimizations showed that the four silyl branches surrounding the central carbon atom were arranged in a near-tetrahedral formation. In order to refine the experimental GED data, parametrized models were written in FORTRAN for each of **1−3**, describing all conformers of each species that were likely to appear in the sample. The parameters used in the models were based on the bond lengths and angles of the most abundant conformer of each species, due to the small difference (less than 0.5 pm) as suggested by the MP2/aug-cc-pVDZ(-PP) geometry optimizations, for the equivalent atomic distances between the conformers. Slight deviations in bond lengths and angles between different conformers were accounted for by applying fixed (nonrefinable) differences to the parameters. For **1**, **2**, and **3**, 32, 26, and 26 parameters were used to describe six, four, and four conformers, respectively. A full and complete description of the models used to describe the molecules can be found in the Supporting Information, with full atomic coordinates for each conformer **1−3** can be found in Tables S5−S7.

Refinements of the experimental data were carried out using the SARACEN method,[59−61] with adjustments made for the effects of vibrational motions using data from SHRINK.[62] SARACEN restraint values were based on the MP2/aug-cc-pVDZ(-PP) calculations, while the ranges of values from a series of geometry optimizations were used to estimate the uncertainties in these values.

Of the parameters, 27, 22, and 20 parameters were restrained, for **1−3**, respectively, while the rest refined freely. In each model, parameters p_1−p_6 describe distances between pairs of atoms in the molecule, parameters p_7−p_{14} are bond angles used to position atoms relative to one another, while parameters p_{15}−p_{26} (and additionally p_{27}−p_{32} for **1**) are sets of dihedral angles to position the four main branches in each molecule relative to each other. Tables S8−S10 contain full lists of parameters and values for each of **1−3**, respectively.

To refine the amplitudes of vibration, the individual atomic distance that produced the largest scattering effect under a particular peak was selected. All other atomic distances under that same peak (not including distances related to hydrogens on a methyl group) had their amplitudes of vibration tied to the selected amplitude at the calculated ratio, with the single amplitude being refined. For **1**, **2**, and **3**, 11, nine, and 11 amplitudes, respectively, were refined, with five, one, and five of these restrained.

The refinements were initially carried out with the amount of each conformer fixed to the calculated proportions reported in Tables 1−3 for **1−3**, respectively. Once the optimal refinement was obtained with these conformer amounts, some of the values were varied in order to determine the experimental amounts of each conformer.

Full lists of interatomic distances, amplitudes of vibration, distance corrections, and SARACEN restraints for **1**, **2**, and **3** can be found in Tables S11−S13.

Parts a−c of Figure 2 show the experimentally obtained radial distribution curves for **1**, **2**, and **3**, respectively. Difference curves can also be seen underneath each radial distribution curve, showing how good a fit was obtained to the experimental data. The related molecular scattering curves for each molecule can be seen in Figure S1a−c. The R_G factors obtained for the least-squares refinements of **1**, **2**, and **3** were 6.1%, 8.7%, and 10.9%, respectively, with R_D factors (which ignore off-diagonal elements of the weight matrix) of 3.1%, 7.4%, 7.2%, respectively. Reference 63, and other references therein, gives
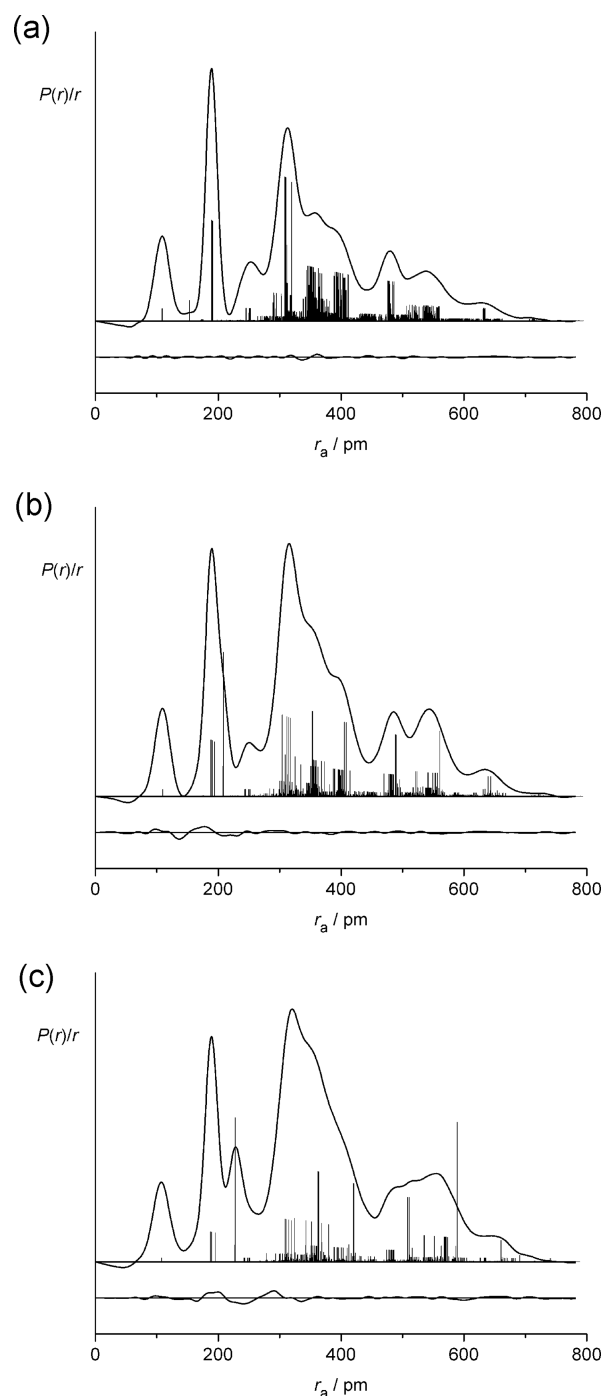
Figure 2. Radial distribution curves and difference curves between theoretical and experimental data for molecules **1** (a), **2** (b) and **3** (c).

Experimental geometric parameters are presented as r_{h1} values, which are formally derived from the vibrationally averaged r_a values that are yielded by the electron diffraction experiments (and which are listed for each pair of atoms in Supporting Information, Tables S11–S13). Vibrational corrections are applied to the r_a distances, first accounting for the amplitudes of vibration, u_{h1}, which act along the vectors between atom pairs, and then by applying the perpendicular vibrational correction, k_{h1}, which is calculated using the SHRINK program. In total this means that for any given atom pair $r_{h1} \approx r_a + u_{h1}^2/r_a - k_{h1}$. The r_e values quoted are determined from the theoretical equilibrium distances obtained from the various quantum chemical calculations.

For **1**, it can be seen from Table 4 that the distances to the central carbon atom, C(48) for the most abundant conformer, have a range of only around 1 pm. This is true for both the experimental and computational results. There is generally good agreement between the GED-derived distances and those from quantum chemical calculations, with the largest deviation observed for the Si–H distance. It is possible that this is due to the poor scattering ability of the lighter H atoms, but it is also likely to be a product of the anharmonicity observed in the vibration between the relatively heavy Si and light H atoms. Comparing the calculations themselves, which were all performed using the aug-cc-pVDZ basis set, both the MP2 and M06-2X theories give values that match the GED values well. The largest deviation observed relates to ∠C(59)–Si(49)–C(60), which differs by just under 3° from the theoretical value. However, the parameters relating to this angle have been restrained according to the SARACEN method, so we should accept this value.

For **2** and **3**, it can be seen from Table 5 that there is also reasonable agreement between calculated and experimental values. Perhaps the most striking difference between the structure of **1**, and those for **2** and **3**, is the effect of the electronegative Cl and Br atoms in the latter. For **2** and **3**, the electron withdrawing properties of atom X cause C–Si distances to the central atom to have a range of around 3 pm, and this is observed for both experimental and calculated values. Bonds to SiMe$_3$ groups [e.g., C(1)–Si(4)] are longer than those to SiMe$_2$X groups [e.g., C(1)–Si(2)]; this was not observed for **1**. Again MP2 and M06-2X theories produced calculated values that are closest to the experimental values. The most significant deviations were for the Si–X distances [X = Cl (**2**), Br (**3**)], and this is likely due to the small size of the basis sets used (necessary because of computational restrictions).

As one would expect when replacing the H of **1** with the larger Cl and Br atoms in **2** and **3**, the experimentally defined angles for C(1)–Si(2)–C(12) and C(12)–Si(2)–C(13) are larger in each case than the equivalent values for **1**. Such trends are also observed from the computational results.

As mentioned before, to find all possible conformers of each of **1**–**3**, calculations were started with each XMe$_2$Si group set to one of three dihedral angles (−40, −160, and +80°), and the majority of optimized dihedral angles fell within 5° of the expected angles. While most of the refined dihedral angles were close to the computationally predicted values, the dihedral angle ϕCl(61)–Si(49)–C(48)–Si(50) for **2**, deviated from the predicted computational range by 5°. However, we might expect more freedom in the range of dihedral angles.

All three theoretical methods (B3LYP, M06-2X, and MP2) gave similar dihedral angles for the same sets of atoms, with the

a full explanation of the differences between R_G and R_D. The refined coordinates of each atom for all conformers of all three species studied can be found in Tables S14–S16.

Tables 4 and 5 contain selected parameters that demonstrate the typical bond lengths, bond angles, and dihedral angles observed for each of **1**–**3**. As the models for the GED refinement were based on the most abundant conformer of each species, with fixed differences to allow for slight deviations between that and other conformers, the bond lengths and angles relating to the main conformer are shown. However, X–Si–C–Si dihedral angles for all conformers are shown as these differ considerably between conformers of the same species.

Table 4. Selected Experimental (r_{h1}) and Theoretical (r_e) Geometric Parameters for 1[a]

parameter	r_{h1}	r_e B3LYP	r_e MP2	r_e M06-2X
rC(48)−Si(49)	190.1(6)	193.0	191.6	190.2
rC(48)−Si(51)	191.0(6)	193.6	191.8	190.5
rSi(49)−C(59)	188.7(1)	190.2	190.1	190.2
rSi(49)−H(61)	153.3(21)	150.1	150.3	149.8
rSi(51)−C(57)	189.0(1)	190.2	190.3	189.4
∠C(48)−Si(49)−H(61)	108.3(6)	107.2	107.6	107.6
∠C(48)−Si(49)−C(59)	115.2(9)	115.0	114.0	112.9
∠C(48)−Si(51)−C(57)	113.3(6)	112.7	112.2	112.1
∠C(57)−Si(51)−C(58)	107.0(7)	106.0	106.4	106.4
∠C(59)−Si(49)−C(60)	102.2(20)	105.0	105.8	106.6
ϕH(14)−Si(2)−C(1)−Si(3)	−160.2(35)	−163.7	−160.6	−159.2
ϕH(15)−Si(3)−C(1)−Si(2)	−41.2(15)	−42.5	−41.6	−42.1
ϕH(61)−Si(49)−C(48)−Si(50)	−163.9(12)	−160.0	−159.5	−159.6
ϕH(62)−Si(50)−C(48)−Si(49)	79.3(30)	75.9	76.2	78.9
ϕH(108)−Si(96)−C(95)−Si(97)	81.8(16)	78.8	78.8	78.4
ϕH(109)−Si(97)−C(95)−Si(96)	−43.3(13)	−40.0	−39.7	−40.3
ϕH(155)−Si(143)−C(142)−Si(144)	−161.5(7)	−162.7	−161.7	−162.3
ϕH(202)−Si(190)−C(189)−Si(191)	79.7(8)	77.7	78.4	78.2
ϕH(249)−Si(237)−C(236)−Si(238)	−42.6(13)	−46.8	−45.3	−45.7

[a]Distances (r) are in pm, angles (∠) and dihedral angles (ϕ) are in degrees. Atom numbering as described in Figure 1. r_e values were calculated using the aug-cc-pVDZ basis set for each respective theory.

Table 5. Selected Experimental (r_{h1}) and Theoretical (r_e) Geometric Parameters for 2 (X = Cl) and 3 (X = Br)[a]

parameter	2				3			
	r_{h1}	r_e B3LYP	r_e MP2	r_e M06-2X	r_{h1}	r_e B3LYP	r_e MP2	r_e M06-2X
rC(1)−Si(2)	190.1(3)	192.7	190.8	189.7	189.6(13)	193.0	190.7	190.1
rC(1)−Si(4)	193.8(3)	196.2	193.8	192.9	195.0(13)	196.5	193.8	193.2
rSi(2)−C(12)	187.7(7)	188.7	188.6	187.6	187.4(2)	188.9	188.6	187.7
rSi(2)−X(14)	208.3(2)	215.1	213.8	213.3	227.7(2)	232.3	229.1	230.3
rSi(4)−C(10)	188.7(5)	189.9	189.7	188.8	188.7(2)	189.8	189.7	188.7
∠C(1)−Si(2)−X(14)	109.6(6)	109.5	108.2	108.6	110.6(7)	111.1	108.9	110.1
∠C(1)−Si(2)−C(12)	116.1(2)	115.6	115.4	115.3	116.3(7)	115.3	115.6	115.1
∠C(1)−Si(4)−C(10)	111.9(3)	112.8	112.1	112.1	112.0(6)	112.8	112.2	112.2
∠C(10)−Si(4)−C(11)	105.9(7)	105.5	106.1	106.0	106.0(7)	105.5	105.9	105.9
∠C(12)−Si(2)−C(13)	107.9(13)	107.4	107.9	107.7	106.8(21)	107.8	108.5	108.4
ϕX(14)−Si(2)−C(1)−Si(3)	−156.7(9)	−159.2	−158.6	−158.9	−158.7(12)	−158.9	−157.9	−158.8
ϕX(15)−Si(3)−C(1)−Si(2)	−43.2(7)	−41.8	−41.2	−41.9	−41.9(13)	−42.3	−41.1	−42.2
ϕX(61)−Si(49)−C(48)−Si(50)	−160.8(5)	−165.8	−165.6	−166.0	−163.1(11)	−166.4	−166.5	−166.8
ϕX(62)−Si(50)−C(48)−Si(49)	74.7(7)	77.6	78.0	77.6	75.7(11)	78.04	78.4	78.2
ϕX(108)−Si(96)−C(95)−Si(97)	−161.5(6)	−161.8	−161.1	−161.6	−161.3(13)	−162.0	−161.0	−161.7
ϕX(155)−Si(143)−C(142)−Si(144)	76.9(4)	75.5	75.7	75.4	76.5(8)	75.2	75.4	75.0

[a]Distances (r) are in pm, angles (∠) and dihedral angles (ϕ) are in degrees. Atom numbering as described in Figure 1. r_e values were calculated using the aug-cc-pVDZ basis set for 2, and aug-cc-pVDZ-PP for 3, for each respective theory, and are based on the most abundant conformer for each molecule.

largest discrepancies being 0.7 and 1.2° between predicted values for 2 and 3, respectively. The three methods also predicted similar dihedral angles for the same set of atoms for 1, although there were some larger discrepancies between methods, with the largest being 4.5° [relating to ϕH(14)−Si(2)−C(1)−Si(3)]. The refined dihedral angles, which were all restrained using SARACEN,[59−61] fell within 5° of the predicted calculations, tending also toward the expected dihedral angles.

In terms of the amount of each conformer present for each molecular species, it was found that for 1 there was little change in the R_G value of the refinement as the conformer ratio was adjusted. This is to be expected of 1 due to the nature of the hydrogen atoms on the silicon group, allowing for free rotation

of the SiHMe$_2$ groups. Therefore, the refinement for this species was performed with the conformers fixed at the proportions predicted in Table 1. For 2 and 3, a noticeable change in the R_G value was observed as the relative amounts of the two lowest energy conformers a and b (as predicted in Tables 2 and 3) were adjusted. The amounts of c and d remained fixed. How the R_G values vary for each of 2 and 3 is illustrated in Figure 3, which also shows the 95% confidence level (represented by a horizontal bar). For 2, a relatively shallow minimum is observed around the proportion predicted in Table 2. Because of this, the conformer ratio for 2 was kept at the values seen in Table 2 for the final refinement. For 3, a more pronounced minimum is observed in Figure 3, with the final refinement performed where the proportion of conformers
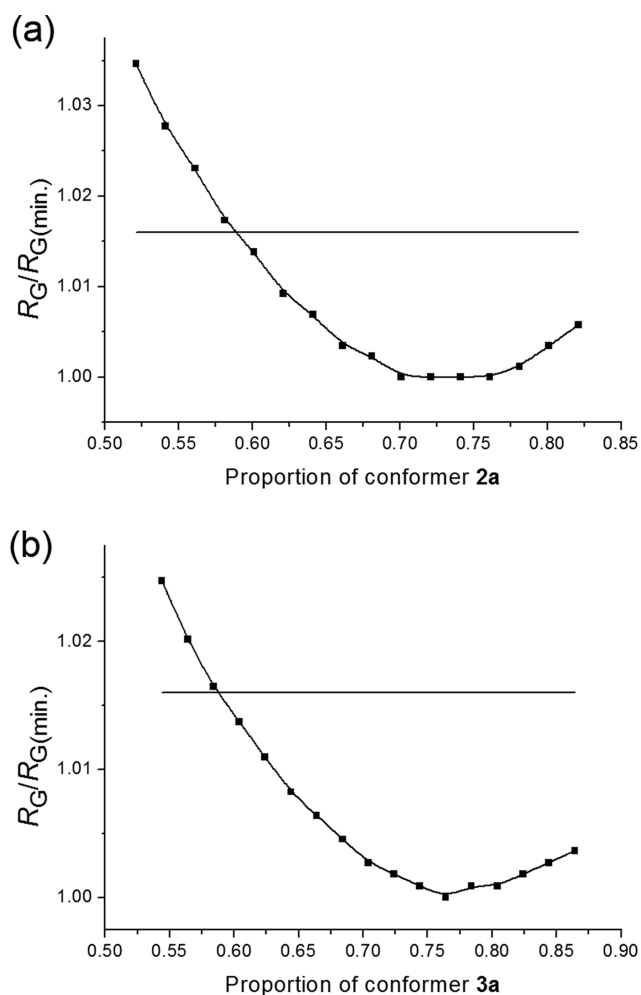
(a)

(b)

Figure 3. Variation in $R_G/R_{G(min.)}$ for (a) **2** and (b) **3** as the proportions of conformers **a** and **b** are varied relative to each other. The proportion of conformers **c** and **d** remained fixed. The horizontal bar represents the 95% confidence limit for the data.

a:b:c:d was 0.764:0.106:0.045:0.085. The results for **2** and **3** show that the theory was accurate in predicting the relative amounts of the most abundant conformers.

The refinements performed here for **1** can be compared to those for $(HMe_2Si)_3CSiH_3$, 11 conformers of which are reported in ref 39. The average bond lengths observed for the various C–Si distances for $(HMe_2Si)_3CSiH_3$ [equivalent to rC(48)–Si(49) and rSi(49)–C(59) in Table 4] were 189.8 and 188.8 pm, respectively. These differ only by 0.3 and 0.1 pm, respectively, from values seen for similar bonds in **1**. Slight deviations from the angles observed for $(HMe_2Si)_3CSiH_3$ are noted for ∠C(48)–Si(49)–C(59), with that reported in ref 39. being 113.8(4)°, while for **1** the value was 115.2(9)°. The larger angle observed in **1**, is most likely due to added strain on the branch due to larger groups around the central carbon (two SiMe_3 groups and an SiMe_2H group), compared to less bulky groups (two SiMe_2H and one SiH_3) for $(HMe_2Si)_3CSiH_3$.

In the case of **2**, comparisons can be made with $(Me_3Si)_3CSiCl_3$, as seen in ref 38. While the structures are quite similar, some structural differences are observed. In general, the bonds in $(Me_3Si)_3CSiCl_3$ are shorter than those in **2** by 1 to 5 pm. For example, the average distance from the central carbon atom to silicon [i.e., the mean of C(1)–Si(2/3/4/5)] for $(Me_3Si)_3CSiCl_3$ is 190.9(8) pm, compared to 192.0

pm for **2**. The average Si–C distance for an SiMe_3 branch is also shorter for $(Me_3Si)_3CSiCl_3$, at 187.8(6) pm compared to 188.7(5) pm for **2**. The largest observed difference in bond lengths occurs with the Si–Cl distance: 203.3(6) pm for $(Me_3Si)_3CSiCl_3$, and 208.3(2) pm for **2**. This is not surprising as the chlorine-containing moiety is quite different; $(Me_3Si)_3CSiCl_3$ exhibits stronger Si–Cl bonds than those in **2**, which is most likely due to that region being highly electronegative and drawing electrons toward it.

Differences are also observed between the two in relation to similar bond angles, with angles generally being wider for $(Me_3Si)_3CSiCl_3$ than for **2**. The C–Si–C angle in $(Me_3Si)_3CSiCl_3$ [which is equivalent to ∠C(10)–Si(4)–C(11) in **2**] is 107.0(11)°, compared to 105.9(7)° in **2**, though this difference is not significant. The biggest difference is once again for a parameter relating to the chlorine atoms. The C–Si–Cl angle [∠C(1)–Si(2)–Cl(14)] in $(Me_3Si)_3CSiCl_3$ is 114.6(11)°, while it is only 109.6(6)° in **2**. This may be due to the added steric hindrance of three chlorine atoms in close proximity.

Solution-Phase Dynamic Structures. Extensive NMR experiments were performed for **2** and **3**, with full details given in the Supporting Information.

(BrMe_2Si)_2C(SiMe_3)_2. The 400 MHz ^{1}H NMR spectrum of $(BrMe_2Si)_2C(SiMe_3)_2$ (**3**) shows, as would be expected, two resonances at room temperature: a slightly broadened singlet for the SiMe_2Br protons and a sharp singlet for the SiMe_3 signal (see Figure S2 in the Supporting Information). However, on lowering the temperature a much more complicated spectrum emerges and, at 213 K, the spectrum shows numerous signals in both the SiMe_2Br and SiMe_3 regions (Figure S2). The ^{1}H NMR spectrum at 201 K recorded at higher field (500 MHz, Figure S3) shows the SiMe_2Br region to have six large signals and at least six smaller signals, while the SiMe_3 region has eight larger signals and at least six smaller signals together with several unidentified signals thought to belong to impurities (Figure S3). The ^{29}Si NMR spectrum recorded at 300 K shows a signal at −0.35 ppm, corresponding to the SiMe_3 groups and a broad signal due to the SiMe_2Br region, which has begun to split out into several signals, extending from 24.38 to 22.11 ppm. These two main signals again split into numerous signals at 201 K (Figure S4) and, together with the ^{1}H spectra, this indicates the presence of more than one conformer at low temperature.

A 2D ^{1}H/^{29}Si NMR shift correlation spectrum of $(BrMe_2Si)_2C(SiMe_3)_2$ was recorded at 201 K in order to correlate ^{1}H NMR signals with ^{29}Si NMR signals. Each ^{29}Si NMR signal in the SiMe_2Br region of the spectrum (shown in Figure 4 and Figure S5) is expected to be associated with two different proton signals. This spectrum shows that proton signals at 0.94 and 0.87 ppm, labeled A and B, correlate with the ^{29}Si NMR resonance at 24.60 ppm (labeled I). The ^{29}Si NMR signal at 23.40 ppm (II) is associated with proton signals C and F at 0.86 and 0.779 ppm. The third, large silicon signal III at 21.85 ppm is linked to proton signals at 0.81 ppm (D) and 0.784 ppm (E). Proton signals α and γ concealed under a large peak at 0.86 ppm and at 0.767 ppm, correlate with the small silicon signal 1 at 24.00 ppm. Silicon signal 2 at 23.29 ppm is linked with the ^{1}H NMR signals a and b at 0.96 ppm and hidden under a large peak at 0.779 ppm. Proton signals β and δ at 0.788 and 0.74 ppm, are associated with the ^{29}Si NMR signal at 20.92 ppm labeled 3.
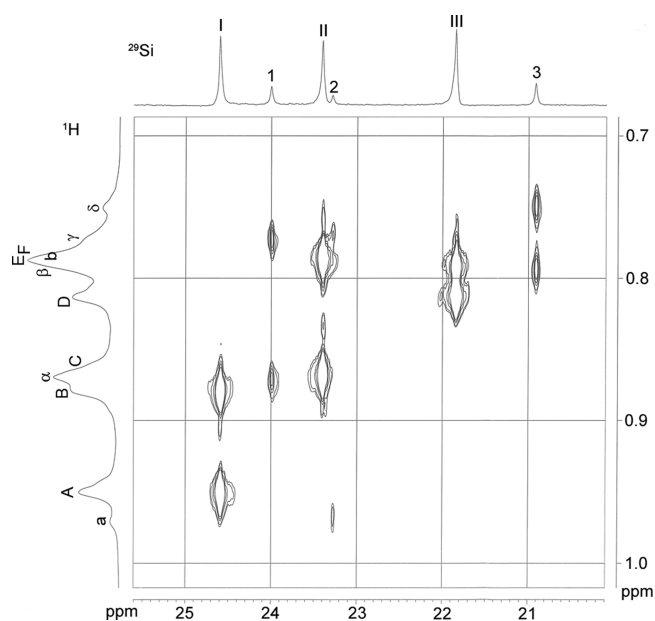
791

Figure 4. 2D ^{1}H/^{29}Si NMR shift correlation spectrum of the SiMe$_2$Br region of (BrMe$_2$Si)$_2$C(SiMe$_3$)$_2$ in CDCl$_3$/CD$_2$Cl$_2$ at 201 K.

As proton signals a and b are assumed to be due to a minor C_2 conformer of (BrMe$_2$Si)$_2$C(SiMe$_3$)$_2$, silicon signal 2 must also be associated with this conformer. Likewise, proton signals α, β, γ and δ assigned to minor conformer C_1 are linked to silicon signals 1 and 3, which must therefore be due to the same conformer.

For the SiMe$_3$ region of the ^{29}Si NMR spectrum (see Figure 5 and Figure S6) each signal is expected to be associated with three ^{1}H NMR signals. Interpretation of the shift correlation spectrum in a manner similar to that used for the SiMe$_2$Br region yields the assignments summarized in Table 6. Several small signals labeled by asterisks do not seem to correlate in a
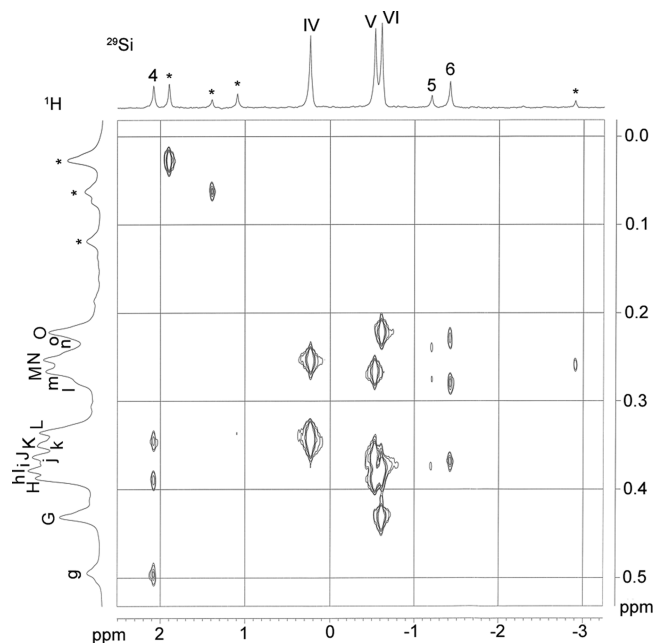

Figure 5. 2D ^{1}H/^{29}Si NMR shift correlation spectrum of the SiMe$_3$ region of (BrMe$_2$Si)$_2$C(SiMe$_3$)$_2$ in CDCl$_3$/CD$_2$Cl$_2$ at 201 K. A star denotes a peak assigned to an impurity.

Table 6. Summary of the 2D ^{1}H/^{29}Si NMR Shift Correlation Assignments in (BrMe$_2$Si)$_2$C(SiMe$_3$)$_2$

major conformers (C_1 and C_2)		minor conformers (C_1 and C_2)	
^{29}Si	^{1}H	^{29}Si	^{1}H
I	A and B	1	α and γ
II	C and F	2	a and b
III	D and E	3	β and δ
IV	K, L, and N	4	g, h, and k
V	H, J, and M	5	i, m, and n
VI	G, I, and O	6	j, l, and o

similar way to the ^{1}H NMR signals and are assumed to be due to impurities which can also be seen at low intensity in the room-temperature spectra.

Several ^{1}H NMR saturation transfer experiments on (BrMe$_2$Si)$_2$C(SiMe$_3$)$_2$ were recorded at 201 K to probe the exchange processes between different conformers at low temperature. Both large and small proton signals in the SiMe$_2$Br region of the proton spectrum were irradiated and it was clear that exchange between the major and minor conformers was occurring, but a full assignment of the enhanced signals is ambiguous in some cases due to overlap between the signals (Figure S7). Similar experiments were also carried out for the SiMe$_3$ region signals and again while exchange processes could be observed, a full assignment could not be made (Figure S8).

A series of 126 MHz ^{13}C{^{1}H} NMR spectra of (BrMe$_2$Si)$_2$C-(SiMe$_3$)$_2$ was recorded from 293 to 213 K (Figure S9). At 293 K signals corresponding to the SiMe$_2$Br and SiMe$_3$ groups, are seen at 9.89 and 4.97 ppm, respectively. As was seen for the ^{1}H and ^{29}Si spectra, the signals in the ^{13}C spectrum split into a complicated pattern as the temperature is lowered (Figure S10). The signals are again consistent with the presence of major C_1 and a major C_2 conformers but a full analysis is hampered by the complexity and overlapping of several signals.

(ClMe$_2$Si)$_2$C(SiMe$_3$)$_2$. The degree of steric crowding in (ClMe$_2$Si)$_2$C(SiMe$_3$)$_2$ is between that of (HMe$_2$Si)$_2$C(SiMe$_3$)$_2$ and (BrMe$_2$Si)$_2$C(SiMe$_3$)$_2$ but, at readily accessible temperatures, its NMR spectra are much more similar to those of the bromide described above. Variable-temperature ^{1}H NMR spectra are shown in Figures S11 and S12, and are reminiscent of those for (BrMe$_2$Si)$_2$C(SiMe$_3$)$_2$, showing two signals at room temperature and many at low temperature. Again this is consistent with the presence of more than one conformation at low temperature. The ^{29}Si{^{1}H} inverse-gated NMR spectrum of (ClMe$_2$Si)$_2$C(SiMe$_3$)$_2$ in CDCl$_3$ at 300 K shows two broad resonances at 25.66 and −1.09 ppm, corresponding to the SiMe$_2$Cl and SiMe$_3$ groups, respectively. On lowering the temperature, these signals split into several new peaks (Figure S13), leading to numerous signals with an overall chemical shift pattern similar to that seen for (BrMe$_2$Si)$_2$C(SiMe$_3$)$_2$ at 201 K (see Figure S4). 2D ^{1}H/^{29}Si NMR shift correlation spectra of (ClMe$_2$Si)$_2$C(SiMe$_3$)$_2$ in a CDCl$_3$/acetone-d_6 solvent mixture were recorded at 203 K (Figures S14 and S15) and have a similar appearance to the analogous spectra for the bromide (Figures 3 and 4). However, the spectra for (ClMe$_2$Si)$_2$C-(SiMe$_3$)$_2$ are less well resolved than for the bromide analogue and although they are consistent with the presence of a major C_1 and a major C_2 conformer together with minor conformers a detailed analysis has not been possible (See Supporting Information for a more detailed discussion.) Several ^{1}H NMR saturation transfer experiments (Figures S16 and S17) at 203 K

were carried out in a similar manner to those described above for $(BrMe_2Si)_2C(SiMe_3)_2$. The results of these saturation transfer experiments again appear to confirm that energy exchange processes at 203 K occur between small and large population conformers as well as between different low abundance conformers. It is not known what the symmetries of these conformers are. Comparison of all ^1H NMR saturation transfer experiments of $(ClMe_2Si)_2C(SiMe_3)_2$ with those of the analogous compound $(BrMe_2Si)_2C(SiMe_3)_2$ show that the energy exchange processes occur, as might be expected, in similar ways in both compounds in solution at low temperature, although exchange processes between minor conformers of $(ClMe_2Si)_2C(SiMe_3)_2$ cannot be confirmed. A series of 126 MHz ^{13}C $\{^1H\}$NMR spectra of $(ClMe_2Si)_2C(SiMe_3)_2$ was also recorded from 293 to 203 K, (Figure S18 and S19). Unfortunately, the low-temperature spectra were complicated, and while they are generally consistent with the presence of the conformers described above, several peaks are not observed, presumably due to accidental signal overlap. Thus, a full analysis cannot be given. The Supporting Information provides further data and a more detailed discussion.

To summarize, at low temperatures it was possible to assign peaks in the multinuclear NMR spectra to conformers with different point-group symmetries. For example, a C_1 and a C_2 conformer of **2** or **3** would be expected to give rise to six and three different proton signals in the Me_3Si region, respectively. Therefore, the presence of nine large and nine small proton signals in the ^1H NMR spectra recorded for **2** and **3** suggests that are two C_1 and two C_2 conformers are present. This is in close agreement with the results of the quantum-chemical calculations.

(HMe_2Si)_2C(SiMe_3)_2. Similar ^1H and ^{29}Si NMR spectra were recorded for $(HMe_2Si)_2C(SiMe_3)_2$ at 213 K. These, however, showed no significant changes when compared to the corresponding spectra recorded at ambient temperature. The ^1H NMR spectrum at 213 K showed a singlet at 0.15 ppm ($SiMe_3$), a doublet ($SiMe_2H$) at 0.24 ppm and a septet ($SiMe_2H$) at 4.04 ppm. Two signals were seen in the $^{29}Si\{^1H\}$ INEPT NMR spectrum of $(HMe_2Si)_2C(SiMe_3)_2$, one at -16.49 ppm due to the $SiMe_2H$ groups and one at -0.46 ppm due to the $SiMe_3$ groups. The proton coupled ^{29}Si NMR spectrum shows complicated multiplets. The signal at -16.49 ppm splits into two multiplets which selective decoupling ^{29}Si DEPT NMR experiments show are due to the expected large doublet $^1J_{Si-H}$ (182.3 Hz), a septet $^2J_{Si-H}$ (6.4 Hz, coupling to two Me groups) and smaller doublet $^3J_{Si-H}$ (3.2 Hz, coupling to Si−H on remote Si). The lack of dynamic processes being observed at low temperatures is presumably due to the relatively small size of H compared to the halides.

X-ray Crystallographic Study. Several unsuccessful attempts were made to carry out single-crystal X-ray diffraction structural analysis of $(Me_3Si)_2C(SiMe_2Br)_2$ at 100 K in an attempt to freeze out any dynamic disorder present. $(Me_3Si)_2C(SiMe_2Br)_2$ was determined to belong to the cubic space group $Pa\overline{3}$ with unit cell lengths of 12.58 Å. This space group requires complete disorder of bromine positions along with at least two different sets of silicon positions. The disorder present precluded the identification of any specific conformer and no model structures could be obtained. A similar problem was noted previously for $C(SiMe_2I)_4$, which also gave a cubic cell with $a = 12.982(1)$ Å.[64]

ASSOCIATED CONTENT

Ⓢ Supporting Information

Additional details relating to the GED experiments (Table S1), least-squares correlation matrices (Tables S2−S4), calculated coordinated and energies (Tables S5−S7), details from the GED models and refinements, including amplitudes of vibration and curvilinear distance corrections (Tables S8−S13), final GED coordinates (Tables S14−S16), plots of molecular-scattering intensity curves (Figure S1), details of the NMR spectroscopic studies (Tables S17−S21, Figures S2−S19) and the full ref 41. This material is available free of charge via the Internet at http://pubs.acs.org.

AUTHOR INFORMATION

Corresponding Authors
*E-mail: derek.wann@york.ac.uk (D.A.W.).
*E-mail: p.lickiss@imperial.ac.uk (P.D.L.).

Notes
$^\perp$Deceased
The authors declare no competing financial interest.

ACKNOWLEDGMENTS

REFERENCES

(1) Eaborn, C. Unusual Mechanistic Pathways. The Novel Chemistry of Compounds with Tris(trimethylsilyl)methyl or Related Ligands on Silicon. *J. Chem. Soc., Dalton Trans.* **2001**, 3397−3406.

(2) Eaborn, C.; Smith, J. D. Organometallic Compounds Containing Tris(trimethylsilyl)methyl or Related Ligands. *J. Chem. Soc., Dalton Trans.* **2001**, 1541−1552.

(3) Lickiss, P. D. *Comprehensive Organic Functional Group Transformations*; Katritzky, A. R.; Meth-Cohn, O.; Rees, C. W., Eds.; Pergamon: Oxford, U.K., 1995, Vol. 6, p377.

(4) Lickiss, P. D. *Comprehensive Organic Functional Group Transformations II*; Katritzky, A. R.; Taylor, R. J. K, Eds.; Elsevier: Oxford, U.K., 2005, Vol. 6, p381.

(5) Eaborn, C.; Jones, K. L.; Lickiss, P. D. Anchimeric Assistance by γ-aryl Groups in Reactions of Organosilicon Iodides. *J. Chem. Soc., Perkin Trans. 2* **1992**, 489−495.

(6) Eaborn, C.; Kowalewska, A.; Smith, J. D.; Stanczyk, W. A. Anchimeric Assistance by γ-substituents Z, Z=MeO, PhO, MeS or PhS, in Reactions of the Bromides $(Me_3Si)_2(ZMe_2Si)CSiMe_2Br$ with $AgBF_4$. *J. Organomet. Chem.* **2001**, *640*, 29−36.

(7) Eaborn, C.; Lickiss, P. D. Some Tetrasilylmethane Derivatives. *J. Organomet. Chem.* **1985**, *294*, 305−313.

(8) Al-Juaid, S. S.; Eaborn, C.; Habtemariam, A.; Hitchcock, P. B.; Smith, J. D. Reactions of Sterically Hindered Organozinc and Organocadmium Compounds Containing Functional Silicon Centres. Crystal Structures of $Zn[C(SiMe_3)_2(SiMe_2OCOCF_3)]_2$ and $Cd[C(SiMe_3)_2(SiMe_2OMe)]_2$. *J. Organomet. Chem.* **1992**, *437*, 41−55.

(9) Eaborn, C.; Reed, D. E. Preparation and Reactions of Difunctional Sterically Hindered Organosilicon Compounds of the Type (Me$_3$Si)$_2$C(SiMe$_2$X)(SiMe$_2$Y). *J. Chem. Soc., Perkin Trans. 2* **1985**, 1687–1693.

(10) Eaborn, C.; Lickiss, P. D.; Taylor, A. D. Reactions of the Sterically Hindered Organosilicon Diol (Me$_3$Si)$_2$C(SiMe$_2$OH)$_2$ and Some of its Derivatives. *J. Organomet. Chem.* **1988**, *340*, 283–292.

(11) Ayoko, G. A.; Eaborn, C. Anchimeric Assistance by and Migration of the Vinyl Group in Reactions of Sterically Hindered Organosilicon Compounds of the Type (Me$_3$Si)$_2$C(SiMe$_2$CH=CH$_2$)(SiR$_2$X). *J. Chem. Soc., Perkin Trans. 2* **1987**, 1047–1058.

(12) Ayoko, G. A.; Eaborn, C. Reactions of Bis[dimethyl(vinyl)-silyl]bis(trimethylsilyl)methane, (Me$_3$Si)$_2$C(SiMe$_2$CH=CH$_2$)$_2$. *J. Chem. Soc., Perkin Trans. 2* **1987**, 381–383.

(13) Eaborn, C.; Hopper, S. P. The Reactions of Tris(trimethylsilyl) silicon Iodides and Hydrides with Iodine Monochloride. *J. Organomet. Chem.* **1980**, *192*, 27–32.

(14) Seyferth, D.; Lefferts, J. L. 1,1,3,3-tetramethyl-2,2,4,4-tetrakis-(trimethylsilyl)-1,3- disilacyclobutane and its 1,3-Digerma and 1,3-Distanna Analogs: Unexpected Products from the Reaction of Bis(trimethylsilyl)bromomethyllithium with Dimethyldihalo Derivatives of Silicon, Germanium and Tin. *J. Organomet. Chem.* **1976**, *116*, 257–273.

(15) Damja, R. I.; Eaborn, C.; Sham, W. C. Reactions of (Me$_3$Si)$_3$CSiMe$_2$R Compounds (R = CH=CH$_2$, CH$_2$CH=CH$_2$, C≡CPh, Ph, and CH$_2$Ph) with Electrophiles. *J. Organomet. Chem.* **1985**, *291*, 25–33.

(16) Eaborn, C.; Jones, K. L.; Lickiss, P. D. Reactions of Compounds of the Type (Me$_3$Si)$_2$C(SiMe$_2$C$_6$H$_4$Y)(SiMe$_2$X) with Trifluoroacetic Acid. *J. Organomet. Chem.* **1993**, *461*, 31–34.

(17) Eaborn, C.; Jones, K. L.; Lickiss, P. D. Preparation of the Iodides (Me$_3$Si)$_2$C(SiMe$_2$C$_6$H$_4$Y)(SiMe$_2$I) and Some Related Compounds. *J. Organomet. Chem.* **1994**, *466*, 35–42.

(18) Buttrus, N. H.; Eaborn, C.; Hitchcock, P. B.; Lickiss, P. D.; Taylor, A. D. Hydrogen Bonding in Organosilicon Hydroxides: Crystal Structures of Dicyclohexylsilanediol and Bis(hydroxydimethylsilyl)bis-(trimethylsilyl)methane. *J. Organomet. Chem.* **1986**, *309*, 25–33.

(19) Eaborn, C.; Lickiss, P. D.; Ramadan, N. A. Cleavage of Silicon–Carbon Bonds in Tris(trimethylsilyl)methylsilicon Compounds by Trifluoroacetic Acid. Rearrangements and Anchimeric Assistance. *J. Chem. Soc., Perkin Trans. 2* **1984**, 267–270.

(20) Eaborn, C.; Lickiss, P. D.; Taylor, A. D. Anchimeric Assistance by the Acetoxy Group in the Solvolysis of (Me$_3$Si)$_2$C(SiMe$_2$OCOMe)-(SiMe$_2$X), X = Cl, NCS or N$_3$. *J. Chem. Soc., Perkin Trans. 2* **1994**, 1809–1813.

(21) Eaborn, C.; Lickiss, P. D.; Taylor, A. D. The Nature of the Anchimeric Assistance by the Acetoxy Group in Solvolysis of (Me$_3$Si)$_2$C(SiMe$_2$)OCOMe)(SiMe$_2$Cl). *J. Organomet. Chem.* **1988**, *338*, C27–C29.

(22) Eaborn, C.; Lickiss, P. D.; Najim, S. T.; Romanelli, M. N. 1,3-Migration of Chloride and Azide Substituents Within Organosilicon Cations, and Anchimeric Assistance by the Azido Group. *J. Organomet. Chem.* **1986**, *315*, C5–C8.

(23) Helluy, X. J.; Kuemmerlen, J.; Sebald, A. Comparative Solid-State NMR Study of the Molecular Dynamics of Si(SiMe$_3$)$_4$ and C(SiMe$_3$)$_4$. *Organometallics* **1998**, *17*, 5003–5008.

(24) Aliev, A. E.; Harris, K. D. M.; Apperley, D. C.; Harris, R. K. Solid State Dynamic Properties of Tetrakis(trimethylsilyl)methane: High-Resolution Solid State ^{13}C and ^{29}Si NMR Investigations. *J. Solid State Chem.* **1994**, *110*, 314–320.

(25) Aliev, A. E.; Harris, K. D. M. Natural Abundance Solid State ^{2}H NMR Studies of Phase Transitions in Rotator Phase Solids. *Mendeleev Commun.* **1993**, 153–155.

(26) Wrackmeyer, B.; Zhou, H. Trimethylsilyl-, Trimethylstannyl- and Trimethylplumbylmethane Derivatives Studied by One- and Two-Dimensional Multinuclear Magnetic Resonance – Sign Inversion of the coupling constants $^1J(^{207}\text{Pb}^{13}\text{C})$. *Spectrochim. Acta, Part A* **1991**, *47*, 849–856.

(27) Dereppe, J. M.; Magill, J. H. Molecular Movements and Phase Transitions in Solids. Tetrakis(trimethylsilyl)methane. *J. Phys. Chem.* **1972**, *76*, 4037–4039.

(28) Lerner, H. W.; Bolte, M. Tetrakis(trimethylsilyl)methane. *Acta Crystallogr. E* **2005**, *61*, 2326–2327.

(29) Dinnebier, R. E.; Carlson, S.; van Smaalen, S. Bulk Modulus and High-Pressure Crystal Structures of Tetrakis(trimethylsilyl)methane C[Si(CH$_3$)$_3$]$_4$ Determined by X-ray Powder Diffraction. *Acta Crystallogr. B* **2000**, *56*, 310–316.

(30) Dinnebier, R. E.; Dollase, W. A.; Helluy, X.; Kummerlen, J.; Sebald, A.; Schmidt, M. U.; Pagola, S.; Stephens, P. W.; van Smaalen, S. Order-Disorder Phenomena Determined by High-Resolution Powder Diffraction: the Structures of Tetrakis(trimethylsilyl)methane C[Si(CH$_3$)$_3$]$_4$ and Tetrakis(trimethylsilyl)silane Si[Si(CH$_3$)$_3$]$_4$. *Acta Crystallogr. B* **1999**, *55*, 1014–1029.

(31) Beagley, B.; Pritchard, R. G.; Titiloye, J. O. On the *T* Symmetry of the Molecule Tetrakis(trimethylsilyl)methane in the Gas Phase. *J. Mol. Struct.* **1989**, *212*, 323–324.

(32) Beagley, B.; Pritchard, R. G.; Titiloye, J. O. The Molecular Structure of Tetrakis(trimethylsilyl)methane Studied by Gas-Phase Electron Diffraction and Molecular Mechanics. *J. Mol. Struct.* **1988**, *176*, 81–87.

(33) Iroff, L. D.; Mislow, K. Molecules with *T* symmetry. Conformational Analysis of Systems of Type M[C(CH$_3$)$_3$]$_4$ and M[Si(CH$_3$)$_3$]$_4$ by the Empirical Force Field Method. *J. Am. Chem. Soc.* **1978**, *100*, 2121–2126.

(34) Bürger, H.; Goetze, U.; Sawodny, W. Schwingungsspektren und Kraftkonstanten der Verbindungsklasse [(CH$_3$)$_3$Si]$_4$El^{IV} (El^{IV} = C, Si, Ge, Sn). Vergleich von (CH$_3$)$_3$Si-Derivaten der 4–7. Hauptgruppe. *Spectrochim. Acta, Part A* **1970**, *26*, 685–693.

(35) Eaborn, C.; Hitchcock, P. B.; Lickiss, P. D.; Pidcock, A.; Safa, K. D. Crystal Structure and Variable-Temperature Hydrogen-1 Nuclear Magnetic Resonance Spectrum of (Dimethylnitratosilyl)-[methyldiphenylsilyl]bis(trimethylsilyl)methane, C-(SiMe$_3$)$_2$(SiMePh$_2$)(SiMe$_2$ONO$_2$). *J. Chem. Soc., Dalton Trans.* **1984**, 2015–2017.

(36) Avent, A. G.; Lickiss, P. D.; Pidcock, A. Structure and Dynamics of Hindered Organosilicon Compounds. The Conformation and Enantiotopomerization of (Chlorodiphenylsilyl)-(methoxydimethylsilyl)bis(trimethylsilyl)methane. *J. Organomet. Chem.* **1988**, *341*, 281–291.

(37) Avent, A. G.; Bott, S. G.; Ladd, J. A.; Lickiss, P. D.; Pidcock, A. Structure and Dynamics of Hindered Organosilicon Compounds. The Conformations of Symmetrical (Me$_3$Si)$_3$C and (PhMe$_2$Si)$_3$C Derivatives. *J. Organomet. Chem.* **1992**, *427*, 9–21.

(38) Anderson, D. G.; Rankin, D. W. H.; Robertson, H. E.; Cowley, A. H.; Pakulski, M. Determination of the Gas-Phase Molecular Structure of Tris(trimethylsilyl)(trichlorosilyl) Methane by Electron Diffraction. *J. Mol. Struct.* **1989**, *196*, 21–29.

(39) Morrison, C. A.; Rankin, D. W. H.; Robertson, H. E.; Lickiss, P. D.; Masangane, P. C. The Synthesis of C[Si(CH$_3$)$_2$X]$_3$SiX$_3$ Compounds (X = H, Cl, Br and OH) and the Molecular Structure of C[Si(CH$_3$)$_2$H]$_3$SiH$_3$ in the Gas Phase; a Study by Electron Diffraction and *ab Initio* Molecular Orbital Calculations. *J. Chem. Soc., Dalton Trans.* **1999**, 2293–2302.

(40) Wann, D. A.; Young, S.; Bätz, K.; Masters, S. L.; Avent, A. G.; Rankin, D. W. H.; Lickiss, P. D. Structures of Tetrasilylmethane Derivatives C(SiXMe$_2$)$_4$ (X = H, F, Cl, Br) in the Gas Phase and their Dynamic Structures in Solution. *Z. Naturforsch. B* **2014**, *69*, 1321–1332.

(41) Frisch, M. J.; Trucks, G. W.; Schlegel, H. B.; Scuseria, G. E.; Robb, M. A.; Cheeseman, J. R.; Montgomery, J. A., Jr.; Vreven, T.; Kudin, K. N.; Burant, J. C. et al. Gaussian 03, Revision C.01; Gaussian, Inc.: Wallingford, CT, 2004. See Supporting Information for full reference text.

(42) Edinburgh Compute and Data Facility (ECDF); http://www.ecdf.ed.ac.uk/.

(43) EPSRC-funded NSCCS; http://www.nsccs.ac.uk/.

(44) Becke, A. Density-Functional Thermochemistry. III. The Role of Exact Exchange. *J. Chem. Phys.* **1993**, *98*, 5648−5652.

(45) Lee, C.; Yang, W.; Parr, R. Development of the Colle-Salvetti Correlation-Energy Formula into a Functional of the Electron Density. *Phys. Rev. B* **1988**, *37*, 785−789.

(46) Miehlich, B.; Savin, A.; Stoll, H.; Preuss, H. Results Obtained with the Correlation Energy Density Functionals of Becke and Lee, Yang and Parr. *Chem. Phys. Lett.* **1989**, *157*, 200−206.

(47) Zhao, Y.; Truhlar, D. G. The M06 Suite of Density Functionals for Main Group Thermochemistry, Thermochemical Kinetics, Non-covalent Interactions, Excited States, and Transition Elements: Two New Functionals and Systematic Testing of Four M06-Class Functionals and 12 Other Functionals. *Theor. Chem. Acc.* **2008**, *120*, 215−241.

(48) Binkley, J.; Pople, J. A.; Hehre, W. J. Self-Consistent Molecular Orbital Methods. 21. Small Split-Valence Basis Sets for First-Row Elements. *J. Am. Chem. Soc.* **1980**, *102*, 939−947.

(49) Gordon, M.; Binkley, J.; Pople, J. A.; Pietro, W. J.; Hehre, W. J. Self-Consistent Molecular-Orbital Methods. 22. Small Split-Valence Basis Sets for Second-Row Elements. *J. Am. Chem. Soc.* **1982**, *104*, 2797−2803.

(50) Kendall, R.; Dunning, T. H.; Harrison, R. Electron Affinities of the First-Row Atoms Revisited. Systematic Basis Sets and Wave Functions. *J. Chem. Phys.* **1992**, *96*, 6796−6808.

(51) Wilson, A.; van Mourik, T.; Dunning, T. H. Gaussian Basis Sets for use in Correlated Molecular Calculations. VI. Sextuple Zeta Correlation Consistent Basis Sets for Boron Through Neon. *J. Mol. Struct.* **1996**, *388*, 339−349.

(52) Woon, D. E.; Dunning, T. H. Gaussian Basis Sets for use in Correlated Molecular Calculations. III. The Atoms Aluminum Through Argon. *J. Chem. Phys.* **1993**, *98*, 1358−1371.

(53) Peterson, K. A.; Figgen, D.; Goll, E.; Stoll, H.; Dolg, M. Systematically Convergent Basis Sets with Relativistic Pseudopotentials. II. Small-Core Pseudopotentials and Correlation Consistent Basis Sets for the Post-d Group 16−18 Elements. *J. Chem. Phys.* **2003**, *119*, 11113−11123.

(54) Møller, C.; Plesset, M. Note on the Approximation Treatment for Many-Electron Systems. *Phys. Rev.* **1934**, *46*, 618−622.

(55) Huntley, C. M.; Laurenson, G. S.; Rankin, D. W. H. Gas-Phase Molecular Structure of Bis(difluorophosphino)amine, Determined by Electron Diffraction. *J. Chem. Soc., Dalton Trans.* **1980**, 954−957.

(56) Fleischer, H.; Wann, D. A.; Hinchley, S. L.; Borisenko, K. R.; Lewis, J. R.; Mawhorter, R. J.; Robertson, H. E.; Rankin, D. W. H. Molecular Structures of Se(SCH$_3$)$_2$ and Te(SCH$_3$)$_2$ using Gas-Phase Electron Diffraction and *ab Initio* and DFT Geometry Optimisations. *Dalton Trans.* **2005**, 3221−3228.

(57) Hinchley, S. L.; Robertson, H. E.; Borisenko, K. R.; Turner, A. R.; Johnston, B. F.; Rankin, D. W. H.; Ahmadian, M.; Jones, J. N.; Cowley, A. H. The Molecular Structure of Tetra-*tert*-butyldiphosphine: an Extremely Distorted, Sterically Crowded Molecule. *Dalton Trans.* **2004**, 2469−2476.

(58) Ross, A. W.; Fink, M.; and Hilderbrandt, R. *International Tables for Crystallography*; Wilson, A. J. C., Ed.; Kluwer Academic Publishers: Dordrecht, The Netherlands, 1992, Vol. C, p245.

(59) Mitzel, N. W.; Smart, B. A.; Blake, A. J.; Robertson, H. E.; Rankin, D. W. H. Conformational Analysis of 1,4-Disilabutane and 1,5-Disilapentane by Combined Application of Gas-Phase Electron Diffraction and *ab Initio* Calculations and the Crystal Structure of 1,5-Disilapentane at Low Temperatures. *J. Phys. Chem.* **1996**, *100*, 9339−9347.

(60) Blake, A. J.; Brain, P. T.; McNab, H.; Miller, J.; Morrison, C. A.; Parsons, S.; Rankin, D. W. H.; Robertson, H. E.; Smart, B. A. Structure Analysis Restrained by Ab Initio Calculations: The Molecular Structure of 2,5-Dichloropyrimidine in Gaseous and Crystalline Phases. *J. Phys. Chem.* **1996**, *100*, 12280−12287.

(61) Mitzel, N. W.; Rankin, D. W. H. SARACEN − Molecular Structures from Theory and Experiment: the Best of Both Worlds. *Dalton Trans.* **2003**, 3650−3662.

(62) Sipachev, V. A. Calculation of Shrinkage Corrections in Harmonic Approximation. *J. Mol. Struct. (THEOCHEM)* **1985**, *121*, 143−151.

(63) Masters, S. L.; Atkinson, S. J.; Hölbling, M.; Hassler, K. Gas-Phase Molecular Structure of 1,1,1,2-tetrabromo-2,2-dimethyldisilane: Theoretical and Experimental Investigation of a Super-Halogenated Disilane and Computational Investigation of the F, Cl and I Analogues. *Struct. Chem.* **2013**, *24*, 1201−1206.

(64) Lickiss, P. D. D.Phil. Thesis, University of Sussex, 1983.

A compact electron gun for time-resolved electron diffraction

Matthew S. Robinson, Paul D. Lane,[a)] and Derek A. Wann[b)]
Department of Chemistry, University of York, Heslington, York YO10 5DD, United Kingdom

A novel compact time-resolved electron diffractometer has been built with the primary goal of studying the ultrafast molecular dynamics of photoexcited gas-phase molecules. Here, we discuss the design of the electron gun, which is triggered by a Ti:Sapphire laser, before detailing a series of calibration experiments relating to the electron-beam properties. As a further test of the apparatus, initial diffraction patterns have been collected for thin, polycrystalline platinum samples, which have been shown to match theoretical patterns. The data collected demonstrate the focusing effects of the magnetic lens on the electron beam, and how this relates to the spatial resolution of the diffraction pattern. © *2015 AIP Publishing LLC.* [http://dx.doi.org/10.1063/1.4905335]

I. INTRODUCTION

Since the work of Davisson and Germer in 1927,[1] the interactions of electron beams with gaseous and crystalline samples have been used extensively to determine the structures of molecular species. Conventional gas electron diffraction experiments, using continuous beams of electrons, are typically conducted over timescales ranging from significant fractions of a second to many minutes or even hours. One consequence of this is that the structures determined are time averaged, with any information about dynamic structural effects being lost. Since the development of ultrafast laser sources and the subsequent application of femtochemical techniques to spectroscopy,[2] electron diffraction has adapted to allow studies to be performed on sub-picosecond timescales.[3] This has now advanced to the point where molecular movies can be recorded, showing the evolution of molecular structures during induced chemical and physical processes.[4]

The early steps in time-resolved electron diffraction (TRED) were taken by Ischenko, who, in 1983, demonstrated a stroboscopic beam of electrons allowing molecular structures to be obtained with microsecond time resolution.[5] These experiments involved the use of electromagnetic deflector plates to manipulate a continuous electron beam and chop it into pulses before performing pump-probe experiments on the photodissociation of excited CF_3I molecules.[5] In 1992, Ewbank introduced a new method of producing short bunches of electrons using a laser and a photocathode;[6] this enabled shorter electron pulses to be obtained more easily. Much of the subsequent early work in this area was performed by Zewail, who achieved electron diffraction with a time resolution on the picosecond timescale.[7–10] Zewail also developed important theory underpinning TRED experiments, detailing the velocity mismatch problem that exists between electron pulses and laser pulses, and proposed changes to the geometry of the beams in the interaction region to minimize velocity mismatch.[11] Further theoretical advances were made by Qian,[12,13] and by

Siwick,[14,15] who debated in the literature the implications of space-charge broadening and how this limits the temporal resolution of the TRED technique. A number of methods have since been employed to obtain better temporal resolution in TRED experiments, including the application of radio-frequency (RF) cavities,[16–18] single-electron electron diffraction,[19,20] and electron diffraction using MeV electrons;[21–23] the latter has the potential to allow single-shot experiments, removing the limitation of studying reversible systems.

A number of studies have been performed using TRED to look at order-disorder transitions such as the melting of aluminum,[21,24,25] as well as order-order transitions in cyclohexadiene,[26] silicon,[27] graphite,[28] bismuth,[29] diarylethene,[30] and ethylene-dioxytetrathiafulvalene (EDO-TTF).[4] The application of TRED in reflection mode (rather than transmission mode) also allows time-resolved studies of surfaces to be performed.[31,32] The majority of studies using TRED have involved crystalline and polycrystalline samples, with relatively few studies published for gas-phase samples beyond the early work of Zewail.[33] One notable exception is the work of Centurion,[34] who recently showed that it is possible to use electron pulses to obtain non-circularly symmetric gas-phase diffraction patterns, by temporarily aligning molecules non-adiabatically with ultrafast laser pulses. Upon resolving these patterns using holographic methods, an increase in the amount of data collected is observed compared to experiments using randomly oriented samples of molecules.[34]

The apparatus described here has been developed primarily to look at molecules in the gas phase, allowing the structures and dynamics of species to be determined in an environment where they are free from solvent interactions and packing forces. Structural information will be obtained for photoactive species with an atomic level of detail not achievable using spectroscopic techniques alone. The diffractometer produces electrons by ionizing a gold photocathode using the third harmonic ($\lambda = 267$ nm) of a Ti:Sapphire laser. The electrons are accelerated across a potential of up to 100 kV towards a grounded anode, after which they propagate in a field-free region where they encounter a sample and are scattered, with the resulting diffraction pattern recorded using a phosphor screen/charge coupled device (CCD) detector.

---

a)Present address: Department of Physics, University of Strathclyde, 107 Rottenrow East, Glasgow G4 0NG, United Kingdom.
b)Electronic mail: derek.wann@york.ac.uk

II. SPACE-CHARGE EFFECTS

One of the main challenges in developing a time-resolved electron diffractometer is minimizing the effects of space-charge repulsion, a factor that has strongly influenced the design of this instrument. While the electron pulses created at the photocathode have similar properties to the laser pulses used to create them,[35] the negative charges mean that the electrons within the pulses repel one another causing the pulses to expand both spatially and temporally. This process starts immediately after the electron pulses leave the photocathode and continues as they propagate through the system. The rate at which the electron pulses expand depends on a number of factors including the initial pulse duration, the number of electrons in the pulse, and the group velocity of the pulse. Siwick et al.[14] reported that a pulse containing 10^4 electrons, accelerated across 30 keV, with an initial duration of 50 fs will have expanded to approximately 6.5 ps after propagating for 4 ns. Moreover, shorter laser pulses produce electron bunches that expand more rapidly because of the greater initial charge density.[14]

Using pulses containing a single electron can effectively nullify the space-charge effects,[17] though implementing such an approach would vastly increase the time required to record data. Another potential tactic for avoiding space-charge repulsion involves using MeV electrons, as Columbic repulsion is far less of a problem when approaching relativistic speeds.[18] However, creating MeV electrons requires the use of a linear accelerator and, while such instruments exist,[18] the further development of tabletop systems is vital to enable cost-effective studies that are accessible to more researchers.

The velocity distribution of the electrons produced by a photocathode can be described as a linear chirp,[14] with the electrons at the front of the pulse being accelerated by the electrons behind them, while the electrons at the rear of the pulse are decelerated by the electrons in front of them. Applying a rapidly switching RF electric field[36] allows the electrons at the front of the pulse to be slowed down and the electrons at the back of the pulse to be accelerated, thus compressing the pulse in the temporal dimension as demonstrated by Miller,[17] and by Siwick.[18] Another approach taken by Schwoerer utilizes the space-charge repulsion to create picosecond electron pulses.[37] A streak camera deflects each pulse in the transverse direction enabling the observation of the entire temporal profile of the pulse at the detector. This has the potential to allow the molecular dynamics of a sample to be recorded in a single shot rather than as a series of experiments with varying pump-probe delay times.[38]

III. INSTRUMENT

For the TRED apparatus described here, we have chosen to address the space-charge problem by designing a compact electron gun; this minimizes the distance that the electrons travel between the gun and the sample, thus limiting the degree of expansion of the pulse. Particle tracing simulations, using General Particle Tracer[39] and SIMION,[40] indicate that a pulse containing 10^4 electrons will have a duration of approximately 1.3 ps full width at half maximum (FWHM) at 45 kV when the

sample is positioned 130 mm from the anode. At this voltage, a FWHM transverse beam diameter of 0.34 mm is predicted at the sample, when using a 150 μm aperture in the anode of the electron gun. Assuming that one can set the transverse diameter of both the laser and molecular beams to a similar size (i.e., ~0.35 mm) an overall experimental time resolution of 2.5 ps is predicted at 45 kV with the experimental set-up described here, where all three beams are orthogonal to one another. Future routine experiments, carried out at 100 kV, are predicted to have pulse durations of 375 fs FWHM, and will also make use of a 150 μm aperture in the anode to produce a FWHM transverse beam diameter of 0.14 mm at the sample. Again, assuming that one can produce both a laser and molecular beam with similar transverse widths (i.e., ~0.15 mm), and intersect the pump and probe beams at an angle of approximately 60°, an experimental time resolution of 670 fs is predicted.[41] Figure 1 shows the layout of the apparatus with the main components of the system discussed in detail below.

A. Optics

The laser system used for the TRED experiments consists of a Ti:Sapphire oscillator and an amplifier to produce pulses of 150 fs at a central wavelength of 800 nm (80 nm bandwidth); the repetition rate is 1 kHz and the beam power is approximately 1 W. The laser beam is then separated into two branches using a 70:30 beam splitter, with 30% of the beam being used to create the electron probe pulse and the remaining 70% used as a pump laser to excite samples. Detailed discussion of pump-probe methodologies is beyond the scope of this paper; for more information on this subject, we refer the reader to Ref. 3. In order to create the electron probe pulse, the laser beam is passed through a frequency tripling system to produce pulses of 267 nm wavelength, which are then separated from the fundamental and second harmonic frequencies using dichroic mirrors. For the experiments described below, the third-harmonic beam (maximum pulse energy approximately 200 nJ) is focused onto the photocathode of the electron gun with a spot size diameter of approximately 200 μm. Small changes in the focus of the laser beam did not appear to affect the electron beam produced from the photocathode. Using an
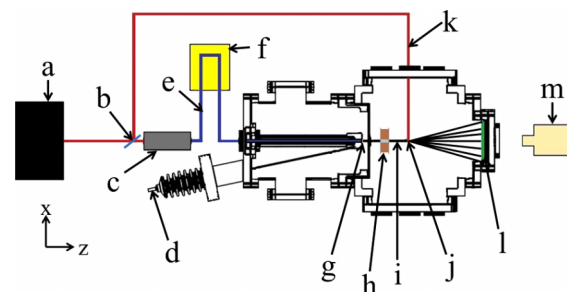

FIG. 1. A schematic diagram (not to scale) of the TRED apparatus showing (a) Ti:Sapphire laser, (b) 70:30 beam splitter, (c) third-harmonic-generation setup, (d) high-voltage feed through, (e) electron ionization laser path, (f) delay stage, (g) photocathode, (h) magnetic lens, (i) electron beam, (j) sample position/interaction region, (k) pump laser path, (l) electron detector, and (m) CCD camera.

unfocused laser, however, results in almost no electrons being produced.

B. Electron gun

The TRED apparatus is designed with the electron gun housed in a differentially pumped vacuum chamber, separate from the diffraction zone. This minimizes the amount of sample gas that can enter the electron gun chamber, as that would increase the likelihood of electrical discharging. The gun chamber typically operates at a pressure of 5×10^{-8} millibars, with a titanium anode forming the boundary between this chamber and the diffraction chamber. In the center of the anode is an aperture allowing the electrons to exit the gun chamber.

The electron gun comprises of a photocathode (labelled (a) in Figure 2), stainless steel electrode (b), and ceramic tube (c). The photocathode is back illuminated by the 267 nm laser light, and is of similar design to the one described by Siwick.[35] It consists of a sapphire disc (13 mm diameter and 0.5 mm thick) coated with a 25 nm layer of gold on the front side and with a 200 nm metallic coating around the edges to provide an electrical contact with the electrode. The majority of the back of the sapphire disc is masked during preparation and remains uncoated so that the laser light can pass through the sapphire disc and reach the gold film on the front. This photocathode sits tightly in a recess on the electrode, with the front of the photocathode flush with the outer edge of the electrode to minimize discontinuities in the electric field that might lead to discharging. The electrode is mounted on a 315 mm long ceramic tube with ribbing on the surface to maximize the surface area and reduce charge creep.[42] The laser beam enters the chamber through a deep ultraviolet (DUV) sapphire viewport in the rear flange and passes through the inner bore of this ceramic tube to the photocathode.

A potential of up to 100 kV is applied to the electrode using a high-precision Heinzinger power supply attached to the high-voltage feed through (d), with a number of precau-

tions taken to reduce the probability of the high-voltage power supply arcing to the chamber. The high-voltage feed through enters the chamber through the rear flange of the electron gun at an angle of 12° to the axis of the ceramic tube. This keeps the bare high-voltage pin (e) far away as possible from the grounded walls of the chamber, and prevents it from having to be bent in order to reach the electrode. The electrode itself is enclosed by a ceramic cup leaving only the photocathode exposed, again to help prevent arcing. The photocathode-to-anode distance used in the experiments described here was 17 mm, although this distance can be adjusted with the introduction of spacer plates. In the center of the anode plate (f), there is an anode plug (g) that is designed to hold various sizes of platinum apertures (of the kind typically used in electron microscopes) allowing control over the emerging electron beam. The advantage of using a smaller aperture is that a less divergent electron beam can be achieved; however, this is at the cost of a reduced number of electrons per pulse and, hence, longer data-acquisition times.

We find that using a magnetic lens to focus the electron beam allows the beam divergence to be further controlled, resulting in a narrower beam without reducing the beam current. However, the inclusion of the lens requires greater space to be left between the photocathode and the sample, resulting in a slightly poorer temporal resolution. The system was designed in as flexible a way as possible so that all of these components can be adjusted or removed as the needs of an experiment are determined. For the initial diffraction studies reported here, we use an aperture 1 mm diameter and the magnetic lens as detailed below.

C. Magnetic lens

The magnetic lens used to focus the electron beam is based on the principles of a solenoid.[43] The core of the lens is an iron spool, which is 20 mm long and with a 10 mm central bore through which the electron beam passes. Around the outside of the spool are approximately 1000 turns of Kapton-coated wire, through which a current of up to 3 A can be applied. By varying the lens current, the electron beam can be focused to reduce its diameter (spot size), which is desirable as the spatial resolution of an electron diffraction experiment is dependent on the spot size. For the 45 keV beam energy used for the initial diffraction study presented here, we find that a current range of 1.1–1.3 A is sufficient to obtain a good focus at the detector, which is 330 mm from the front of the anode. Overfocusing the electron beam can create a large Coulomb-repulsion effect that causes the beam to expand rapidly in both the spatial and temporal frames, resulting in a marked loss of resolution.

The lens is mounted on an *xyz* manipulator, allowing fine control of its position with respect to the electron beam. If the beam is not passing through the center of the lens, or if the lens winding is uneven, the beam could be deflected away from its desired position at the center of the detector. A power supply stable to within 0.01 A is used as fluctuations in current can cause the electron beam to be deflected. The heat generated by the lens must be dissipated as the resistance of the wire varies with temperature and so the lens is cooled using liquid
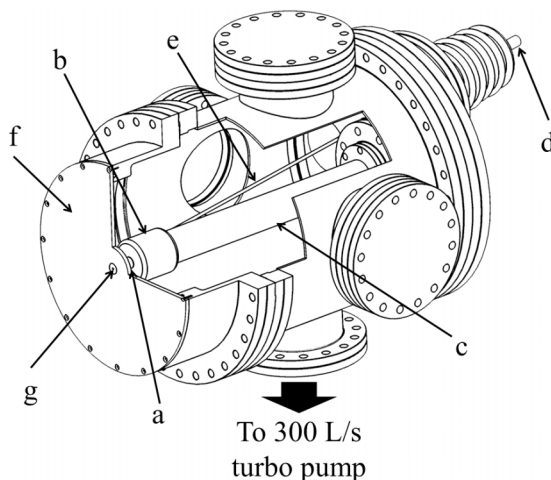

FIG. 2. A cut-through diagram of the electron-gun chamber showing (a) photocathode, (b) electrode, (c) ceramic tube, (d) high-voltage feed through, (e) high-voltage pin, (f) anode plate, and (g) anode plug.

nitrogen. A copper braid connects the liquid nitrogen vessel to the lens and the temperature is monitored using thermocouples.

D. Diffraction chamber

The apparatus has been designed primarily to study gas-phase samples and the main chamber needs to handle a large throughput of gas while maintaining an appropriate vacuum. A large turbomolecular pump attached to the base of the chamber is used to evacuate the system at a rate of up to 2200 L/s. The cubic design of the chamber allows for ports to be situated at five different anode-to-sample distances (the ports are centered at 40, 50, 130, 210, and 220 mm from the anode), allowing some control over how long the electron pulse propagates before it interacts with the sample. Having three DN40CF flanges (left, right, and top) at each distance enables the sample to be introduced through the top of the chamber (directly opposite the pump), while other components such as a cold trap and pump laser can be brought in through the side ports. The availability of pairs of opposite ports will also allow grating-enhanced ponderomotive measurements to be performed,[44] in order to determine the electron-pulse durations at the sample positions.

As a test of the apparatus, we recorded diffraction patterns for a polycrystalline sample of platinum mounted on an *xyz* translator at a distance of 115 mm from the anode (introduced through the 130 mm port); the phosphor screen detector was 215 mm beyond the sample. For future gas-phase studies, the sample holder which supports TEM grids perpendicularly to the electron beam will be replaced by a gas-inlet system, while other aspects of the apparatus setup will remain relatively unchanged.

E. Detector

Diffraction images are recorded using a micro-channel plate (MCP)/phosphor screen/CCD camera setup. An aluminum beam cup (7.5 mm in diameter) is mounted in front of the center of the detector to prevent the unscattered electron beam from hitting the phosphor which could both damage the screen and result in a very bright spot of light that would dominate the diffraction pattern; it also acts as a Faraday cup to measure the current of the electron beam. Electrons scattered by the diffraction sample first encounter a grounded mesh ensuring that they propagate through a field-free region. Immediately after the mesh is the MCP, which has an active area 80 mm in diameter; a potential of up to +2 kV is applied across the MCP. The enhanced diffraction pattern is then imaged on a 115 mm phosphor screen, comprising a 3 mm thick glass plate coated with 50 μm of P22 phosphor and 50 nm of aluminum, allowing for the dissipation of charge. The screen is held in an aluminum mount at a potential of up to +5 kV relative to the grounded mesh, and this is further mounted on a DN160CF flange with a viewport through which a Stingray F-146B CCD records the diffraction patterns. The camera is coupled to a Schneider 17 mm focal-length lens with an f/0.95 aperture, allowing the camera to be positioned a few millimeters from the viewport with the whole screen visible; the wide aperture allows the lens to work well in low light conditions.

Image enhancement using the MCP was incorporated into the design because of the very small beam currents used in the TRED experiments. For each electron that impinges on a pore in the MCP, approximately 10^6 additional electrons are produced to enhance the image.[45] Without the MCP, we were able to image unscattered electron beams only when there were more than 5000 electrons per pulse; in this set-up, observing a diffraction pattern was difficult even when recording images for a number of hours. With the MCP, it was possible to observe an image of a beam with a current that was below the noise level of the picoammeter used to record the current (estimated to be less than 500 electrons per pulse).

With the detector positioned 215 mm from the sample, it allows for diffraction data to be observed to a maximum of $s = 195$ nm^{-1}, for 45 keV electrons, where s is a function of the scattering angle, θ, and the electron wavelength, λ, such that $s = (4\pi \sin\theta)/\lambda$.

IV. CALIBRATION AND RESULTS

A. Number of electrons

The number of electrons per pulse affects both the beam spot size and pulse duration, and these in turn influence both the spatial and temporal resolutions of the apparatus. In order to obtain the desired characteristics (small transverse beam size and short electron pulse duration), it is important to be able to measure and control the number of electrons per pulse. This is achieved by varying the power of the laser reaching the photocathode by adjusting the alignment of the optical axis of the second harmonic generation (SHG) crystal. The laser power is measured using a power meter and the number of electrons determined using a picoammeter to measure the average beam current and dividing by the repetition rate of the laser. With an average laser power of approximately 0.3 W entering the harmonics setup, we can accurately measure between 10^3 and 10^7 electrons per pulse which can be varied depending on whether we required better time resolution or shorter collection times for a given experiment. Figure 3 shows the number of electrons observed per pulse with respect to the angle of the SHG crystal.
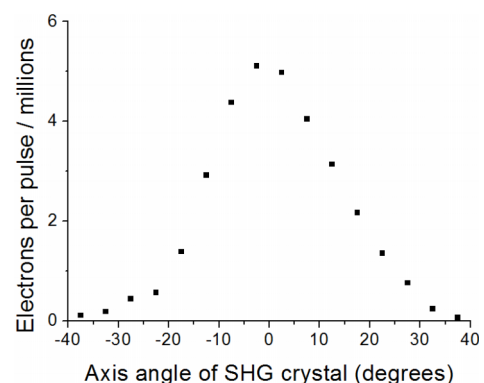

FIG. 3. The number of 45 keV electrons passing through a 1 mm diameter aperture in the anode, with respect to the axis angle of the second harmonic generation crystal.
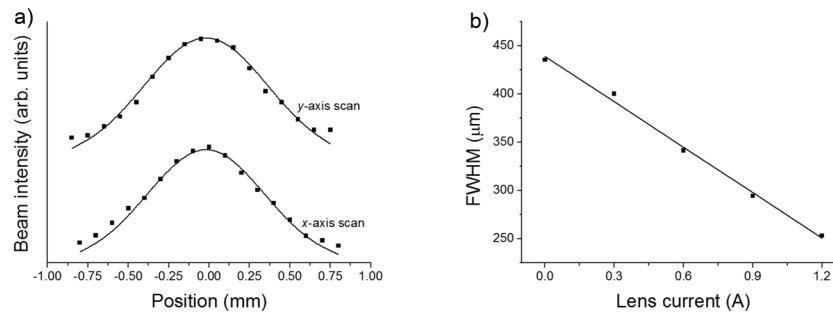
FIG. 4. (a) The perpendicular transverse beam widths (x and y) at the sample position, for a 45 keV electron beam containing approximately 10^4 electrons per pulse (average FWHM size of 435 μm, maximum intensity measured as 650 fA). (b) The average FWHM beam size at the sample position as a function of magnetic lens current.

B. Beam size and magnetic lens

In order to achieve good spatial resolution, we require the electron beam spot size to be small at the sample and at the detector. To help achieve this, the magnetic lens discussed in Sec. III C is used to focus the beam. To quantitatively demonstrate the focusing properties of the magnetic lens on the electron beam width, a beam containing approximately 10^4 electrons per pulse was directed towards a 500 μm aperture at the sample position. The aperture blocks part of the beam and those electrons that do pass through hit the Faraday cup where the current is measured. By scanning the position of the aperture across the beam and recording how the current varies, two-dimensional profiles of the beam in the x and y directions are obtained [see Figure 4(a)].

The measurements show the electron beam to be Gaussian in shape, with the FWHM beam size reducing linearly as the lens current is increased, as shown in Figure 4(b). Extensive simulations (to be published separately)[41] have also shown that, for certain lens currents, the beam will remain well collimated as it travels to the detector, with only a small increase in pulse duration predicted.

C. Diffraction

While this instrument was developed as a time-resolved gas-phase diffractometer, the first study performed was for a polycrystalline sample of platinum; the well-defined, predictable, closely spaced rings produced by a polycrystalline sample allow for the instrument to be easily calibrated without the added complexities of introducing a gaseous sample. A

20 nm thick layer of Pt was deposited onto a carbon-coated TEM grid, mounted on an *xyz* manipulator, and positioned in the electron beam. Images were recorded with potentials of +1.9 kV applied to the MCP, and +4.1 kV applied to the phosphor screen. Individual images were stacked before background images, recorded under identical conditions, but without the sample present, were subtracted from the sample data. By doing this, we remove any background electron scattering, reflected light, or systematic errors which would distort the data. For comparison of the effectiveness of our magnetic lens, diffraction patterns for the Pt sample were recorded both with the magnetic lens off and on. The scattering intensities of the observed diffraction rings for both sets of data were extracted by radially averaging around the center of the pattern using custom-written MATLAB code. The intensity curves obtained from both experiments are shown in Figure 5(a). One can clearly see that the resolution of the experiment has improved with the introduction of the magnetic lens, as the peaks become more defined, compared to the broader, overlapping, and, in some cases, barely discernible features recorded without the magnetic lens.

The extracted diffraction data have also been compared to a theoretical scattering intensity curve, shown as dashed lines in Figure 5(a), based on the expected face-centered cubic polycrystalline diffraction pattern for platinum, with peak widths based on the best electron beam width we hope to have at the detector. One can clearly see that the positions of the peaks in the theoretical and experimental data match when data are collected with the magnetic lens on. We have shown the same theoretical curve on top of the data extracted
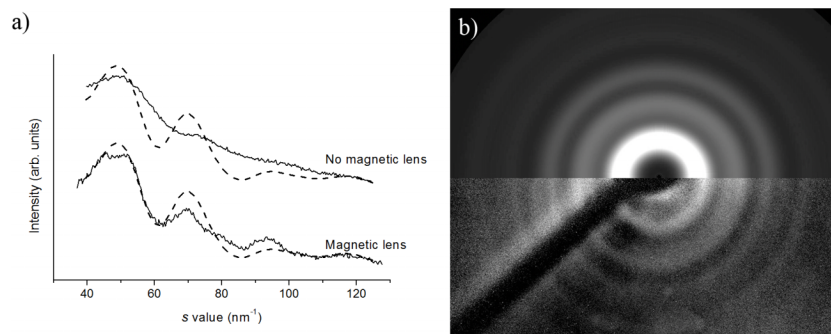

FIG. 5. (a) Comparison of diffraction intensities from experiments with the magnetic lens off (top), and on (bottom); the curves are offset for clarity. Theoretical scattering curves showing what is predicted for a well-focused electron beam are shown as a dashed line. (b) Comparison of theoretical diffraction pattern (top) and experimental diffraction pattern (bottom) collected using the magnetic lens.

from diffraction patterns recorded without the magnetic lens, highlighting the lack of resolution when the lens is omitted. From the data, it is possible to calculate the resolution of the experiment as $\Delta s = 6.7 \text{ nm}^{-1}$ with the magnetic lens present. Using the predicted scattering curve, it was also possible to create a theoretical diffraction pattern. This is overlaid on the experimental diffraction pattern in Figure 5(b), again emphasizing the match between experimental and theory.

V. SUMMARY AND CONCLUSIONS

We have designed, built, and tested an electron diffractometer that uses a compact electron gun to produce pulses of electrons predicted to have a duration of approximately 375 fs, and with a potential experimental time resolution of approximately 670 fs at 100 kV, for experiments that do not use tilted laser wavefronts.[46] We have demonstrated that this pulsed electron gun can yield diffraction patterns for a polycrystalline sample of platinum in a timely manner, and that the spatial resolution of the experiment can be enhanced with the use of a magnetic lens. Our focus now moves to performing static gas-phase studies, before collecting time-resolved data for photoinduced dynamic systems in the near future.

ACKNOWLEDGMENTS

[1]C. Davisson and L. H. Germer, Nature **119**, 558 (1927).
[2]T. S. Rose, M. J. Rosker, and A. H. Zewail, J. Chem. Phys. **88**, 6672 (1988).
[3]G. Sciaini and R. J. D. Miller, Rep. Prog. Phys. **74**, 096101 (2011).
[4]M. Gao, C. Lu, H. Jean-Ruel, L. C. Liu, A. Marx, K. Onda, S. Koshihara, Y. Nakano, X. Shao, T. Hiramatsu, G. Saito, H. Yamochi, R. R. Cooney, G. Moriena, G. Sciaini, and R. J. D. Miller, Nature **496**, 343 (2013).
[5]A. A. Ischenko, V. V. Golubkov, V. P. Spiridonov, A. V. Zgurskii, A. S. Akmanov, M. G. Vabischevich, and V. N. Bagratashvilli, Appl. Phys. B: Lasers Opt. **32**, 161 (1983).
[6]J. D. Ewbank, W. L. Faust, J. Y. Luo, J. T. English, D. L. Monts, D. W. Paul, Q. Dou, and L. Schäfer, Rev. Sci. Instrum. **63**, 3352 (1992).
[7]J. C. Williamson and A. H. Zewail, Proc. Natl. Acad. Sci. U. S. A. **88**, 5021 (1991).
[8]J. C. Williamson, M. Dantus, S. B. Kim, and A. H. Zewail, Chem. Phys. Lett. **196**, 529 (1992).
[9]J. C. Williamson, J. Cao, H. Ihee, H. Frey, and A. H. Zewail, Nature **386**, 159 (1997).
[10]H. Ihee, V. A. Lobastov, U. M. Gomez, B. M. Goodson, R. Srinivasan, C.-Y. Ruan, and A. H. Zewail, Science **291**, 458 (2001).
[11]J. C. Williamson and A. H. Zewail, Chem. Phys. Lett. **209**, 10 (1993).
[12]B.-L. Qian and H. E. Elsayed-Ali, J. Appl. Phys. **91**, 462 (2002).
[13]B.-L. Qian and H. E. Elsayed-Ali, J. Appl. Phys. **94**, 803 (2003).
[14]B. J. Siwick, J. R. Dwyer, R. E. Jordan, and R. J. D. Miller, J. Appl. Phys. **92**, 1643 (2002).
[15]B. J. Siwick, J. R. Dwyer, R. E. Jordan, and R. J. D. Miller, J. Appl. Phys. **94**, 807 (2003).
[16]T. van Oudheusden, P. L. E. M. Pasmans, S. B. van der Geer, M. J. de Loos, M. J. van der Wiel, and O. J. Luiten, Phys. Rev. Lett. **105**, 264801 (2010).
[17]M. Gao, H. Jean-Ruel, R. R. Cooney, J. Stampe, M. De Jong, M. Harb, G. Sciaini, G. Moriena, and R. J. D. Miller, Opt. Exp. **20**, 12048 (2012).
[18]R. P. Chatelain, V. R. Morrison, C. Godbout, and B. J. Siwick, Appl. Phys. Lett. **101**, 081901 (2012).
[19]J. D. Geiser and P. M. Weber, Proc. SPIE **2521**, 136 (1995).
[20]P. Baum, Chem. Phys. **423**, 55 (2013).
[21]J. B. Hastings, F. M. Rudakov, D. H. Dowell, J. F. Schmerge, J. D. Cardoza, J. M. Castro, S. M. Gierman, H. Loos, and P. M. Weber, Appl. Phys. Lett. **89**, 184109 (2006).
[22]R. Li, W. Huang, Y. Du, J. Shi, J. Hua, H. Chen, T. Du, H. Xu, and C. Tang, Rev. Sci. Instrum. **81**, 036110 (2010).
[23]P. Musumeci, J. T. Moody, C. M. Scoby, M. S. Gutierrez, and M. Westfall, Appl. Phys. Lett. **97**, 063502 (2010).
[24]B. J. Siwick, J. R. Dwyer, R. E. Jordan, and R. J. D. Miller, Science **302**, 1382 (2003).
[25]B. J. Siwick, J. R. Dwyer, R. E. Jordan, and R. J. D. Miller, Chem. Phys. **299**, 285 (2004).
[26]R. C. Dudek and P. M. Weber, J. Phys. Chem. A **105**, 4167 (2001).
[27]M. Harb, R. Ernstorfer, C. T. Hebeisen, G. Sciaini, W. Peng, T. Dartigalongue, M. A. Eriksson, M. G. Lagally, S. G. Kruglik, and R. J. D. Miller, Phys. Rev. Lett. **100**, 155504 (2008).
[28]R. K. Raman, Y. Murooka, C.-Y. Ruan, T. Yang, S. Berber, and D. Tománek, Phys. Rev. Lett. **101**, 077401 (2008).
[29]G. Sciaini, M. Harb, S. G. Kruglik, T. Payer, C. T. Hebeisen, F.-J. Meyer zu Heringdorf, M. Yamaguchi, M. Horn-von Hoegen, R. Ernstorfer, and R. J. D. Miller, Nature **458**, 56 (2009).
[30]H. Jean-Ruel, M. Gao, M. A. Kochman, C. Lu, C. Liu, R. R. Cooney, C. A. Morrison, and R. J. D. Miller, J. Phys. Chem. B **117**, 15894 (2013).
[31]A. Janzen, B. Krenzer, P. Zhou, D. Von der Linde, and M. Horn-von Hoegen, Surf. Sci. **600**, 4094 (2006).
[32]A. Hanisch-Blicharski, A. Janzen, B. Krenzer, S. Wall, F. Klasing, A. Kalus, T. Frigge, M. Kammler, and M. Horn-von Hoegen, Ultramicroscopy **127**, 2 (2013).
[33]H. Ihee, V. A. Lobastov, U. M. Gomez, B. M. Goodson, R. Srinivasan, C.-Y. Ruan, and A. H. Zewail, Science **291**, 458 (2001).
[34]C. J. Hensley, J. Yang, and M. Centurion, Phys. Rev. Lett. **109**, 133202 (2012).
[35]B. J. Siwick, "Femtosecond electron diffraction studies of strongly-driven structural phase changes," Ph.D. thesis (University of Toronto, 2004).
[36]T. van Oudheusden, E. F. de Jong, S. B. van der Geer, W. P. E. M. Op't Root, O. J. Luiten, and B. J. Siwick, J. Appl. Phys. **102**, 093501 (2007).
[37]G. H. Kassier, K. Haupt, N. Erasmus, E. G. Rohwer, H. M. von Bergmann, H. Schwoerer, S. M. M. Coelho, and F. D. Auret, Rev. Sci. Instrum. **81**, 105103 (2010).
[38]M. Eichberger, N. Erasmus, K. Haupt, G. H. Kassier, A. von Flotow, J. Demsar, and H. Schwoerer, Appl. Phys. Lett. **102**, 121106 (2013).
[39]See http://www.pulsar.nl/gpt for General Particle Tracer.
[40]D. A. Dahl, Int. J. Mass Spectrom. **200**, 3 (2000).
[41]M. S. Robinson, P. D. Lane, and D. A. Wann, "Simulations of the temporal and spatial resolutions for a compact time-resolved electron diffractometer," J. Phys. Chem. A (unpublished).
[42]G. Blaise, A. J. Duran, C. Le Gressus, B. G. A. Jüttner, R. Latham, A. Maitland, B. Mazurek, H. C. Miller, H. Padamsee, M. F. Rose, A. M. Shroff, and N. Xu, High Voltage Vacuum Insulation: Basic Concepts and Technological Practice (Harcourt Brace and Company, 1995).
[43]See for example, D. J. Griffiths, Introduction to Electrodynamics, 3rd ed. (Pearson, 1998).
[44]C. T. Hebeisen, R. Ernstorfer, M. Harb, T. Dartigalongue, R. E. Jordan, and R. J. D. Miller, Opt. Lett. **31**, 3517 (2006).
[45]R. S. Fender, "Advances in gas-phase electron diffraction," Ph.D. thesis (University of Edinburgh, 1996).
[46]P. Baum and A. H. Zewail, Proc. Natl. Acad. Sci. U. S. A. **103**, 16105 (2006).